Queen Mary, University of London

Measurement of the cross section and muon charge asymmetry from charged current Drell-Yan process at 13 TeV centre of mass energy with the ATLAS detector

Andres Ramirez-Morales

Submitted in partial fulfilment of the requirements of the
Degree of Doctor of Philosophy

London, December 2018

Declaration

I, Andres Ramirez Morales, confirm that the research included within this thesis is my own work or that where it has been carried out in collaboration with, or supported by others, that this is duly acknowledged below and my contribution indicated. Previously published material is also acknowledged below.

I attest that I have exercised reasonable care to ensure that the work is original, and does not to the best of my knowledge break any UK law, infringe any third party's copyright or other Intellectual Property Right, or contain any confidential material.

I accept that the College has the right to use plagiarism detection software to check the electronic version of the thesis.

I confirm that this thesis has not been previously submitted for the award of a degree by this or any other university.

The copyright of this thesis rests with the author and no quotation from it or information derived from it may be published without the prior written consent of the author.

Signature:

Date: 6 December 2018

Abstract

This thesis documents the measurements of the $W \to \mu\nu$ (charged current Drell-Yan Process) production cross section and the muon charge asymmetry. Experimental data and Monte Carlo samples, from proton-proton collisions at a centre of mass energy of 13 TeV, corresponding to a total integrated luminosity of 44.3 fb^{-1} are utilised; the data presented was recorded by the ATLAS experiment at the Large Hadron Collider during the year 2017. The measurements are performed differentially in muon pseudorapidity $|\eta^{\mu}|$ and are within the W boson invariant mass in a kinematic fiducial volume of muon and neutrino transverse momentum $p_T^{\mu,\nu} > 30$ GeV and muon pseudorapidity $|\eta^{\mu}| < 2.4$. The fiducial measurements uncertainties are below 2% empowering these measurements to constrain the modelling of the proton composition.

Acknowledgements

Thanks to my parents Andres Ramirez Rodriguez and Maria Guadalupe Morales Gutierrez for all the support and love I have received from them.

I would like to thank my supervisor Dr. Eram Rizvi for his support and patience during the four years of the PhD. This work would have not been completed without his guidance and encouragement.

Thanks to the people from the PPRC for their constant help and advice, specially to Adelina D'Onofrio and John Morris while working on the service task.

I am very grateful for the amazing experience of living in Switzerland, the knowledge and the friends that I found were invaluable. Specially to Stephanie Bron who made my life there significantly better.

I would like to thank my friend Rodrigo Gamboa Goni, for his friendship and keeping me sane during my PhD.

I am very lucky to have such nice flatmates Chloe Cordon, Jorge Salmon, Marc Mora and Rachel Clancy; they made the writing days much better, and thanks for the numerous BBQ's we had during the summer.

Thanks to all my friends in Mexico and the new friends that I made during my PhD, all the laughters and conversations we shared helped me a lot to overcome difficult times.

This work was supported by Consejo Nacional de Ciencia y Tecnologia (CONACYT) and Consejo Zacatecano de Ciencia, Tecnlogia e Innovacion (COZCYT).

Contents

A mis hermanas Andrea y Alejandra
To my sisters Andrea and Alejandra

Acronyms

QFTs Quantum Field Theories

EWI Electroweak Interaction

QCD Quantum Chromodynamics

SM Standard Model

LHC Large Hadron Collider

CERN Conseil Europeen pour la Recherche Nucleaire (European Organization for Nuclear Research)

pp proton-proton

ATLAS A Toroidal LHC ApparatuS

PDFs Parton Distribution Functions

PDG Particle Data Group

QED Quantum Electrodynamics

SSB Spontaneous Symmetry Breaking

DIS Deep Inelastic Scattering

DGLAP Dokshitzer-Gribov-Lipatov-Altarelli-Parisi

LO Leading Order

NLO Next to Leading Order

NNLO Next to Next to Leading Order

NCDY Neutral Current Drell-Yan

CCDY Charged Current Drell-Yan

CKM Cabibbo-Kobayashi-Maskawa

CMS Compact Muon Spectrometer

HERA Hadron Electron Ring Accelerator

LINAC Linear accelerator

PSB Proton Synchrotron Booster

SPS Super Proton Synchrotron

PS Proton Synchrotron

IP Interaction Point

ALICE A Large Ion Collider Experiment

SUSY Super Symmetry

EM Electromagnetic

ID Inner Detector

SCT Semiconductor Tracker

TRT Transition Radiation Tracker

LAr Liquid Argon

HEC Hadronic end-cap

FCal Forward Calorimeter

MS Muon Spectrometer

MDT Monitored Drift Tubes

CSC Cathode Strip Chambers

RPC Resistive Plate trigger-Chambers

TGC Thin Gap trigger-Chambers

L1 Level-1

L2 Level-2

L1Calo Level-1 Calorimeter

L1Muon Level-1 Muon

CTP Central Trigger Processor

RoI Region of Interest

HLT High-Level trigger

DAQ Data Acquisition

GRL Good Runs List

MC Monte Carlo

NLL Next to leading logarithmic

FSR Final State Radiation

AMI ATLAS Metadata Interface

CB Combined Muon

ME Extrapolated Muon

ST Segment-Tagged Muon

CT Calorimeter-Tagged Muon

SF Scale Factor

MCP Muon Combined Performance

JVT Jet Vertex

TST Track Soft Term

HLT High Level Trigger

TTVA Track-to-Track Vertex Association

FR Fitting Region

SR Signal Region

NP Nuisance Parameter

JER Jet Energy Resolution

LUCID LUminosity Cherenkov Integrating Detector

Chapter 1

Introduction

The understanding at the most fundamental level of Nature has been a critical goal of scientific research since the beginning of modern science. Physics has helped substantially to achieve this ambitious goal. Namely, Elementary Particle Physics is an ideal candidate given it addresses the task to describe the interaction of elementary particles (the building blocks of matter) at the smallest scale; the theoretical description is based on powerful quantum field theories (QFTs) which yield an unprecedented physical insight of this kind of interactions. The combination of two QFTs, Electroweak Interaction (EWI) and Quantum Chromodynamics (QCD), makes up the Standard Model (SM) of Elementary Particle Physics and describes the particle behaviour at subatomic level. High energy experiments have been widely used to test the SM, as the constituents of matter interact in a simple way, in which case the most precise theoretical predictions exist. Nowadays, the highest energy experimentally produced in the laboratory is provided by the Large Hadron Collider (LHC) at CERN near Geneva, Switzerland, and whose centre of mass energy, for proton-proton (pp) collisions, is 13 TeV [1]. Consequently the validity of the Standard Model it is being tested in a new energy range.

The ATLAS detector, one of the main detectors located at the LHC, collected data during the year 2017; these data have been studied to extract information about the structure of the proton, being the proton a composite particle of elementary quarks and gluons. Considering the charged Drell-Yann process in pp collisions aims to improve the current precision of some definite parton distribution functions (PDFs) and thus throwing light to the underlying dynamics of the strongly interacting particles (QCD) associated with them.

The thesis is structured as follows: Chapter 2 contains the theory needed to appreciate the physics behind the charged current Drell-Yan process and guide the measurements

performed in this thesis. Chapter 3 explains very briefly the LHC and the ATLAS experiment, focussing in the more relevant variables and components for the present measurements. Chapter 5 gives a description of the data used in this analysis and the simulated samples, in order to compare the experimental data against prediction. Chapter 6 describes how events in the ATLAS detector are simulated and reconstructed, and explains the way of which the detector effects change the event reconstruction. Chapter 7 presents the event selection cuts chosen to select the largest possible amount of W bosons while maintaining the potential background signals low. Chapter 8 details the methodology to compute the multijet background which is not reliably calculated using standard Monte Carlo techniques, it is found that this background contributes approximately 1% to the final number of events. Chapter 9 treats the uncertainties that affect the final measurements, yielding a total uncertainty of around 2%. Chapter 10 displays a comparison between data and predicted signal and backgrounds of key kinematic distributions, this helps to validate the selection criteria and event weights considered. Chapter 11 presents the cross section and muon charge asymmetry measurements, along with the unfolding techniques and propagation of uncertainties. Conclusions are presented in Chapter 12.

The analysis documented in the present thesis, was carried out utilising several types of inputs:

- The samples considered for data and Monte Carlo in this analysis are centrally produced by the ATLAS Physics Modelling Group (PMG). The author requested derived samples[1] to the PMG, the samples were needed to comply with the Charged Current Drell-Yan analysis phase space (see Chapter 5).

- The author customised an official ATLAS software; namely, the *AnalysisTop*[2] software was chosen, given its high flexibility and the fact that it is under constant development and improvement. AnalysisTop performs all the centrally produced corrections and calibrations to physics objects derived by the ATLAS physics groups (JetEtMiss, Muon Combined Performance, Pileup). Additionally, AnalysisTop handles most of the corresponding systematics. The software customisation consisted in adapting it to process the truth information coming from W bosons and adding extra variables and corrections.

- Once the calibrations and corrections are done, the author created a framework to

[1] Derived samples are samples which have passed several different kinematic cuts. It is convenient to use derived samples to reduce the size of them and consider only events of interest in a given analysis.

[2] https://twiki.cern.ch/twiki/bin/viewauth/AtlasProtected/AnalysisTop21

process the outcome of the customised AnalysisTop software. The plots and tables presented in Chapters 5-11 are the result of this framework, *i.e.* the plots labelled with the legend "CCDY Analysis" were produced with this framework and the tables which contain the results are also part of the framework's outcome.

Chapter 2

Theory

This chapter is devoted to give the theoretical ideas which motivate and guide the measurements within the LHC and the ATLAS experiment. It starts with a short recapitulation of the Standard Model of Elementary Particle Physics. Parton distribution functions are presented, since setting constrains on them is one of the main aims of the $W \to \mu\nu$ measurement. Then, the Drell-Yan process is explained. Finally, a brief landscape of the measurement documented in this thesis is provided.

2.1 The Standard Model

The Standard Model asserts that matter in the Universe is made up of elementary *fermions*, half integer spin particles, that interact through fields; these fields have associated elementary particles called *bosons*, integer spin particles. The fundamental fermion interactions described by the SM can be: *i*) electromagnetic and weak interactions whose mediators are the photon γ and the $W^{\pm}$ and Z bosons and the QFT which describes them is the Electroweak theory and *ii*) strong interaction, whose mediators are the gluons and Quantum Chromodynamics is its QFT [2].

The SM fermions are classified as leptons and quarks. Leptons are particles which are affected only by the electroweak interaction; leptons are divided as charged and neutral leptons, the former carry electric charge of integer units of the electron charge e and the latter carry no electric charge. On the other hand, quarks have fractional electric charges $+2/3$, $-1/3\,e$; moreover, besides the electromagnetic and weak forces, quarks are also affected by the strong interaction as they have an extra degree of freedom called colour charge described theoretically by QCD. It is a remarkable fact that in Nature is possible to find

	Spin ($\hbar$)	Charge (e)	Mass (MeV)
Electron e	1/2	-1	0.51
Electron neutrino ν_e	1/2	0	$<$ 0.002 (95% CL)
Muon μ	1/2	-1	105.66
Muon Neutrino ν_μ	1/2	0	
Tau τ	1/2	-1	1776.82
Tau Neutrino ν_τ	1/2	0	

Table 2.1: List of the SM leptons together with their spin, charge and mass. They fall in to three generations, which in the table are separated by a horizontal line; the difference between each generation is the flavour quantum and mass found in the Particle Data Group (PDG) report [4].

leptons in free states, meanwhile, due to the colour confinement, quarks are always found in bound colourless particle states called hadrons.

By construction the SM is consistent with special relativity and quantum mechanics, empowering it to describe elementary particles which are subatomic and relativistic. The combination of special relativity and quantum mechanics establishes the existence of antifermions, *i.e.* there is an antifermion for each fermion already stated before with opposite quantum numbers.

Symmetries play a fundamental role within the SM. Noether's theorem, which states that symmetries in a theory manifest themselves as laws of conservation, leads to the experimentally observed conservation of energy, angular momentum and charge, when requiring the SM Lagrangian to be invariant under local-gauge transformations. Each generator of a gauge invariant theory must correspond to a gauge boson, a force carrier. The SM follows the gauge group $SU(3)_c \times SU(2)_L \times U(1)_Y$ symmetry[1], where the $SU(3)$ factor stands for QCD and its eight gauge bosons (gluons); the electroweak sector is symmetric under $SU(2) \times U(1)$ transformation yielding the gauge bosons $W^{\pm}$, Z^0 and the photon γ [2, 3].

Table 2.1 shows the leptons and their properties, Table 2.2 the quarks, and Table 2.3 displays the interaction mediators bosons [4].

2.1.1 Electroweak theory

The electroweak sector of the Standard Model is composed by the electromagnetic and weak quantum field theories. In a quantum field theory, particles interact by exchanging virtual *quanta* which mediate the force. The simplest and most successful QFT is Quantum Elec-

[1]The subscripts have only physical significance, *i.e.*, c refers to colour, L to the left chiral nature of $SU(2)$ and Y to the weak hypercharge quantum number.

	Spin ($\hbar$)	Charge (e)	Mass (GeV)
Up u	1/2	+2/3	0.002
Down d	1/2	−1/3	0.005
Charm c	1/2	+2/3	1.275
Strange s	1/2	−1/3	0.095
Top t	1/2	+2/3	173.21
Bottom b	1/2	−1/3	4.18

Table 2.2: List of the SM quarks together with their spin, charge and mass. They fall in to three generations, which in the table are separated by a horizontal line, the difference between each generation is the flavour quantum and mass found in the Particle Data Group (PDG) report [4].

	Spin ($\hbar$)	Charge (e)	Mass (GeV)
Photon γ	1	0	0
Z Boson	1	0	91.1876
$W^{\pm}$ Bosons	1	$\pm$1	80.385
Gluon g	1	0	0
Higgs H^0	1	0	125.7

Table 2.3: List of the SM interaction carrier bosons together with their spin, charge and mass found in the Particle Data Group (PDG) report [4].

trodynamics (QED) and takes care of describing the electromagnetic interaction between charged leptons and photons (mediators). The SM is written in terms of Lagrangian densities, from which equations of motion are derived. To obtain the QED Lagrangian density, start with the Lagrangian density for a charged lepton, or charged fermion field $\psi(x)$:

$$\mathcal{L} = \frac{i}{2}[\bar{\psi}(x)\gamma^{\mu}\partial_{\mu}\psi(x) - \partial_{\mu}\bar{\psi}(x)\gamma^{\mu}\psi(x)] - m\bar{\psi}(x)\psi(x), \tag{2.1}$$

where the bar above the fermion field denotes the Dirac conjugation, γ^{μ} are the Dirac matrices[2] and m the lepton mass. Following Noether's theorem for conserved electric charge, and the fact that the charge produces the electromagnetic field in space, it is required $\mathcal{L}$ to be invariant under the local $U(1)$-group transformation,

$$\psi(x) \rightarrow \psi'(x) = \exp[i\alpha(x)]\psi(x), \tag{2.2}$$

where $\alpha(x)$ is the phase angle which generates the $U(1)$ local rotations, and

$$\partial_{\mu}\psi(x) \rightarrow \exp[i\alpha(x)][\partial_{\mu}\psi(x) + i\psi(x)\partial_{\mu}\alpha(x)]. \tag{2.3}$$

Evidently, the above transformation does not keep the same structure of $\mathcal{L}$, and to remedy the latter, a *covariant* derivative D_{μ} is defined that satisfies

$$D_{\mu}\psi(x) \rightarrow \exp[i\alpha(x)]D_{\mu}\psi(x), \tag{2.4}$$

the invariance of the derivative on $\psi(x)$, expressed in the previous equation, is achieved if

$$D_{\mu} = \partial_{\mu} - igA_{\mu}(x); \qquad A_{\mu} \rightarrow A_{\mu}(x) + g^{-1}\partial_{\mu}\alpha(x), \tag{2.5}$$

where g is the called the coupling constant and $A_{\mu}(x)$ is a gauge field. The insertion of the vector field $A_{\mu}(x)$, has to be accounted for in $\mathcal{L}$ by adding a free term consistent with the local gauge invariance,

$$F_{\mu\nu} = \partial_{\mu}A_{\nu}(x) - \partial_{\nu}A_{\mu}(x). \tag{2.6}$$

To write $\mathcal{L}$ for QED, identify g with the electron charge e and $A_{\mu}(x)$ with the photon γ, therefore the QED Lagrangian density reads as:

$$\mathcal{L}_{QED} = \bar{\psi}(x)(i\gamma^{\mu}D_{\mu}\psi(x) - m)\psi(x) - \frac{1}{4}F_{\mu\nu}(x)F^{\mu\nu}(x). \tag{2.7}$$

[2]The notation is such that x represents the four dimensional space-time and the Greek indices, *e.g.* μ run over this coordinate system ($\mu = 1, 2, 3, 4$).

Finally it is important to mention that the $U(1)$ gauge boson is Abelian, therefore the photon has no self-interactions.

To account for the dynamics of the neutrally charged neutrinos and to describe slow processes such as nuclear β decays[3], a weak interaction force is introduced. In principle the symmetry group for the weak factor of the theory is $SU(2)_L$, nevertheless, charged leptons are also affected by this weak interaction, hence is natural to encapsulate both the electromagnetic and weak interaction in a $SU(2)_L \times U(1)_Y$ gauge transformation. The choice of the $SU(2)_L$ symmetry is inspired by having a theory which supersedes the problems of the Fermi's contact theory and to incorporate novel experimental observations, *e.g.* parity violation, μ and τ decays or heavy quarks and mixing. The Lagrangian density parity violation feature, is incorporated with the division in right-hand and left-hand components of the fermion field $\psi(x)$, $\psi_L(x) = (1/2)(1-\gamma_5)\psi(x)$ and $\psi_R(x) = (1/2)(1+\gamma_5)\psi(x)$,

$$\mathcal{L}_f = i \sum_{f=leptons,quarks} [\bar{\psi}_{fL}(x)\gamma^\mu \partial_\mu \psi_{fL}(x) + \bar{\psi}_{fR}(x)\gamma^\mu \partial_\mu \psi_{fR}(x)]. \tag{2.8}$$

The local $SU(2)_L \times U(1)_Y$ transformation applies in a different manner to the left-hand and right-hand components of the lepton field,

$$\psi'_L(x) = \exp[i(\boldsymbol{\alpha}(x)\cdot \mathbf{S}^W + \frac{i\beta(x)Y^W}{2})]\psi_L(x), \qquad \psi'_R(x) = \exp[\frac{i\beta(x)Y^W}{2}]\psi_R(x), \tag{2.9}$$

here the weak isospin $\mathbf{S}^W$ and the weak hypercharge $Y^W/2$ are the generators of the gauge transformations of $SU(2)_L$ and $U(1)_Y$, respectively; $\boldsymbol{\alpha}(x)$ and $\beta(x)$ are the phases used to localise the gauge transformations. To maintain the symmetry under this transformation, analogous to the electromagnetic previous case, covariant derivatives are defined as:

$$D_\mu \psi_{fL}(x) = [\partial_\mu - \frac{ig}{2}\boldsymbol{\sigma}\cdot \mathbf{W}_\mu(x) + \frac{ig'}{2}B_\mu(x)]\psi_{fL}(x), \qquad D_\mu \psi_{fR}(x) = [\partial_\mu + ig' B_\mu(x)]\psi_{fR}(x), \tag{2.10}$$

where $\boldsymbol{\sigma}$ are the Pauli matrices, $\mathbf{W}_\mu$ and B_μ the gauge fields, and g' the gauge coupling. Note when $S^W = 1/2$ the matrices $\sigma_k/2$ are the generators of the $SU(2)$ transformations. Following the previous case, a free Lagrangian term for the fields just introduced is determined by

$$\mathcal{L}_0 = -\frac{1}{4}W_{a\mu\nu}(x)W_a^{\mu\nu}(x) - \frac{1}{4}B_{\mu\nu}(x)B^{\mu\nu}(x), \tag{2.11}$$

[3]These processes were regarded as slow/weak since the mean lives of decays are very long (minutes), compared with typical nuclear electromagnetic decays ($\sim 10^{-15}$ s).

where $W^a_{\mu\nu}(x)$ is a tensor of a non-Abelian field $(a, b, c = 1, 2, 3)$,

$$W_{a\mu\nu}(x) = \partial_\mu W_{a\nu}(x) - \partial_\nu W_{a\mu}(x) + g\epsilon_{abc} W_{b\eta}(x) W_{c\mu}(x), \tag{2.12}$$

$B_{\mu\nu}(x)$ is a tensor field of an Abelian field

$$B_{\mu\nu}(x) = \partial_\mu B_\nu(x) - \partial_\nu B_\mu(x). \tag{2.13}$$

The interpretation of the previous equations could be summarised as claiming that the unbroken local $SU(2)_L \times U(1)_Y$ symmetry leads to the existence of four massless vector bosons, three correspond to $SU(2)_L$ with gauge coupling g and one to $U(1)_Y$ with gauge coupling g'. Gauge invariant theories do not allow mass terms for gauge bosons because they would break the gauge invariance and spoil the renormalisability. This appears to be problematic for weak interactions, which are short-ranged and require massive mediators. A simple application of spontaneous symmetry breaking (SSB)[4] could solve the present problem, particularly the Higgs mechanism. The Higgs Lagrangian density for a scalar complex Higgs field $\phi(x)$ is:

$$\mathcal{L}_H = |D_\mu \phi(x)|^2 - V(\phi), \tag{2.14}$$

where D_μ is a covariant derivative and the Higgs potential $V(\phi)$ is defined as

$$V(\phi) = \frac{1}{2}\mu^2 \phi^\dagger(x)\phi(x) + \frac{1}{4}\lambda[\phi^\dagger(x)\phi(x)]^2, \tag{2.15}$$

with $\lambda > 0$, $\mu^2 < 0$, the vacuum expectation value $\langle 0|\phi(x)|0\rangle \neq 0$ and $\phi = 0$ is a local minimum. Adding $\mathcal{L}_H$ to the theory and choosing a convenient gauge[5], the vacuum is no longer invariant under local gauge transformations and the Higgs Lagrangian density can be expressed in terms of the Higgs field around the non-zero vacuum expectation value. Finally, to identify the gauge fields W^a_μ and B_μ of Equation (2.10) with the Z, $W^\pm$ bosons, consider the covariant derivative in Equation (2.10) and insert it in $\mathcal{L}_H$, to obtain

$$|D_\mu \phi(x)|^2 = m_W^2 W^*_\mu(x) W^\mu(x) + \frac{1}{2} m_Z^2 Z_\mu(x) Z^\mu(x), \tag{2.16}$$

where

$$m_Z = \frac{v\sqrt{g^2 + g'^2}}{2}, \qquad m_W = \frac{gv}{2}, \tag{2.17}$$

[4] *Spontaneously* broken symmetry is when the symmetry of the equations of motion is broken adding small terms in the solutions; conversely, the symmetry may be broken *explicitly* adding small terms in the equations themselves.

[5] A convenient gauge means that, by the Higgs mechanism, the Goldstone bosons become the longitudinal components of the massive vector bosons $W^\pm$ and Z.

are the Z and W boson masses, respectively; v the minimum of the Higgs potential, and

$$W^{\pm} = \frac{W^1_\mu \mp iW^2_\mu}{\sqrt{2}}, \qquad W_\mu \equiv W^-_\mu,\ W^*_\mu \equiv W^+_\mu. \tag{2.18}$$

Thus, the weak interaction bosons acquire mass whereas the photon is kept massless. The W and Z bosons were discovered at CERN by the UA1 and UA2 collaborations in 1983 [5, 6].

2.1.2 Quantum chromodynamics

QCD is the theory of strong interactions between quarks and gluons, each *flavour* or type of quark, u, s, d, c, b, t has colour charge, which are conventionally labelled as red (R), green (G) and blue (B). There is an unbroken non-chiral (parity conserving) symmetry $SU(3)_c$ that generate the above mentioned 8 gauge massless gluons, G^i. The simplest interactions between quarks/gluons are quark-quark interaction mediated by a gluon. Additional interactions in the $SU(3)_c$ group are non-Abelian, there are three- and four-point gluon self interactions. Additionally, dominant higher order corrections can be taken into account in an effective running coupling $g_s(Q^2)$ where Q^2 is the momentum transfer; $g_s(Q^2)$ depends on the renormalisation scale μ.

The strong force becomes stronger at long distances or low-momentum transfer, and weaker at short distances or high momentum transfer, this is manifested in colour confinement and asymptotic freedom, these features of the strong interactions are contained in the running coupling written as,

$$g_s(Q^2) = \frac{g_s(\mu^2)}{[1 + g_s(\mu^2)\beta_0 \ln(Q^2/\mu^2)]}; \qquad \beta_0 = \frac{33 - 2N_\mathrm{f}}{12\pi}, \tag{2.19}$$

where N_f is the number of quark flavours present at the scale Q^2. It is important to state that there is a similar expression for QED, but with negative sign for the logarithmic part.

The Lagrangian density for QCD, $\mathcal{L}_{QCD}$, is constructed in the same way as the QED and electroweak cases,

$$\mathcal{L}_{QCD} = -\frac{1}{4}G^i_{\mu\nu}G^{\mu\nu i} + \sum_r \bar{q}^\alpha_r i \not{D}^\beta_\alpha q_{r\beta} - \sum_r m_r \bar{q}^\alpha_r q_{r\alpha} + \frac{\theta_{QCD}}{32\pi^2} g_s^2 G^i_{\mu\nu}\tilde{G}^{\mu\nu i}, \tag{2.20}$$

$q_{r\alpha}$ are the quark fields with α =R,G,B and r runs on the quark flavours, m_r are the current

quark masses; the gluon field is expressed as,

$$G^i_{\mu\nu} = \partial_\mu G^i_\nu - \partial_\nu G^i_\mu - g_s f_{ijk} G^j_\mu G^k_\nu; \tag{2.21}$$

and the quark gauge covariant derivative is

$$D^{\mu\beta}_\alpha \equiv (D^\mu)_{\alpha\beta} = \partial^\mu \delta^\beta_\alpha + \frac{ig_s}{\sqrt{2}} G^{\mu\beta}_\alpha, \qquad G^\beta_\alpha = (G^\alpha_\beta)^\dagger = \sum_{i=1}^{8} G^i \frac{\lambda^i_{\alpha\beta}}{\sqrt{2}}, \tag{2.22}$$

here G^β_α represents the gluon field in matrix notation.

2.2 The structure of the proton: PDFs

The current knowledge of QCD and proton structure is a vital tool in helping disentangle and interpret potential signals of new physics at the LHC. The progress of understanding the proton structure began with deep inelastic scattering (DIS) experiments where one energetic lepton hits a proton; the target was dissociated to large invariant mass states in the interaction. The data from the SLAC experiments in 1967 prompted Feynman to develop the parton model for DIS experiments, in which the observed scaling behaviour is naturally explained as point-like elastic scattering of free partons within the protons, subsequently these point-like constituents were identified as the quarks [7].

The quark parton model describes the nucleons as consisting of massless point-like spin 1/2 quarks which are free within the nucleon. The parton distribution functions $f_i(x)$ in the quark parton model are a number of densities of parton flavour i with fraction x of the parent nucleon's energy and longitudinal momentum. Often the momentum weighted $x_i f(x)$ are used. In standard notation the antiquark PDFs are denoted $x_i \bar{f}(x)$, and PDFs for each quark flavour u, d, s, c, b [8].

Deeply inelastic lepton-nucleon scattering cross sections are calculated from incoherent sums of elastic lepton-parton processes. More generally, the hadronic cross section for a process of two hadrons A and B interacting, $A + B \to X$, being X any final state, is written as

$$\sigma_{A,B\to X} = \sum_{i,j} \int\int \mathrm{d}x_1 \mathrm{d}x_2 f^A_i(x_1) f^B_j(x_2) \cdot \hat{\sigma}_{i,j\to X} + [x_1 \leftrightarrow x_2], \tag{2.23}$$

where $\hat{\sigma}_{i,j\to X}$ is the partonic cross section for interactions of two partons with flavour i and j. The fact that the PDFs in the last equation are universal is known as the factorisation property: PDFs extracted from an analysis of inclusive DIS measurements can be used to calculate cross sections of other processes in lepton-hadron or hadron-hadron interactions.

The domain of validity of this first order approximation is the asymptotic 'scaling' limit, $s \to \infty$, M_X^2/s fixed, where s is the centre-of-mass energy and M_X is the invariant mass of the decay products. To include gluon corrections is necessary to take account of the logarithmic divergences into the PDFs making them dependent on a factorisation scale μ_F, therefore the PDFs in Equation (2.23) are substituted by $f_i^A(x_1, \mu)$ and $f_j^B(x_2, \mu)$, the μ evolution is given by the DGLAP equations,

$$\frac{dG(x,\mu^2)}{d\ln\mu^2} = \frac{g_s(\mu^2)}{2\pi}\int_x^1 \frac{dz}{z}\left[\sum_j P_{Gq}\left(\frac{x}{z}\right) q_j(z,\mu^2) + P_{GG}\left(\frac{x}{z}\right) G(z,\mu^2)\right], \tag{2.24}$$

$$\frac{dq_i(x,\mu^2)}{d\ln\mu^2} = \frac{g_s(\mu^2)}{2\pi}\int_x^1 \frac{dz}{z}\left[\sum_j P_{qq}\left(\frac{x}{z}\right) q_i(z,\mu^2) + P_{qG}\left(\frac{x}{z}\right) G(z,\mu^2)\right] \tag{2.25}$$

here q_i, the quark densities, include both q_i and $\bar{q}_i$, G is the gluon density; $P_{f_i f_j}$ are the splitting functions which describe the probability of a parton f_i to emit a parton f_j carrying a fraction $z \leq 1$ of the f_i momentum. The splitting functions are perturbative and can be expanded in g_s. The zeroth order yields the leading-order (LO) approximation (one factor g_s is already extracted in Equation (2.24)-Equation (2.25)). The next-to-leading-order (NLO) terms of the order of $\mathcal{O}(g_s^n(\ln\mu^2)^{n-1})$, involve the $\mathcal{O}(g_s)$ corrections to the splitting functions. The splitting functions have been calculated to next-to-next-leading-order (NNLO) which are used in recent analyses of PDFs [9–12].

2.3 Charged Current Drell-Yan

In their paper [14] Sidney D. Drell and Tung-Mow Yan predicted the dilepton production, *i.e.* a neutral current process of large lepton invariant mass pair production in a hadron-hadron collision, based on parton model ideas; this is referred to as neutral current Drell-Yan (NCDY) process since the mediator boson involved carries neutral electric charge, the Z boson, and the two final state leptons possess opposite electric charges, the sum of their charges is zero. For the charged current Drell-Yan (CCDY) process, the principles are the same as for NCDY process, where the basic process is a quark and antiquark interacting to produce an on-shell or off-shell charged W boson of invariant mass m_W and decaying into one charged lepton and a neutral charged lepton ($q\bar{q} \to W^\pm \to l^\pm \nu_l$), the sum of the charges of the final state leptons is *not* zero, see Figure 2.1. This cross section is easily obtained using similar techniques of quantum electrodynamics, with the addition of appropriate colour and charge factors [15],

$$\hat{\sigma}_0^{q\bar{q}'} = \frac{\pi}{3}\sqrt{2} G_F m_W^2 |V_{qq'}|^2 \delta(\hat{s} - m_W^2), \tag{2.26}$$

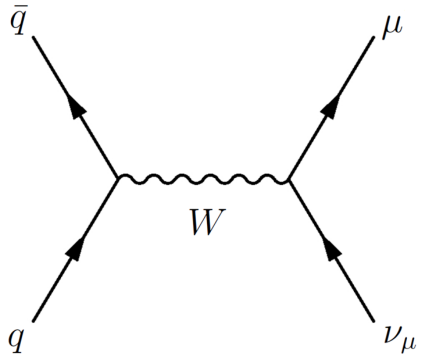

Figure 2.1: Feynman diagram of the partonic W production process. The quark and anti-quark are assumed to come from the colliding protons. The W bosons have leptonic and hadronic decay modes. The former corresponds to a charged lepton and a neutral lepton in the final state, $W \to l^{\pm}\nu$, where l represents either a electron, a muon or a tau (in this work only the decay to muons is considered); the hadronic decay modes are $W \to \pi^{+}\gamma$, $W \to D_s^{+}\gamma$, $W \to cX$, $W \to c\bar{s}$, where π^{+} is a pi meson, γ is a photon, D_s^{+} is a d meson, c is a charm quark, s is a strange quark and X is a inclusive final state. Finally the W boson could decay into a charged particle with momentum below experimental detectability (< 200 MeV).

where G_F is the Fermi weak coupling constant, $V_{qq'}$ is the Cabibbo-Kobayashi-Maskawa (CKM) matrix element[6] corresponding to the qq' quarks, $\hat{s}$ is the square of the centre-of-mass energy of the incoming quarks $q\bar{q}'$, and δ is the Dirac delta distribution. The use of the Fermi constant manifests that the cross section it is calculated at leading-order.

To calculate the CCDY cross section in a hadron-hadron collision is necessary to relate the hadron and parton dynamics. The square centre-of-mass energy of a hadron-hadron collision s, in terms of the four-momentums of the incoming partons p_1^{μ} and p_2^{μ}, reads as,

$$p_1^{\mu} = \frac{\sqrt{s}}{2}(x_1, 0, 0, x_1), \qquad p_2^{\mu} = \frac{\sqrt{s}}{2}(x_2, 0, 0, -x_2), \tag{2.27}$$

it follows that $\hat{s} = x_1 x_2 s$. By combining Equation (2.23), Equation (2.26) and Equation (2.27) it is obtained the hadron-hadron CCDY cross section,

[6]The CKM matrix is a unitary matrix whose elements characterise the strength of the flavour changing electroweak decays.

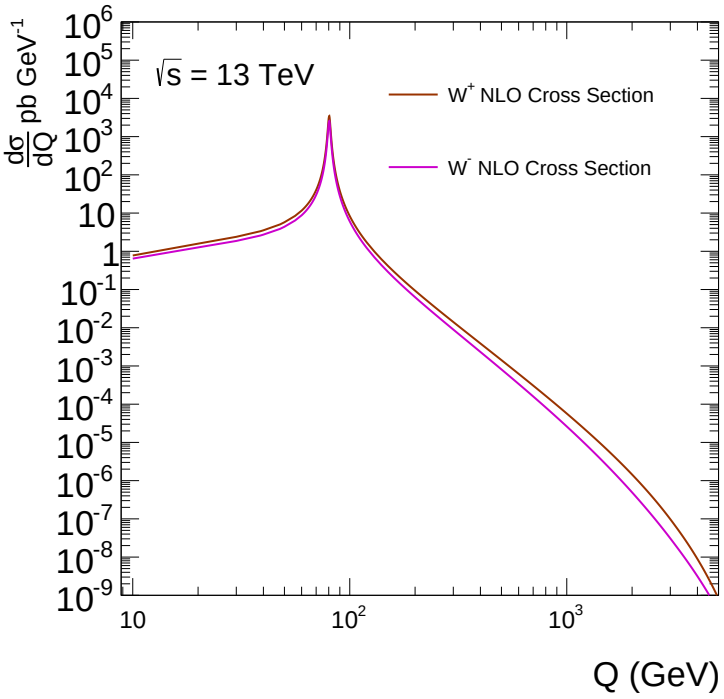

Figure 2.2: Plot showing W^+ and W^- cross sections. Note that the W^+ cross section is higher in the full range since the LHC collides positively charged protons [13].

$$\frac{\mathrm{d}\sigma}{\mathrm{d}m_W^2} = \frac{\pi}{3}\sqrt{2}G_F m_W^2 \int_0^1 \mathrm{d}x_1 \mathrm{d}x_2 \delta(x_1 x_2 s - m_W^2) \times \left[\sum_{k,k'} |V_{q_k q_{k'}}|^2 \left(q_k(x_1, m_W^2)\bar{q}_{k'}(x_2, m_W^2) + [1 \leftrightarrow 2]\right)\right]. \tag{2.28}$$

The resulting cross section can then be multiplied by the branching ratios for any particular hadronic or leptonic final state of interest. These calculations have been performed to the next-to-leading-order precision using a given set of PDFs, this is shown in Figure 2.2.

In the context of LHC experimental measurements, in this range of energies the production cross sections of weak vector bosons (charged current Drell-Yan processes) are relatively large and since these processes provide an easily identifiable decays to leptonic final states, they offer a clean experimental signature which can be measured to high precision. The cross sections are dependent on the parton distribution functions (PDFs) and thus to the underlying dynamics of strongly interacting particles (QCD). In particular, the production and decay to an antimuon (muon) and a neutrino (antineutrino) of the $W^{\pm}$ charged bosons

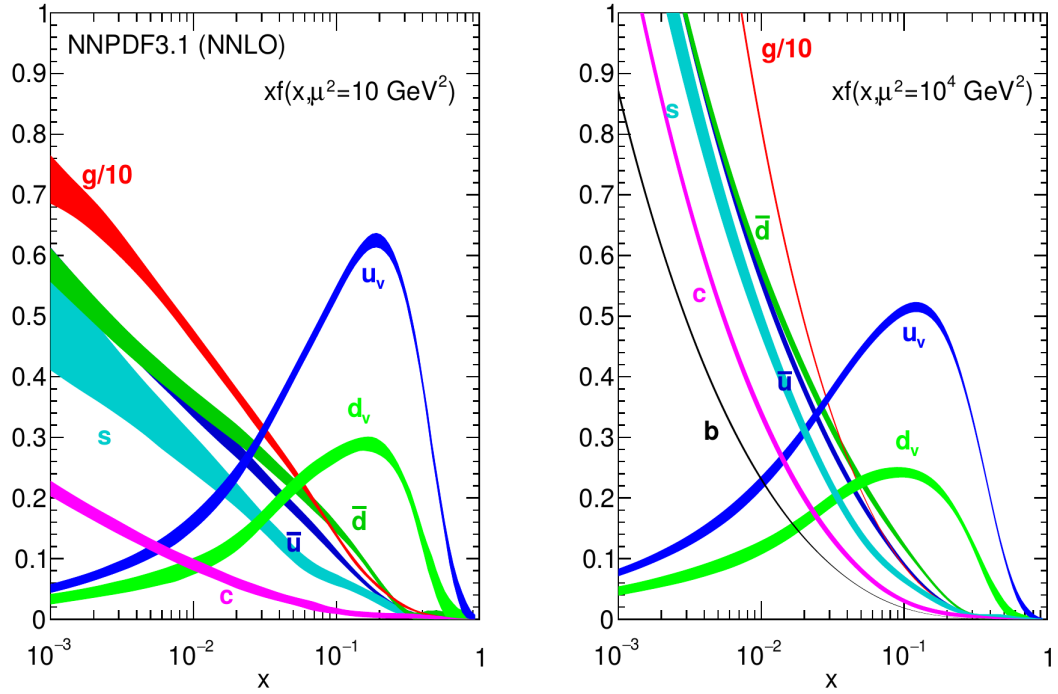

Figure 2.3: The NNPDF3.1 NNLO PDFs, *left-plot* evaluated at $\mu^2 = 10$ GeV^2; *right-plot* evaluated at $\mu^2 = 10^4$ GeV^2 [12].

$pp \to W^{\pm} \to \mu^{\pm}\nu_{\mu}$ is of interest because it is expected to contain information of the interplay of pairs of parton (quark) flavour distributions, *i.e.* $u\bar{d}$, $u\bar{s}$, $u\bar{b}$, $c\bar{d}$, $c\bar{s}$, $c\bar{b}$ for the W^+ boson and $d\bar{u}$, $d\bar{c}$, $s\bar{u}$, $s\bar{c}$, $b\bar{u}$, $b\bar{c}$ for the W^- boson. Therefore, the benchmark measurements of the $W^{\pm}$ production offer a unique opportunity to test models of parton dynamics at the LHC. The kinematic region accessible, is in part driven by the detectors, for example the ATLAS detector has a rapidity constrain of $|y| < 2.5$ (for precision analyses); in the case of W/Z boson production from partons with momentum fractions x_1 and x_2, $m_{W,Z} = sx_1x_2$, inspecting Equation (2.27) the rapidity of the lepton pair it is deduced to be $y = 1/2 \ln x_1/x_2$, and

$$x_1 = \frac{m_{W,Z}}{\sqrt{s}} e^{y}, \qquad x_2 = \frac{m_{W,Z}}{\sqrt{s}} e^{-y}. \tag{2.29}$$

These expressions restrict the x range at $\sqrt{s} = 7$ TeV to approximately $10^{-3} < x < 10^{-1}$, the range will be enhanced by a factor of two when the LHC reaches its design centre of mass energy of $\sqrt{s} = 14$ TeV.

2.4 Next-to-next-leading-order parton distribution functions

The probability to find a parton (quarks and gluons) of a given flavour in the proton, is described by the PDFs as a function of the fraction of the proton's momentum carried by the parton. One of the most recent parton distributions sets, is the NNPDF3.1 set determined at NNLO [12]. The determination of the PDFs relies on experimental results from hard scattering interaction experiments; *e.g.*:

- The H1 and ZEUS experiments, at the HERA electron-proton collider, provided the majority of the precision DIS structure functions data over a wide kinematic region [16]. The precision achieved by these experiments was of few percentages. Additionally, the HERA experiments determined the behaviour of the valence PDFs at low Bjorken $x \sim 10^{-3}$ with an unprecedented precision, this was done with the aid of neutral current measurements [17]. Lastly, charged current DIS experiments provided important advance to constrain the quark flavour separation [18].

- The experiments E605 and E775 measured the di-muon production in Drell-Yan interactions of a proton off a fixed target. These experiments were fed by the Tevatron proton beam and double-differential cross sections in invariant mass and the rapidity of the di-lepton pair were determined. Important information on the up and down sea quark densities was extracted [19, 20].

- The D0 and CDF experiments located at the Tevatron, which collided proton and anti-protons, measured the lepton charge asymmetry, which gave information of the up and down quark PDFs [21, 22]; precise measurements of the rapidity distribution in $Z \to l^+l^-$ were performed to provide constraints on the quark densities at $Q^2 \sim M_Z^2$, over a broad range in Bjorken x [23, 24].

It is of special interest, for searches of physics beyond the SM, to bring the precision of PDFs down to percent level; to achieve the latter a number of recent experimental results need to be combined, namely, Tevatron's W boson asymmetries, LHC (ATLAS, CMS, LHCb) experiments have released inclusive jet production, gauge boson production and top quark production results, and the above mentioned legacy measurements of DIS structure functions from HERA are available. Moreover, new high-precision QCD calculations of hadron collider processes with direct sensitivity to PDFs are completed. All these ingredients are used to determine the PDFs displayed in Figure 2.3. The methodology to extract the PDFs from experimental data is outlined for example in [7]. In the plots of Figure 2.3, the vertical axis

is the parton density and the horizontal axis is the parton fractional momentum; the shapes shown, are accompanied by bands to state the uncertainties (from both experiment and theory); the labels for each curve, related by colours, refer to the parton flavour; moreover, q_v specifies the correspondence to a valence quark. Left plot of Figure 2.3 displays the PDFs in the case of $\mu^2 = 10$ GeV^2, the valence quarks, u_v and d_v, dominate at high momentum fraction, whilst the sea quarks dominate at low momentum. Right plot of Figure 2.3 displays the PDFs in the case of $\mu^2 = 10^4$ GeV^2, the behaviour is similar with respect to the previous case, the only difference is that sea quark densities are larger at low momentum.

2.5 Measurement overview

The charge asymmetry of the W boson production (*i.e.* the cross section of the produced W boson is larger or smaller depending on its charge) in pp head-on collisions arises since the positive charged valence quarks are slightly more dominant inside the positive charged proton, henceforth this result helps to study definite quark distributions as stated below. The asymmetry between the production of W^+ and W^- bosons have been reported for the experiments carried out by the CDF and D0 collaborations [21, 22, 25, 26] at the Fermilab's Tevatron; these measurements proved their importance to constrain the proton PDFs. Namely the u and d quark distributions reached stronger constrains w.r.t. previous determinations [21, 25]; the available centre of mass energy was 1.8 TeV, and the Bjorken x was explored in the $0.007 < x < 2.4$ boundary, nevertheless these measurements, published in 1995-1998, suffered large experimental uncertainties. In 2008 and 2009 new results were available from the D0 [22, 26] and the CDF [27] collaborations, two orders of magnitude more of Tevatron's data allowed to reduce the total uncertainty to ∼15%, the latter constrained further the u and d PDFs using both the electron and muon channels. Fermilab analyses conducted proton-antiproton results; whereas the LHC collided only protons and opened a new Bjorken x range with the centre of mass energy of $\sqrt{s} = 7$ TeV. In 2011 the ATLAS [28] and CMS [29, 30] collaborations determined the charge asymmetry with a precision of ∼8%, improving further the proton PDFs. The latest published result was performed by the CMS collaboration [31] in 2014; in their paper the muon charge asymmetry was reckoned using 4.7 fb^{-1} of pp data with centre of mass energy of 7 TeV, the precision achieved is of ∼1.6% in every pseudorapidity bin; their paper also shows the constrain of the proton distributions of light quarks by fitting the unfolded data, the PDFs determination is improved in the x range from 10^{-3} to 10^{-1}. The ATLAS collaboration will publish a similar result for $\sqrt{s} = 8$ TeV data using 20 fb^{-1} pp collision data.

Chapter 3

Experiment

This chapter presents a general overview of the Large Hadron Collider functioning. Furthermore, it contains a summary of the details of the ATLAS experiment and the different components that comprises the latter. Special care is given to the muon detection system, as muons are the central focus of this thesis.

3.1 Large Hadron Collider

One recently exploited approach to study elementary particles, is the use of particle accelerators by means of colliding the former. High energies make possible to produce massive particles[1]; likewise, high energetic particles help to probe the structure of hadrons, since the collision energy typically exceeds the binding effect of the strongly interacting hadron constituents. The highest energy and largest particle accelerator in the world is the Large Hadron Collider; it is a two-ring-superconducting-magnet-hadron synchrotron and collider installed in a 26.7 km tunnel 100 meters underground between France and Switzerland near Geneva at CERN, the European Organization for Nuclear Research. The LHC second period of operations started in 2015; from then on, proton collisions[2] at the LHC have reached a centre of mass energy of 13 TeV (14 TeV is the design energy), *i.e.* each of its two rings accelerates protons at 6.5 TeV and then are bring to collide head-on at an energy of 13 TeV. In order to achieve the highest energy, starting from a simple bottle of hydrogen gas, several *different stages* take place: an electric field is used to strip hydrogen atoms of their electrons to yield protons. Linac 2, the first accelerator in the process, accelerates the protons to the

[1] Mass can transform into energy and vice-versa in accordance with Einstein's equation $E = mc^2$.

[2] Before the construction of the LHC, in the same tunnel was installed the Large Electron-Positron collider (LEP), nevertheless, in spite to the fact that such collisions were clean (no QCD multijet contamination) with respect to proton collisions, the energy was limited due to losses from synchrotron radiation.

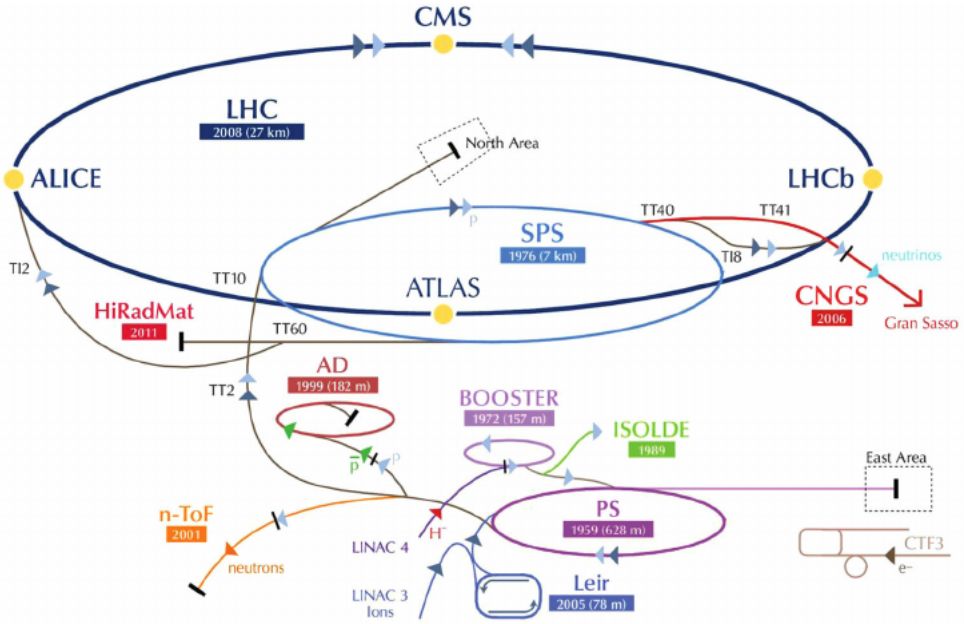

Figure 3.1: Diagram of CERN's accelerator complex [32].

energy of 50 MeV. The beam is then injected into the Proton Synchrotron Booster (PSB), which accelerates the protons to 1.4 GeV, followed by the Proton Synchrotron (PS), which pushes the beam to 25 GeV. Protons are then sent to the Super Proton Synchrotron (SPS) where they are accelerated to 450 GeV. Finally the protons are fed to the two beam pipes of the LHC; the beam pipes circulate protons in opposite directions, in this manner head on proton-proton take place at the interaction points (IP), see Section 3.2. The beam pipes are in a ultra-high vacuum to avoid collisions or interactions with gas molecules. Figure 3.1 depicts the configuration of the CERN's accelerator complex and sketches the positions of each accelerator [32].

In accelerator physics a very useful quantity called luminosity, L, is defined as measure of amount of data collected:

$$\sigma \int L\, dt = N, \tag{3.1}$$

where σ is the cross section (event rate) of the process, N is the number of events and dt is the time interval. The luminosity of a beam made of particles is the number of particles passing down the beamline per unit time, per unit area [33],

$$L = f\, n_b \frac{n_p^2}{A}, \tag{3.2}$$

where f is the rotation frequency of the beams, n_b is the number of particle bunches per beam, A is the transverse colliding area of the beam and n_p is the number of protons in the beam. L is a variable which can be controlled, hence with this parameter it is possible to enhance the event rate of a process of interest, which usually has a small cross section.

In the LHC, protons circulate around the rings in well-defined bunches (the bunch structure of a modern accelerator is the result of the radio frequency acceleration scheme). In the LHC, the proton beams have 2808 bunches each containing about 10^{11} protons. The bunches are squeezed and expanded at various places of the LHC; for instance, they get squeezed as much as possible around the interaction point to increase the probability of a collision, *i.e.*, reducing A in Equation (3.2) increases the luminosity, on the other hand, the bunches are expanded to study the elastic scattering of protons, *i.e.*, the area of interaction becomes smaller, therefore it is less likely that the protons break down and only exchange momentum takes place. Increasing the number of bunches is one of the ways to increase the luminosity; at full luminosity, the LHC uses a bunch spacing of 25 ns (or 7.5 m), which means that the proton bunches collide 40 million times per second. The LHC design instantaneous luminosity at 14 TeV is $10^{34}\,\mathrm{cm}^{-2}\,\mathrm{s}^{-1}$.

A consequence of requiring high luminosities, when two bunches of protons cross at the IP, is the occurrence of additional proton-proton collision besides the physics interesting one, this is effect is called *pileup* [32, 34]. A very careful treatment of pileup must to be considered, as the pileup will affect the detector response when looking at a pp interaction of interest *i.e.* the detector will observe it as the superposition of its final state and the products of the additional pileup and zero-bias interactions (inelastic hadron-hadron collisions dominated by low momentum) that occurred during the same bunch crossing. Pileup thus affects the majority of the objects reconstructed in the final state and compromises the precision at which the kinematic properties of these objects can be measured: energy deposits originated from pileup decay products could potentially overlap with interesting particle/objects signatures, leading to energy, momentum and topology miscalculation; namely, the main pileup contribution comes from hadrons, hence the most affected final objects are the ones which contain hadrons, but also affecting isolation criteria for leptons and photons [35].

Integrating (summing) the luminosities of data taking during the years 2015, 2016 and 2017 yields a total luminosity of nearly $80\,\mathrm{fb}^{-1}$. Figure 3.2 shows the luminosity delivered by the LHC, the luminosity recorded by ATLAS and the luminosity useful for physics. The delivered luminosity accounts for the luminosity delivered from the start of stable beams until the LHC control centre requested ATLAS to configure the detector in a safe standby mode to allow beam dumps or beam studies. The recorded luminosity reflects the DAQ inefficiency, as well as the inefficiency of the so-called “warm start”. The All Good Data

Quality criteria require all detector sub-systems to be fully operational.

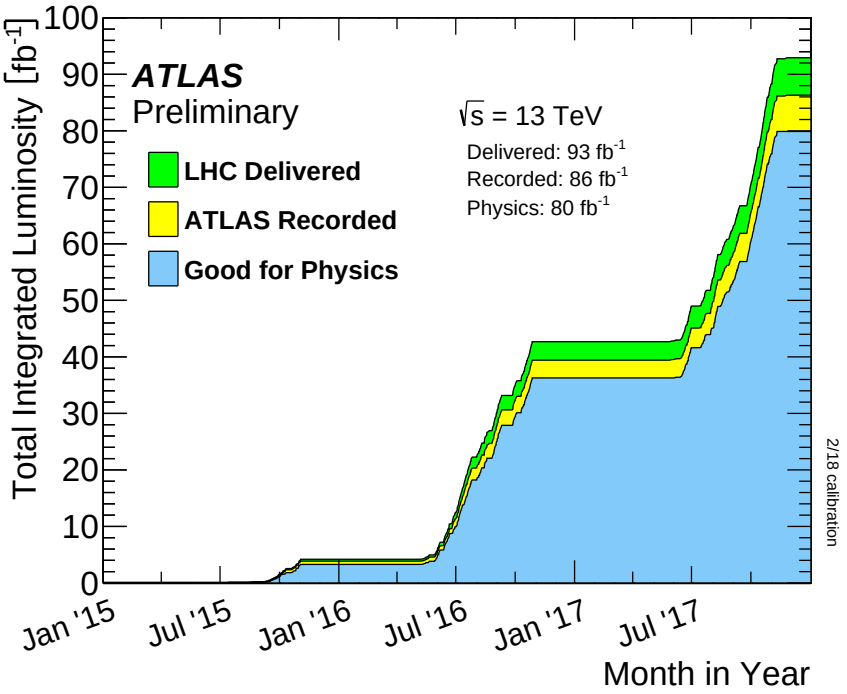

Figure 3.2: Cumulative luminosity versus time delivered to ATLAS (green), recorded by ATLAS (yellow), and certified to be good quality data (blue) during stable beams for pp collisions at 13 TeV centre-of-mass energy in 2015-2017. The data quality assessment shown corresponds to the All Good efficiency shown in the 2015, 2016 and 2017 Full Dataset [36].

3.2 ATLAS Experiment

Around the LHC are four main interaction points, where four experiments/detectors were constructed: ATLAS, ALICE, LHCb and CMS [34]. ATLAS and CMS are multipurpose experiments devoted to measure a wide variety of processes (Higgs, SM, SUSY, new physics). The LHCb experiment is for b and c hadron physics and ALICE is dedicated to measure heavy ion collisions.

The ATLAS ("A toroidal LHC apparatus") detector is the one used to perform the $W \to \mu\nu_\mu$ measurement in this thesis. As mentioned above, it is difficult to observe interesting physics because of their small cross sections; furthermore, pileup and the QCD multijet background, due to the nature of pp collisions, dominate the cross sections; more precisely, the W production cross section is six orders of magnitude smaller with respect to the total pp cross section: a good interesting physics signatures identification is demanded.

The capability to detect a particle is dictated by the nature of the particle itself. Heavy particles are not possible to be detected given their short life times; quantum confinement forbids to directly detect gluons and quarks; thus, the particles that can be directly detected are photons, electrons, muons, protons, neutrons and long-lived mesons such as pions and kaons. Neutrinos are not detected in ATLAS because their weak interaction with matter would require much larger apparatus dimensions [37].

Integrating all the above regards to detect the pp collisions debris, the ATLAS detector requires fast, radiation-hard electronics and sensor elements; in addition, high detector granularity is needed to handle the particle fluxes and to reduce the effects of overlapping events. Is essential to have a good charged-particle momentum resolution and reconstruction efficiency. Very good electromagnetic (EM) calorimetry for electron and photon identification/measurements, complemented by hadronic calorimetry for jet and missing transverse energy are also required. Furthermore, needs to have good muon identification and momentum resolution. Finally the triggering on low transverse momentum objects with sufficient background rejection is very important. Following all these main guidelines the ATLAS detector was designed and constructed. The ATLAS detector is nominally forward-backward[3] symmetric with respect to the interaction point; has three main sub detectors: the inner detector (ID), the hadronic and electromagnetic calorimeters, and the muon spectrometer. The magnet configuration comprises a thin superconducting solenoid surrounding the ID cavity, and three large superconducting toroids (one barrel and two end-caps) arranged with an eight-fold azimuthal symmetry around the calorimeters. Finally trigger and data acquisition systems are part of the ATLAS detector. Upcoming sections address individually these systems. Figure 3.3 shows the schematic diagram of the detector.

3.2.1 ATLAS coordinate system and variables

The ATLAS coordinate reference frame is as follows. The nominal interaction point is defined as the origin of the coordinate system, while the beam direction defines the z-axis and the x-y plane is transverse to the beam direction. The positive x-axis is defined as pointing from the interaction point to the centre of the LHC ring and the positive y-axis is defined as pointing upwards. The azimuthal angle ϕ is measured around the beam axis, and the polar θ is the angle from the beam axis. It is kinematically more convenient to use the

[3]Forward refers to the ATLAS large $|\eta|$ regions, where η is defined in Equation (3.3). These regions are covered by special sub-detector components.

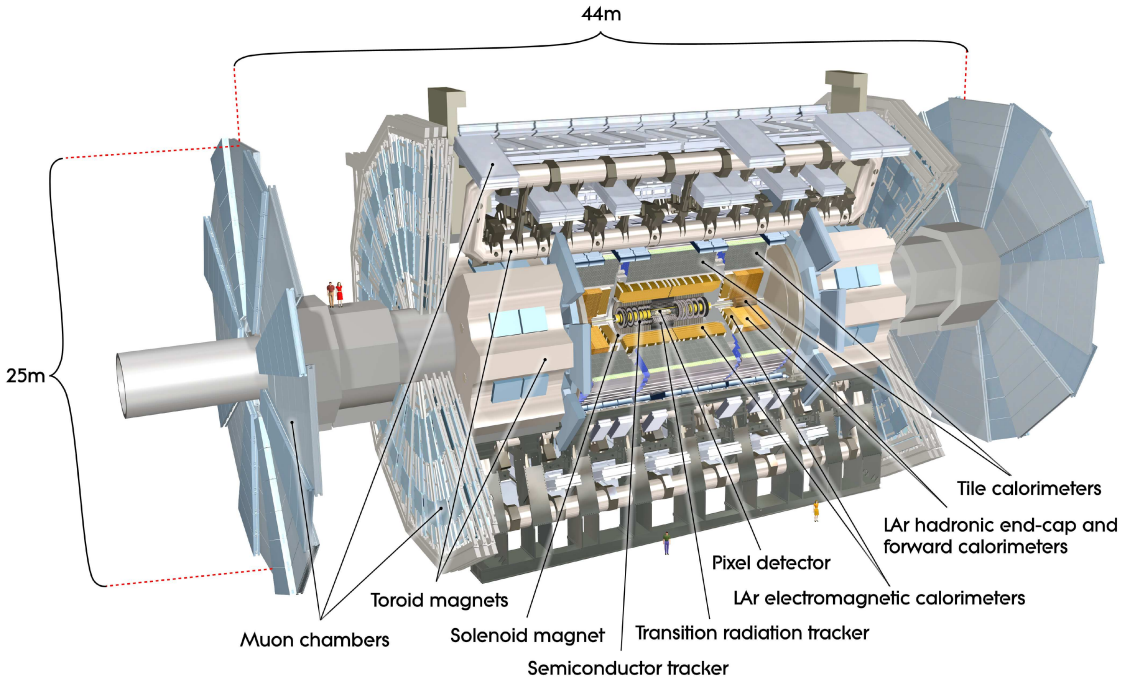

Figure 3.3: Diagram of the ATLAS detector [38].

pseudorapidity coordinate instead of θ, defined as,

$$\eta = -\ln\left[\tan\left(\frac{\theta}{2}\right)\right], \tag{3.3}$$

(for massive objects, the rapidity $y = \ln[(E + p_z)/(E - p_z)]$ is used). The distance ΔR in the pseudorapidity-azimuthal angle space is defined as,

$$\Delta R = \sqrt{\Delta\eta^2 + \Delta\phi^2}. \tag{3.4}$$

In the LHC, protons are accelerated around the rings and collide head-on. Given the complexity of the proton's structure, when a collision takes place, a significant amount of the collision energy escapes down through the pipe (in the above established reference frame this corresponds to the z direction), *i.e.*, when an interesting physics collision takes place, *a hard collision*, only one parton of each proton participates in the process, whereas the momentum of the remaining partons is not greatly changed. Furthermore, considering conservation of energy and momentum, it is noted that the initial momentum before the collision in the transverse plane to the beam pipe (x-y plane) is zero, henceforth this quantity must be also zero after the collision. Thus it is extremely practical to define variables in the

transverse plane. For example the transverse momentum p_T, which is the magnitude of the momentum vector projected on the x-y plane, of a final state particle, is highly enhanced in hard collisions, as opposed to elastic/diffractive scattering of the incoming particles. Moreover the transverse momentum of invisible particles for a detector, result of hard collisions, is inferred with the transverse momentum of the detectable particles participating in this process, defining the missing transverse energy E_T^{miss}, see Section 6.4. The previous two regards imply the usefulness of the transverse plane variables in both pp and e^+e^- colliders [38].

3.2.2 Inner Detector

The Inner Detector (ID) is dedicated to measure charged particle trajectories and locate interaction vertices in a range of $|\eta| < 2.5$; it is immersed in a 2 T solenoid field (5.3 m long with a diameter of 2.5 m) permitting a transverse momentum reconstruction resolution of 0.05%, by utilising the Lorentz force to relate it to the curvature of the particle's trajectory. Momentum and vertex measurements and electron identification are achieved with a combination of discrete high-resolution silicon pixel (the closest to the IP) and semiconductor tracker (SCT) strip detectors in the inner part of the tracking volume, and straw-tube tracking detector with the capability to generate and detect transition radiation[4] in its outer part, the transition radiation tracker (TRT). The ID is sketched in Figure 3.4.

Next to the vertex region, the highest granularity is attained by the pixel silicon detectors; the pixel layers are segmented in R-ϕ and z, three pixel cylindrical layers around the beam and three disks perpendicular to the these. All pixel sensors are identical and have a pixel size in R-$\phi \times z$ of $50 \times 400\,\mu\text{m}^2$. The hit resolutions in the barrel are $10\,\mu$m (R-ϕ) and $115\,\mu$m (z) and in the disks are $10\,\mu$m (R-ϕ) and $115\,\mu$m (R). The pixel detector has approximately 80.4 million readout channels to collect the charged signals of a particle that hits a pixel.

The SCT strip layers have similar geometry with respect to the ID. In the barrel region, the SCT uses double silicon strip layers, one with a small stereo angle (40 mrad) to measure both coordinates (z and R-ϕ), and one parallel to the beam direction, measuring R-ϕ. In the end-cap region, the detectors have a set of strips running radially and a layer of stereo strips at an angle of 40 mrad. The mean pitch of the strips is also approximately 80 μm. The intrinsic spatial hit resolutions per module in the barrel are 17 μm (R-ϕ) and 580 μm (z) and in the disks are 17 μm (R-ϕ) and 580 μm (R). The total number of readout channels in the SCT is approximately 6.3 million.

A large number of hits (typically 36 per track) is provided by the 4 mm diameter straw

[4]Transition radiation is the electromagnetic radiation produced when a electrically charged particle passes through a boundary of two different media.

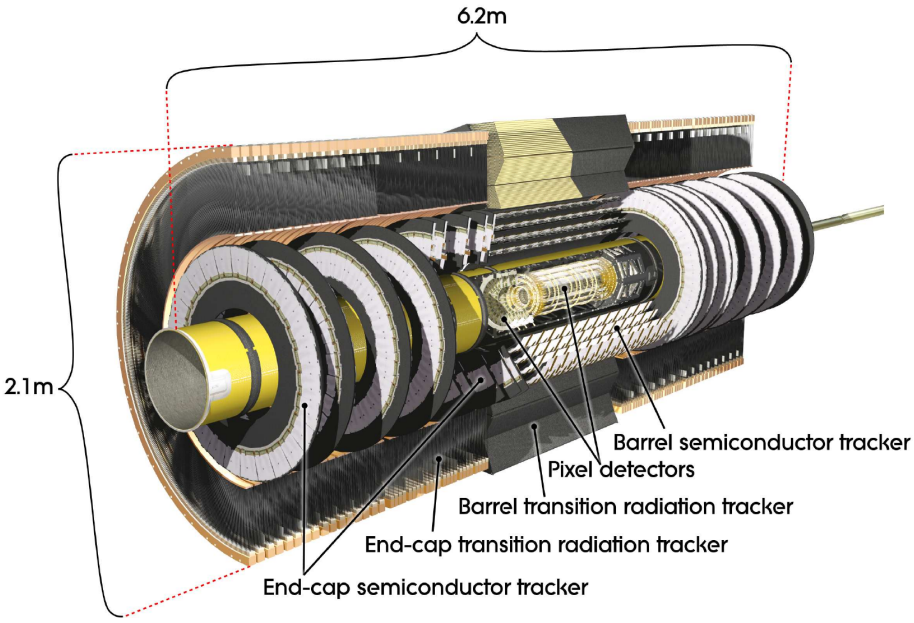

Figure 3.4: Diagram of the Inner detector [38].

tubes (drift tubes) of the TRT, which enables track-following up to $|\eta| = 2.0$. The TRT only provides R-ϕ information, for which it has an intrinsic hit resolution of 130 μm per straw. In the barrel region, the straws are parallel to the beam axis and are 144 cm long, with their wires divided into two halves, approximately at $\eta = 0$. In the end-cap region, the 37 cm long straws are arranged radially in wheels. The total number of TRT readout channels is approximately 351,000.

Combining the pixel and SCT trackers at small radii with the TRT at a larger radius, gives a very good precision, in both R-ϕ and z coordinates, making possible to have a transverse momentum measurement resolution of 0.05%. The straw hits at the outer radius contribute significantly to the momentum measurement, since the lower precision per point, compared to the silicon, is compensated by the large number of measurements and longer measured track length. The inner detector system provides tracking measurements in a range matched by the precision measurements of the electromagnetic calorimeter. The electron identification capabilities are enhanced by the detection of transition-radiation photons in the xenon-based gas mixture of the straw tubes.

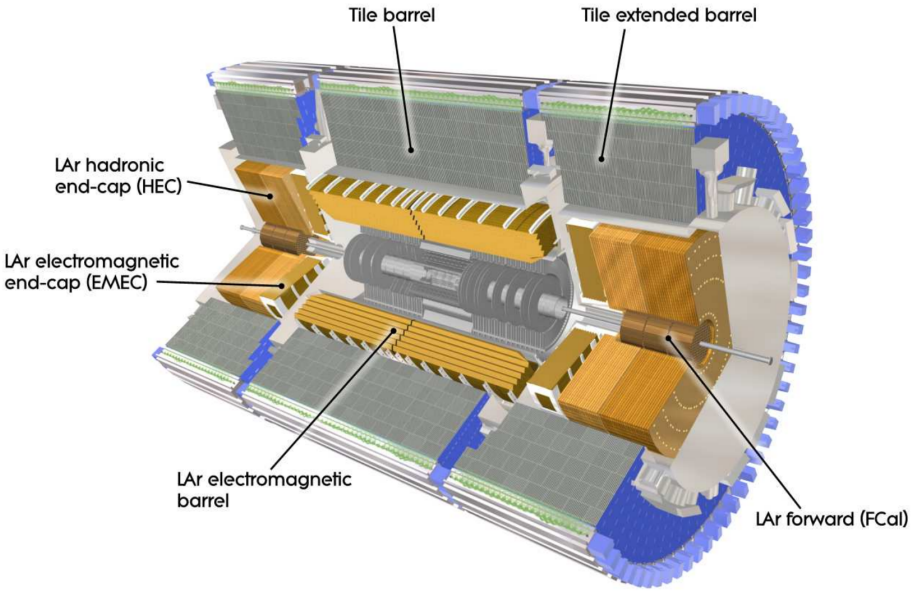

Figure 3.5: ATLAS calorimetry cut away [38].

3.2.3 Calorimeters

The next step in the detector chain within ATLAS is the calorimetry system; the calorimetry system surrounds the ID. This system is designed to absorb all the known particles coming from a collision, except muons and neutrinos. The calorimeters measure the energy a particle releases when going through the detector using layers of a passive material interleaved with layers of an active medium. During this process the particle produces electromagnetic (electrons and photons) and hadronic (jets, see Section 6.3 for a jet definition) showers[5] when interacting with the passive material which then ionise the active material, Figure 3.6 depicts an electromagnetic shower. Accordingly, the calorimeters must enclose these streams of particles and limit punch-through into the muon system, *i.e.* the calorimeter depth is an important design consideration.

The components of the ATLAS calorimetry system are: high granularity liquid-Argon (LAr) electromagnetic sampling calorimeters that cover the pseudorapidity range $|\eta| < 3.2$; and the hadronic calorimetry in the range $|\eta| < 1.7$ which is provided by a scintillator-tile calorimeter, separated into a large barrel and two smaller extended barrel cylinders, one on either side of the central barrel. In the end-caps, $|\eta| > 1.5$, LAr technology is also used for the hadronic calorimeters, matching the outer $|\eta|$ limits of the end-cap electromagnetic

[5]In this context, a particle shower is generated when an energetic particle interacts with a medium, this interaction results in a torrent of secondary particles which will repeat this process until it is energetically forbidden.

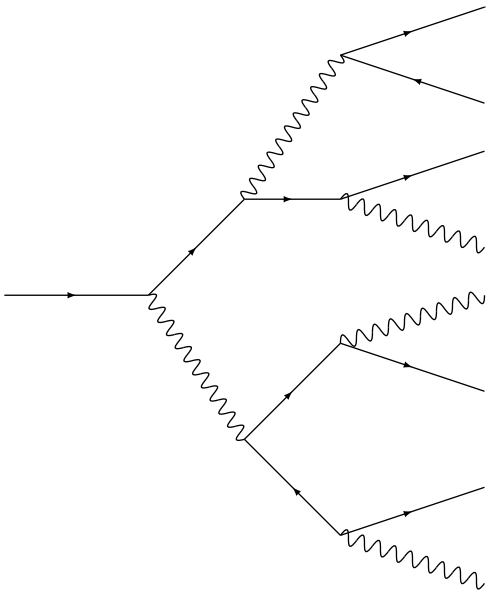

Figure 3.6: Electromagnetic shower. Particles are produced via the interaction of electrons (positrons) with the matter. In this diagram the arrows represent electrons of the process; the curly lines represent the photons which mediate the interaction.

calorimeters. The LAr forward calorimeters provide both electromagnetic and hadronic energy measurements and extend the coverage to $|\eta| < 4.9$. A view of the sampling calorimeters is presented in Figure 3.5.

The electromagnetic (EM) calorimeter is accordion-shaped over its full coverage, this geometry provides a complete ϕ symmetry without azimuthal cracks. The EM calorimeter is divided into a barrel part, $|\eta| < 1.475$, and two end-cap components that cover the $1.375 < |\eta| < 3.2$ region. The total thickness of the EM calorimeter is $> 22\,X_0$ (the radiation length X_0, is the mean distance an electron travels before its energy is reduced to $1/e$ via bremsstrahlung radiation) in the barrel and $> 24\,X_0$ in the end-caps. Given the proximity to the central solenoid and to optimise material/performance, the EM calorimeter and the central solenoid share a common vacuum vessel. The lead thickness in the absorber plates has been optimised as a function of η in terms of EM calorimeter energy resolution performance. For precision physics, $|\eta| < 2.5$, the EM calorimeter is segmented in three sections in depth. For the end-cap inner wheel, the calorimeter is segmented in two sections in depth and has a coarser lateral granularity compared with the rest of the acceptance. In the region of $|\eta| < 1.8$, a presampler detector is used to correct for the energy lost by electrons and photons upstream of the calorimeter.

Outside the EM calorimeter, the hadronic tile calorimeter is installed, its barrel region

covers $|\eta| < 1.0$ and its extended barrels $0.8 < |\eta| < 1.7$. Instead of using LAr as active material, the tile hadronic calorimeter uses scintillating tiles as the active material that produces scintillation photons, measured in photomultiplier tubes, with hadronic and electromagnetic showers. The tile calorimeter dimensions form an inner radius of 2.28 m to an outer radius of 4.25 m segmented in three layers, of approximately 1.5, 4.1 and 1.8 interaction lengths (the interaction length, λ, is the average distance a hadron travels through a medium before interacting) thick for the barrel and 1.5, 2.6, and 3.3 λ thick for the extended barrel. The total detector thickness, at the outer edge of the tile-instrument region, is 9.7 λ in the $\eta = 0$ region. The hadronic calorimeter is bigger than the EM calorimeter, since the hadrons travel longer times before decaying and therefore it takes more distance to be able to correctly detect the hadronic showers.

The end-cap regions are covered by an hadronic end-cap calorimeter (HEC), consists of two independent wheels per end-cap, located after the EM calorimeter end-cap. To reduce drop in material density at the transition regions between the HEC and the forward calorimeter, and the HEC and the tile calorimeter, overlap between the HEC and the tile is set by extending the HEC in a pseudorapidity of $1.5 < |\eta| < 3.2$. Each wheel is built from wedges-shaped modules, inside there are cooper plates as the passive material and LAr the active medium.

Finally, the forward calorimeter (FCal) is integrated in the end-cap to improve the coverage and reduce radiation backgrounds arising from the passage to the muon spectrometer. The front face of the FCal is recessed by ~ 1.2 m with respect to the EM calorimeter front face to control neutron backscattering and radiation coming from the ID. The FCal needs to be highly dense, is approximately 10 interaction lengths deep, and consists of three modules in each end-cap: the first, made of copper, is optimised for electromagnetic measurements, while the other two, made of tungsten, measure predominantly the energy of hadronic interactions. In the measurements reported in this document, only the region for precision physics ($|\eta| < 2.5$) is considered, hence muons detected by the FCal are not directly used.

3.2.4 Muon Spectrometer

The last subdetector of ATLAS is the muon spectrometer (MS). The calorimeters and the inner detector are surrounded by the MS owing the fact that muons penetrate them. The MS is capable to detect charged particles and to measure their momentum, the detection is done through the Lorentz force experienced by charged particles under the influence of the MS magnetic field, see Section 6.1.1. The air-core toroid system, with a long barrel and two inserted end cap magnets, generates strong bending power for the muon tracks in a

large volume within a light and open structure; the high magnetic field strength is needed to measure with good resolution high transverse momentum muons (at 1 TeV the MS has a resolution of 10%). The large barrel toroid provides the magnetic bending in the range of $|\eta| < 1.4$, whilst the end-caps cover the $1.6 < |\eta| < 2.7$; finally, in the transition region, $1.4 < |\eta| < 1.6$, magnetic deflection is provided by a combination of barrel and end-cap fields. This configuration of magnets yields a magnetic field that it is mostly orthogonal to the muon trajectories, while minimising the degradation of the multiple scattering, as it is expected that the proton-proton collision produce a high amount of particles, the design and choice of the spectrometer instrumentation has been driven by the optimisation of parameters such as rate capability, granularity, ageing properties, and radiation hardness. In the barrel region, tracks are measured in chambers arranged in three cylindrical layers around the beam axis; in the transition and end-cap regions, the chambers are installed in planes perpendicular to the beam, also in three layers.

The magnetic system is configured as follows, the two end-caps are inserted in the barrel toroid at each end and aligned with the central solenoid. The toroids consist of eight coils assembled radially and symmetrically around the beam axis. The end-cap toroid coil system is rotated by 22.5° with respect to the barrel toroid system in order to provide radial overlap and to optimise the bending power at the interface between the two coil systems. The performance of the bending power is given by the magnetic field integral, being the magnetic field normal to the muon direction and the integral is calculated along an infinite-momentum muon trajectory, between the innermost and the outermost muon-chamber planes. The barrel toroid provides 1.5 to 5.5 Tm of bending power in the pseudorapidity range of $0 < |\eta| < 1.4$, and the end-cap toroids approximately 1 to 7.5 Tm in the region $1.6 < |\eta| < 2.7$. The bending power is lower in the transition region where the two magnets overlap.

The MS covers the range of $|\eta| < 2.7$, and it is conformed by monitored drift tubes (MDT), cathode strip chambers (CSC), resistive plate trigger-chambers (RPC) and thin gap trigger-chambers (TGC). The MS defines the overall dimensions of the ATLAS detector, Figure 3.7 shows the layout of the MS system [38].

MDT

The MDT chambers perform the precise determination of the muon momentum; consist of three to eight layers of drift tubes and operate with Ar/CO_2 gas at a pressure of 3 bar, the electrons resulting from the ionisation are collected by central tungsten-rhenium wires, the wires have a concentricity with respect to the tube with an accuracy of $\sigma < 10\,\mu$m. Building the precision-tracking chambers using individual tubes, gives mechanical robustness as result of the tube precision assembly; moreover, these chambers are reliable, since a failure of a

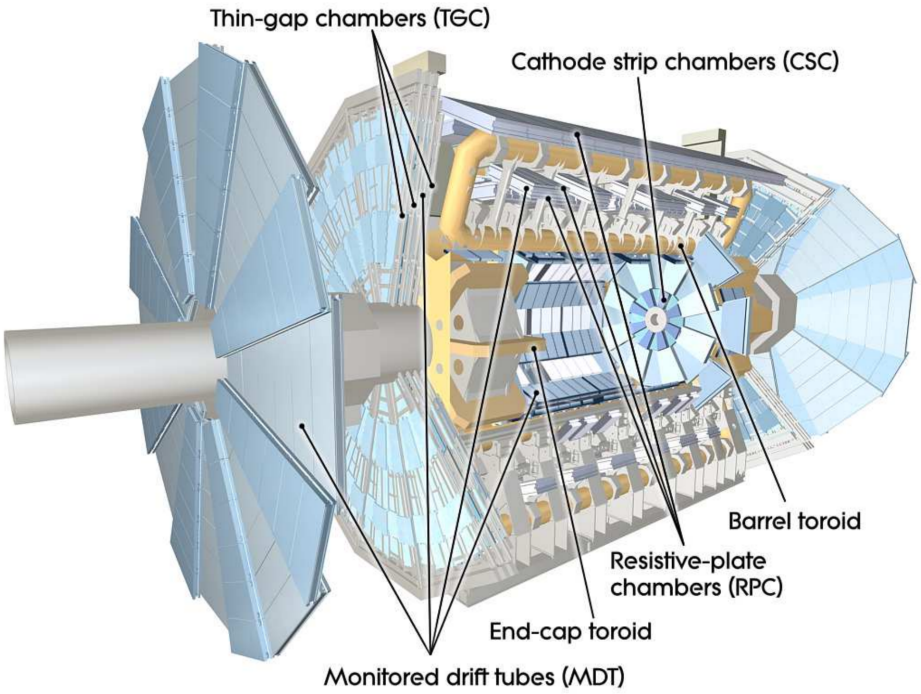

Figure 3.7: ATLAS muon spectrometer system cut away [38]

single tube does not affect the operation of most of the other tubes; finally, the cylindrical geometry produces a radial electric field, consequently the measurement accuracy depends weakly on the angle of incidence of the track on the chamber plane. The MDTs provide an average resolution of 80 μm per tube or 35 μm per chamber.

CSC

In the forward region, $2.0 < |\eta| < 2.7$, CSC chambers are instrumented in the end-cap inner most tracking layer, due to their higher rate capability and time resolution with respect to the MDTs; the CSC are multiwire chambers with cathode planes segmented into strips in orthogonal directions, which combine high spatial, time and double track resolution with high-rate capability and low neutron sensitivity; the region where the CSC chambers operate is predicted to have a higher particle particle density flux. The whole CSC system consists of two disks with eight chambers each, the chambers contain four CSC planes resulting in four independent measurements in η and ϕ along each track; this allows both coordinates to be measured using the induced charge distribution. The resolution of a CSC chamber is 40 μm in the bending plane and about 80 mm in the transverse plane.

RPC

The resistive plate chambers act as trigger instrumentation in the barrel region. The RPCs are located above and/or below the MDTs, forming three trigger stations and are capable to select high or low momentum tracks depending on the trigger station. Each station consists of two independent detector layers that measure η and ϕ coordinates. A RPC is a gaseous parallel electrode-plate detector, that are kept to each other at a distance of 2 mm by insulting spacers; the electric field between the plates is about 4.9 kV/mm and allows avalanches to form along the ionising tracks towards the anode. The signal is read out via capacitive coupling to metallic strips, which are mounted on the outer faces of the resistive plates. The gas used is a mixture of $C_2H_2F_4$/Iso-C_4H_{10}/SF_6 (94.7/5/0.3), this mixture combines relatively low operating voltage, non-flammability and low cost, while providing comfortable plateau for safe avalanche operation. The RPCs detection efficiency is $\geq 98.5\%$ per layer and $\geq 97\%$ including spacers and frames.

TGC

The thin gap chambers are installed in the end-cap muon spectrometer, they perform triggering functions and determine a complement measurement of the azimuthal coordinate coming from the MDTs: the middle layer of the MDTs in the end-cap is complemented by seven layers of TGCs; the inner layer is complemented by two layers. The radial (bending) coordinate is measured by the TGC wire groups, whilst the azimuthal coordinate by radial strips. The TGCs are multi-wire proportional chambers with the characteristic that the wire-to-cathode distance of 1.4 mm is smaller than the wire-to-wire distance of 1.8 mm.

Combining both the RPC and TGC systems, fast trigger information of muon tracks is provided. The RPC covers the barrel region $|\eta| < 1.05$ and the TGC the end cap region $1.4 < |\eta| < 2.4$. The trigger chambers measure both coordinates of the track, one in the bending (η) plane and one in the non-bending (ϕ) plane. The purpose of the precision-tracking chambers is to determine the coordinate of the track in the bending plane. After matching the MDT and trigger chamber hits in the bending plane, the trigger chamber's coordinate in the non-bending plane is adopted as the second coordinate of the MDT measurement. This method assumes that in any MDT/trigger chamber pair, a maximum of one track per event is present, since having two or more tracks forbids the η and ϕ hits combination in an unambiguous way. Simulations have shown that the probability to find a track in the muon spectrometer with $p_T > 6$ GeV is close to 6×10^{-3} per beam-crossing, corresponding to about 1.5×10^{-5} per chamber. Assuming uncorrelated tracks, this leads to a negligible

probability to find more than one track in any MDT/trigger chamber pair. When correlated close-by-muon-tracks occur, caused for example by two-body-decays of low-mass particles, the ambiguity in η and ϕ assignment will be resolved by matching the muon track candidates with tracks from the inner detector.

3.2.5 Trigger system

Many proton-proton collisions at the LHC are needed because the phenomena searched by physicists occur at extremely low rates, meaning that these interesting events are difficult to see; consequently, to have a significant chance to observe one such event, it is advantageous a high proton-proton collision rate. Hence in the detectors there will be many events that are not of high interest, to handle this and select/study only relevant events, a mechanism to separate interesting and not interesting events was developed: the *triggersystem*. The pp interaction rate at the design luminosity is approximately 1 GHz, while the event data recording, is limited to about 200 Hz. This requires an overall rejection factor of 5×10^6 against minimum-bias processes while maintaining maximum efficiency for interesting physics. The rejection is performed by a trigger system consisting of three levels: Level-1 (L1), Level-2 (L2), and event filter.

Level-1 trigger

The L1 trigger is implemented using custom-made electronics. The L1 trigger system uses a subset of the total detector information to make a decision on whether or not to continue processing an event, reducing the data rate to approximately 75 kHz; this is done searching for high transverse momentum (interesting physics processes are characterised by having high transverse momentum final state particles) muons , electrons, photons, jets, and tau leptons decaying to hadrons, it also selects events with large missing transverse energy and large total transverse energy. The L1 triggering systems are:

- *L1 Calorimeter trigger (L1Calo).* All the calorimeters of ATLAS (electromagnetic and hadronic; barrel, end-cap and forward). This system aims to identify high-E_T objects such electrons, photons, jets, τ-leptons and missing energy.

- *L1 Muon trigger (L1Muon).* The L1 Muon trigger is based on signals in the muon trigger chambers: the RPCs in the barrel and the TGCs in the end-caps. The trigger searches for high p_T muons originating in the interaction point.

- *Central trigger processor (CTP).* The overall decision to keep an event at Level-1 is done by the central trigger processor that integrates the triggering information coming

from the different objects. The CTP implements a trigger *menu* made up of trigger selections.

In each event, the L1 trigger also defines one or more Regions of Interest (RoIs), *i.e.* the coordinates in η and ϕ, of those regions within the detector where its selection process has identified interesting physics. This information is subsequently used by the high-level trigger.

High-level trigger

The subsequent two levels, collectively known as the high-level trigger (HLT), are the Level-2 (L2) trigger and the event filter. They provide the reduction to a final data-taking rate of approximately 200 Hz [38]. The L2 selection is seeded by the RoI information provided by the L1 trigger over a dedicated data path. L2 selections use, at full granularity and precision, all the available detector data within the RoIs. The L2 menus are designed to reduce the trigger rate to approximately 3.5 kHz, with an event processing time of about 40 ms, averaged over all events. The final stage of the event selection is carried out by the event filter, which reduces the event rate to roughly 200 Hz. Its selections are implemented using offline analysis procedures within an average event processing time of the order of four seconds.

The data acquisition (DAQ) system consists in monitoring the flux of events from the detector to the disk storage. As stated above, the first step is the selection by the L1 trigger with a latency maximum of 25 μs, the event data are buffered in memories located within the detector-specific front-specific electronics. The information from L1 trigger is transferred to the DAQ/HLT system utilising over 1574 readout links, having first transited through the detector-specific readouts. The 1574 event fragments are received into readout buffers, contained in a special readout system units where they are temporarily stored and provided to the subsequent stages of the DAQ/HLT system. Level-2 trigger performs full event reconstruction on restricted RoI info to make a decision, and then HLT performs full event reconstruction to make the final decision of writing the event to disk.

Chapter 4

Level 1 Calorimeter optimisation

This chapter contains the studies regarding the optimisation of the L1 Calorimeter trigger rates and efficiencies. These studies are in the context of the ATLAS detector functioning and they illustrate the power of the tag and probe method, which is widely used to compute correction efficiencies. Additionally a better insight of the ATLAS L1 Calorimeter trigger is pictured. This work is a team effort and it is the bulk of the requirements to complete the ATLAS collaboration service task.

4.1 Introduction

The future plans of the LHC programme are to increase the luminosity, *i.e.* the amount of protons circulating the rings is planned to be risen. This poses a critical problem in the processing of the data collected by the ATLAS detector, since having a higher luminosity means that the number of proton-proton collisions will increase accordingly beyond the ATLAS data storage capabilities. During previous and current LHC operations, dedicated triggers were used to select data that potentially contain interesting physics events, henceforth adapting the data collection to realistic storage capabilities. The ATLAS triggering system has different stages and components (see Chapter 3), the studies presented in this Chapter are aimed to provide an optimised configuration of the L1 Calorimeter trigger hardware to cope with the increased luminosity, the latter is done by simulating the hardware and investigate the impact of changing its parameters on the signal efficiencies and trigger rates.

4.2 Optimisation strategy

The L1Calo efficiencies and trigger rates optimisation is determined after data taking (offline optimisation) and follows the main steps:

- Simulation of the L1Calo custom electronics.
- Calculate efficiencies for different simulated hardware configurations based on a $Z \rightarrow ee$ sample.
- Calculate trigger rates for different simulated hardware configurations based on a sample enriched with low-p_T events (LHC minimum bias events).
- Study the interplay among the efficiencies and rates and find the simulated hardware configuration which minimises the trigger rates whilst maintaining the efficiencies high.

The subsequent sections describe in greater detail the previously mentioned steps.

4.2.1 Simulation of L1Calo

The L1Calo system is conformed of custom electronics, it is a pipelined digital system with a dead time of 2.5 μs. L1Calo is located outside the ATLAS detector cavity in the USA15 cavern. The L1Calo is fed with information coming from all the ATLAS electromagnetic and hadronic calorimeters. In order to organise the input and ease the processing of the data, the calorimeters are divided in the so-called *trigger towers*, which consist of regions of space within the detector, described by the pseudorapidity and azimuthal angle coordinates. The dimensions of a trigger tower depend on the region of the detector, see Table 4.1.

Position	$\Delta\eta \times \Delta\phi$
$\lvert\eta\rvert < 2.5$	0.1×0.1
$2.5 < \lvert\eta\rvert < 3.1$	0.2×0.2
$3.1 < \lvert\eta\rvert < 3.2$	0.1×0.2
$3.2 < \lvert\eta\rvert < 4.9$	0.4×0.4125

Table 4.1: Trigger tower granularity for several $|\eta|$ slices and one quadrant in $\phi\,(0° - 90°)$.

The L1Calo has three main sub-systems:

- Pre-Processor(PPr): it digitises the analogue calorimeter pulses, associates the trigger tower signals with the correct LHC bunch-crossing and converts ADC counts to energy.

- Cluster Processor (CP): electron, photon and single hadron identification is done by the CP; it uses a 0.1×0.1 granularity and operates in the $|\eta| < 2.5$ region.

- Jet/Energy-sum processor (JEP): this system performs the jet finding and energy sums; its granularity corresponds to 0.2×0.2 where sums of the electromagnetic and hadronic layers of L1Calo take place. The JEP operates over the whole of the ATLAS region ($|\eta| < 4.9$).

The PPr provides the energy deposited in each of the electromagnetic calorimeter trigger towers to the CP and JEP processors; particle searching algorithms are used by these processors to find features in overlapping sliding windows and the final results are sent on cables to the CTP. Each CP consists of four crate systems and each of them contains 14 Cluster Processor Modules (CPMs) which handles one calorimeter quadrant. The CP chips on every CPM are large Field Programmable Gate Arrays (FPGAs). CPMs carry out the e/γ and τ algorithms and count the multiplicity of successes, or hits, in the region covered by each module.

The e/γ algorithm searches for narrow high E_T showers in the EM calorimeters. The large rate of hadronic jets contaminates the showers in the EM calorimeters; consequently, isolation requirements are implemented to discriminate between the electromagnetic and the hadronic showers and to enhance the selection at L1. Moreover, showers are required to not penetrate the hadronic calorimeter. The CP provides several sets of energy threshold and isolation conditions and each threshold can be chosen independently.

To handle the higher occupancies in the calorimeter system, result of the increased pileup, the ouput data format has been extended from simple hit counts to more descriptive Trigger Objects (TOBs) which include also the topological trigger: η, ϕ and E_T of the candidate electron, the former is shown in Figure 4.1. A TOB specifies a RoI along with its associated transverse energy and likelihood to be related with a particle produced in a collision.

The offline code[1] simulates the hardware in two steps: first the trigger towers and then the TOBs are simulated. This procedure allows to reprocess the trigger towers varying the noise cuts; likewise the reprocessing of TOBs, changing the isolation cuts on CPMs, is available. Details of the trigger simulation are:

- Access the database: the initialisation uses COOL-derived values (Condition Objects for LHC, COOL, is the ATLAS-wide conditions database found in the computing grid).

- Retrieve the database containers and cancel the dead time or disabled channels.

[1]The offline code was written by the QMUL L1Calo group: Adele D'Onofrio, Antony Fray, Jonh Morris, Andres Ramirez-Morales.

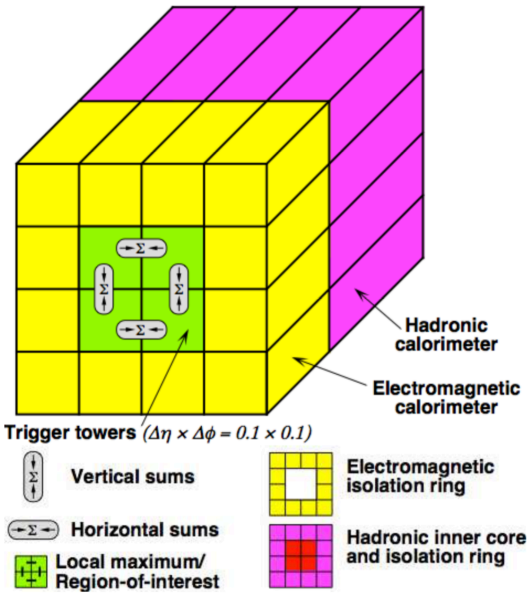

Figure 4.1: Elements used for the e/γ and τ algorithms in CPMs. Consider the 2×2 trigger tower region at the centre of the 4×4 trigger tower window: in the EM calorimeter E_{T} values are summed for the towers in each of the four possible 1×2 and 2×1 pairs within the region, in order to find relatively narrow showers and the sum of the inner 2×2 region must be a local maximum compared to its eight overlapping nearest neighbours.

- Get input trigger towers from the input collection and copy ADC digits into a digit vector for reprocessing with a suitable granularity for the different $|\eta|$ regions listed in Table 4.1.

- Emulate finite-impulse-response (FIR) filter, bunch crossing identification and look up tables (LUT), and create/fill reprocessed trigger towers.

The FIR filter is needed since the width of the pulses contains several bunch crossings, thereupon it is extremely important to associate the correct LHC bunch-crossing to the trigger towers signals. This is carried out passing the pulses through different filters which multiply five consecutive samples by pre-defined coefficients and sum the resulting values. The coefficients are optimised for the pulse shape of each type of calorimeter. Afterwards, a peak finder algorithm is implemented which compares the sum with the values from the previous and following bunch-crossings, looking for a maximum. When a peak is found, the

LUT is used to convert the output of the FIR filtering into transverse energy.

There is a linear relation between the peaks and the signal energy; the LUT provides the calibration curve established by a slope and an offset where the pedestal effect is subtracted and the noise threshold is applied. Hence simulating the LUT permits changes in the noise cuts for both the cluster and jet energy processors, aiming to analyse the impact of the different configurations on the final efficiency and rates. Finally, the reprocessed triggers are stored in the *Trigger Elements* (TEs), which represent a trigger-relevant object in the event.

The TOBs simulation requires three further steps: get trigger towers from TEs, form CPMTowers from triggers towers and store the CPMTowers in the TEs. The CPMTowers are filled with user-supplied vectors of trigger towers adding their transverse energy and angular parameters. With this information the CPMs are able to perform the e/γ and τ algorithms.

4.2.2 L1Calo efficiencies

The studies presented in this section are determined with 2016 data recorded by the ATLAS detector during proton-proton collisions when the LHC circulated 6.5 TeV centre of mass energy proton beams. The data examined for the efficiencies corresponds to 1 pb^{-1}. The data sample derivation (see Chapter 5) used for these studies should be appropriate to examine the characteristics of the L1Calo, namely the L1CALO1 derived samples contain all the required information to perform the present studies.

The physics efficiencies are evaluated via a $Z \rightarrow ee$ "tag and probe" analysis on data, *i.e.* one electron is tagged with tight identification selections, the di-electron invariant mass is required to be consistent with the Z boson mass and a loose selection is applied to the second electron, the latter is referred to as probe electron and it is the one used for efficiency studies. More precisely, the selection is as follows.[2]

Event level cuts:

- The event must be included in the 2016 ATLAS data quality good runs list.
- The event is required to contain at least one primary vertex.
- The event must pass through standard calorimeter cleaning at the calibration stage.
- The di-electron invariant mass must be in the range of 66 GeV and 116 GeV.

[2]The selection criteria described here are individually described in Chapter 7, the reader is referred to this Chapter for greater details on each criterion.

Tag electron cuts:

- High level trigger selection, following the ATLAS e/γ group recommendations, either the HLT_e26_lhtight_nod0_ivarloose or HLT_e60_lhmedium_nod0 or HLT_e140_lhloose_nod0 to be triggered by the electron in the event.
- The electron must posses a transverse momentum greater than 27 GeV.
- The electron must be found in the detector region of $|\eta| < 2.47$, whilst electronsq in the crack region, between the barrel and the end-caps of the electromagnetic calorimeters, $1.37 < |\eta| < 1.52$ are excluded.
- The electron identification is performed applying the Loose Likelihood (LLH) criteria and requiring a tight selection.
- The isolation requirements are applied depending on the trigger efficiency that it is being studied.
- The selected electron is required to be matched with the trigger.

Probe electron cuts:

- The electron must have a transverse momentum greater than 7 GeV.
- The electron must be found in the detector region of $|\eta| < 2.47$, whilst electrons in the crack region, between the barrel and the end-caps of the electromagnetic calorimeters, $1.37 < |\eta| < 1.52$ are excluded.
- Loose electron isolation is required.

The previous event and object level cuts combined assure a very good purity for the Z boson sample. To check the validity of the selection criteria, the control plots of Fig. 4.2-4.4 were produced and examined; it is seen that the distributions conform well to expectation, suggesting that the purity is sufficient in the selected $Z \to ee$ sample to be used for trigger efficiency studies.

Trigger efficiency calculation

The efficiencies are calculated using the *tag and probe* method: given the reconstructed tag electron, the reconstruction efficiency of the probe electron, after the application of a specific selection, is determined in the $Z \to ee$ sample described above. The trigger selection efficiency is to be measured using probe electrons matched to a L1 TOB. The efficiency calculation requires the following selection criteria of the probe electron and the TOB:

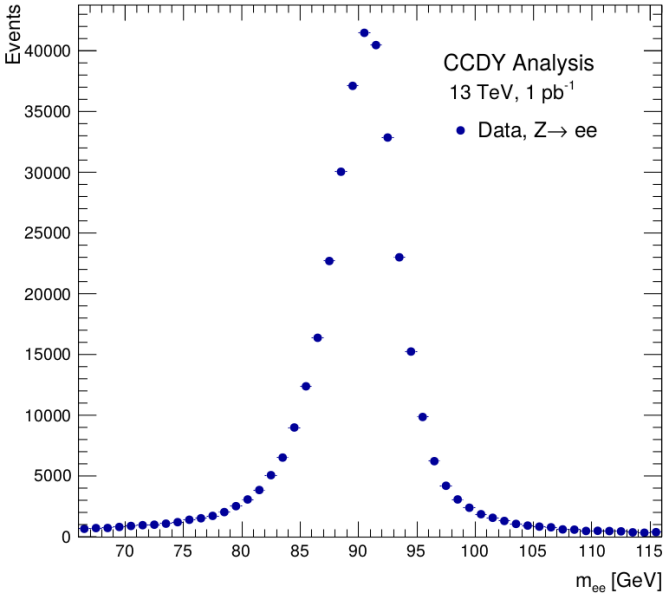

Figure 4.2: Reconstructed invariant mass of the di-electron system, obtained from the $Z \rightarrow ee$ sample in 2016 data.

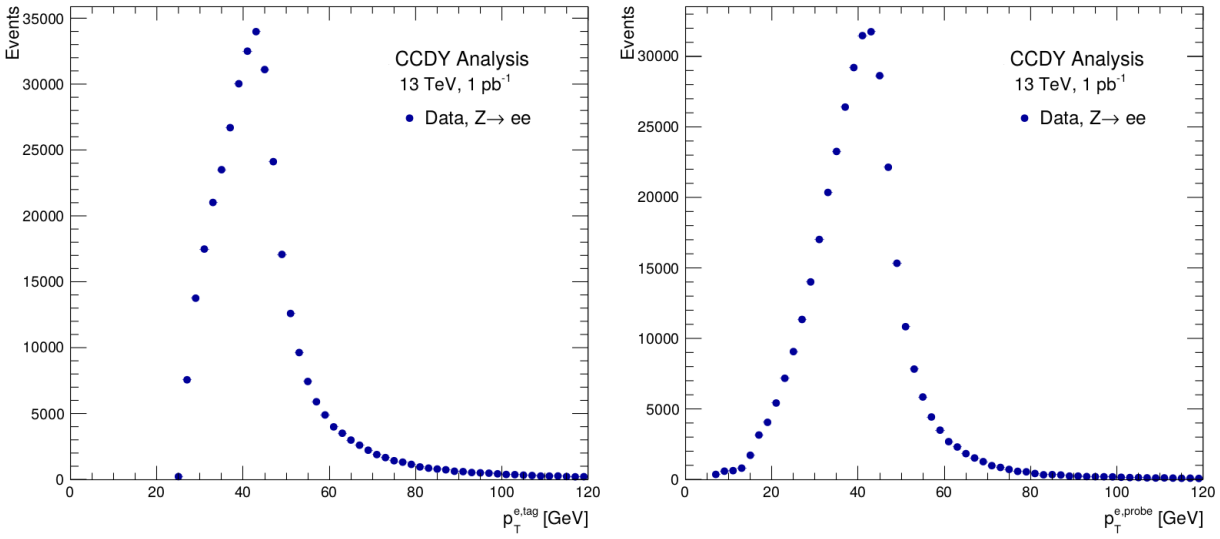

Figure 4.3: p_T^e distributions for tag (left) and probe (right) electrons, obtained from the $Z \rightarrow ee$ sample in 2016 data.

- The angular matching between the probe electron and the TOB must hold:

$$\Delta \mathrm{R} = \sqrt{\Delta\phi^2_{e,\mathrm{TOB}} + \Delta\eta^2_{e,\mathrm{TOB}}} < 0.15, \tag{4.1}$$

where $\Delta\eta$ and $\Delta\phi$ are the differences between the probe electron and the TOB in

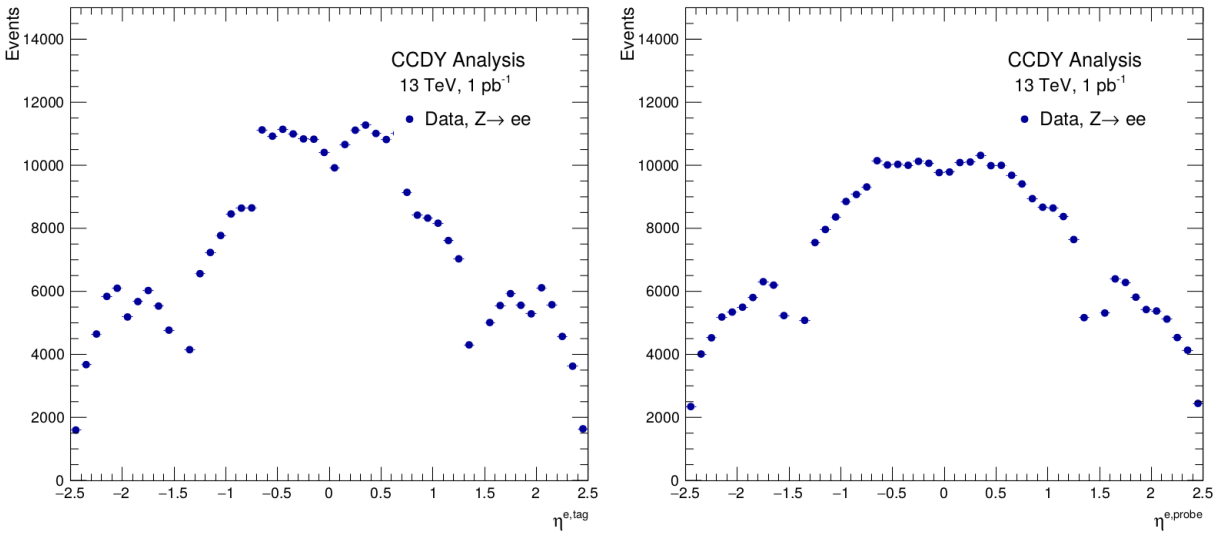

Figure 4.4: η^e distributions for tag (left) and probe (right) electrons, obtained from the $Z \to ee$ sample in 2016 data.

pseudorapidity and azimuthal angles respectively.

- The TOB must be reconstructed in a suitable RoI of dimension $\Delta\eta \times \Delta\phi = 0.4 \times 0.4$. The majority of the energy is required to be deposited in the second layer of the electromagnetic calorimeter.

- The trigger selections of interest are:

  – EM15.

  – EM15HI.

  – EM20VHI.

  – EM22VHI.

  – EM24VHI.

  where EM refers to the EM calorimeter, the number following EM indicates the minimum transverse energy requirement in GeV. Next, the letters refer to different types and levels of isolation: "I" stands for the EM ring isolation applied, where the EM energy is within an isolation ring surrounding the core 2×2 trigger towers; "H" refers to the hadronic core isolation energy threshold applied (which is E_T-dependent, no isolation for L1 $E_T > 50$ GeV); "V" refers to η-dependent trigger energy threshold applied which follows the variation in η of the energy response.

The electron efficiencies ϵ are the ratio between the number of probe electrons associated to a TOB passing the above mentioned criteria and the total number of probe electrons,

$$\epsilon = \frac{\mathrm{N}_e(\mathrm{Trigger\quad Selection\quad and\quad \Delta R})}{\mathrm{N}_e(\mathrm{All\quad probe\quad electrons})}. \tag{4.2}$$

Total and differential (in probe electron p_T^e and η^e bins) efficiencies are calculated.

4.2.3 Trigger rates

Conversely to physics interesting data used to calculate efficiencies, studying the trigger systems requires the use of a sample that represents as much as possible the LHC collisions, *i.e.* the majority of events coming from pp collisions at LHC consist of low p_T events (minimum bias events), trigger rate estimations are better calculated with "enhanced minimum bias" events.

For the present studies, the enhanced events are selected demanding each TOB to be reconstructed within a suitable RoI of the detector by requiring to be located in the first layer of the EM calorimeter. The trigger threshold list is analysed and if at least one TOB of the event passes a given threshold, the event is considered triggered by that trigger label (the trigger thresholds labels used are: EM15, EM15HI, EM20VHI, EM22VHI and EM24VHI). A definition of the *effective* trigger rate is determined as the number of events triggered by a specific trigger over the total number of events in the sample fulfilling a simple RoI selection. Events from the enhanced bias sample are reweighted using specific enhanced bias weights factorising away the enhanced selection and correcting the effective rates to what is expected in regular data.

4.3 Simulation bias

The simulation procedure[3] described in Section 4.2.1 needs to be compared with the original online chain, an offline analysis is devoted for this which compares the default objects and quantities with the reprocessed ones. These tests are important to validate the offline simulation methodology. Nevertheless the studies of the parameter optimisation are done comparing exclusively the reprocessed objects and quantities, therefore the results presented in next sections are not affected by the biases found in this section.

With the aim of spotting possible bias of the hardware response versus the offline hardware simulation, several tests were performed; starting from the reprocessing that creates

[3]The main two steps are the creation of trigger towers followed by the simulation of the processors

the reprocessed trigger towers, and then input of the original trigger towers to the modified processors to test the second reprocessing step; finally, the full two-step procedure is checked comparing the original TOBs with the ones generated by both the reprocessing steps. Here, only the final checks are presented, which show the rates and efficiencies comparison calculated with both the reprocessed and the default TOBs. The efficiency plots in Figure 4.5-4.6 are shown differentially in p_T^e and η^e bins, satisfying Equation (6.3). The rates described in Section 4.2.3 are displayed in Figure 4.7.

The difference between the hardware response and the hardware simulation is negligible. This agrees with the previous checks (not shown here) of the different stages of the simulation procedure. Two central bins in the electron pseudorapidity efficiency are the most affected by the simulation bias, this is work in progress.

4.4 Results

The aim of the studies shown in this Chapter is to find optimal noise cut values to improve (lower) the trigger rates while maintaining the reconstruction efficiency high.

The efficiencies were evaluated using different noise cuts and trigger thresholds. In the same manner, trigger rates were computed. An ansatz of the noise cut range to be investigated, is set around the default value $4.0k$, *i.e.* from $2.0k$ to $8.0k$ in $2.0k$ steps, this is called the "wide range".

Efficiencies corresponding to the first ansatz are shown differentially in probe electron transverse momentum bins in Figure 4.8, a separate plot corresponds to each of the various trigger thresholds. Reducing the value of the noise cut leads to higher LUT values in the isolation ring, whilst increasing the noise cut values leads to higher LUT values in the isolation ring. Hence a slight effect on the efficiency it is seen in the EM15 trigger selection as there is no isolation requirement. Nevertheless in all the trigger thresholds, the *turn-on* region in the isolation curve, exhibits a discrepancy in the efficiency values for different noise cuts.

To study the efficiencies as a function of the probe electron pseudorapidity, only electrons passing a p_T^e cut, which depends on each trigger threshold, were considered in the numerator of Equation (6.3), removing the turn-on region in the transverse momentum efficiency curves. Namely, the p_T^e cuts for the listed trigger thresholds are:

- EM15, p_T >20 GeV;
- EM15HI, p_T >20 GeV;

cut value	EM15	EM15HI	EM20VHI	EM22VHI	EM24VHI
2.0 k	99.28	95.44	95.60	95.61	92.65
4.0 k	99.28	97.34	97.27	97.27	93.20
6.0 k	99.28	98.16	97.93	97.93	94.81
8.0 k	99.26	98.42	98.12	97.12	94.99

Table 4.2: Trigger efficiency values as a function of the wide range of noise cut values. Efficiencies are calculated considering in the numerator only probe electrons passing a p_{T}^{e} cut that depends on the specific trigger threshold analysed (in order to remove the efficiency turn-on region). The values are given in percentage.

- EM20HI, p_T >25 GeV;
- EM22HI, p_T >27 GeV;
- EM24HI, p_T >29 GeV.

These efficiencies are displayed in Figure 4.9. Similarly to the p_T^e binned efficiencies, the EM15 noise cuts have a negligible effect on the efficiency, furthermore the changes of efficiencies are significant when looking trigger thresholds which include isolation cuts.

The efficiency calculations are condensed in Table 4.2. Here the total efficiencies are integrated over the p_T^e and η^e variables; the values are obtained applying the above electron transverse momentum cuts. It is the main interest to explore the variation of the different cuts w.r.t. the default noise cut ($4.0k$), defined as,

$$\Delta_{\mathrm{eff}} = \frac{\mathrm{test}_{\mathrm{eff}} - \mathrm{default}_{\mathrm{eff}}}{\mathrm{default}_{\mathrm{eff}}}, \tag{4.3}$$

where $\mathrm{default}_{\mathrm{eff}}$ is the trigger efficiency calculated for the default noise cut, while $\mathrm{test}_{\mathrm{eff}}$ is the efficiency of the alternative noise cut being considered in the test. The aim is to obtain the highest possible efficiency, consequently a positive Δ_{eff} is pursued. The Δ_{eff} values are presented in Table 4.3.

In the same manner the rates are summarised in Table 4.4 and a rate variation is defined as,

$$\Delta_{\mathrm{rate}} = \frac{\mathrm{default}_{\mathrm{rate}} - \mathrm{test}_{\mathrm{rate}}}{\mathrm{default}_{\mathrm{rate}}}, \tag{4.4}$$

where $\mathrm{default}_{\mathrm{rate}}$ is the effective trigger rate calculated for the default $4.0k$ noise cut, while $\mathrm{test}_{\mathrm{rate}}$ is the rate of the alternative noise cut considered in the test. The aim is to obtain the lowest possible rates, consequently a positive Δ_{eff} is pursued. The Δ_{rate} values are presented in Table 4.4.

cut value	EM15	EM15HI	EM20VHI	EM22VHI	EM24VHI
2.0 k	0	-1.95	-1.71	-1.71	-1.59
4.0 k	DEFAULT				
6.0 k	0	0.84	0.68	0.68	0.63
8.0 k	0.02	1.11	0.87	0.87	0.81

Table 4.3: Variation of the trigger efficiencies as a function of the wide range of noise cut values. The variation is evaluated as explained in the text with respect to the default ($4.0k$) noise cut. Efficiencies are calculated considering in the numerator only probe electrons passing a p_{T}^{e} cut that depends on the specific trigger threshold analysed (in order to remove the efficiency turn-on region). The values are given in percentage.

cut value	EM15	EM15HI	EM20VHI	EM22VHI	EM24VHI
2.0 k	0.81	0.43	0.36	0.35	0.35
4.0 k	0.80	0.49	0.38	0.37	0.36
6.0 k	0.79	0.57	0.40	0.38	0.37
8.0 k	0.78	0.59	0.41	0.40	0.38

Table 4.4: Effective trigger rates as a function of the wide range of noise cut values. The values are given in percentage.

Examining the efficiency and rate variations displayed in Tables 4.3 and 4.4, it is concluded that the $2.0k$ noise cut corresponds to a loss in efficiency of more that 1%. Analogously the $8.0k$ noise cut, in spite of the fact that the efficiency is raised, the increase of the trigger rates is not negligible. Hence, the first proposed noise cut range is narrowed around the default noise cut of $4.0k$: the study is repeated in the range from $3.0k$ to $5.0k$, in $0.5k$ steps. Figure 4.10 displays the efficiencies in this new range as a function of the probe electron transverse momentum for the different trigger thresholds and noise cuts. Equivalently, Figure 4.11 shows the efficiency as a function of the probe electron pseudorapidity; in the numerator of Equation (6.3) only probe electrons passing the above-mentioned p_T^e cuts, which depend on each trigger threshold, are taken into account. In addition, the rates plots are found in Figure 4.12.

To be more quantitatively, the total efficiencies and their variations w.r.t. the default value in the narrower noise cut range, are compiled in Tables 4.5 and 4.8. The corresponding rates results are contained in Tables 4.7 and 4.8.

Considering the efficiency and rate variations, it is suggested that the $3.5k$ noise cut corresponds to a minimal loss of efficiency ($< 1\%$), while reducing the rates of an interesting percentage. This is the main result of these studies.

cut value	EM15	EM15HI	EM20VHI	EM22VHI	EM24VHI
3.0 k	99.28	96.35	96.43	96.40	93.27
3.5 k	99.28	96.94	96.92	96.87	93.70
4.0 k	99.28	97.33	97.27	97.20	93.96
4.5 k	99.28	97.61	97.50	97.41	94.12
5.0 k	99.28	97.81	97.65	97.57	94.18

Table 4.5: Trigger efficiency values as a function of the narrow range of noise cut values. Efficiencies are calculated considering in the numerator only probe electrons passing a p_{T}^{e} cut that depends on the specific trigger threshold analysed (in order to remove the efficiency turn-on region). The values are given in percentage.

cut value	EM15	EM15HI	EM20VHI	EM22VHI	EM24VHI
3.0 k	0	-1.01	-0.86	-0.82	-0.73
3.5 k	0	-0.69	-0.36	-0.34	-0.28
4.0 k	DEFAULT				
4.5 k	0	0.28	0.24	0.22	0.17
5.0 k	0	0.49	0.39	0.38	0.23

Table 4.6: Variation of the trigger efficiencies as a function of the narrow range of noise cut values. The variation is evaluated as explained in the text with respect to the default ($4.0k$) noise cut. Efficiencies are calculated considering in the numerator only probe electrons passing a p_{T}^{e} cut that depends on the specific trigger threshold analysed (in order to remove the efficiency turn-on region). The values are given in percentage.

cut value	EM15	EM15HI	EM20VHI	EM22VHI	EM24VHI
3.0 k	0.80	0.47	0.37	0.36	0.35
3.5 k	0.80	0.49	0.38	0.37	0.36
4.0 k	0.80	0.51	0.38	0.37	0.36
4.5 k	0.80	0.52	0.39	0.37	0.36
5.0 k	0.80	0.54	0.39	0.38	0.35

Table 4.7: Effective trigger rates as a function of the narrow range of noise cut values. The values are given in percentage.

4.5 Additional checks

The matching of the probe electrons and the TOBs are of fundamental importance for the efficiency and rates calculations. The angular association between trigger objects (defined at L1) and the probe electrons (reconstructed by the HLT) is performed using Equation (4.1). The first step is to check that the matching procedure outlined in Section 4.2.2 ensures to

cut value	EM15	EM15HI	EM20VHI	EM22VHI	EM24VHI
3.0 k	0.00	7.84	2.63	2.70	2.78
3.5 k	0.00	3.92	0.00	0.00	0.00
4.0 k	DEFAULT				
4.5 k	0.00	-1.96	-2.63	0.00	0.00
5.0 k	0.00	-5.88	-2.63	-2.70	2.78

Table 4.8: Variation of the effective trigger rates as a function of the narrow range of noise cut values. The variation is evaluated as explained in the text with respect to the default ($4.0k$) noise cut. The values are given in percentage.

find only one TOB per each probe electron, this is well satisfied as shown in Figure 4.13.

Moreover the $\Delta\eta$ distributions between the selected probe electron and the corresponding TOB are checked. The distributions are shown in Figure 4.14 and are as follows:

- Top-left plot shows the $\Delta\eta$ distribution in the full η^e spectrum for the different trigger thresholds of interest and a fixed noise equal to $4.0k$.
- Top-right plot displays the same as the latter in one single probe electron pseudorapidity bin ($0.0 \leq |\eta^e| \leq 0.5$).
- Bottom-left plot shows the $\Delta\eta$ distribution for one trigger threshold and the narrow range of noise cuts.
- Bottom-right plot displays the $\Delta\eta$ distribution of five η^e bins with a fixed noise cut equal to $4.0k$.

These sanity checks show that the TOB-probe electron association works in an appropriate manner and there are no anomalies in the angular matching between them.

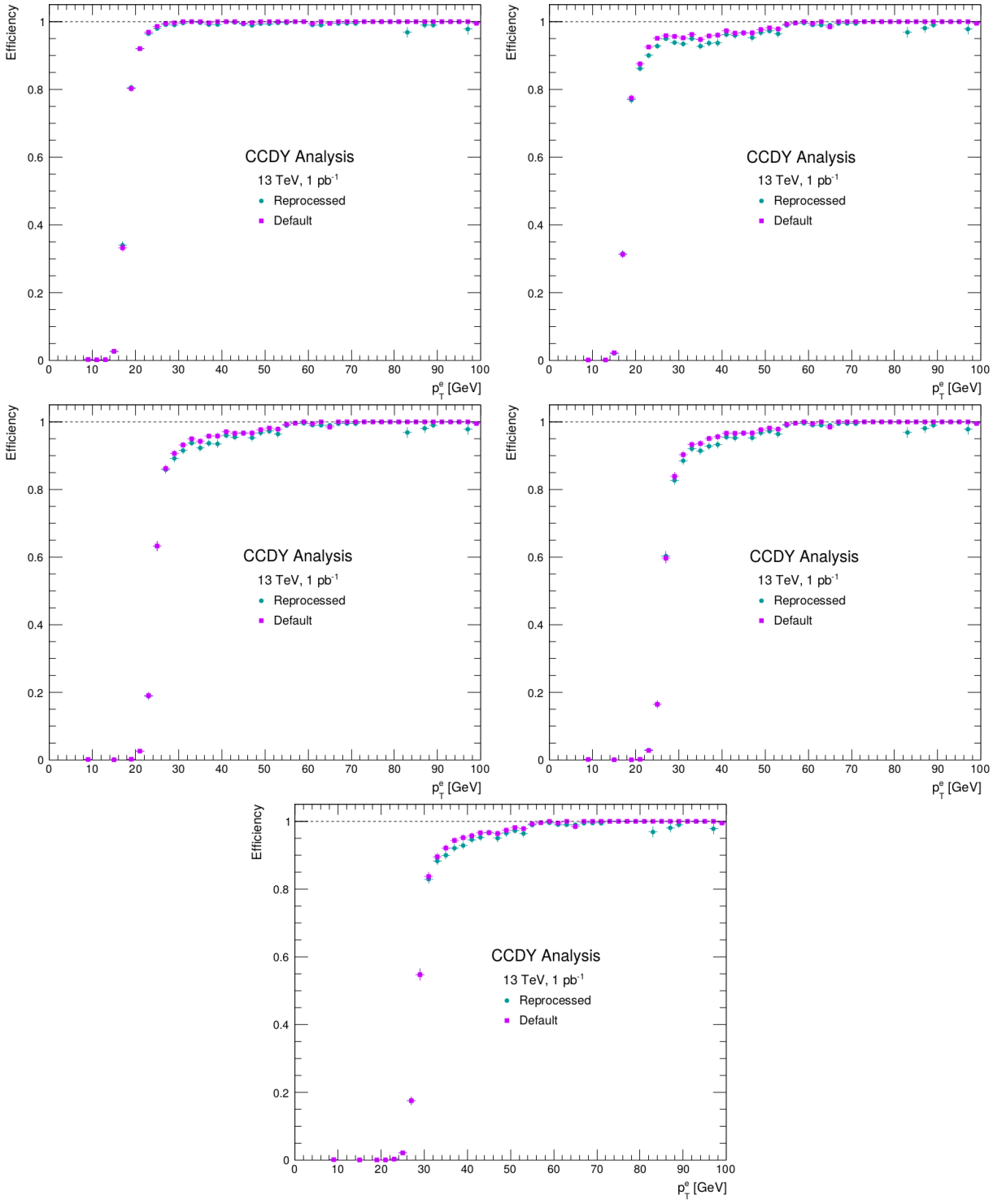

Figure 4.5: Trigger efficiencies for both default and reprocessed TOBs, as a function of the offline reconstructed probe electron p_T^e in the various trigger selections considered. *Top-left* plot corresponds the EM15 trigger threshold; *top-right* plot corresponds the EM15HI trigger threshold; *middle-left* plot corresponds the EM20VHI trigger threshold; *middle-right* plot corresponds the EM22VHI trigger threshold; *bottom* plot corresponds the EM24VHI trigger threshold.

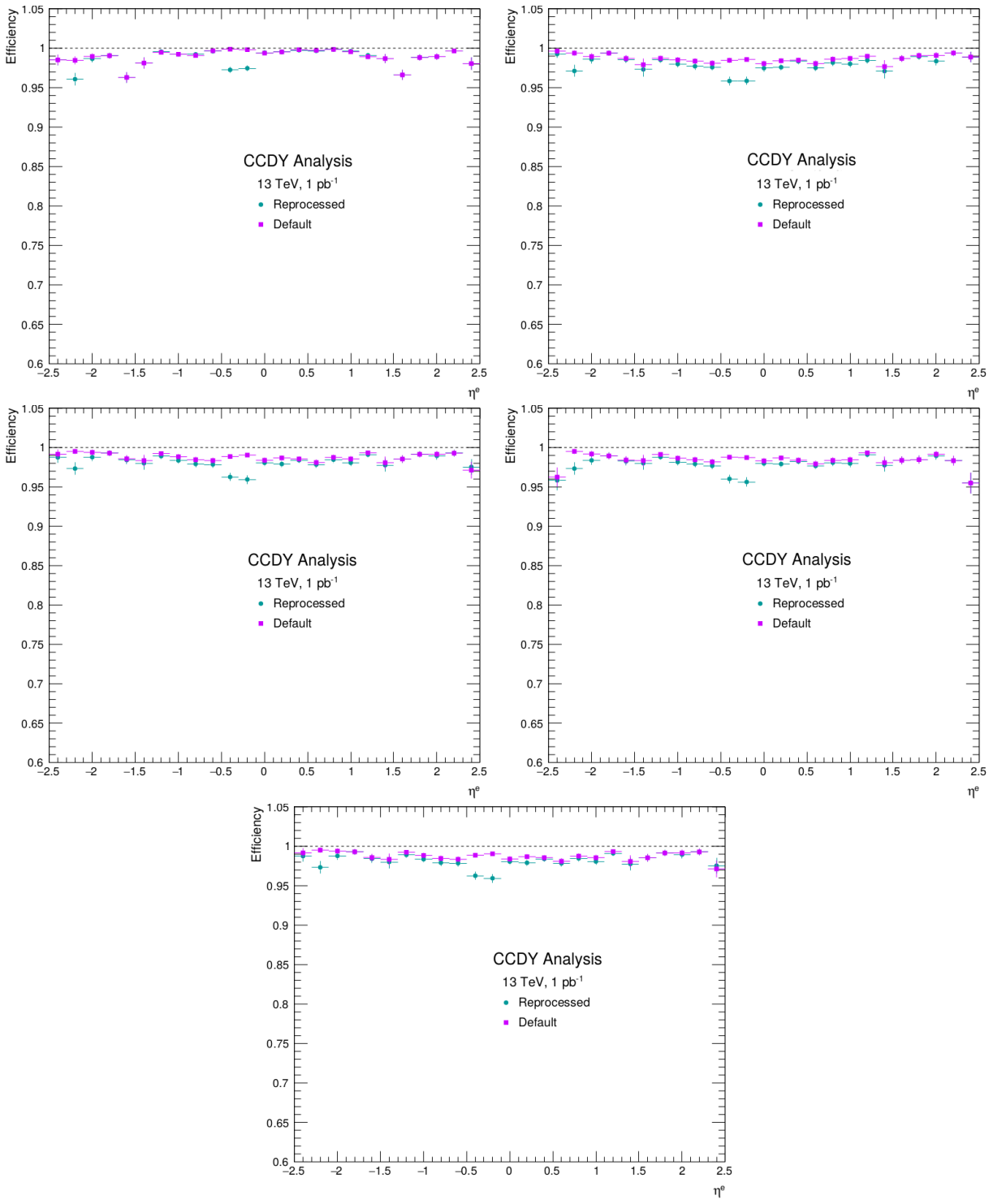

Figure 4.6: Trigger efficiencies for both default and reprocessed TOBs, as a function of the offline reconstructed probe electron η^e in the various trigger selections considered. *Top-left* plot corresponds the EM15 trigger threshold; *top-right* plot corresponds the EM15HI trigger threshold; *middle-left* plot corresponds the EM20VHI trigger threshold; *middle-right* plot corresponds the EM22VHI trigger threshold; *bottom* plot corresponds the EM24VHI trigger threshold.

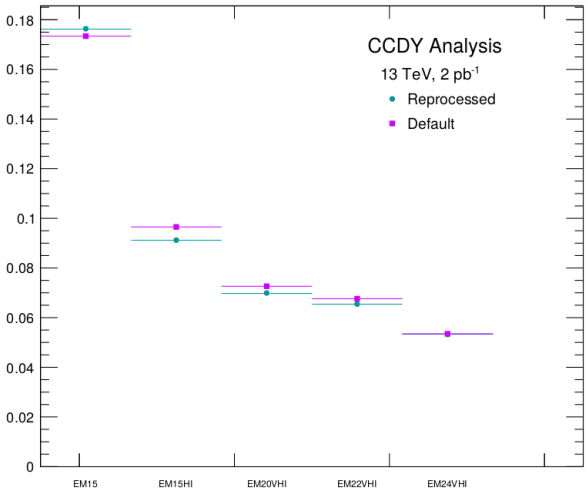

Figure 4.7: Effective trigger rates for default and reprocessed TOBs (values reported in percentage), as a function of the various trigger thresholds considered. The enhanced bias weights are not being applied here.

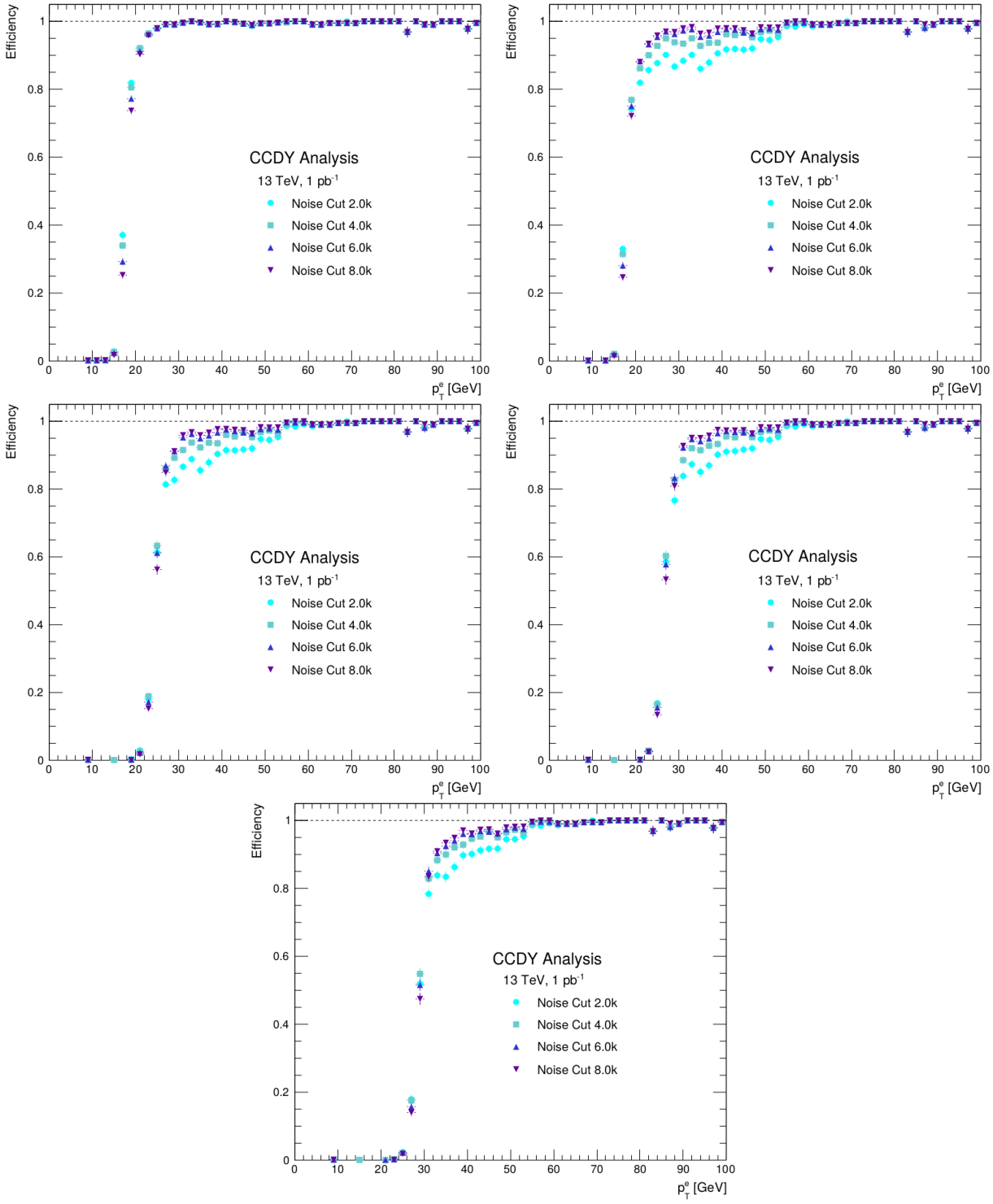

Figure 4.8: Trigger efficiency for reprocessed TOBs as a function of the offline reconstructed probe electron p_T^e in the wide range of noise cuts. *Top-left* plot corresponds the EM15 trigger threshold; *top-right* plot corresponds the EM15HI trigger threshold; *middle-left* plot corresponds the EM20VHI trigger threshold; *middle-right* plot corresponds the EM22VHI trigger threshold; *bottom* plot corresponds the EM24VHI trigger threshold.

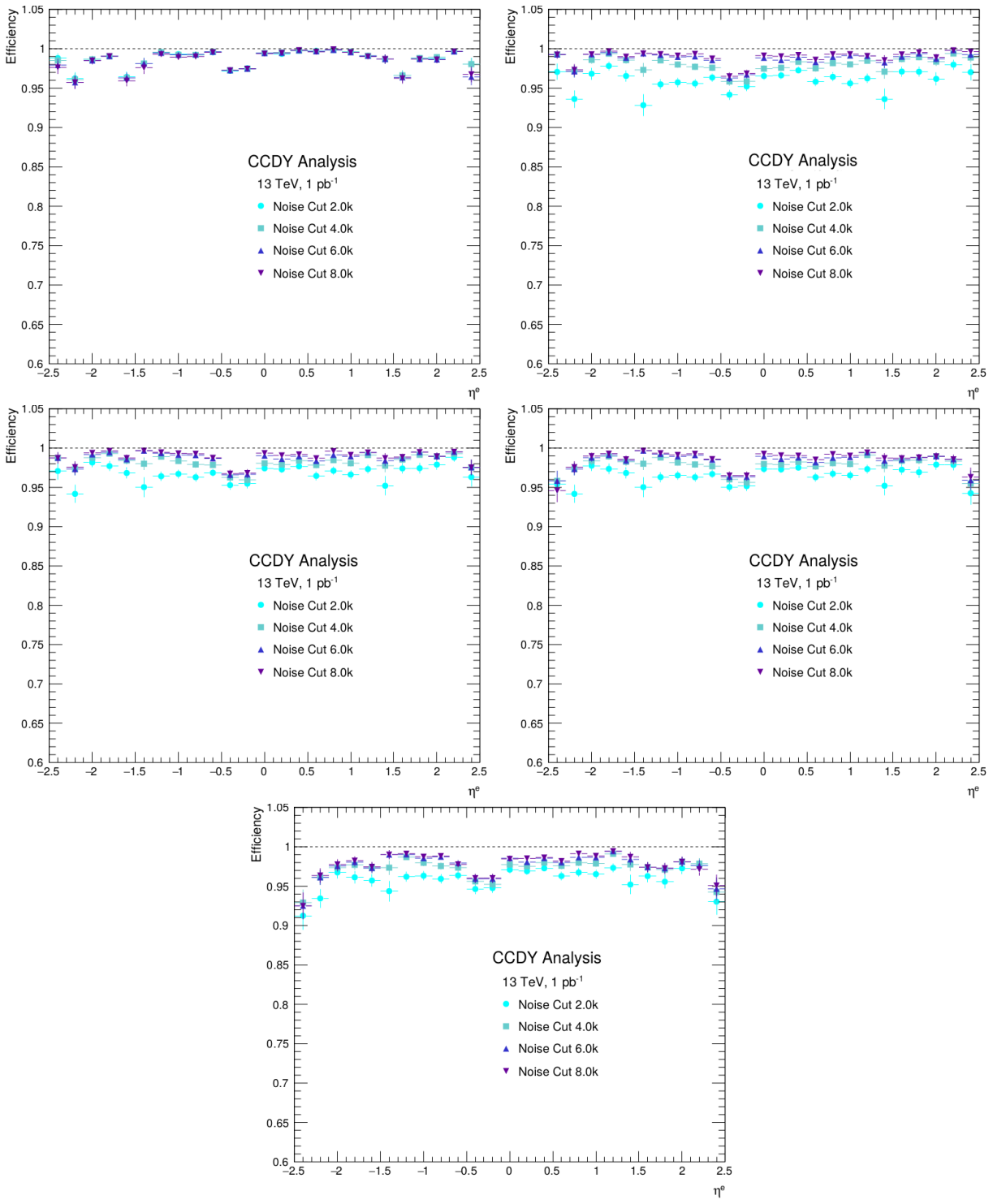

Figure 4.9: Trigger efficiency for reprocessed TOBs as a function of the offline reconstructed probe electron η^e in the wide range of noise cuts. *Top-left* plot corresponds the EM15 trigger threshold; *top-right* plot corresponds the EM15HI trigger threshold; *middle-left* plot corresponds the EM20VHI trigger threshold; *middle-right* plot corresponds the EM22VHI trigger threshold; *bottom* plot corresponds the EM24VHI trigger threshold.

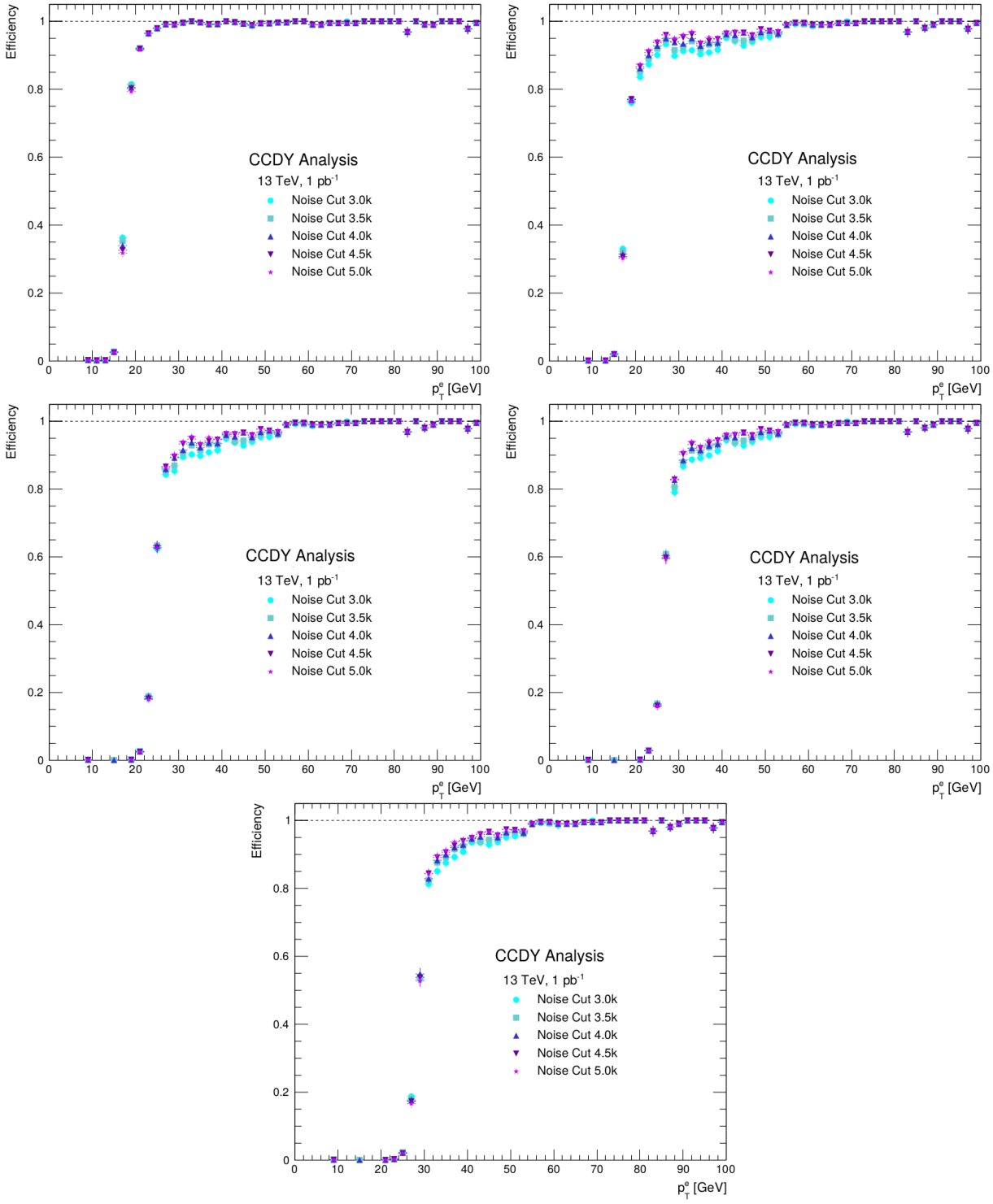

Figure 4.10: Trigger efficiency for reprocessed TOBs as a function of the offline reconstructed probe electron p_T^e in the narrow range of noise cuts. *Top-left* plot corresponds the EM15 trigger threshold; *top-right* plot corresponds the EM15HI trigger threshold; *middle-left* plot corresponds the EM20VHI trigger threshold; *middle-right* plot corresponds the EM22VHI trigger threshold; *bottom* plot corresponds the EM24VHI trigger threshold.

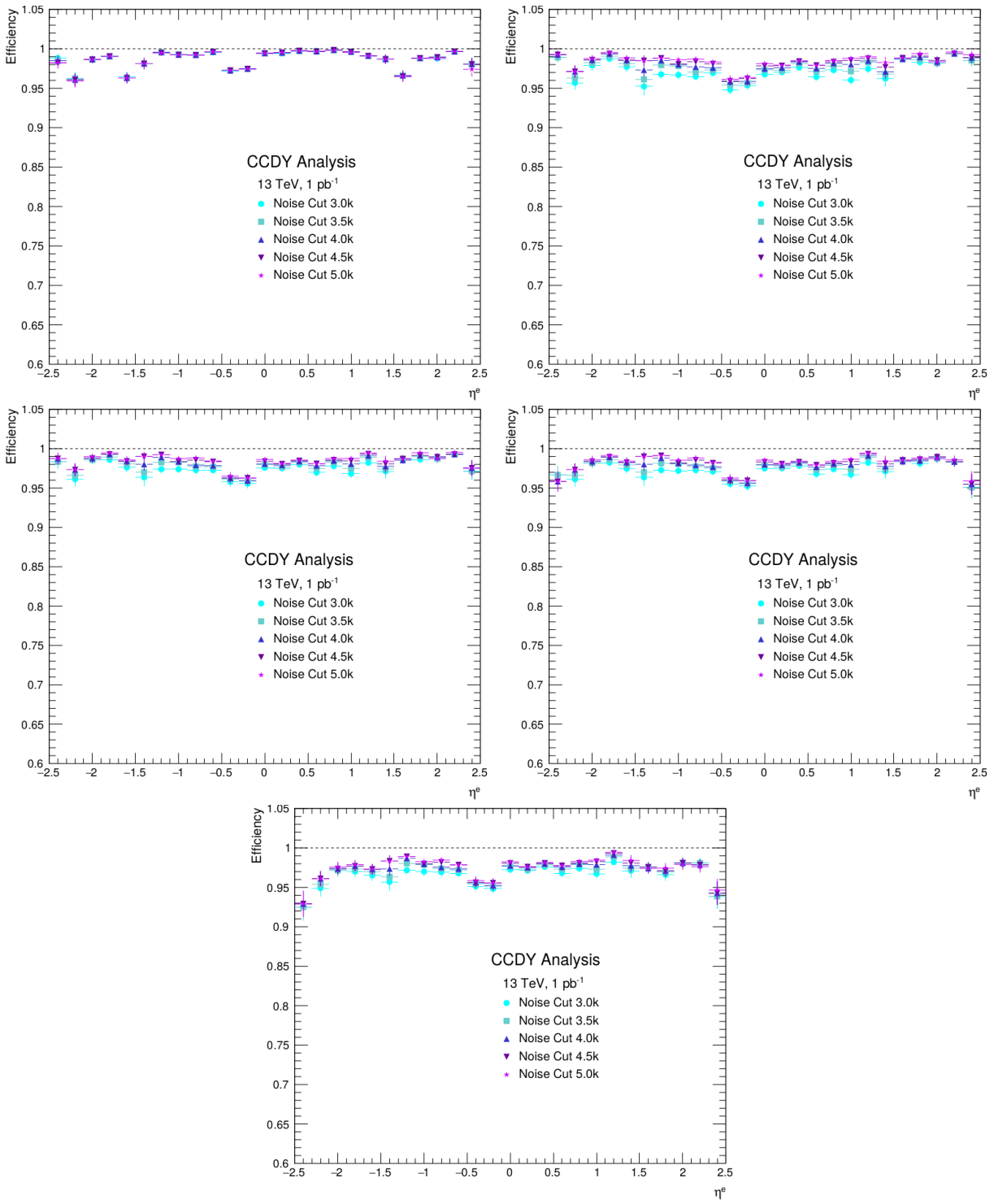

Figure 4.11: Trigger efficiency for reprocessed TOBs as a function of the offline reconstructed probe electron η^e in the narrow range of noise cuts. *Top-left* plot corresponds the EM15 trigger threshold; *top-right* plot corresponds the EM15HI trigger threshold; *middle-left* plot corresponds the EM20VHI trigger threshold; *middle-right* plot corresponds the EM22VHI trigger threshold; *bottom* plot corresponds the EM24VHI trigger threshold.

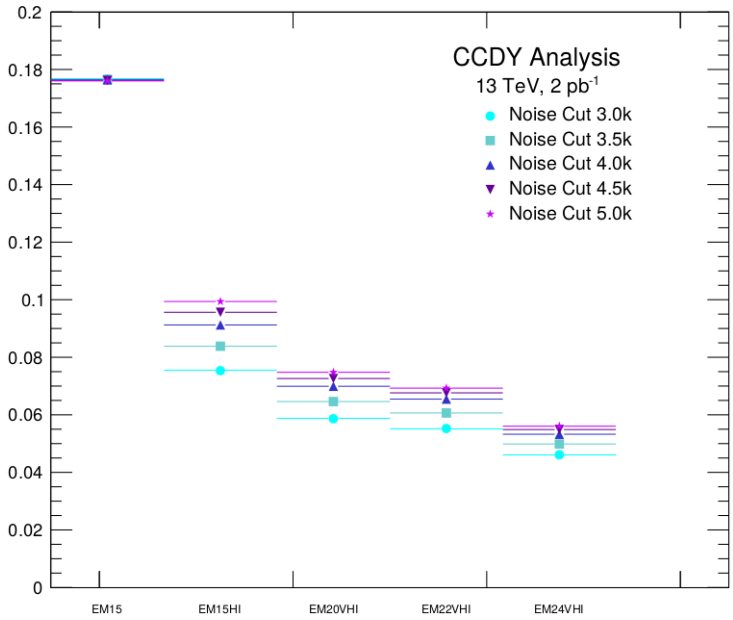

Figure 4.12: Effective trigger rates (values in percentage) as a function of the analysed trigger thresholds in the narrow range of noise cut values.

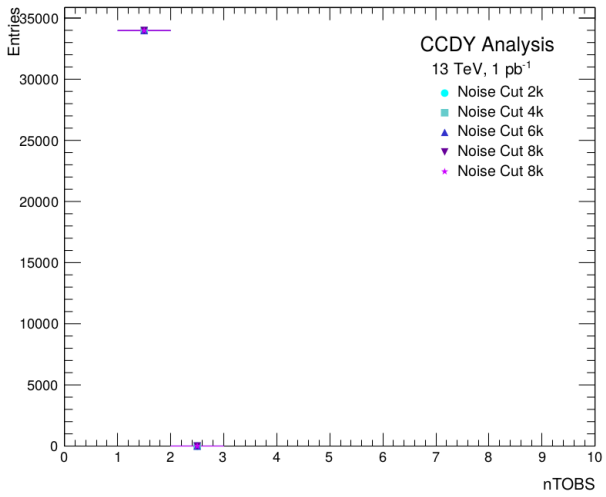

Figure 4.13: Number of TOBs per probe electron for several noise cuts. Only in 2 cases out of 33982 the probe electron is associated to two TOBs.

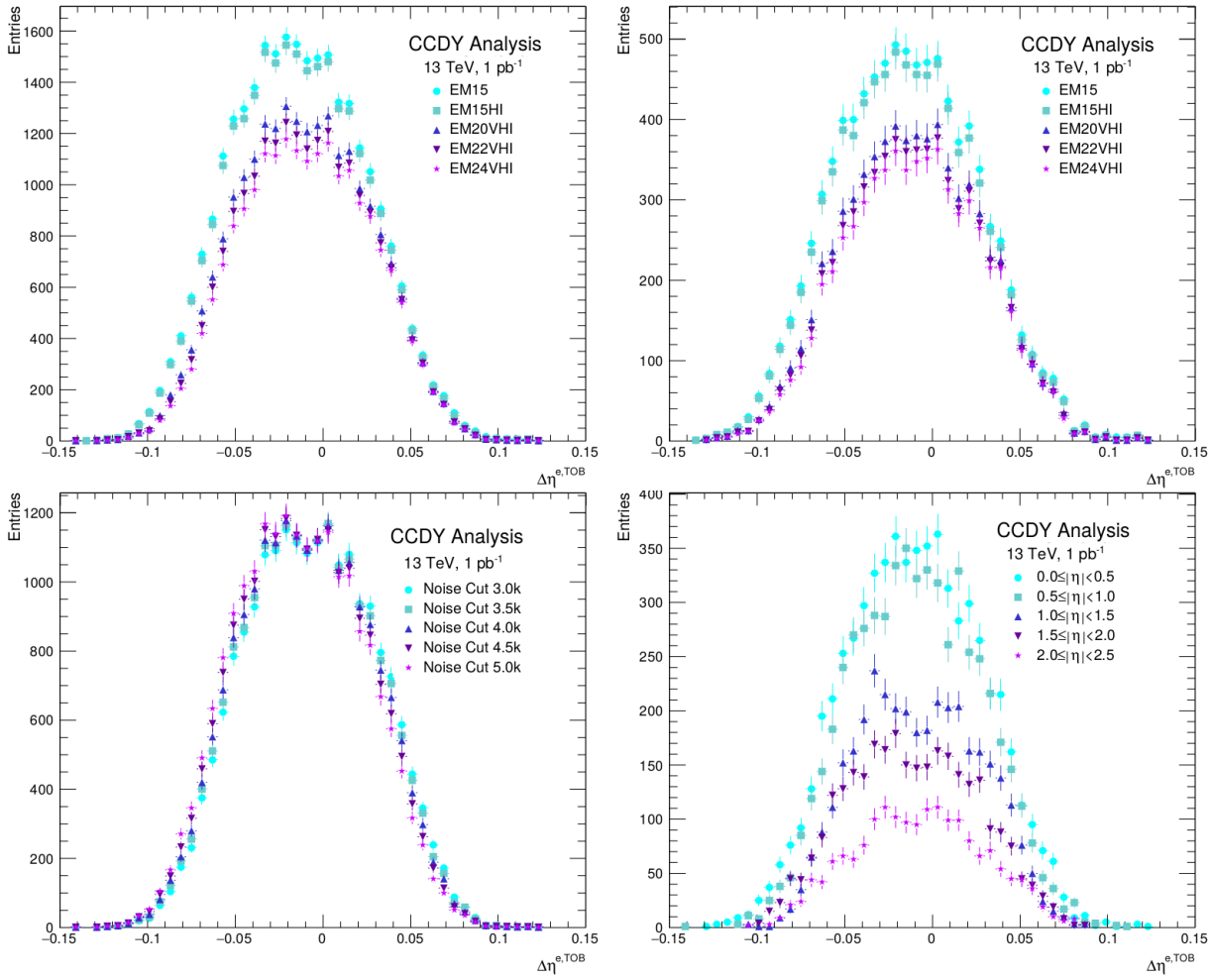

Figure 4.14: Angular matching ($\Delta\eta$) between the offline reconstructed probe electron and the corresponding TOB. *Top-left*: varying threshold, fixed noise cut and full η^e range. *Top-right:* Varying threshold, fixed noise cut and $0.0 \leq |\eta^e| \leq 0.5$. *Bottom-left:* full range of η^e and different noise cuts applied. *Bottom-right:* fixed noise cut at $4.0k$ and different η^e steps.

Chapter 5

Data and Monte Carlo samples

This chapter comprises the information regarding the data collected by the ATLAS detector and the Monte Carlo simulation samples used for the $W \to \mu\nu$ analysis.

5.1 Data

The data set used in this analysis is constituted by the collection made with the ATLAS detector during the year 2017; in this period the LHC circulated proton beams with an energy of 6.5 TeV and bunch spacing of 25 ns, the data correspond to head-on proton-proton collisions. For the present analysis only data taken during stable beam conditions and when the ATLAS detector was fully operational are considered. The latter is established within the good run lists, provided by the ATLAS data quality group[1], which in overall sums a total integrated luminosity of 44.3 fb^{-1}. The years, when the data were collected, are divided by periods to maintain stable beam conditions, good detector performance and sufficient amount of data collected; a break down of the year is shown in Table 5.1.

Due to the fact that detector and beam conditions changed throughout data taking years, *e.g.* the average pp interactions, the need of using different triggers arose with the intent to optimise the data taking. For muons, the change of triggers between years is not significant; conversely, for electrons various triggers changed (in this document electrons play a minor role, for more detailed treatment see reference [39], for example). Table 5.2 displays the muon triggers designated for 2015, 2016 and 2017; in the case of having more than one trigger, the event is recorded if any of the triggers is triggered.

The data were handled using the ATLAS reconstruction software *Athena*[2] release 21.2[41].

[1] https://twiki.cern.ch/twiki/bin/viewauth/AtlasProtected/GoodRunListsForAnalysisRun2.

[2] Athena is the ATLAS software framework that allows event generation, simulation, reconstruction and derivation production, granting the users the ability to plug in physics analysis tools. Athena is also used

Year	Period	L_{int} [pb^{-1}]	N_{Events}	L_{inst} [$\times 10^{30}$cm$^{-2}s^{-1}$]	$< \mu >$
2017	B	6242	216881771	15815	51.2
	C	2850	88220360	16776	46.9
	D	6423	183918918	17466	48.8
	E	5262	183733897	14059	45.6
	F	3448	122272383	12070	45.0
	H	2434	89772813	14165	52.8
	I	7900	292115799	18456	70.4
	K	15715	565850803	20614	78.6
Total	NA	50274	1742766744	NA	NA

Table 5.1: 13 TeV pp collision periods used in this measurement. The periods are further divided in luminosity blocks grouped in runs labelled by a unique label called run number (not shown here) and the GRL file indicates which luminosity blocks are good for physics analysis [40]. The first column indicates the data taking year; the second column displays the periods in which the data year is divided; the third and fourth columns are the luminosity and number of events, respectively, delivered by the LHC in each period; the fifth and sixth columns are the instantaneous luminosity and the average pp interactions, respectively, in each period. The total integrated luminosity is found at the bottom of the table. All the numbers in this table correspond to quantities obtained before the GRL selection is made.

Year	Runs	Trigger	L_{int} [fb^{-1}]
2015	266904-284484	mu_20iloose or mu_50	3.2
2016	296939-310216	mu_26ivarmedium or mu_50	36.1
2017	324839-341649	mu_26ivarmedium or mu_50	46.9

Table 5.2: Triggers used for the charged current Drell-Yan measurement. The data taking years are shown in the first column. The second column displays the run numbers that correspond to each year. The third column states the trigger chain used by the high-level trigger algorithms to record the event, the explanation of the trigger names is detailed in Section 7.1.5. The total luminosity collected with the corresponding trigger chain is displayed in the last column; the luminosity is integrated over a given period of time, hence the total luminosity is expressed in inverse cross section units, see Equation (10.1).

It was found convenient to adopt the centrally produced STDM4 derivations [42] in this analysis given the signature of the $W \to \mu\nu$ process and the chosen phase space, see Chapter 7. The STDM4 filter cuts are simple: the event must have one or more leptons; muons and electrons are required to have a transverse momentum greater than 15 GeV and 20 GeV, respectively; furthermore, a $|\eta| < 2.6$ cut is imposed on them; finally, they are required to pass single lepton triggers, explained in detail in Section 7.1.5, see Table 5.2.

during the data taking in the ATLAS High Level Trigger [41].

5.2 Monte Carlo simulations

To be able to compare what it is observed in the experiment with the theory predictions, it is necessary to have simulations that combine both the physics processes that appear in proton-proton collisions and the manner in which the ATLAS detector responds to the particles, result of the pp collisions, passing through its different components. To achieve this task, dedicated Monte Carlo simulations exist. The first step is to carefully simulate each component of the ATLAS detector. The second step is to produce samples that describe the physics involved; this corresponds to the $W \to \mu\nu$ process referred to as *signal*, the background processes that potentially could pass the signal selection cuts imposed and contaminate the signal[3], the effect of the multiple pp collisions that occur at the same time as the signal process, which are not of physics interest (pileup), and finally the secondary interactions between the remaining partons not participating in the main hard interaction: the so-called underlying event. When these steps are combined, a description of $W \to \mu\nu$ events inside the ATLAS detector is available.

5.2.1 Monte Carlo event generators

Monte Carlo simulations are needed as a consequence of the complexity of the ATLAS detector and the physics processes themselves, *i.e.* it is not feasible to couple every single response of each ATLAS detector component with all the physics processes involved in pp collisions utilising direct fundamental theory calculations. A Monte Carlo simulation resolves the latter by means of *event-level* simulations, which are based on random number generation and assumes that the system is described by probability density functions (coming from data, theory predictions or fitted data to theory predictions), to yield the event rate behaviour differentially in several kinematic variables. This step is repeated to build a Monte Carlo sample statistically significant.

Event generator sub-processes

The pp collisions event generation in ATLAS consists of several sub-processes[4]:

- Perturbative calculation at fixed order of the hard process matrix element using a defined PDF set.

[3]The background contamination emerges since the ATLAS detector records all physics processes and it is possible that some of them mimic the $W \to \mu\nu$ signal.

[4]It is assumed a negligible interference between the sub-processes in a event and therefore it can be factorised.

- Non-perturbative low energy (∼1 GeV) calculations of the parton showers associated with the incoming and outgoing coloured participants in the subprocess.
- Computation of the underlying event using perturbative and non-perturbative techniques; this results in parton showers, in which case the parton showers are hard processes of energy larger than 10 GeV.
- Pileup is calculated non-pertubatively.
- Hadronisation is performed for the remaining partons in the collisions into colourless hadrons[5].
- Calculation of the decays of the colourless hadrons into detectable particles.
- Electromagnetic final state radiation or initial state quarks is added to the final state charged leptons.
- Radiation can be simulated either as part of the matrix element or as part of a parton shower based on resummation calculations. Care must be taken to not double count radiation from both approaches; every MC generator performs this in a different manner.

Event generators

For this analysis, the generators used are:

- Powheg. Next-to-leading-order calculations for the highest p_T objects are done with exact NLO matrix elements, when Powheg is interfaced with shower algorithms that use p_T ordering for the summation of next-to-leading-logarithmic (NLL) corrections, the desired accuracy is achieved [43–45].
- Pythia. This program has the capability to generate all classes of processes in high-energy collisions typically at leading-order matrix element: hard processes, parton showers, parton interactions, beam remnants, string fragmentation and particle decays [46]. For this analysis, Pythia is used to simulate parton showering.
- Photos. QED radiative and Bremsstrahlung corrections to decays of particles or resonances can be calculated using Photos [47].

[5]Hadronisation is the process behind the production of observable final state hadrons, result from a hard collision of quarks or gluons; the hadronisation is a consequence of colour confinement, *i.e.*, quarks and gluons are not found in free states, thus energy from the vacuum is taken to create the corresponding antiparticles to form hadronic bound states.

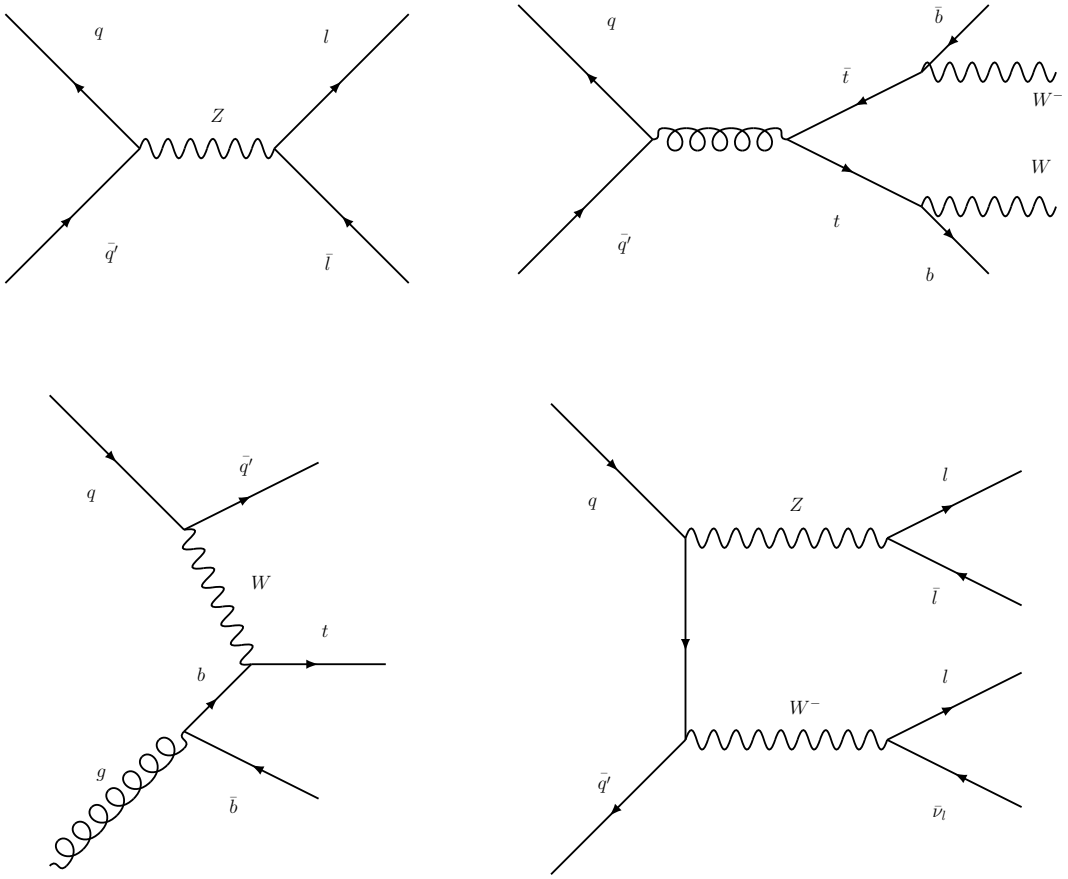

Figure 5.1: Feynman graphs for the background processes. *Top-left* corresponds to the neutral current Drell-Yan production and includes muon and tau decay channels. *Top-right* shows the $t\bar{t}$ production chain that contains W production decaying to muon and taus. *Bottom-left* is for the single top process chain that contains W production decaying to muon and taus. *Bottom-right* diboson production that includes muon and tau decay channels. The symbols q, g, l, ν correspond respectively to quarks, gluons, leptons and neutrinos of any flavour and colour (where applicable); b stands for any colour b-quark.

5.2.2 Monte Carlo samples for the $W \to \mu\nu$ analysis

The charged current Drell-Yan process $W \to \mu\nu$ is simulated using the Powheg program which employs the CT10 [48] parton distribution functions set interfaced with Pythia 8.2 to include hadronisation effects, parton shower and underlying event with the AZNLO CTEQL1 tune [49]. Photos[47] is utilised to simulate the radiation of photons after the collision, called final state radiation (FSR). The backgrounds considered are also simulated employing Powheg and Pythia, these background processes are: $W \to \tau\nu$ where the tau decays into a muon, $Z \to \mu\mu$ where one of the muons is not properly reconstructed or identified, $Z \to \tau\tau$ where the tau decays into a muon and the second lepton is not reconstructed or identified, or

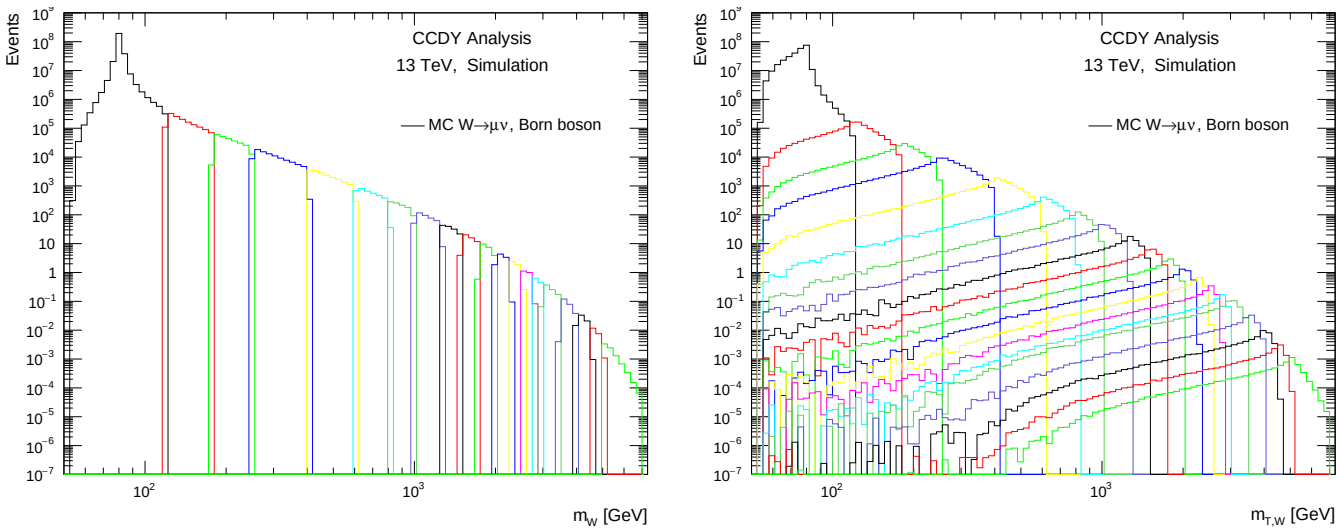

Figure 5.2: Generator level spectra. These plots display the contribution to the full distributions of each mass slice, here defined by a different colour. *Left-hand* side corresponds to the invariant mass distribution, whereas *right-hand* side corresponds to the transverse mass. No cuts, other than the STDM4 derivation ones, are applied. Generator level weights are considered in these plots, see Chapter 5.

the second tau decays hadronically, $t\bar{t}$ and single top quark where the decay chain[6] involves a W boson decaying to a neutrino and muon, and a b quark that could fake a muon, and diboson production (WW, ZZ, WZ) that could have similar signature to a single W boson. Figure 5.1 displays the Feynman graphs of some of these processes. As for data, the handling of the simulated physics was done using Athena release 21.2 and STDM4 derivations were used.

The detector and beam conditions changed significantly between the years 2015/2016 and 2017, accordingly, two different Monte Carlo production "campaigns" were carried out to simulate these different conditions separately: the *campaign a* simulations are used to compare the simulation with data taken during 2015 and 2016; the *campaign d* simulations are used to compare the simulation with data taken during 2017. Both campaigns are independent of each other. The *campaign a* and data 2015+2016 were used for early comparisons with 2015/2016 data, and are not further used in this analysis. The physics simulations are combined with the ATLAS detector simulation based on the GEANT4 program [50] in order to directly compare the data with the prediction.

[6]The top quark mass is the largest of the SM particles, therefore it is extremely short lived to be detected; the top quark decays via the weak interaction producing a W boson and a quark; subsequently the quark goes through hadronisation and the W boson decays leptonically or hadronically, the latter are the final states observed in the detector.

To obtain better statistical precision and modelling in the tails of the invariant mass and transverse mass spectra (for the definition of transverse mass, see Section 7.1.10), high boson invariant mass slices were considered for the W and Z bosons, resulting in smooth invariant mass and transverse mass distributions at high off-shell invariant mass ($m_{W/Z} >$ 1 TeV). The normalisation applied to each slice (and the inclusive samples) considers the cross section found in AMI [51] and includes the so-called K factor, k_{Factor}, (the definition of the k_{Factor} is given in Equation (5.1)) which corrects the cross section to the next-to-next-to-leading-order for QCD effects and next-to-leading-order for electroweak effects; the above mentioned k_{Factor} is a function of the boson invariant mass for the single W and Z boson production; on the other hand the k_{Factor} is applied as a fixed value to the diboson and top processes. Figure 5.2 shows the invariant mass and transverse at generator level, *i.e.* without considering detector effects, before selection cuts are applied. Tables 5.3-5.7 list the samples used and present the relevant information to correctly normalise the Monte Carlo simulations to data, see Chapter 10.

5.3 High order perturbation theory corrections

The Monte Carlo generators produce physics simulations only at second order of perturbation theory (NLO), see Chapter 6. To accurately model what it is found in the experiment, corrections at higher order are introduced: for processes related with the quark and gluons interactions (QCD), characterised by g_s, corrections are obtained at next-to-next-to-leading-order; whereas, for electroweak processes between leptons and quarks, characterised by α_{EW}, the corrections are calculated at NLO. These corrections are included in the distributions and cross sections by defining an event weight as,

$$k_{Factor}(m) = k_{QCD} \times k_{EW}, \tag{5.1}$$

where k_{QCD}, contains the QCD correction and is defined as the ratio between the NNLO to NLO or LO cross section; k_{EWK} contains the electroweak corrections, *i.e.* leading-order electroweak corrections matched with next-to-leading-order corrections. The k_{Factor} varies as function of the invariant mass for W and Z bosons and for the remaining backgrounds it is a constant. An average of the k_{Factor} weights is presented in Figure 5.3. It is interesting to observe the behaviour of k_{Factor} as function of the transverse mass, given that is expected to be a variation in function of the event transverse mass m, since in principle the boson invariant mass is closely related with m_T, see Section 7.1.10, the variation follows the same response with respect to the invariant mass up to 1 GeV; at higher masses the response

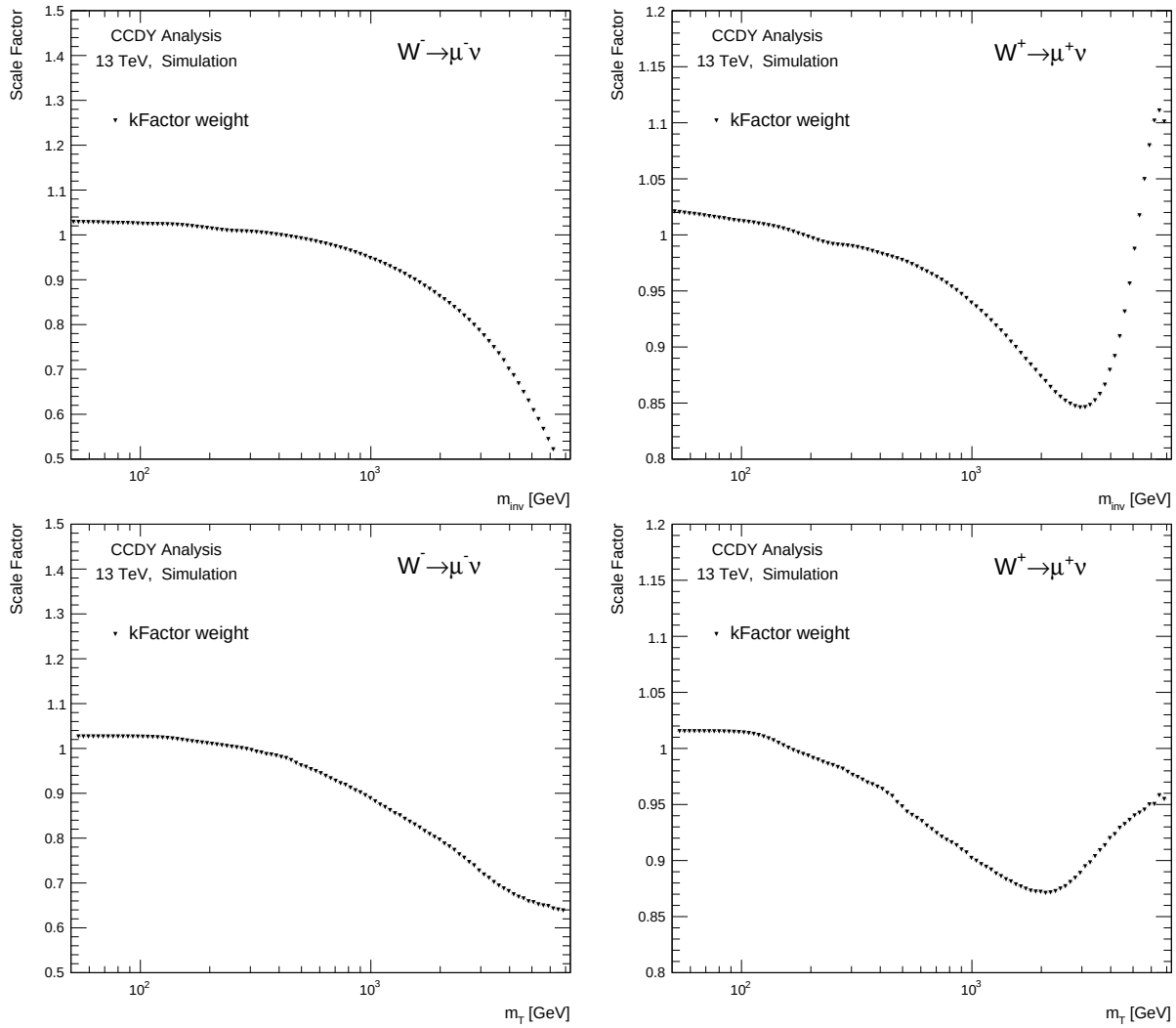

Figure 5.3: Average high order perturbation theory correction weights, for $W^- \to \mu^-\nu$ (left) and $W^+ \to \mu^+\nu$(right), as a function of W boson invariant mass m_{inv} (top) and transverse mass (bottom).

deviates of what is compatible with the invariant mass dependence; lastly, the predicted [52] difference between the positive and negative channels is manifest in the plots of Figure 5.3.

MC ID	Process	$N_{evt}[k]$	Generator σB [pb]	k_{Factor}	L_{int} [fb^{-1}]
361101	$W^+ \to \mu\nu$	31978(a)/39952(d)	211 306.90	$k_{Factor}(m)$	2.80(a)/3.50(d)
301100	W^+(120,180)$\to \mu\nu$	500(a)/500(d)	132.06	$k_{Factor}(m)$	$1.50 \cdot 10^1$(a)/$1.50 \cdot 10^1$(d)
301101	W^+(180,250)$\to \mu\nu$	250(a)/250(d)	55.00	$k_{Factor}(m)$	$5.00 \cdot 10^1$(a)/$5.00 \cdot 10^1$(d)
301102	W^+(250,400)$\to \mu\nu$	150(a)/150(d)	81.75	$k_{Factor}(m)$	$8.50 \cdot 10^1$(a)/$8.50 \cdot 10^1$(d)
301103	W^+(400,600)$\to \mu\nu$	100(a)/100(d)	30.31	$k_{Factor}(m)$	$3.20 \cdot 10^2$(a)/$3.20 \cdot 10^2$(d)
301104	W^+(600,800)$\to \mu\nu$	50(a)/50(d)	80.06	$k_{Factor}(m)$	$8.20 \cdot 10^2$(a)/$8.20 \cdot 10^2$(d)
301105	W^+(800,1000)$\to \mu\nu$	50(a)/50(d)	20.02	$k_{Factor}(m)$	$2.80 \cdot 10^3$(a)/$2.80 \cdot 10^3$(d)
301106	W^+(1000,1250)$\to \mu\nu$	50(a)/50(d)	60.01	$k_{Factor}(m)$	$6.80 \cdot 10^3$(a)/$6.80 \cdot 10^3$(d)
301107	W^+(1250,1500)$\to \mu\nu$	50(a)/50(d)	10.00	$k_{Factor}(m)$	$1.90 \cdot 10^4$(a)/$1.90 \cdot 10^4$(d)
301108	W^+(1500,1750)$\to \mu\nu$	50(a)/50(d)	50.00	$k_{Factor}(m)$	$5.00 \cdot 10^4$(a)/$5.00 \cdot 10^4$(d)
301109	W^+(1750,2000)$\to \mu\nu$	50(a)/50(d)	10.00	$k_{Factor}(m)$	$1.10 \cdot 10^5$(a)/$1.10 \cdot 10^5$(d)
301110	W^+(2000,2250)$\to \mu\nu$	50(a)/50(d)	20.00	$k_{Factor}(m)$	$2.50 \cdot 10^5$(a)/$2.50 \cdot 10^5$(d)
301111	W^+(2250,2500)$\to \mu\nu$	50(a)/50(d)	$59.30 \cdot 10^{-5}$	$k_{Factor}(m)$	$5.30 \cdot 10^5$(a)/$5.30 \cdot 10^5$(d)
301112	W^+(2500,2750)$\to \mu\nu$	50(a)/50(d)	$14.60 \cdot 10^{-5}$	$k_{Factor}(m)$	$1.00 \cdot 10^6$(a)/$1.00 \cdot 10^6$(d)
301113	W^+(2750,3000)$\to \mu\nu$	50(a)/50(d)	$22.30 \cdot 10^{-5}$	$k_{Factor}(m)$	$2.10 \cdot 10^6$(a)/$2.10 \cdot 10^6$(d)
301114	W^+(3000,3500)$\to \mu\nu$	50(a)/50(d)	$21.80 \cdot 10^{-5}$	$k_{Factor}(m)$	$2.70 \cdot 10^6$(a)/$2.70 \cdot 10^6$(d)
301115	W^+(3500,4000)$\to \mu\nu$	50(a)/50(d)	$95.10 \cdot 10^{-6}$	$k_{Factor}(m)$	$9.80 \cdot 10^6$(a)/$9.80 \cdot 10^6$(d)
301116	W^+(4000,4500)$\to \mu\nu$	50(a)/50(d)	$31.43 \cdot 10^{-6}$	$k_{Factor}(m)$	$3.50 \cdot 10^7$(a)/$3.50 \cdot 10^7$(d)
301117	W^+(4500,5000)$\to \mu\nu$	50(a)/50(d)	$14.01 \cdot 10^{-7}$	$k_{Factor}(m)$	$1.20 \cdot 10^8$(a)/$1.20 \cdot 10^8$(d)
301118	W^+(>5000)$\to \mu\nu$	50(a)/50(d)	$31.53 \cdot 10^{-7}$	$k_{Factor}(m)$	$3.20 \cdot 10^8$(a)/$3.20 \cdot 10^8$(d)
361104	$W^- \to \mu\nu$	31973(a)/31978(d)	28 282.90	$k_{Factor}(m)$	3.80(a)/3.80(d)
301120	W^-(120,180)$\to \mu\nu$	500(a)/500(d)	122.19	$k_{Factor}(m)$	$2.20 \cdot 10^1$(a)/$2.20 \cdot 10^1$(d)
301121	W^-(180,250)$\to \mu\nu$	250(a)/250(d)	53.28	$k_{Factor}(m)$	$7.60 \cdot 10^1$(a)/$7.60 \cdot 10^1$(d)
301122	W^-(250,400)$\to \mu\nu$	150(a)/150(d)	81.08	$k_{Factor}(m)$	$1.30 \cdot 10^2$(a)/$1.30 \cdot 10^2$(d)
301123	W^-(400,600)$\to \mu\nu$	100(a)/100(d)	30.18	$k_{Factor}(m)$	$5.70 \cdot 10^2$(a)/$5.70 \cdot 10^2$(d)
301124	W^-(600,800)$\to \mu\nu$	50(a)/50(d)	0.8 030 979	$k_{Factor}(m)$	$1.60 \cdot 10^3$(a)/$1.60 \cdot 10^3$(d)
301125	W^-(800,1000)$\to \mu\nu$	50(a)/50(d)	0.2 008 286	$k_{Factor}(m)$	$6.00 \cdot 10^3$(a)/$6.00 \cdot 10^3$(d)
301126	W^-(1000,1250)$\to \mu\nu$	50(a)/50(d)	0.6 003 159	$k_{Factor}(m)$	$1.50 \cdot 10^4$(a)/$1.50 \cdot 10^4$(d)
301127	W^-(1250,1500)$\to \mu\nu$	50(a)/50(d)	0.1 001 003	$k_{Factor}(m)$	$4.90 \cdot 10^4$(a)/$4.90 \cdot 10^4$(d)
301128	W^-(1500,1750)$\to \mu\nu$	50(a)/50(d)	0.5 000 368	$k_{Factor}(m)$	$1.30 \cdot 10^5$(a)/$1.30 \cdot 10^5$(d)
301129	W^-(1750,2000)$\to \mu\nu$	50(a)/50(d)	0.1 000 149	$k_{Factor}(m)$	$3.30 \cdot 10^5$(a)/$3.30 \cdot 10^5$(d)
301130	W^-(2000,2250)$\to \mu\nu$	50(a)/50(d)	$6.25 \cdot 10^{-5}$	$k_{Factor}(m)$	$7.60 \cdot 10^5$(a)/$7.60 \cdot 10^5$(d)
301131	W^-(2250,2500)$\to \mu\nu$	50(a)/50(d)	$3.50 \cdot 10^{-5}$	$k_{Factor}(m)$	$1.60 \cdot 10^6$(a)/$1.60 \cdot 10^6$(d)
301132	W^-(2500,2750)$\to \mu\nu$	50(a)/50(d)	$1.14\,549 \cdot 10^{-5}$	$k_{Factor}(m)$	$3.40 \cdot 10^6$(a)/$3.40 \cdot 10^6$(d)
301133	W^-(2750,3000)$\to \mu\nu$	50(a)/50(d)	$7.20 \cdot 10^{-6}$	$k_{Factor}(m)$	$7.10 \cdot 10^6$(a)/$7.10 \cdot 10^6$(d)
301134	W^-(3000,3500)$\to \mu\nu$	50(a)/50(d)	$6.20 \cdot 10^{-6}$	$k_{Factor}(m)$	$8.30 \cdot 10^6$(a)/$8.30 \cdot 10^6$(d)
301135	W^-(3500,4000)$\to \mu\nu$	50(a)/50(d)	$1.95\,975 \cdot 10^{-6}$	$k_{Factor}(m)$	$3.10 \cdot 10^7$(a)/$3.10 \cdot 10^7$(d)
301136	W^-(4000,4500)$\to \mu\nu$	50(a)/50(d)	$4.3721 \cdot 10^{-7}$	$k_{Factor}(m)$	$1.00 \cdot 10^8$(a)/$1.00 \cdot 10^8$(d)
301137	W^-(4500,5000)$\to \mu\nu$	50(a)/50(d)	$1.14\,279 \cdot 10^{-7}$	$k_{Factor}(m)$	$3.50 \cdot 10^8$(a)/$3.50 \cdot 10^8$(d)
301138	W^-(>5000)$\to \mu\nu$	50(a)/50(d)	$6.31\,624 \cdot 10^{-8}$	$k_{Factor}(m)$	$8.10 \cdot 10^8$(a)/$8.10 \cdot 10^8$(d)

Table 5.3: $W \to \mu\nu$ boson signal Monte Carlo samples. For each sample, this table lists the ATLAS Monte Carlo run number, the physics process (the numbers inside the parentheses (x, y) delimitate the boson invariant mass interval), the number of generated events, the cross section times branching ratio, k_{Factor} ($k_{Factor}(m)$ indicates a dependence on boson invariant mass), and the equivalent integrated luminosity. The letters inside the parentheses (a,d) denote which Monte Carlo campaign the value next to it corresponds to.

MC ID	Process	$N_{evt}[k]$	Generator σB [pb]	k_{Factor}	L_{int} [fb^{-1}]
361102	$W^+ \to \tau\nu$	2038(a)/2286(d)	211 306.90	$k_{Factor}(m)$	$1.80 \cdot 10^{-1}$(a)/$2.00 \cdot 10^{-1}$(d)
301140	W^+(120,180)$\to \tau\nu$	74(a)/76(d)	132.06	$k_{Factor}(m)$	2.30(a)/2.30(d)
301141	W^+(180,250)$\to \tau\nu$	52(a)/53(d)	55.00	$k_{Factor}(m)$	$1.00 \cdot 10^{1}$(a)/$1.00 \cdot 10^{1}$(d)
301142	W^+(250,400)$\to \tau\nu$	39(a)/40(d)	81.75	$k_{Factor}(m)$	$2.20 \cdot 10^{1}$(a)/$2.30 \cdot 10^{1}$(d)
301143	W^+(400,600)$\to \tau\nu$	32(a)/32(d)	30.31	$k_{Factor}(m)$	$1.00 \cdot 10^{2}$(a)/$1.00 \cdot 10^{2}$(d)
301144	W^+(600,800)$\to \tau\nu$	19(a)/18(d)	80.06	$k_{Factor}(m)$	$3.10 \cdot 10^{2}$(a)/$3.00 \cdot 10^{2}$(d)
301145	W^+(800,1000)$\to \tau\nu$	21(a)/20(d)	20.02	$k_{Factor}(m)$	$1.20 \cdot 10^{3}$(a)/$1.10 \cdot 10^{3}$(d)
301146	W^+(1000,1250)$\to \tau\nu$	23(a)/22(d)	60.01	$k_{Factor}(m)$	$3.20 \cdot 10^{3}$(a)/$3.00 \cdot 10^{3}$(d)
301147	W^+(1250,1500)$\to \tau\nu$	26(a)/24(d)	10.00	$k_{Factor}(m)$	$1.00 \cdot 10^{4}$(a)/$9.80 \cdot 10^{3}$(d)
301148	W^+(1500,1750)$\to \tau\nu$	28(a)/27(d)	50.00	$k_{Factor}(m)$	$2.90 \cdot 10^{4}$(a)/$2.70 \cdot 10^{4}$(d)
301149	W^+(1750,2000)$\to \tau\nu$	30(a)/29(d)	10.00	$k_{Factor}(m)$	$7.00 \cdot 10^{4}$(a)/$6.80 \cdot 10^{4}$(d)
301150	W^+(2000,2250)$\to \tau\nu$	31(a)/30(d)	20.00	$k_{Factor}(m)$	$1.60 \cdot 10^{5}$(a)/$1.50 \cdot 10^{5}$(d)
301151	W^+(2250,2500)$\to \tau\nu$	33(a)/32(d)	$59.30 \cdot 10^{-5}$	$k_{Factor}(m)$	$3.50 \cdot 10^{5}$(a)/$3.40 \cdot 10^{5}$(d)
301152	W^+(2500,2750)$\to \tau\nu$	34(a)/32(d)	$14.60 \cdot 10^{-5}$	$k_{Factor}(m)$	$7.40 \cdot 10^{5}$(a)/$7.10 \cdot 10^{5}$(d)
301153	W^+(2750,3000)$\to \tau\nu$	35(a)/34(d)	$22.30 \cdot 10^{-5}$	$k_{Factor}(m)$	$1.50 \cdot 10^{6}$(a)/$1.40 \cdot 10^{6}$(d)
301154	W^+(3000,3500)$\to \tau\nu$	36(a)/35(d)	$21.80 \cdot 10^{-5}$	$k_{Factor}(m)$	$2.00 \cdot 10^{6}$(a)/$1.90 \cdot 10^{6}$(d)
301155	W^+(3500,4000)$\to \tau\nu$	37(a)/36(d)	$95.00 \cdot 10^{-6}$	$k_{Factor}(m)$	$7.50 \cdot 10^{6}$(a)/$7.30 \cdot 10^{6}$(d)
301156	W^+(4000,4500)$\to \tau\nu$	38(a)/38(d)	$31.00 \cdot 10^{-6}$	$k_{Factor}(m)$	$3.80 \cdot 10^{7}$(a)/$3.80 \cdot 10^{7}$(d)
301157	W^+(4500,5000)$\to \tau\nu$	39(a)/36(d)	$14.01 \cdot 10^{-7}$	$k_{Factor}(m)$	$9.80 \cdot 10^{7}$(a)/$9.10 \cdot 10^{7}$(d)
301158	W^+(>5000)$\to \tau\nu$	40(a)/40(d)	$3.53 \cdot 10^{-7}$	$k_{Factor}(m)$	$2.60 \cdot 10^{8}$(a)/$2.60 \cdot 10^{8}$(d)
361105	$W^- \to \tau\nu$	1416(a)/1581(d)	28 282.60	$k_{Factor}(m)$	$1.70 \cdot 10^{-1}$(a)/$1.90 \cdot 10^{-1}$(d)
301160	W^-(120,180)$\to \tau\nu$	64(a)/72(d)	122.19	$k_{Factor}(m)$	2.90(a)/3.20(d)
301161	W^-(180,250)$\to \tau\nu$	46(a)/48(d)	53.28	$k_{Factor}(m)$	$1.40 \cdot 10^{1}$(a)/$1.40 \cdot 10^{1}$(d)
301162	W^-(250,400)$\to \tau\nu$	34(a)/35(d)	81.08	$k_{Factor}(m)$	$3.20 \cdot 10^{1}$(a)/$3.20 \cdot 10^{1}$(d)
301163	W^-(400,600)$\to \tau\nu$	29(a)/29(d)	30.18	$k_{Factor}(m)$	$1.60 \cdot 10^{2}$(a)/$1.60 \cdot 10^{2}$(d)
301164	W^-(600,800)$\to \tau\nu$	17(a)/16(d)	80.03	$k_{Factor}(m)$	$5.50 \cdot 10^{2}$(a)/$5.40 \cdot 10^{2}$(d)
301165	W^-(800,1000)$\to \tau\nu$	19(a)/18(d)	20.01	$k_{Factor}(m)$	$2.30 \cdot 10^{3}$(a)/$2.20 \cdot 10^{3}$(d)
301166	W^-(1000,1250)$\to \tau\nu$	20(a)/20(d)	60.00	$k_{Factor}(m)$	$6.30 \cdot 10^{3}$(a)/$6.60 \cdot 10^{3}$(d)
301167	W^-(1250,1500)$\to \tau\nu$	24(a)/23(d)	10.00	$k_{Factor}(m)$	$2.40 \cdot 10^{4}$(a)/$2.30 \cdot 10^{4}$(d)
301168	W^-(1500,1750)$\to \tau\nu$	26(a)/25(d)	50.00	$k_{Factor}(m)$	$7.20 \cdot 10^{4}$(a)/$7.00 \cdot 10^{4}$(d)
301169	W^-(1750,2000)$\to \tau\nu$	28(a)/28(d)	10.00	$k_{Factor}(m)$	$1.90 \cdot 10^{5}$(a)/$1.80 \cdot 10^{5}$(d)
301170	W^-(2000,2250)$\to \tau\nu$	30(a)/29(d)	$26.50 \cdot 10^{-5}$	$k_{Factor}(m)$	$4.70 \cdot 10^{5}$(a)/$4.50 \cdot 10^{5}$(d)
301171	W^-(2250,2500)$\to \tau\nu$	31(a)/31(d)	$53.00 \cdot 10^{-5}$	$k_{Factor}(m)$	$1.00 \cdot 10^{6}$(a)/$1.00 \cdot 10^{6}$(d)
301172	W^-(2500,2750)$\to \tau\nu$	33(a)/32(d)	$11.50 \cdot 10^{-5}$	$k_{Factor}(m)$	$2.20 \cdot 10^{6}$(a)/$2.10 \cdot 10^{6}$(d)
301173	W^-(2750,3000)$\to \tau\nu$	34(a)/33(d)	$27.00 \cdot 10^{-6}$	$k_{Factor}(m)$	$4.90 \cdot 10^{6}$(a)/$4.80 \cdot 10^{6}$(d)
301174	W^-(3000,3500)$\to \tau\nu$	35(a)/35(d)	$26.00 \cdot 10^{-6}$	$k_{Factor}(m)$	$5.90 \cdot 10^{6}$(a)/$5.80 \cdot 10^{6}$(d)
301175	W^-(3500,4000)$\to \tau\nu$	37(a)/36(d)	$92 \cdot 10^{-6}$	$k_{Factor}(m)$	$1.80 \cdot 10^{7}$(a)/$1.80 \cdot 10^{7}$(d)
301176	W^-(4000,4500)$\to \tau\nu$	38(a)/37(d)	$34.72 \cdot 10^{-7}$	$k_{Factor}(m)$	$8.10 \cdot 10^{7}$(a)/$8.00 \cdot 10^{7}$(d)
301177	W^-(4500,5000)$\to \tau\nu$	39(a)/39(d)	$11.43 \cdot 10^{-7}$	$k_{Factor}(m)$	$2.70 \cdot 10^{8}$(a)/$2.70 \cdot 10^{8}$(d)
301178	W^-(>5000)$\to \tau\nu$	40(a)/39(d)	$36.16 \cdot 10^{-8}$	$k_{Factor}(m)$	$6.50 \cdot 10^{8}$(a)/$6.40 \cdot 10^{8}$(d)

Table 5.4: $W \to \tau\nu$ boson background Monte Carlo samples. For each sample, this table lists the ATLAS Monte Carlo run number, the physics process (the numbers inside the parentheses (x, y) delimitate the boson invariant mass interval), the number of generated events, the cross section times branching ratio, k_{Factor} ($k_{Factor}(m)$ indicates a dependence on boson invariant mass), and the equivalent integrated luminosity. The letters inside the parentheses (a,d) denote which Monte Carlo campaign the value next to it corresponds to.

MC ID	Process	$N_{evt}[k]$	Generator σB [pb]	k_{Factor}	L_{int} [fb^{-1}]
361107	$Z \to \mu\mu$	79874(a)/79919(d)	21 901.10	$k_{Factor}(m)$	$4.20 \cdot 10^1$(a)/$4.20 \cdot 10^1$(d)
301020	Z(120,180)$\to \mu\mu$	1500(a)/1486(d)	117.48	$k_{Factor}(m)$	$8.50 \cdot 10^1$(a)/$8.50 \cdot 10^1$(d)
301021	Z(180,250)$\to \mu\mu$	900(a)/898(d)	52.92	$k_{Factor}(m)$	$3.00 \cdot 10^2$(a)/$3.00 \cdot 10^2$(d)
301022	Z(250,400)$\to \mu\mu$	1195(a)/1195(d)	81.08	$k_{Factor}(m)$	$1.10 \cdot 10^3$(a)/$1.10 \cdot 10^3$(d)
301023	Z(400,600)$\to \mu\mu$	900(a)/900(d)	30.20	$k_{Factor}(m)$	$4.60 \cdot 10^3$(a)/$4.60 \cdot 10^3$(d)
301024	Z(600,800)$\to \mu\mu$	500(a)/495(d)	80.04	$k_{Factor}(m)$	$1.30 \cdot 10^4$(a)/$1.30 \cdot 10^4$(d)
301025	Z(800,1000)$\to \mu\mu$	250(a)/250(d)	20.01	$k_{Factor}(m)$	$2.30 \cdot 10^4$(a)/$2.30 \cdot 10^4$(d)
301026	Z(1000,1250)$\to \mu\mu$	100(a)/100(d)	60.00	$k_{Factor}(m)$	$2.30 \cdot 10^4$(a)/$2.30 \cdot 10^4$(d)
301027	Z(1250,1500)$\to \mu\mu$	50(a)/50(d)	10.00	$k_{Factor}(m)$	$3.50 \cdot 10^4$(a)/$3.50 \cdot 10^4$(d)
301028	Z(1500,1750)$\to \mu\mu$	50(a)/50(d)	50.00	$k_{Factor}(m)$	$9.10 \cdot 10^4$(a)/$9.10 \cdot 10^4$(d)
301029	Z(1750,2000)$\to \mu\mu$	50(a)/50(d)	10.00	$k_{Factor}(m)$	$2.10 \cdot 10^5$(a)/$2.10 \cdot 10^5$(d)
301030	Z(2000,2250)$\to \mu\mu$	50(a)/50(d)	20.00	$k_{Factor}(m)$	$4.80 \cdot 10^5$(a)/$4.80 \cdot 10^5$(d)
301031	Z(2250,2500)$\to \mu\mu$	50(a)/50(d)	$54.90 \cdot 10^{-5}$	$k_{Factor}(m)$	$1.00 \cdot 10^6$(a)/$1.00 \cdot 10^6$(d)
301032	Z(2500,2750)$\to \mu\mu$	50(a)/50(d)	$12.40 \cdot 10^{-5}$	$k_{Factor}(m)$	$2.00 \cdot 10^6$(a)/$2.00 \cdot 10^6$(d)
301033	Z(2750,3000)$\to \mu\mu$	50(a)/50(d)	$21.30 \cdot 10^{-5}$	$k_{Factor}(m)$	$3.80 \cdot 10^6$(a)/$3.80 \cdot 10^6$(d)
301034	Z(3000,3500)$\to \mu\mu$	50(a)/50(d)	$21.00 \cdot 10^{-5}$	$k_{Factor}(m)$	$5.00 \cdot 10^6$(a)/$5.00 \cdot 10^6$(d)
301035	Z(3500,4000)$\to \mu\mu$	50(a)/50(d)	$93.00 \cdot 10^{-6}$	$k_{Factor}(m)$	$1.60 \cdot 10^7$(a)/$1.60 \cdot 10^7$(d)
301036	Z(4000,4500)$\to \mu\mu$	50(a)/50(d)	$31.04 \cdot 10^{-6}$	$k_{Factor}(m)$	$4.80 \cdot 10^7$(a)/$4.80 \cdot 10^7$(d)
301037	Z(4500,5000)$\to \mu\mu$	50(a)/50(d)	$12.81 \cdot 10^{-7}$	$k_{Factor}(m)$	$1.70 \cdot 10^8$(a)/$1.70 \cdot 10^8$(d)
301038	Z(>5000)$\to \mu\mu$	40(a)/50(d)	$31.26 \cdot 10^{-7}$	$k_{Factor}(m)$	$3.10 \cdot 10^8$(a)/$3.90 \cdot 10^8$(d)
361108	$Z \to \tau\tau$	5507(a)/5429(d)	21 901.10	$k_{Factor}(m)$	2.90(a)/2.80(d)
301040	Z(120,180)$\to \tau\tau$	105(a)/108(d)	117.48	$k_{Factor}(m)$	6.00(a)/6.10(d)
301041	Z(180,250)$\to \tau\tau$	149(a)/148(d)	52.92	$k_{Factor}(m)$	$5.10 \cdot 10^1$(a)/$5.00 \cdot 10^1$(d)
301042	Z(250,400)$\to \tau\tau$	182(a)/184(d)	81.08	$k_{Factor}(m)$	$1.60 \cdot 10^2$(a)/$1.70 \cdot 10^2$(d)
301043	Z(400,600)$\to \tau\tau$	276(a)/224(d)	30.20	$k_{Factor}(m)$	$1.40 \cdot 10^3$(a)/$1.10 \cdot 10^3$(d)
301044	Z(600,800)$\to \tau\tau$	261(a)/254(d)	80.04	$k_{Factor}(m)$	$6.90 \cdot 10^3$(a)/$6.80 \cdot 10^3$(d)
301045	Z(800,1000)$\to \tau\tau$	286(a)/277(d)	20.01	$k_{Factor}(m)$	$2.70 \cdot 10^4$(a)/$2.60 \cdot 10^4$(d)
301046	Z(1000,1250)$\to \tau\tau$	310(a)/300(d)	60.00	$k_{Factor}(m)$	$7.20 \cdot 10^4$(a)/$7.00 \cdot 10^4$(d)
301047	Z(1250,1500)$\to \tau\tau$	333(a)/324(d)	10.00	$k_{Factor}(m)$	$2.30 \cdot 10^5$(a)/$2.20 \cdot 10^5$(d)
301048	Z(1500,1750)$\to \tau\tau$	274(a)/267(d)	50.00	$k_{Factor}(m)$	$5.00 \cdot 10^5$(a)/$4.90 \cdot 10^5$(d)
301049	Z(1750,2000)$\to \tau\tau$	191(a)/188(d)	10.00	$k_{Factor}(m)$	$8.30 \cdot 10^5$(a)/$8.10 \cdot 10^5$(d)
301050	Z(2000,2250)$\to \tau\tau$	377(a)/371(d)	20.00	$k_{Factor}(m)$	$3.60 \cdot 10^6$(a)/$3.50 \cdot 10^6$(d)
301051	Z(2250,2500)$\to \tau\tau$	300(a)/297(d)	$54.90 \cdot 10^{-5}$	$k_{Factor}(m)$	$6.10 \cdot 10^6$(a)/$6.00 \cdot 10^6$(d)
301052	Z(2500,2750)$\to \tau\tau$	306(a)/303(d)	$12.40 \cdot 10^{-5}$	$k_{Factor}(m)$	$1.20 \cdot 10^7$(a)/$1.20 \cdot 10^7$(d)
301053	Z(2750,3000)$\to \tau\tau$	311(a)/308(d)	$21.20 \cdot 10^{-5}$	$k_{Factor}(m)$	$2.50 \cdot 10^7$(a)/$2.50 \cdot 10^7$(d)
301054	Z(3000,3500)$\to \tau\tau$	212(a)/314(d)	$21.00 \cdot 10^{-5}$	$k_{Factor}(m)$	$2.10 \cdot 10^7$(a)/$3.10 \cdot 10^7$(d)
301055	Z(3500,4000)$\to \tau\tau$	367(a)/365(d)	$93.00 \cdot 10^{-6}$	$k_{Factor}(m)$	$1.20 \cdot 10^8$(a)/$1.20 \cdot 10^8$(d)
301056	Z(4000,4500)$\to \tau\tau$	293(a)/292(d)	$31.00 \cdot 10^{-6}$	$k_{Factor}(m)$	$2.90 \cdot 10^8$(a)/$2.90 \cdot 10^8$(d)
301057	Z(4500,5000)$\to \tau\tau$	329(a)/327(d)	$12.81 \cdot 10^{-7}$	$k_{Factor}(m)$	$1.10 \cdot 10^9$(a)/$1.10 \cdot 10^9$(d)
301058	Z(>5000)$\to \tau\tau$	331(a)/331(d)	$31.26 \cdot 10^{-7}$	$k_{Factor}(m)$	$2.60 \cdot 10^9$(a)/$2.60 \cdot 10^9$(d)

Table 5.5: Z boson background Monte Carlo samples. For each sample, this table lists the ATLAS Monte Carlo run number, the physics process (the numbers inside the parentheses (x, y) delimitate the boson invariant mass interval), the number of generated events, the cross section times branching ratio, k_{Factor} ($k_{Factor}(m)$ indicates a dependence on boson invariant mass), and the equivalent integrated luminosity. The letters inside the parentheses (a,d) denote which Monte Carlo campaign the value next to it corresponds to.

MC ID	Process	$N_{evt}[k]$	Generator σB [pb]	k_{Factor}	L_{int} [fb^{-1}]
364250	$Z \to llll$	10513(a)/21379(d)	1.252	1	$8.40 \cdot 10^3$(a)/$1.70 \cdot 10^4$(d)
364253	$WZ \to lll\nu$	10152(a)/21025(d)	4.576	1	$2.20 \cdot 10^3$(a)/$4.50 \cdot 10^3$(d)
364254	$VV \to ll\nu\nu$	11363(a)/22726(d)	12.501	1	$9.00 \cdot 10^2$(a)/$1.80 \cdot 10^3$(d)
364255	$WZ \to l\nu\nu\nu$	3244(a)/6507(d)	3.234	1	$1.00 \cdot 10^3$(a)/$2.00 \cdot 10^3$(d)
363360	$W^+W^- \to l\nu qq$	3588(a)/7212(d)	24.726	1	$1.40 \cdot 10^2$(a)/$2.90 \cdot 10^2$(d)
363359	$W^+W^- \to qql\nu$	3596(a)/14428(d)	24.701	1	$1.40 \cdot 10^2$(a)/$5.80 \cdot 10^2$(d)
363489	$WZ \to l\nu qq$	3653(a)/14680(d)	11.419	1	$3.20 \cdot 10^2$(a)/$1.20 \cdot 10^3$(d)
363358	$WZ \to qqll$	3568(a)/14251(d)	3.433	1	$1.00 \cdot 10^3$(a)/$4.10 \cdot 10^3$(d)
363356	$ZZ \to qqll$	3632(a)/3640(d)	15.563	1	$2.30 \cdot 10^2$(a)/$2.30 \cdot 10^2$(d)

Table 5.6: Diboson background Monte Carlo samples. For each sample, this table lists the ATLAS Monte Carlo run number, the physics process, the number of generated events, the cross section times branching ratio, k_{Factor}, and the equivalent integrated luminosity. The letters inside the parentheses (a,d) denote which Monte Carlo campaign the value next to it corresponds to.

MC ID	Process	$N_{evt}[k]$	Generator σB [pb]	k_{Factor}	L_{int} [fb^{-1}]
410470	$t\bar{t} \to lX$	40512(a)/50176(d)	396.878	1.1398	$1.00 \cdot 10^2$(a)/$1.20 \cdot 10^2$(d)
410013	s-channel Wt	2062(a)/2066(d)	34.009	1.054	$6.00 \cdot 10^1$(a)/$6.00 \cdot 10^1$(d)
410014	s-channel $W\bar{t}$	1535(a)/2065(d)	33.99	1.054	$4.50 \cdot 10^1$(a)/$6.00 \cdot 10^1$(d)
410025	s-channel single t	544(a)/547(d)	2.0514	1.0048	$2.60 \cdot 10^2$(a)/$2.60 \cdot 10^2$(d)

Table 5.7: Top background Monte Carlo samples. For each sample, this table lists the ATLAS Monte Carlo run number, the physics process, the number of generated events, the cross section times branching ratio, k_{Factor}, and the equivalent integrated luminosity. The letters inside the parentheses (a,d) denote which Monte Carlo campaign the value next to it corresponds to.

Chapter 6

Event reconstruction

The event reconstruction must take into account all the objects involved in the $W \to \mu\nu$ production through pp collisions: muons, electrons, jets, missing energy, pileup interactions and underlying event. Several algorithms are used to reconstruct and identify these objects in both data and Monte Carlo simulations; furthermore, corrections to Monte Carlo simulations are applied following the recommendations from the ATLAS combined performance groups. This chapter treats the event reconstruction with emphasis on the muon and missing energy, the most relevant objects for the charged current Drell-Yan process in the muon channel.

6.1 Muons

6.1.1 Muon identification

The Lorentz force[1], $\vec{F} = q\vec{v} \times \vec{B}$, serves to relate the curvature that a particle of charge q describes (travelling at velocity $\vec{v}$), under the influence of a magnetic field $\vec{B}$, with its momentum; this is obtained through matching the Lorentz force against the centripetal force, $\vec{F} = mv^2\hat{r}/r$, result of the particle's, of mass m, motion in a curve parametrized by r which direction, $\hat{r}$, is towards the centre of the curve. This matching is used in both Inner Detector and Muon Spectrometer subdetector systems to reconstruct the muon momentum, since muons are expected to traverse both the ID and the MS (the ATLAS outer subdetector). Specifically, for the case of a constant magnetic field,

$$qB = mvr = p_T \sin\theta r, \tag{6.1}$$

[1]For practical purposes, the electric field is considered to be equal to zero and thus it does not contribute to the Lorentz force.

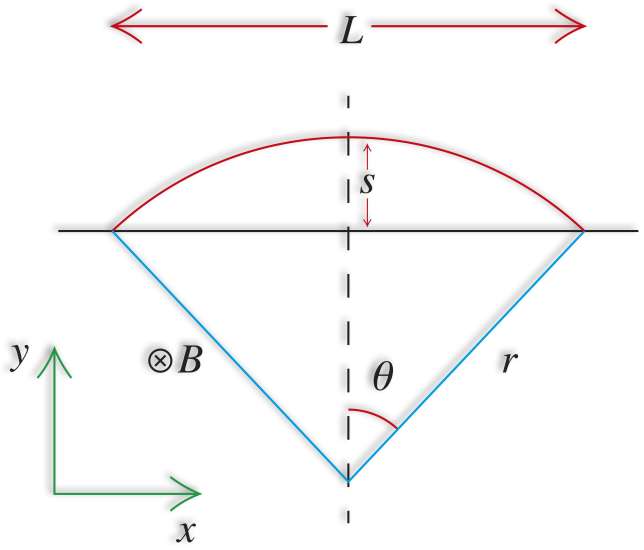

Figure 6.1: Diagram of the curvature made by the particle in the presence of a magnetic field. The reference frame is the same as defined in Section 3.2.1, *i.e.*, the magnetic field $\vec{B}$ is pointing inside the page which corresponds to the direction of the beam pipe. θ and r are parameters that define the curve followed by the muon. s is the arc's sagitta defined by the θ and r. Finally, L is the distance between the points that define the arc.

where p_T is the particle's transverse momentum and θ is the angle that characterizes the curved trajectory; it is convenient to use the sagitta, s, of the trajectory's arc, instead of r and θ to measure the particle transverse momentum. From Figure 6.1 a relation between the sagitta and r and θ is obtained, $s = r(1 - \cos\theta)$; moreover, for large r and small θ, it is found that,

$$p_T = \frac{L^2 qB}{8s}, \tag{6.2}$$

where L is the distance in between the points which define the trajectory's arc and B is the magnetic field magnitude. Equation (6.2) is used by ATLAS to determine the muon's momentum. The difference among the muon and electron trajectories resides on their different masses, in Equation (6.1) the transverse momentum dependence on the mass is established.

To achieve good muon momentum measurement, individual information from the IP, ID and MS detectors is employed, see Chapter 3. Four muon definitions are used in the reconstruction: A combined (CB) muon track reconstruction is done via a global fit that uses hits from ID and MS. Extrapolated (ME) muons are defined when the trajectory is reconstructed based only on the MS track and it is related with the IP; ME muons extend the acceptance to $2.5 < |\eta| < 2.7$. Segment-tagged (ST) muons are the tracks in the ID that, when extrapolated to the MS, are associated with at least one local track segment in the

MDT or CSC chambers. Calorimeter-tagged (CT) muons are the ID tracks, when matched to an energy deposit in the calorimeter, are compatible with a minimum-ionising particle[2]; they recover acceptance in the region where the MS cabling is found, and the CT muons are optimised for $|\eta| < 0.1$ and $15 < p_T < 100$ GeV. In the case of a muon falling in more than one definition, preference is given to CB, then to ST and finally to CT definition. A good muon momentum measurement in the ID requires at least one pixel hit and five SCT hits, fewer than three pixel or SCT holes[3], and at least 10% of the TRT hits originally assigned to the track must be included in the final fit [53].

The *medium* identification criteria for muons are considered in this analysis. Only CB and ME tracks are used. The former are required to have ≥ 3 hits in a minimum of two MDT layers, except for tracks in the $|\eta| < 0.1$ region, where tracks with at least one MDT layer but no more than one MDT hole layer are allowed. The latter are required to have at least three MDT/CSC layers, and are employed only in the $2.5 < |\eta| < 2.7$ region to extend the acceptance outside the ID coverage. A loose selection on the compatibility between ID and MS momentum measurements is applied to suppress the contamination due to hadrons misidentified as muons. Specifically, the q/p significance (the absolute value of the difference between the ratio of the charge and momentum of the muons in the ID and MS divided by the sum in quadrature of the uncertainties) is required to be less than seven [53].

6.1.2 Muon performance

Tag and probe method

A widely used methodology to calculate efficiencies in ATLAS is the tag and a probe method. The method consists in considering a Standard Model process, *e.g.* $Z \to \mu\mu$, of which the properties and correlations of its decay products are well-known, then take one lepton as the "tag" to study the other "probe" lepton. The tag lepton is required to pass stringent selection cuts, while for the probe lepton a particular cut is dropped to quantify the effect, a diagram is found in Figure 6.2.

Efficiencies obtained with this methodology are computed for data and Monte Carlo, subsequently these efficiencies are employed to calculate *efficiency scale factors* and apply them to the MC in order to accommodate the data mismodelling. A general efficiency scale factor, SF, reads as

$$SF = \frac{\epsilon_{data}}{\epsilon_{MC}}, \tag{6.3}$$

[2]Relativistic charged particles passing through matter, lose energy by ionisation and atomic excitation, this is described by the Bethe-Bloch equation; minimum-ionising particles are relativistic particles which have mean energy loss rates close to the minimum set by the Bloch-Bethe equation [4].

[3]A hole is defined as an active sensor traversed by the track but containing no hits.

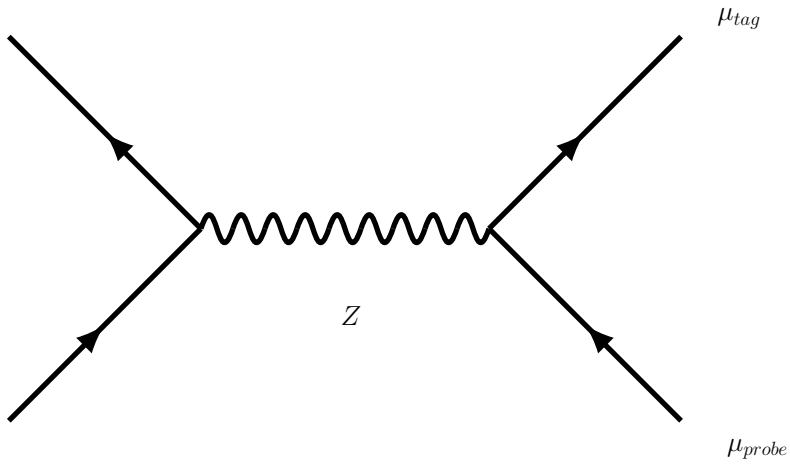

Figure 6.2: Tag and probe method diagram. In the diagram a Z boson is produced by any mechanism, and the decay products are restricted to be one muon and its antiparticle. In Section 4.2.2 a detailed description of the method is given using electrons; the same remarks apply for muons: one muon is tagged (tag muon, here in the diagram referred to as μ_{tag}) with tight identification selections, the di-muon system invariant mass is required to be consistent with the Z boson invariant mass, finally a loose selection is applied to the second muon (probe muon, here in the diagram referred to as μ_{probe}). Then the probe muons are used to calculate the efficiency of a specific selection criterion.

where ϵ_{data} and ϵ_{MC} are the efficiencies for data and MC respectively. This quantity corrects for the difference between simulation and data and is applied as weight to every Monte Carlo event.

Identification efficiency

The efficiency originated from the medium muon identification selection is provided by the ATLAS Muon Combined Performance group (MCP), it is based on a tag and probe technique that uses $Z \to \mu\mu$ and $J/\Psi \to \mu\mu$ data samples coming from 13 TeV pp collisions recorded in 2015 and 2016. The tag muons follow the medium criteria and the probe muons satisfy the CT requirements. Figure 6.3 displays the identification efficiency corresponding to medium muons; the plot displays the data and MC efficiencies from which the efficiency scale factors are calculated using Equation (6.3). For the charged current Drell-Yan selection (see Chapter 7) these scale factors were considered, Figure 6.4 shows the average identification efficiency scale factors as a function of muon p_T, muon η, and transverse mass defined in Section 7.1.10. From the plots it is concluded that the muon identification efficiency scale factors do not depend on the muon p_T and the dependence on the muon η is small. The behaviour is consistent with the results shown in Figure 6.3. The scale factors are applied

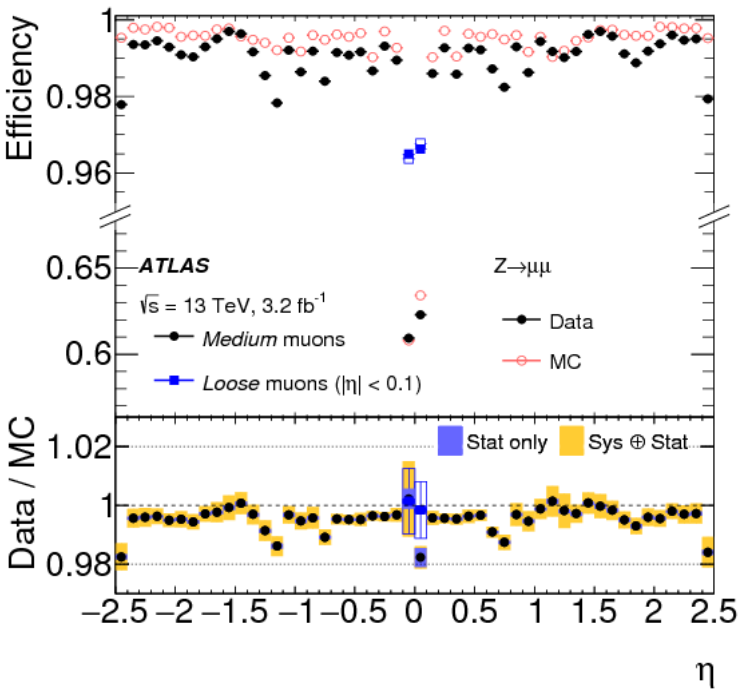

Figure 6.3: Muon identification efficiency as a function of η measured in $Z \to \mu\mu$ events for muons with $p_T > 10$ GeV for *Medium* muon selection. In addition, the plot also shows the efficiency of the *Loose* selection (squares) in the region $|\eta| < 0.1$ where the *Loose* and *Medium* selections differ significantly. The error bars on the efficiencies indicate the statistical uncertainty. The panel at the bottom shows the ratio of the measured to predicted efficiencies, this ratio corresponds to the efficiency scale factor, with statistical and systematic uncertainties [53].

event by event to the signal and electroweak background Monte Carlo simulations, and are close to 99%.

Muon momentum scale and resolution

It is desired to have a muon momentum scale accurate to the per mille level and a muon momentum resolution accurate to the percent level. Data and simulation comparisons are performed with the aid of $Z \to \mu\mu$ and $J/\Psi \to \mu\mu$ samples to carry out the required corrections. A muon momentum calibration is performed using only CB muons that use the p_T reconstructed in the ID and the MS detectors, the calibration is performed separately for each detector and is divided in two components [53]:

- *Muon momentum scale corrections.* These corrections aim to correct for the inaccuracy in the description of the magnetic field integral and the dimension of the detector

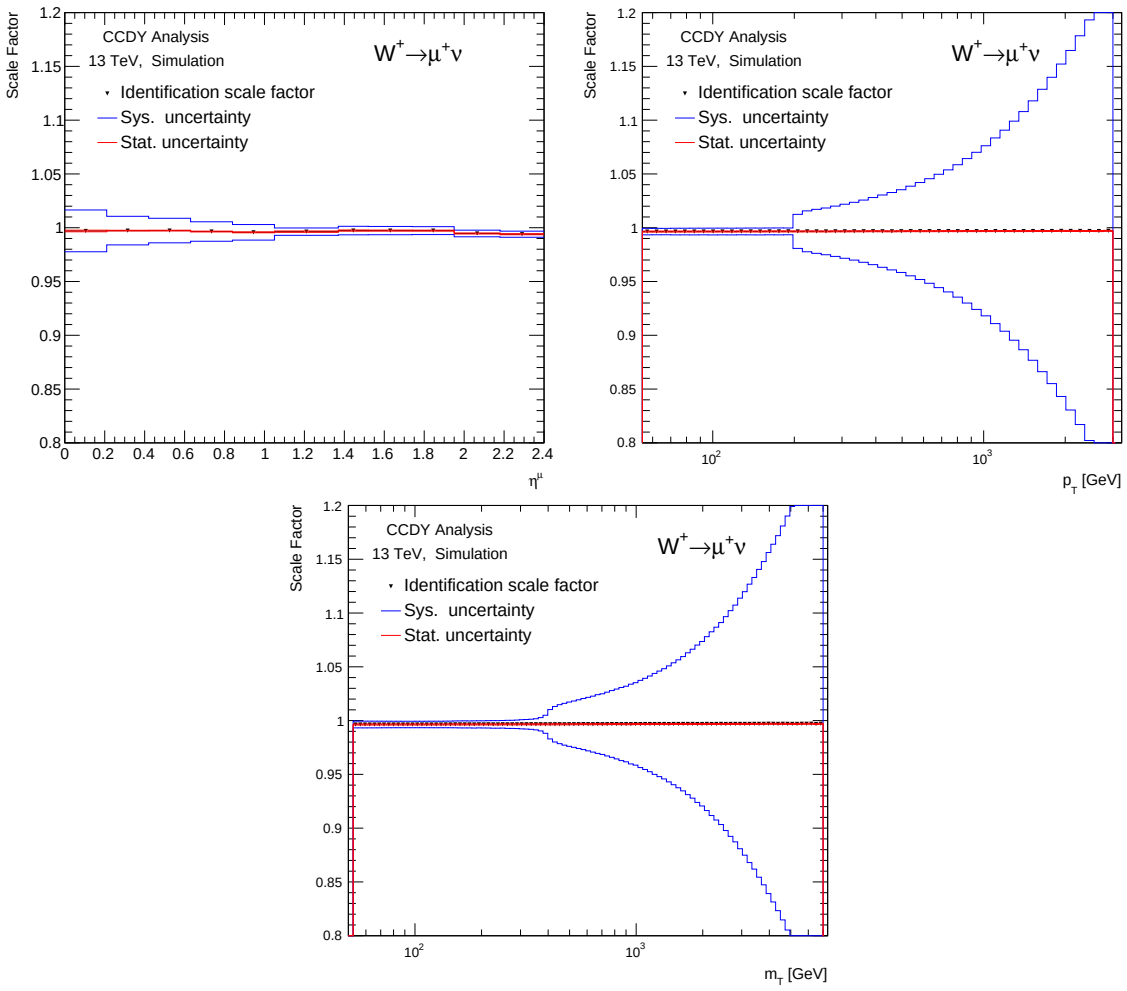

Figure 6.4: Average identification efficiency scale factor plots. These plots show the $W^+ \to \mu^+\nu$ selection average scale factors as a function of muon η (top-left), muon p_T (top-right), transverse mass (bottom). The individual systematics and statistical one standard deviations are displayed with blue and red lines respectively, which are described in more detail in Chapter 9. The same behaviour is seen for $W^- \to \mu^-\nu$.

perpendicular to the magnetic field. Furthermore, corrections are carried out to accommodate the imperfect description by the simulation of the energy loss in the calorimeter and other materials between the interaction point and the MS; for the negligible energy loss in the ID, no correction is done.

- *Muon momentum resolution smearing.* This accounts for energy loss fluctuations in the traversed material. Moreover, multiple scattering, local magnetic field inhomogeneities and displacements of the hits are considered. Finally, resolution effects, emerging from the spatial resolution of the hit measurements and by residual misalignment of the

muon spectrometer, are included in these calibrations.

Muon sagitta corrections

Due to imperfect alignment and deformations, the ID and MS detectors exhibit movements orthogonal to the track trajectory, leading to antisymmetric modifications of the track curvature between positively and negatively charged particles, these are referred as *sagitta biases*. The sagitta biases corrections can be obtained by comparing the transverse momentum of opposite charged muons in a $Z \to \mu\mu$ sample. A complementary determination of the sagitta biases is carried out by studying the E/p ratio for the electrons in $Z \to ee$ observed[4] in the ID detector and determine the difference with respect to the analogous quantity in the electromagnetic calorimeter where these biases, are in principle absent. Moreover, the muon η distributions in Chapter 10 display a difference in shapes for the W^+ and W^- channels, as a consequence it is needed that the sagitta biasses corrections to be derived differentially in η. A corrected transverse muon momentum, p_T^{meas} [54],

$$p_T^{meas} = \frac{p_T^{reco}}{(1+\alpha(\eta))(1+q\times\delta_{sagitta}(\eta)\times p_T^{reco})}, \tag{6.4}$$

mitigate the sagitta biases, where p_T^{reco} is the muon momentum calculated with Equation (6.2), $\delta_{sagitta}(\eta)$ is the sagitta bias as function of muon η; a correction that takes into account the radial biases is contained in $\alpha(\eta)$ and also depends on the muon η. These corrections are performed by the MCP group [53].

6.2 Electrons

Similar to muons, electrons are reconstructed taking into account the curved tracks that they leave. Nevertheless, electrons do not traverse beyond the electromagnetic calorimeter, therefore the tracking reconstruction information originates exclusively from the inner detector. To complement the electron momentum measurement and identification, the electromagnetic calorimeter retrieves the energy coming from the photons produced by the electrons, via Bremsstrahlung radiation, when interacting with the calorimeter material; the energy of these photons is a function of the electron mass (or any other particle mass) and goes as m_e^{-2}. The identification takes into account the shape of the cluster of energy in the calorimeter, the track characteristics in the ID and the matching between them. The *loose* electron

[4]The Z boson decay modes into two charged leptons are widely used to obtain efficiencies and calibrations, owing the fact that their signature is relatively simple to distinguish; furthermore these processes have been thoroughly characterised at the LHC and previous particle colliders.

identification criteria is considered [55]. Electrons must at least have a $p_T > 7$ GeV and to be found in a pseudorapidity range of $|\eta| < 2.47$, excluding barrel-endcap transition region ($1.37 < |\eta| < 1.52$). Furthermore, electrons must be isolated from other tracks and energy deposits to reduce the multijet background.

6.3 Jets

Jets are objects that are composed by a group of particles encapsulated in a small cone; these particles are the result of the hadronisation and fragmentation of coloured particles (quarks and gluons coming from a pp collision) due to colour confinement, it follows the creation of a large number of hadrons travelling approximately in the same direction. The anti-k_t algorithm [56], with radius parameter R=0.4, is used to reconstruct and identify jets. The jet calibration is based on electromagnetic detector topologies where is required $p_T > 20$ GeV and $|\eta| < 2.4$ cuts. Then the jet vertex algorithm (JVT) [57] cuts are included in the selection to mitigate pileup effects; the JVT efficiency weight is displayed in Figure 6.5, it is seen that this effect is less than 1%. Lastly an overlap removal is applied, consisting of removing electrons that share a track with a muon; remove single jets closest to an electron, within a $\Delta R < 0.2$; remove electrons with $\Delta R < 0.4$ of the jet; and remove muons within $\Delta R < 0.4$ of any jet.

6.4 Missing energy

One important characteristic of the charged current Drell-Yan process, is the fact that the neutrino is not observable by the ATLAS detector. In order to be able to study W events of this kind, is necessary to indirectly determine the neutrino kinematics. The typical way of doing this, is to start with the assumption that in a proton-proton collision, the transverse momentum (perpendicular to the beam axis) is conserved, *i.e.* before the collision the transverse momentum is zero and therefore must be zero after the collision[5]. Then it is possible to obtain the transverse energy of the neutrino, by summing all the high p_T particles in the final state plus soft tracks (low p_T) not associated with the former particles; any *missing energy* is attributed to the neutrino energy for the $W \to \mu\nu$ process, more precisely is the absolute value of the negative vector sum of these objects, and is constructed as follows.

[5]The same remarks apply for e^+e^- colliders since this kind of collisions also produce invisible particles and the usage of transverse momentum variables represents identical advantages [58].

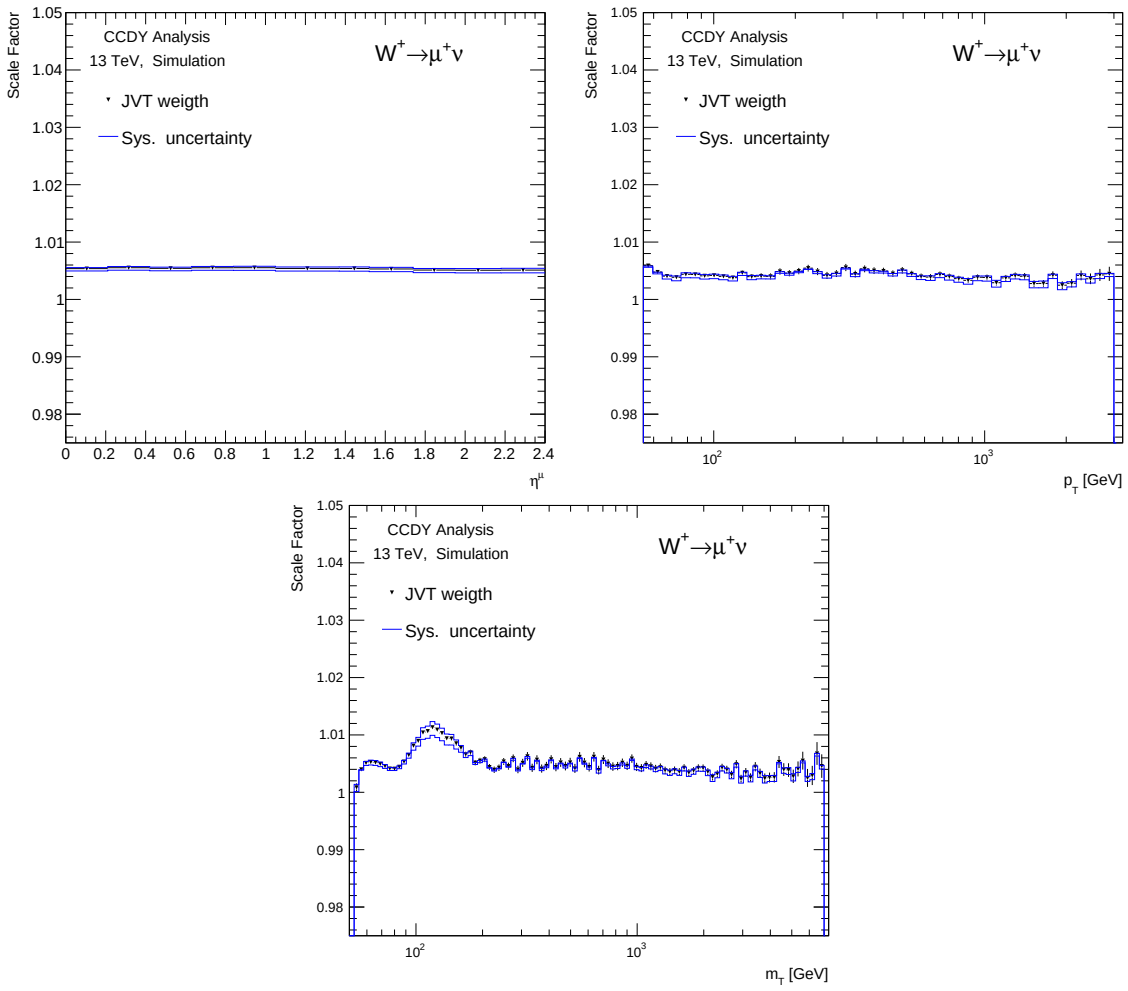

Figure 6.5: Average JVT weight plots for $W^+ \to \mu^+\nu$ as a function of muon η (top-left), muon p_T (top-right), transverse mass (bottom). The systematic one standard deviation is displayed with the blue line, which is described in more detail in Chapter 9. The same behaviour is seen for $W^- \to \mu^-\nu$.

$$E^{miss}_{x(y)} = -\sum_{i\in\{\text{hard objects}\}} p_{x(y),i} - \sum_{j\in\{\text{soft signals}\}} p_{x(y),j}, \tag{6.5}$$

where p_x and p_y are the momentum components on the transverse plane perpendicular to the beam axis. The first term on the right hand side of Equation (6.5) includes the so-called hard objects: electrons, photons, hadronically decaying τ-leptons, muons and jets; the sum is done following that order since it is aimed to avoid double counting of potential shared tracks. The inclusion of electrons and muons in the missing energy calculation is defined by the specific analysis requirements. For photons, τ-leptons and jets in addition to the analysis requirements a further inclusion/rejection could take place due to the resolution ambiguity

between tracks.

The second term of Equation (6.5) represents the tracks which are associated with the hard vertex but not with the selected hard objects, they include signals or signal traces from scattered soft particles arising from the underlying event accompanying the hard-scatter interaction, or from statistically completely independent pileup interactions. In addition, the soft term could include tracks from particles and jets which do not satisfy the hard-object quality criteria, or are below the kinematic threshold. For the inclusion/rejection in the missing energy calculation, the soft tracks are assigned the lowest priority in the sum, *i.e.*, in case of sharing a track with any other object, these are not taken into account. The missing energy being computed with this track soft terms (TST) methodology is referred as the TST missing energy.

The missing energy vector is

$$\mathbf{E}_T^{miss} = (E_x^{miss}, E_y^{miss}), \tag{6.6}$$

with its magnitude given by,

$$E_T^{miss} = |\mathbf{E}_T^{miss}| = \sqrt{(E_x^{miss})^2 + (E_y^{miss})^2}, \tag{6.7}$$

and direction in the transverse plane,

$$\phi^{E_T^{miss}} = \tan^{-1}(E_y^{miss}/E_x^{miss}). \tag{6.8}$$

Equations (6.6)-(6.8) define the missing energy (neutrino for the charged current DY process) transverse momentum vector.

For the particular case of this analysis, the requirements are simple. The electrons included in the E_T^{miss} calculation satisfy the Tight likelihood [59] criteria without isolation requirements and a transverse momentum cut of $p_T > 20$ GeV. Taus and photons are not considered. Muons follow the cuts of the $W \to \mu\nu$ selection defined in Chapter 7.

ID tracks from the hard-scatter collision vertex are used to construct the soft-event signal requiring $p_T > 400$ MeV, $|\eta| < 2.5$, number of pixel hits > 0, number of SCT hits > 5. Finally, with respect to the primary vertex, the tracks must satisfy $|z_0 \sin\theta| < 1.5$ mm and $|d_0| < 1.5$ mm (definitions of $z_0 \sin\theta$ and d_0 are presented in Section 7.1.3).

6.5 Multiple *pp* interactions: pileup

The multiple *pp* interactions or pileup, see Section 3.1, are included in the event simulation, and influences the analysis:

- Through the computation of the E_T^{miss}, in which pileup jets distort the E_T^{miss} distribution.

- By applying a *pileup weight* to match[6] the average number of interactions seen in data to the *campaign a* simulations and to match the actual number of interactions seen in data to the *campaign d* simulations. To appreciate the difference among the two different approaches, see Figure 6.6 which shows both campaigns event pileup weights; from this plot it is concluded that considering the actual pileup distribution, leads to an improvement of statistics ($\approx 20\%$), as a consequence of less pileup weight values being equal to zero with respect to the case that considers the average pileup. Unfortunately, the use of the actual pileup distribution is only available for *campaign d* simulation samples. The definition of the pileup weight is documented in Reference [60] which states that the pileup weight is,

$$w_{pileup} = \frac{L_{A_i}/L}{N_{A_i}/N}, \tag{6.9}$$

  where L_{A_i} is the integrated luminosity of all data in the runs assigned to A (A is a given set of detector conditions) in a pileup bin i, L_{A_i} is the quantity that considers either the average pileup or actual pileup distributions; L is the total integrated luminosity of the data, N is the sum of generator-weights of the whole MC sample, and N_{A_i} is the sum of MC generator-weights in the same pileup bin i.

  The pileup weight is applied in an event by event basis. Figure 6.7 shows the pileup weights as a function of muon p_T, muon η and transverse mass for charged current Drell-Yan events; the dependence of the pileup weight on muon p_T and η is negligible, however an interesting transverse mass dependence is displayed, it is a result of the pileup affecting the missing energy distribution used to define m_T.

[6] Matching data and Monte Carlo multiple *pp* interactions is needed since the Monte Carlo simulations were produced with a generic pileup profile before data taking.

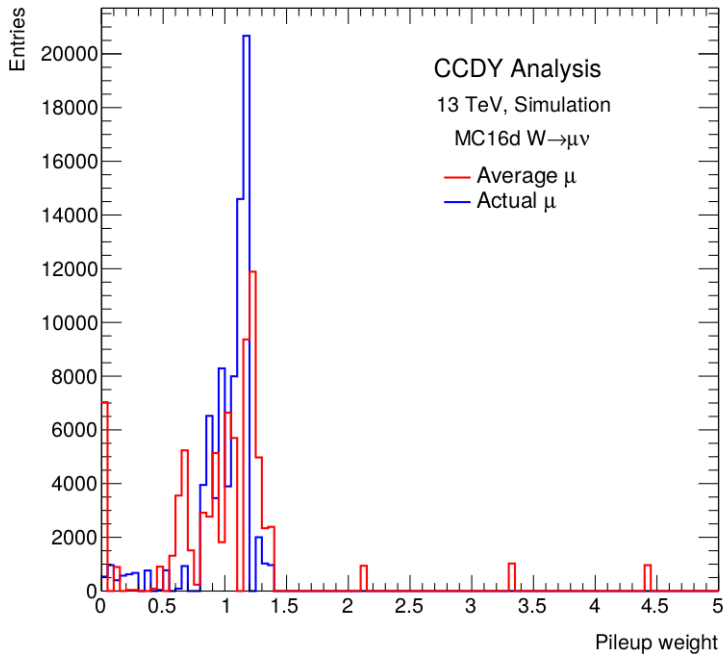

Figure 6.6: Pileup weights. The red curve represents the pileup weights that considered the average pileup distribution in data. The blue curve represents the pileup weights that considered the actual pileup distribution in data.

6.6 ATLAS Combined Performance tools

The corrections and calibrations applied to the physics objects described in previous sections, are implemented using the official ATLAS Combined Performance tools. The analysis treated in the present thesis was performed adapting the official ATLAS software AnalysisTop release 21 to the specific demands of $W \to \mu\nu$ signature. It is important to mention that the tools also handle the systematic uncertainties further discussed in Chapter 9. Table 6.1 lists the tools used in this analysis.

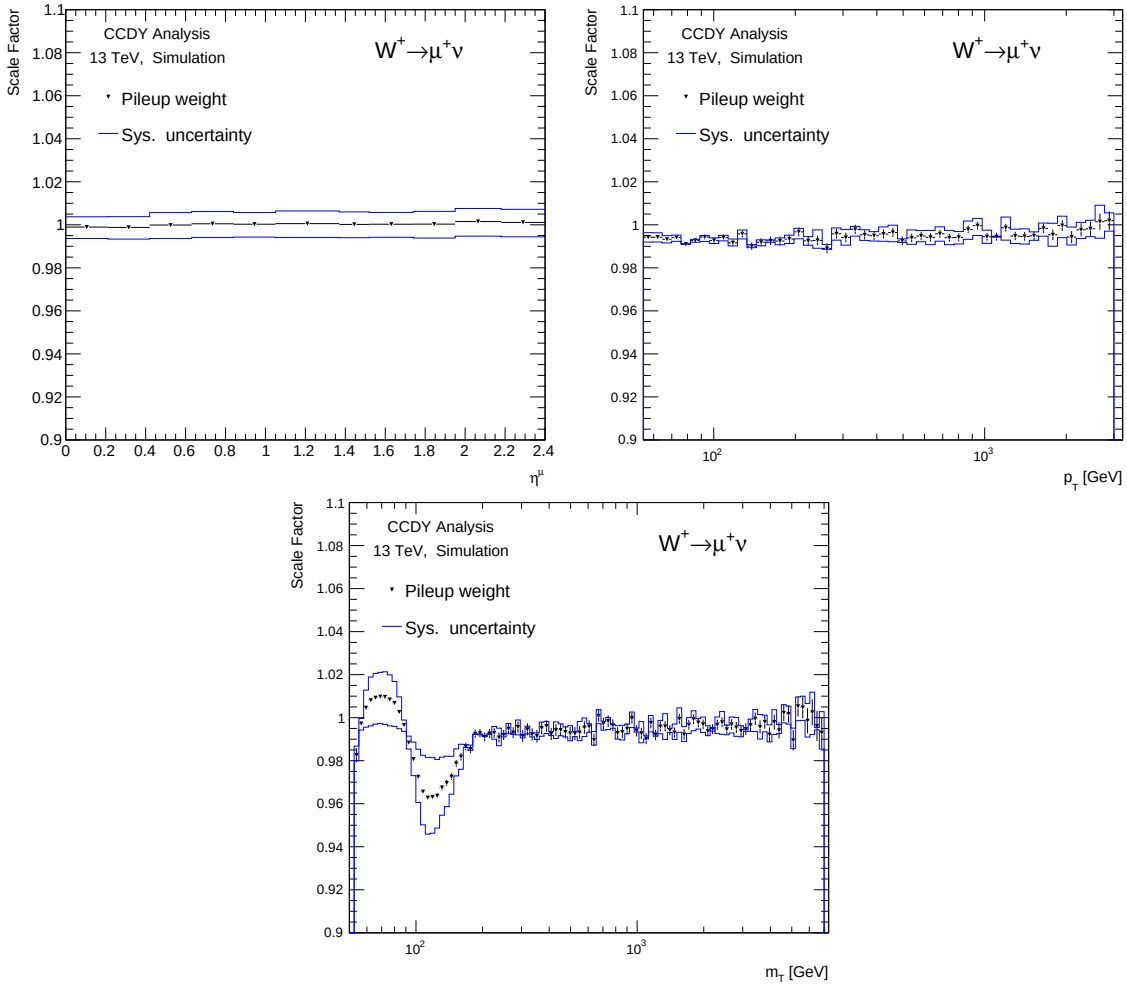

Figure 6.7: Average pileup weight plots. These plots show the $W^+ \to \mu^+\nu$ selection average pileup weight as a function of muon η (top-left), muon p_T (top-right) and transverse mass (bottom). The systematic variation by one standard deviation is displayed with a blue line, which is described in more detail in Chapter 9. The same behaviour is seen for $W^- \to \mu^-\nu$.

Object	Tool name and version tag
Muon calibration	MuonCalibrationAndSmearingTool
Muon efficiency	MuonEfficiencyCorrections
Electron calibration	EgammaCalibrationAndSmearingTool
Electron efficiency	AsgElectronEfficiencyCorrectionTool
Jet calibration	JetCalibrationTool
Jet energy scale	JetUncertaintiesTool
Missing energy builder	METMaker
Missing energy systematics	METSystematicsTool
Jet calibration	JetJERTool
Jet vertex tagger	JetVertexTaggerTool
Pileup reweighting	TPileupReweightingTool

Table 6.1: List of the official tools or packages used to calibrate the physics objects for the charged current Drell-Yan measurement.

Chapter 7

Event selection

This chapter is dedicated to outline the selection cuts performed to efficiently select charged current Drell-Yan events.

7.1 Event Selection

The real time selection during data taking of interesting physics events recorded by ATLAS has to be done carefully by means of the trigger systems; once these high p_T events are recorded, they must be further filtered at the analysis stage, depending on the type of physics signature that is the subject of study. To select charged current Drell-Yan candidates, event level and object level cuts are applied which reduce the background contamination, avoid selecting "fake" muons and achieve high selection efficiency. The following sections briefly explain the event and object level cuts that were studied and applied in the $W \rightarrow \mu\nu$ selection.

7.1.1 Good Run List

The ATLAS data quality group is in charge of providing the information about the detector status during the data taking. The information is stored in a file named the Good Run List (GRL), and contains whether the conditions of the detector and the LHC operations were optimal or not. It determines which runs or fractions[1] of them are good for physics analyses.

[1]Each run in the ATLAS context, is divided by time periods of approximately 60 seconds, called lumi-blocks.

7.1.2 LAr error

Veto events with LAr noise burst. Noise bursts are defined when several thousands of calorimeter cells, experience persistent noise deviations with respect to the standard Gaussian noise coming from electronics.

Data integrity is checked by the LAr real time software during data taking, to ensure that meaningful data is propagated to online systems, trigger decisions and event recording. Events are vetoed if data is corrupted, *i.e.* failing one or more of these checks [61].

7.1.3 Primary vertex

Only events containing at least one primary vertex with three or more tracks associated with it [62] are accepted in the $W \to \mu\nu$ analysis. A primary vertex is established as a point in space where a proton-proton collision has been found. To correctly reconstruct a primary vertex, tracks coming from the SCT detector and pixel detector are used; each track must fulfil the following cuts:

- Transverse momentum cut, $p_T > 400$ MeV.
- Transverse impact parameter, d_0, cut, $|d_0| < 4$ mm, where d_0 is the distance of closest approach in the transverse plane of a track to the primary vertex, as shown in Figure 7.1.
- Transverse impact parameter uncertainty $\sigma(d_0)$, cut $\sigma(d_0) < 5$ mm.
- Longitudinal impact parameter uncertainty, $\sigma(z_0 \sin\theta)$, cut, $\sigma(z_0 \sin\theta) < 10$ mm, where $z_0 \sin\theta$, the longitudinal parameter, expresses the distance of the track to the primary vertex in the longitudial plane at the point of closest approach in the $r - \phi$ plane.

7.1.4 Jet cleaning

Jet cleaning refers to the process of selecting events that contain poorly reconstructed or non collision-related jets. First, jets are classified depending on their origin, whether if it is a hard collision or if it is any other process. The jets are then classified as "good" or "bad", in this way an event is rejected if a bad jet is found. This analysis uses jets that satisfy the Loose criteria [63].

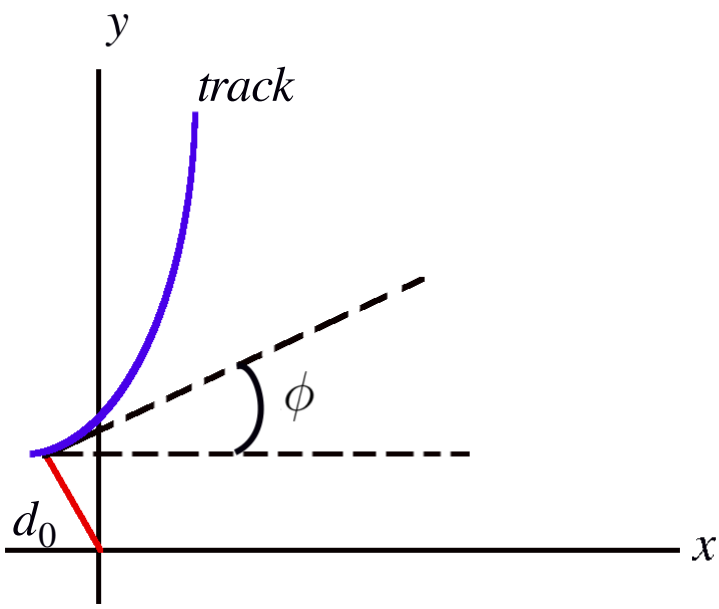

Figure 7.1: Impact parameter, d_0, diagram. The red line represents the impact parameter and it is the distance of closest approach of the particle track, represented with a blue line, to the primary vertex; here the primary vertex is found at the origin of coordinates in x-y plane. In this diagram the conventional ATLAS reference frame is adopted.

7.1.5 Trigger selection and trigger matching

High level triggers are standard requirements in most physics analysis. The high level triggers, the last step in the ATLAS triggering system, are software triggers and the trigger decision is stored so it is available for after-data-taking (offline) analyses. This analysis, uses a trigger chain of two triggers, HLT_mu26_ivarmedium and HLT_mu50. It is called a trigger chain because the trigger requires a chain of logical conditions from L1 and HLT to trigger an event. The event is recorded if either trigger is passed. The different parts of the triggers' names indicate the criteria that must be satisfied: "HLT" stands for high level trigger; "mu" means that the trigger is applied to muons which is accompanied by a number that corresponds to a transverse momentum requirement; and the third part, when applicable, states the isolation cut that the object is needed to have. These triggers aim to select muons with adequate reconstruction quality and physics interesting kinematics. The first trigger in the chain has a muon p_T threshold of 26 GeV and an "ivarmedium" isolation requirement[2]. In order to compensate for possible loss of efficiency at high p_T, a second trigger with a muon $p_T > 50$ GeV, is also used. Moreover, trigger matching is required in such a way that the

[2]The isolation ivarmedium criteria are specified by $\Delta R < 0.3$ and $\sum p_T^{Track}/p_T < 0.07$ cuts (see Section 7.1.6 for details on how the muon isolation is defined).

selected muon is the one which fired the trigger *i.e.* the reconstructed muon and the trigger muon are related with $\Delta R < 0.1$.

Trigger efficiency scale factors are calculated using a $Z \to \mu\mu$ tag and probe data driven study. The trigger efficiency scale factors correct the difference in efficiencies between the data and simulation after applying the trigger selections; the study, carried out by the Combined Muon Performance group, follows the procedure outlined in Section 6.1.2 and it is summarised in Equation (6.3). Figure 7.2 displays the average muon trigger efficiency as a function of muon p_T and η, and transverse mass m_T. The trigger efficiency scale factor dependence on muon p_T and transverse mass is small; on the other hand a strong muon η dependence is present in the barrel region, this is expected since in that region the detector efficiency it is relatively low and it is more difficult to model in the simulation due to the geometry of the MDT trigger chambers in the barrel region of the MS, see Chapter 3.

7.1.6 Muon Isolation

To reduce the inclusion of muons coming from multijet background (heavy flavour decays and jets faking muons), the concept of lepton isolation is introduced. It is possible that multijet backgrounds produce leptons in the final state that comply with the signal selection requirements; nevertheless, leptons arising from this background usually are surrounded by abundant energy deposits from additional particles, as opposed to signal leptons that are expected to be found isolated where most of the energy deposits correspond to them. A quantity that incorporates this information is the muon (lepton) isolation,

$$I^{\mu} = \frac{p_T^{\text{coneSize}}}{p_T^{\mu}}, \tag{7.1}$$

where p_T^{coneSize} is the transverse momentum sum of all the objects inside a cone which size is given by a specific ΔR; p_T^{μ} is the muon transverse momentum, the sum in the numerator of Equation (7.1) excludes p_T^{μ}.

Tracking and calorimeter information is available to define the energy deposits to be consider in calculating the muon isolation. The Muon Combined Performance group has defined several *isolation working points* depending on which subdetectors are used. In this analysis the FixedCutTightTrackOnly working point was chosen, and as the name suggests, this working point only uses tracking information, which in the case of the muons come from the ID and the MS. The FixedCutTightTrackOnly working point is determined by:

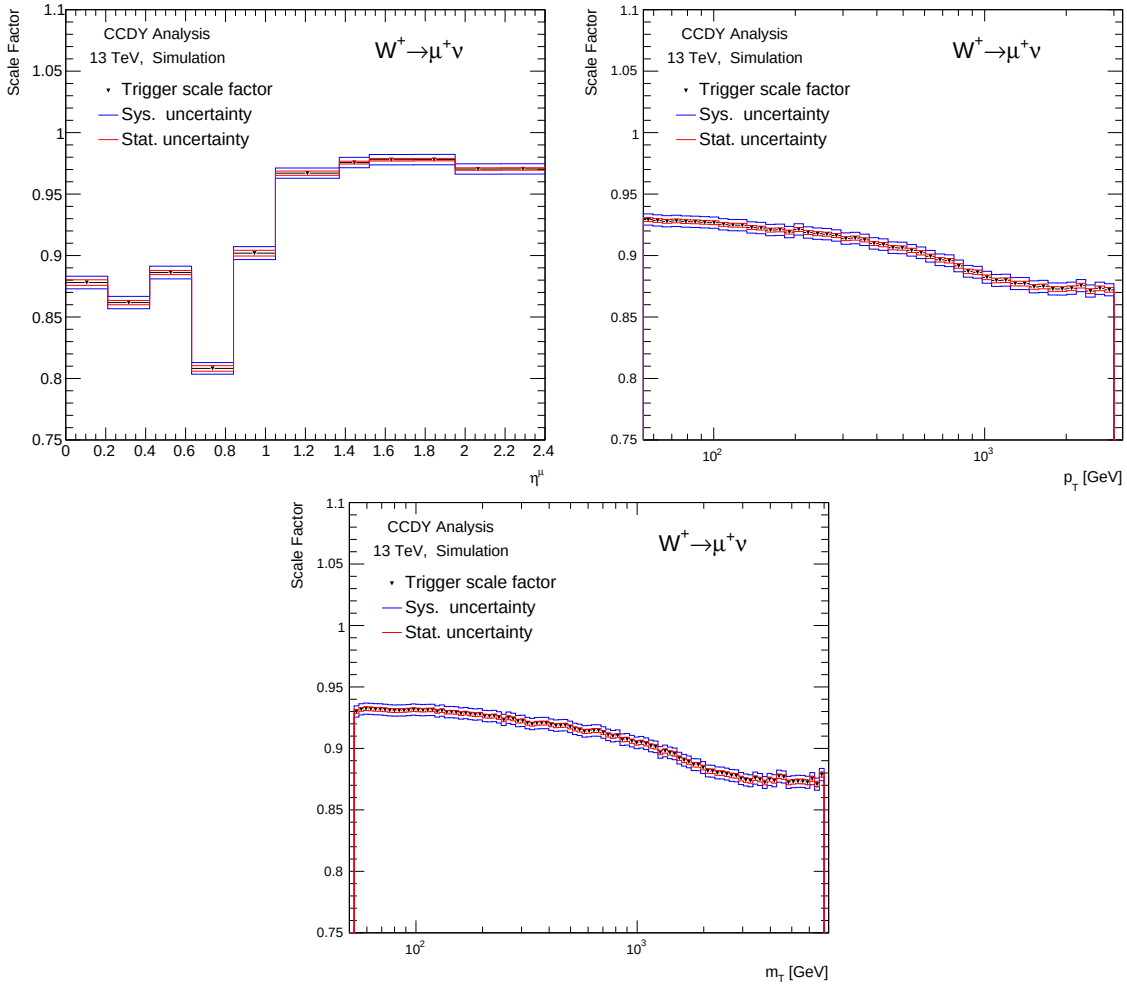

Figure 7.2: Average trigger cut efficiency scale factor plots. These plots show the $W^+ \to \mu^+\nu$ selection average scale factors as a function of muon η (top-left), muon p_T (top-right), and transverse mass (bottom). The individual systematics and statistical one standard deviations are displayed in blue and red respectively. The same behaviour is seen for $W^- \to \mu^-\nu$.

- The size of the cone in Equation (7.1) is a function of the muon p_T^μ, namely,

$$\Delta R = \min\left(\frac{k_T}{p_T^\mu}, R\right), \tag{7.2}$$

  where $k_T = 10$ GeV is a parameter optimised for muons, p_T^μ is the muon momentum and $R = 0.3$ is the maximum size of the cone. Isolated muons are expected to be found in the region of low I^μ close to zero ($I^\mu < 0.06$).

Isolation efficiency scale factors were calculated by the MCP group employing the standard tag and probe methodology. In the same fashion as for the trigger efficiency scale factors, a $Z \to \mu\mu$ sample was used to determine the efficiencies and then obtain the corrections for the simulation to match the data. Figure 7.3 displays the average muon isolation scale factors; the dependence on muon p_T and η is very small, the same behaviour is observed for the dependence on m_T. The isolation scale factors are close 99%.

7.1.7 Muon kinematics

Imposing a high p_T^μ cut, is useful for three reasons. First, it is expected that muons coming from W bosons decays are energetic, therefore a $p_T^\mu > 30$ GeV is considered. Second, the multijet background is efficiently rejected, as muons from this background generally are low-p_T, see Chapter 8. Finally, since the lowest trigger transverse momentum of the triggers considered in this analysis is 26 GeV, it is recommended to establish the p_T^μ above this value to avoid effects from low efficiency.

A geometrical cut is applied on the muons requiring $|\eta| < 2.4$, given the acceptance of ATLAS that is defined by the trigger chambers, the MS and ID acceptance of $|\eta| = 2.7$ and $|\eta| = 2.5$ respectively. Furthermore, it is important to have access to the muon reconstruction efficiencies provided by the MCP group which are given in a region of $|\eta| < 2.5$.

7.1.8 Track-to-track vertex association

With the aim to reduce background events coming from multijet processes (see Chapter 8 for a discussion about this background), an association of the muon tracks with the hard interaction vertex is achieved with the following muon selections:

- $|d_0/\sigma_{d_0}| < 3$,
- $z_0 \sin\theta < 0.5$ mm,

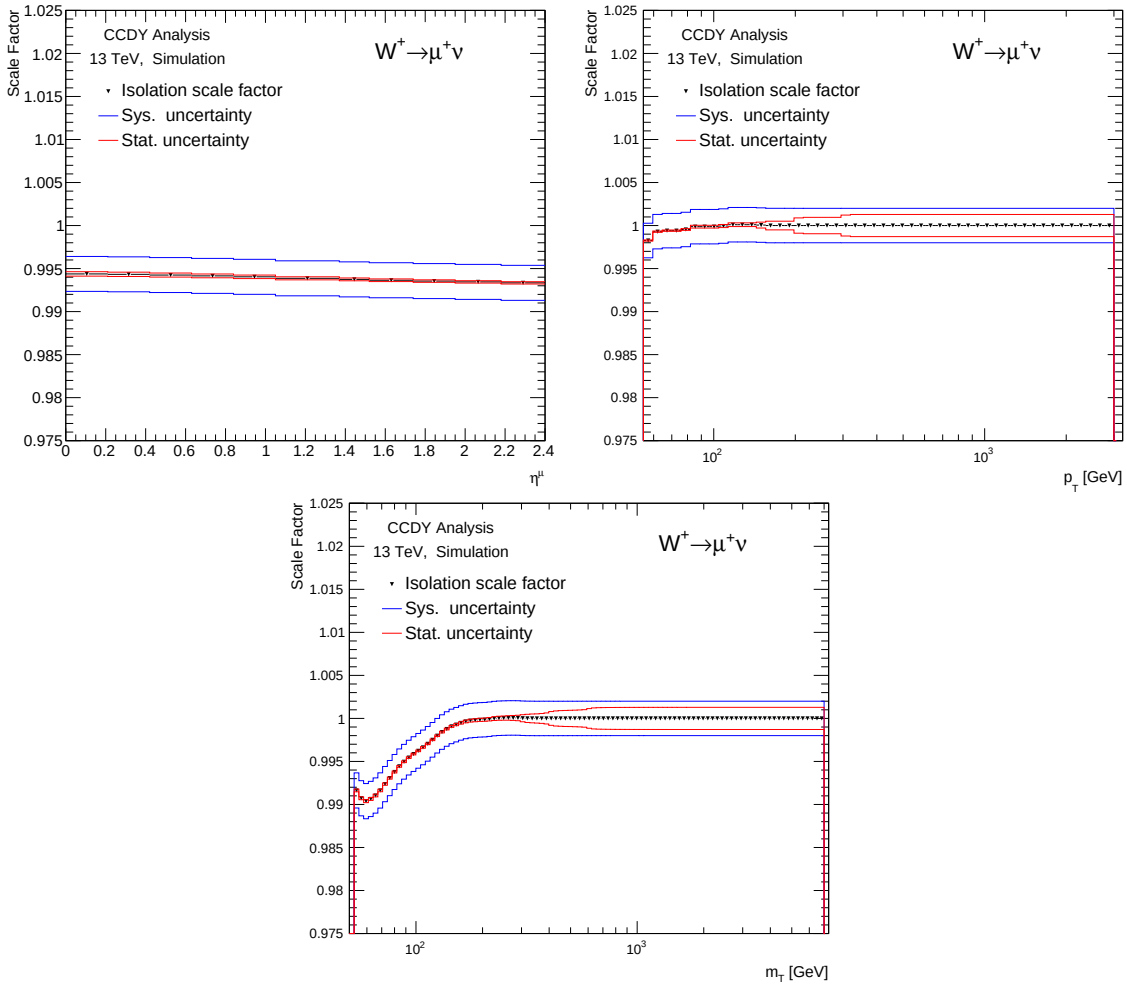

Figure 7.3: Average isolation cut efficiency scale factor plots. These plots show the $W^+ \to \mu^+\nu$ selection average scale factors as a function of muon η (top-left), muon p_T (top-right), and transverse mass (bottom). The individual systematics and statistical one standard deviations are displayed in blue and red respectively. The same behaviour is seen for $W^- \to \mu^-\nu$.

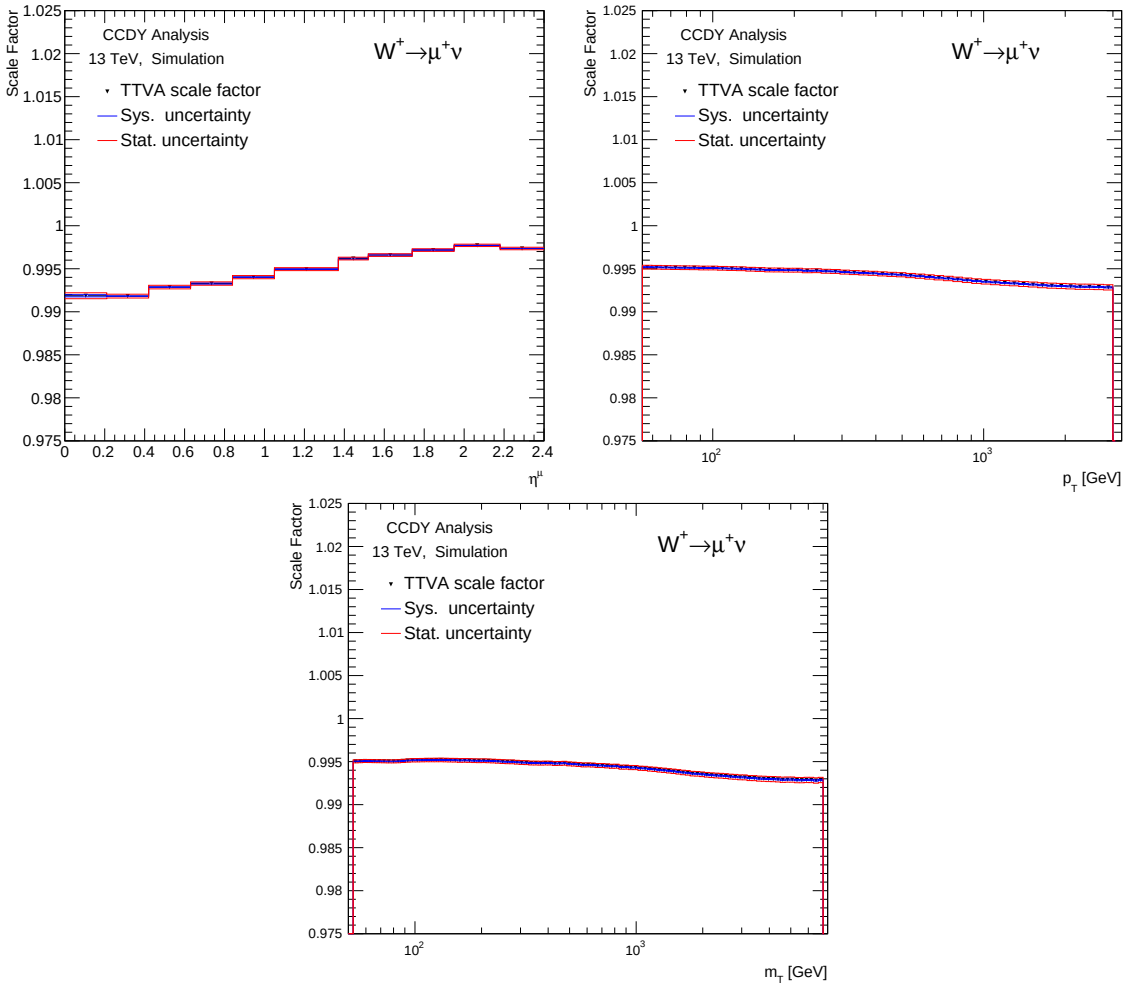

Figure 7.4: Average TTVA cut efficiency scale factor plots. These plots show the $W^+ \to \mu^+\nu$ selection average scale factors as a function of muon η (top-left), muon p_T (top-right), and transverse mass (bottom). The individual systematics and statistical one standard deviations are displayed in blue and red respectively. The same behaviour is seen for $W^- \to \mu^-\nu$.

this association is named the track-to-track vertex association (TTVA). The previous selections help to reduce the multijet production events, as a fraction of the leptons from multijet objects is predicted to arise from the decays of secondary hadrons that have travelled away from the IP before decaying, meaning that the vertex where the multijet leptons are produced should not match the hard collision vertex. Efficiency differences that appear from TTVA cuts are used by the MCP group to calculate TTVA efficiency scale factors, with the same isolation and identification methodology. Figure 7.4 displays the average muon TTVA scale factors; the dependence on muon p_T, η and m_T is very small. The TTVA efficiency scale factors are close 99%.

7.1.9 Missing transverse energy

Cutting on the missing transverse energy, once more helps to reduce the backgrounds. Furthermore, in the charged current Drell-Yan process the missing energy should roughly balance the muon transverse momentum, hence a similar cut is imposed; nevertheless for theoretical interest, see Section 11.1.2, this cut has been set to be slightly different to $E_T^{miss} > 25$ GeV.

7.1.10 Transverse mass

For the neutral current Drell-Yan channel (Z/γ^* boson production) ATLAS is able to fully reconstruct the boson kinematics with the two final state charged leptons. In contrast for the W boson production, only one charged lepton and the missing energy vector, an approximate for the neutral charged lepton, could be reconstructed. Thus, the transverse mass m_T variable is defined which can help to discriminate W boson events from background, and to perform the cross section measurement:

$$m_T = \sqrt{2p_T^{\mu} E_T^{miss}(1 - \cos(\phi^{\mu} - \phi^{E_T^{miss}}))}, \tag{7.3}$$

where p_T^{μ} is the muon transverse momentum, E_T^{miss} is the magnitude of the missing energy vector and ϕ^{μ} and $\phi^{E_T^{miss}}$ are the muon and missing energy azimuthal angles, respectively. This analysis requires is $m_T > 55$ GeV (55 GeV or 50 GeV is a benchmark cut), this cut also reduces background contributions.

7.1.11 Event selection summary

Event level cuts

- The event must be included in the ATLAS data quality good runs list (GRL).
- The event is rejected if the LAr quality check is not passed.
- Primary vertex cut.
- Trigger selection, either HLT_mu26_ivarmedium or HLT_mu50 triggers have to be triggered by a muon in the event.
- The selected muon is required to be matched with the trigger (trigger matching).
- Jet cleaning (Loose bad).
- Overlap removal between jet and leptons.

- Only one muon and no further leptons in the event.

Object (muon) level cuts

- The quality of the muon is required to be *medium*.
- The muon should pass the FixedTightTrackOnly isolation criteria.
- The muon should be well associated with the hard scattering vertex (TTVA cut).
- The muon transverse momentum $p_\mu > 30$ GeV.
- The muon has to be found in the $|\eta_\mu| < 2.4$ region.
- The missing energy of the event $E_T^{miss} > 25$ GeV.
- The transverse mass of the event $m_T > 55$ GeV.

Chapter 8

Multijet background estimation

This chapter summarises the data driven procedures performed to estimate the multijet background. First, the provenance of the multijet background is explained; next, a global summary of the calculation strategy is given; then, the several estimation steps are explained in more detail; finally, the results of the multijet background estimation are presented. The systematic uncertainties of the multijet estimation are covered in Chapter 9.

8.1 Introduction

Multijet events are characterised by a signature involving several jets (> 3 jets); coloured interactions are responsible of these processes, consequently at the LHC multijet events have enormous cross sections. The jets of these events could be identified as part of a physics interesting signal, hence multijet events represent a prime background of most LHC analyses. The multijet background was not discussed in Chapter 5; the reason is that the multijet background differs from the electroweak and top quark backgrounds, in the sense that Monte Carlo simulations are not capable to accurately[1] characterise all the sources responsible for its existence. This measurement's final state consists in one muon accompanied by a neutrino, therefore when a multijet process gives rise to the same final state it contaminates the charged current Drell-Yan number of events. For the muon channel the main multijet background emerges from semileptonic decays of bottom and charm quarks or when a hadron (pion or kaon) formed within a jet decays into leptons; lastly, jets faking muons also contribute to the multijet background. A jet in the ATLAS detector is seen as collection of particle tracks in the MS and ID sub-detectors, in addition energy deposits in the calorimeters aid to identify the jet; this collection of particles has a definite cone shape which is identified

[1]The inaccuracies are associated with theoretical uncertainties of QCD modelling, leading to an imprecise knowledge of the cross section values or to the approximate description of the underlying hadronic activity.

using specialised algorithms, see Section 6.3.

Many of the selection filters applied to select W candidates are thought to reduce the multijet contamination:

- Leptons from a hard collision are expected to be isolated, *i.e.* these leptons are expected to be found in a restricted spatial region where the deposited energy comes only from the leptons themselves.
- An event rate that is not dominated by multijet contamination must not contain low transverse momentum leptons, low transverse mass and low missing energy.
- It is expected that the muon d_0 significance distribution follows a Gaussian shape centred at zero, consistent with the experimental resolution. Real muons from W decays have small impact parameter, whereas muons from multijet background have large impact parameter.
- Charged current Drell-Yan decay products (muon and neutrino) are expected to be roughly kinematically balanced in transverse momentum.

The cross section of the multijet background is considerably larger than the rest of the processes participating in proton-proton collisions, as a consequence, notwithstanding the selection criteria established in Chapter 7, it is not possible to completely remove this background. Given that the Monte Carlo simulations are not used to account for estimating the multijet background, data driven techniques are typically adopted. The following sections contain the data driven procedure used to estimate the multijet events in the present thesis.

8.2 Multijet estimation strategy

The multijet background was calculated with the aid of data driven techniques, in particular, the fraction fit method inspired on the W mass measurement methodology [64], was considered. The major steps are summarised as follows:

- *First step: multijet shape.* Computation of the multijet shape in a phase space constructed by applying the full nominal W selection criteria, plus an inverted selection criterion, which enriches this phase space with multijet events. The procedure is performed for every control distribution of interest.
- *Second step: normalisation.* The multijet background cross section, as opposed to the electroweak and top cross sections, is not known; hence, it is needed to obtain it

using a multijet dominated phase space. The later is achieved by means of a fraction template fit of the transverse mass and the missing energy distributions, performed on data within a multijet dominated fit phase space, where no transverse mass nor missing energy cuts are applied, and obtain the fractions of the purely multijet sample and the Monte Carlo simulated backgrounds that conform these distributions. The fraction of the purely multijet sample is equivalent to the multijet background cross section.

- *Third step: final normalisation.* The normalisation of the multijet background shape associated with the first step, is determined from the cross section obtained in the second step; these are the multijet distributions and number of events in the complete charged current Drell-Yan phase space. The multijet cross section is assumed to be global, *i.e.* is the same in both the fit and signal phase spaces.

8.3 Multijet estimation

8.3.1 Multijet discriminant variable

Ordinarily, one of the most used discriminant variables between signal and multijet processes is the lepton isolation. Nevertheless, the present analysis employs a trigger chain, to select high p_T objects, which incorporates a trigger with an intrinsic muon isolation (see Chapter 7); furthermore, the cross section and muon charge asymmetry measurements are performed differentially in muon pseudorapidity bins, demanding enough statistics to estimate the multijet background in each bin; taking into account the latter points, the use of muon isolation implicates scarce statistics for good multijet estimation performance attained.

Alternatively, in this analysis a different discriminant variable was explored: the muon d_0 significance, $|d_0/\sigma(d_0)|$. The muon d_0 significance acts as a discriminant variable included in the TTVA cut, in which a d_0 significance requirement ($|d_0/\sigma(d_0)| < 3$) is intended to discard muons originated from decaying pions, product of jet hadronisation[2]. Therefore, the phase space with $|d_0/\sigma(d_0)| > 3$ is expected to be multijet dominated.

The *top-left* plot of Figure 8.1 displays the data and MC muon d_0 significance distributions, in the phase space that includes all the W boson selection criteria with the TTVA cut applied; the lower panel shows the ratio between data and MC; from this ratio it is seen that the Monte Carlo prediction is not describing accurately the recorded data. The latter

[2]Pions found in jets live long enough in such a way that their decays take place farther from the primary vertex compared with W bosons; consequently, the pion decaying muons tracks are expected to be described by a large impact parameter.

is expected in the $|d_0/\sigma(d_0)| > 3$ region as it is multijet enriched, where the Monte Carlo simulation loses prediction power. However, in the region with $|d_0/\sigma(d_0)| < 3$, the multijet contribution is relatively small and it is expected to not affect the shape of the data and MC agreement; accordingly, a correction to accommodate the data and MC offset for the $|d_0/\sigma(d_0)|$ distribution is indispensable in order to properly discriminate between electroweak and top processes against multijet processes.

The correction is constituted in two steps:

- Shift the average mean of the MC distribution to match the average mean which corresponds to data.
- Perform a reweighting of the MC muon d_0 significance distribution to match the corresponding data distribution.

The weight is a function of the muon d_0 significance variable and it is calculated with the ratio between a Gaussian distribution fitted to the data and a Gaussian distribution fitted to the MC simulation; the range of the Gaussian fits covers the interval $-2.5 \leq d_0/\sigma(d_0) \leq 2.5$, which is a region where the multijet contribution has a negligible effect, and hence the transverse impact parameter of prompt muons is expected to behave in a Gaussian manner.

To compute the weight in the full d_0 significance interval, the Gaussian fit parameters from data and MC are used to extrapolate the ratio between the fits. In order to prevent anomalously high weights to be assigned to regions where multijet background is expected to be present, the weight is set to a constant value for $|d_0/\sigma(d_0)| \geq 5$, equal to the value of the weight function evaluated in those points. Finally, the d_0 significance weight is an event by event weight thus, a normalisation is applied to ensure that the weights do not affect the final number of predicted events.

The *top-right* plot of Figure 8.1 shows the weight function applied for the negative charged current Drell-Yan selection (the equivalent plot is available for the positive channel). The bottom plots of Figure 8.1 display the d_0 significance distributions, in the region $|d_0/\sigma(d_0)| < 3$ (left) and where there is no $|d_0/\sigma(d_0)|$ restriction (right), after the corrections on the MC simulation have been applied; the agreement is good in the low multijet region. These corrections are important since a mismodelling of the discriminant variable leads to the underestimation or overestimation of the multijet number events.

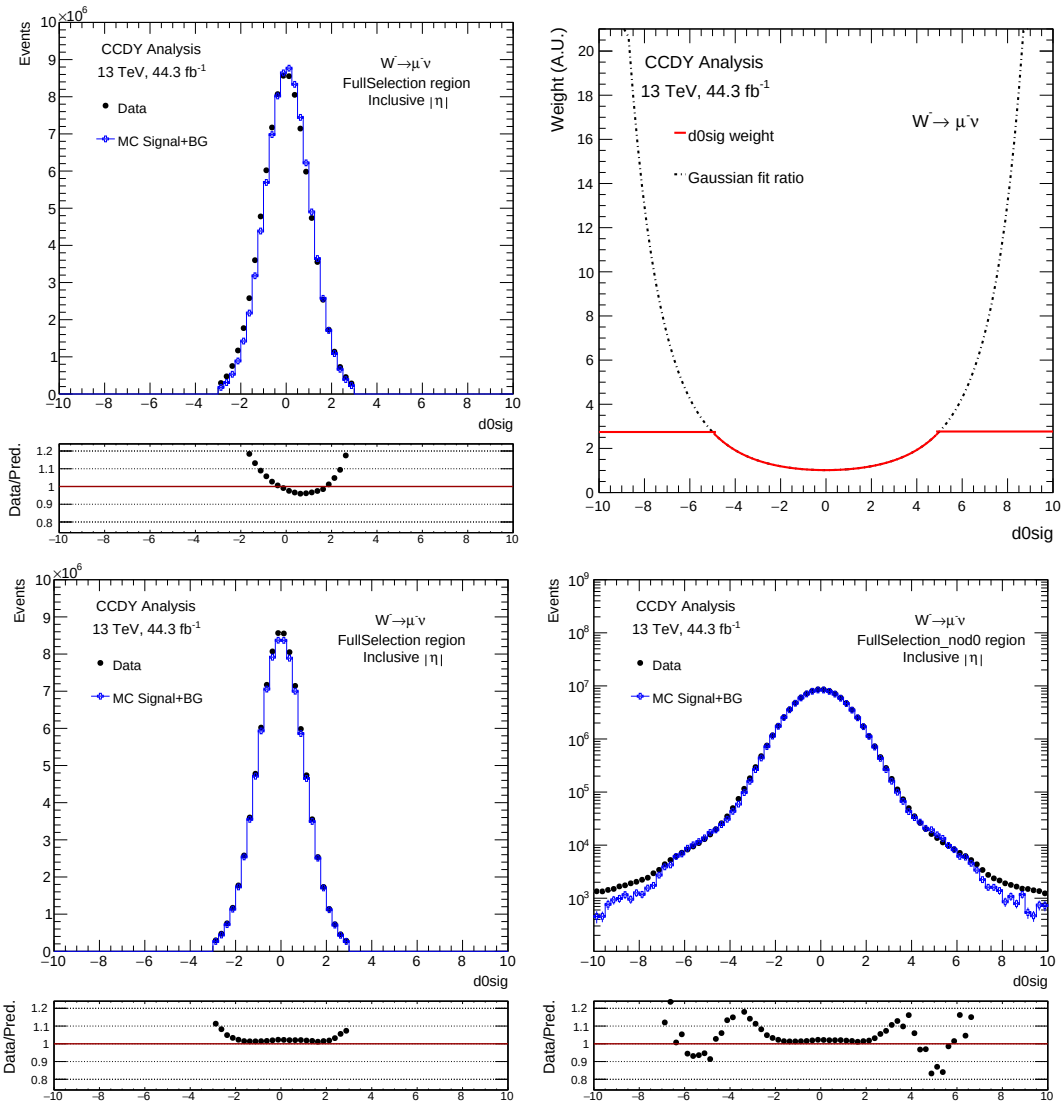

Figure 8.1: d_0 significance plots. *Top-left* plot corresponds to the muon d_0 significance distribution before any corrections; *top-right* plot is the d_0 significance weight applied to the MC simulations; *bottom-left* displays the d_0 significance distribution after the correction weight to the MC simulation has been applied; *bottom-right* plot corresponds to the corrected d_0 significance distribution with no d_0 significance cut applied.

8.3.2 Multijet shape

The first step of the multijet estimation is to determine the shape of the multijet in each control kinematic distribution. The phase space of interest is where the full criteria to select charged current Drell-Yan events are imposed. To obtain the shape in this phase space, the d_0 significance cut is inverted, *i.e.* $|d_0/\sigma(d_0)| > 3$, while maintaining the rest of the cuts unchanged; the procedure is performed on data which will provide a purely multijet enriched sample once the electroweak (including signal $W \to \mu\nu$) and top processes are subtracted. Figure 8.2 - Figure 8.4 embody the multijet shape determination; the data and the simulation are displayed in the plots, the difference between them provides the multijet shape.

8.3.3 Multijet normalisation

The multijet normalisation is extracted from a fraction fit methodology. In the procedure, the transverse mass and missing energy distributions in data are fitted, within a phase space that it is multijet enriched, to the equivalent distributions in Monte Carlo and purely multijet samples. The details of the procedure are explained in the following:

- The fitting region (FR), which is multijet enriched, is defined as the region where the transverse mass m_T and the missing energy E_T^{miss} cuts are dropped, together with a cut on the W boson transverse momentum ($p_T^W < 30$ GeV) requirement; FR is defined for both signal and inverted muon d_0 significance selections. The transverse mass and missing energy cuts are dropped given that the multijet backgrounds peak at lower values with respect to the $W \to \mu\nu$ process; the W boson transverse mass cut was set to remove a poorly MC modelled region.

- The cross section and charge asymmetry measurement phase space that considers the full selection criteria is referred to as signal region (SR). Table 8.1 summarises the cuts applied in the phase spaces considered to perform the fit.

- The fit is performed in the E_T^{miss} and m_T variables (fitting variables). The analytical expression used to perform the fit reads as,

$$T \times N_{jet}^{FR-antid_0} + \alpha \times N_{MC}^{FR-d_0} = N_{data}^{FR-d_0}, \tag{8.1}$$

  where T and α are the fractions corresponding to the multijet contribution and the Monte Carlo simulations in the fit, respectively; $N_{jet}^{FR-antid_0}$ is the distribution of the fitting variable, of which its integral is the number of multijet events in the fit region with the inverted d_0 significance ($antid_0$) cut; $N_{MC}^{FR-d_0}$ is the distribution of the fitting

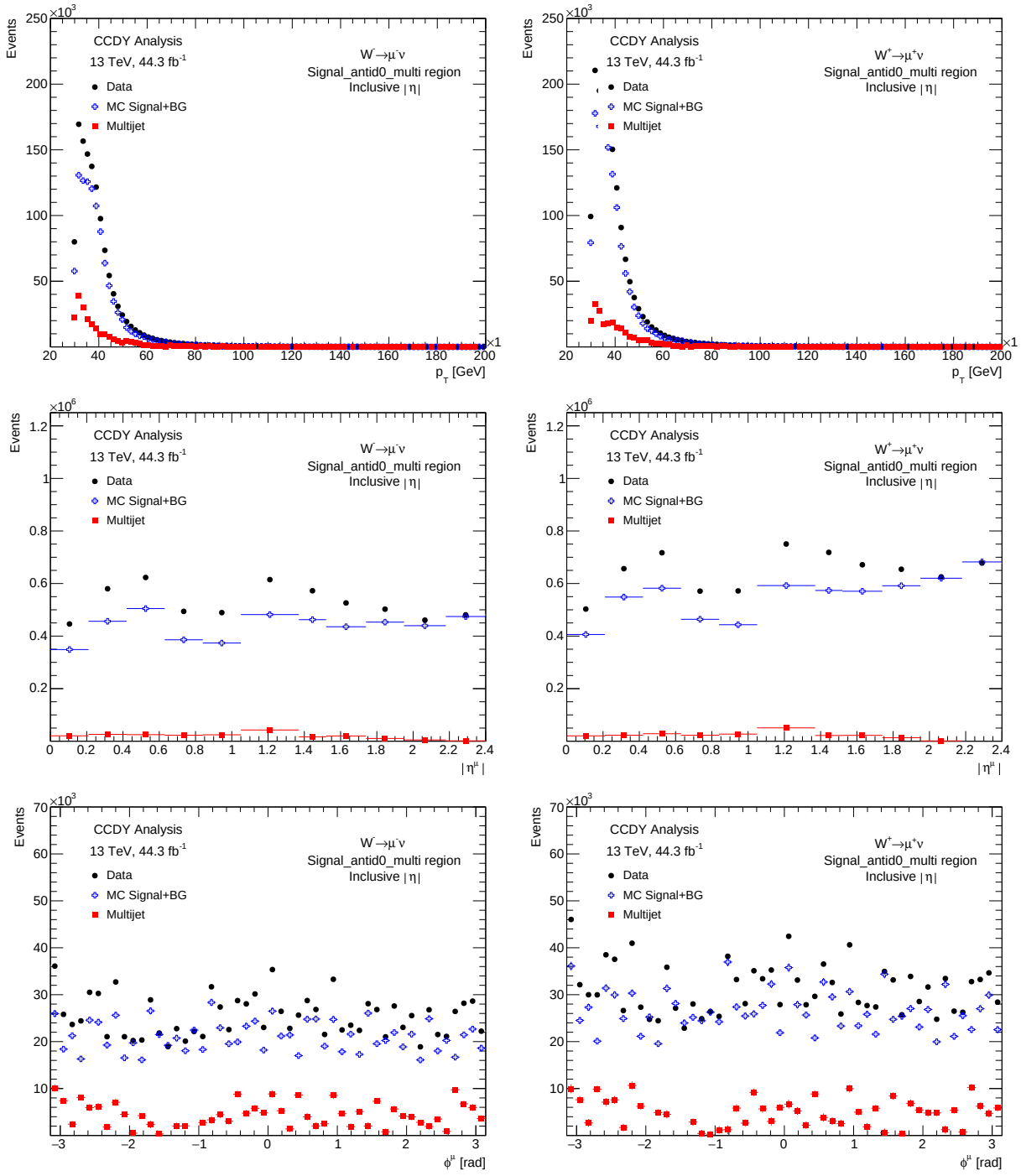

Figure 8.2: Multijet shape plots. Muon p_T (*top-plots*), muon $|\eta|$ (*middle-plots*) and muon ϕ (*bottom-plots*) distributions in a region where the full W boson selection is applied considering the d_0 significance cut inverted. Both data and MC are displayed and the multijet shape is the difference between them. *Left-hand* plots are for the negative channel and *right-hand* plots are for the positive channel.

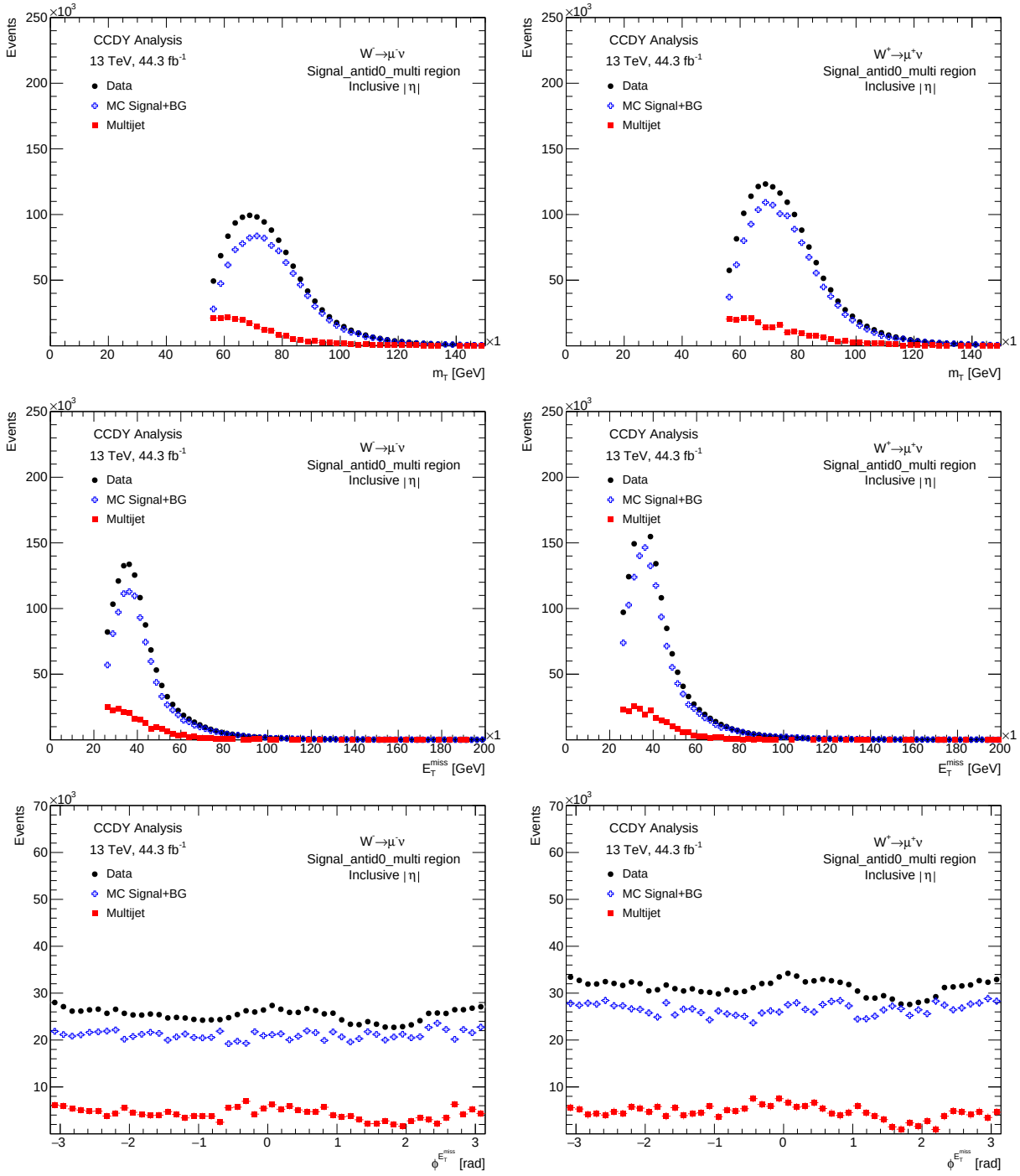

Figure 8.3: Multijet shape plots. Transverse mass (*top-plots*), transverse missing energy (*middle-plots*) and transverse missing energy ϕ (*bottom-plots*) distributions in a region where the full W boson selection is applied considering the d_0 significance cut inverted. Both data and MC are displayed and the multijet shape is the difference between them. *Left-hand* plots are for the negative channel and *right-hand* plots are for the positive channel.

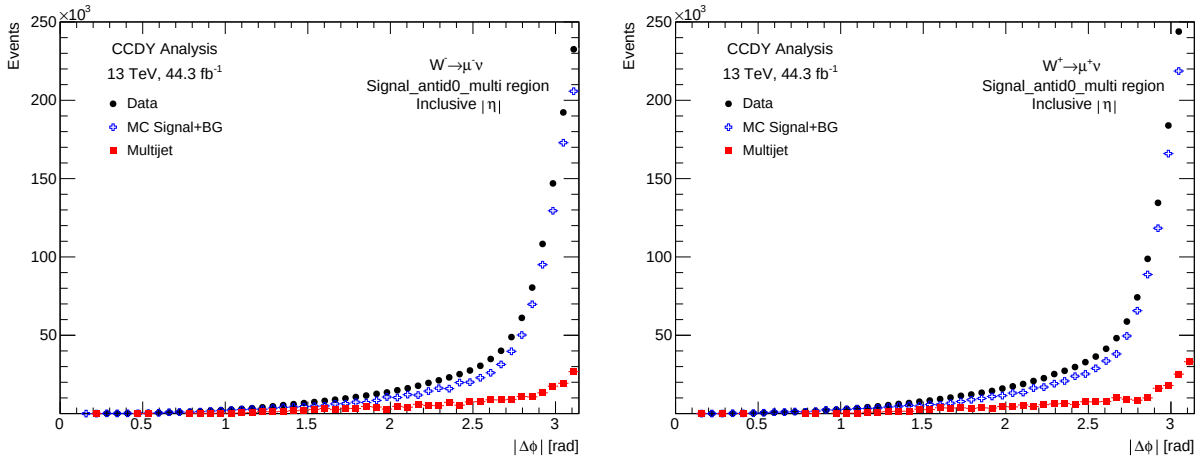

Figure 8.4: Multijet shape plots. $|\Delta\phi|$ distribution in a region where the full W boson selection is applied considering the d_0 significance cut inverted. Both data and MC are displayed and the multijet shape is the difference between them. *Left-hand* plot is for the negative channel and *right-hand* plot is for the positive channel.

variable of which its integral is the MC number of events in the fit region with the d_0 significance cut applied; and $N_{data}^{FR-d_0}$ is the distribution of the fitting variable which its integral is the number of data events in the fitting region with the d_0 significance cut applied. $N_{data}^{FR-d_0}$ shape and number of events are known and it is claimed to be fully described by a purely multijet sample plus a MC sample, therefore the goal of the fraction fit methodology is to calculate the fraction of each of the multijet and Monte Carlo contributions; when the fit is being carried out, α and T are admitted to vary, while the intrinsic normalisations of the Monte Carlo samples involved, are set to the proton-proton collisions cross sections along with the data luminosity utilised. The data distribution $N_{data}^{FR-d_0}$ includes the d_0 significance cut, which is the muon d_0 significance requirement for the $W \to \mu\nu$ cross section and muon charge asymmetry; thus the methodology relies on the assumption that T, the multijet normalisation (cross section), is the same for both the fit and the measurement phase spaces, further details are provided in Appendix A.

- The final multijet number of events in the signal region with the d_0 significance cut applied is,

$$N_{jet}^{SR-d_0} = T \cdot N_{jet}^{SR-antid_0}. \tag{8.2}$$

To correctly use Equation (8.1) and Equation (8.2) it is necessary to obtain the involved distributions for the SR and FR regions:

	Muon d_0 significance	E_T^{miss}	m_T	p_T^W
Signal	Applied/Inverted	> 25 GeV	> 55 GeV	No cut
Fit	Applied/Inverted	No cut	No cut	< 30 GeV

Table 8.1: Summary of the different cuts that define the phase spaces used to carry out the fraction fit methodology.

- The MC and data distributions in signal and fit regions with the d_0 significance cut, denoted as,

$$N_{data}^{SR-d_0}, N_{MC}^{SR-d_0}, N_{data}^{FR-d_0}, N_{MC}^{FR-d_0}, \tag{8.3}$$

  where the superindices reference the region that it is being accounted, $SR - d_0$ is the signal region plus the d_0 significance cut applied and $FR - d_0$ stands for the fitting region plus the d_0 significance cut applied. Figure 8.5 and Figure 8.6 show these distributions.

- The multijet enriched distributions using the inverted d_0 significance criterion (this inverted selection is demanded because it is expected that the decay products of hadrons produced in multijet processes are found within $|d_0/\sigma(d_0)| > 3$), in both the signal and fitting regions, are constructed with the difference between data and MC, namely,

$$N_{jet}^{FR-antid_0} = N_{data}^{FR-antid_0} - N_{MC}^{FR-antid_0}, \tag{8.4}$$

$$N_{jet}^{SR-antid_0} = N_{data}^{SR-antid_0} - N_{MC}^{SR-antid_0}, \tag{8.5}$$

  where the subindex jet indicates the multijet sample and the superindices denote the region that is being accounted for: $FR - antid_0$ is the fitting region criteria plus the inverted d_0 significance cut, $SR - antid_0$ is the W selection criteria plus the inverted d_0 significance. These distributions are displayed in Figure 8.7 and Figure 8.8.

Taking into account the distributions described by Equation (8.3)-Equation (8.5) (displayed in Figure 8.5-Figure 8.8) it is possible to perform the fit of Equation (8.1). The results of the fit are shown in Figure 8.9. In overall, the performance of the fit is good; since the fit is performed in a bin-by-bin basis, the bins with low statistics are prone to be not well accounted for. The lower panels in each plot compare the distribution in data denoted as $N_{data}^{FR-d_0}$ against the outcome of the fit, the agreement is at subpercent level in the high statistics bins and at percent level in the low statistics bins. The full methodology was performed in each muon pseudorapidity bin of the final measurement, see Chapter 11. The plots in Figure 8.9 correspond to the inclusive $|\eta^\mu|$, however the same class of plots were

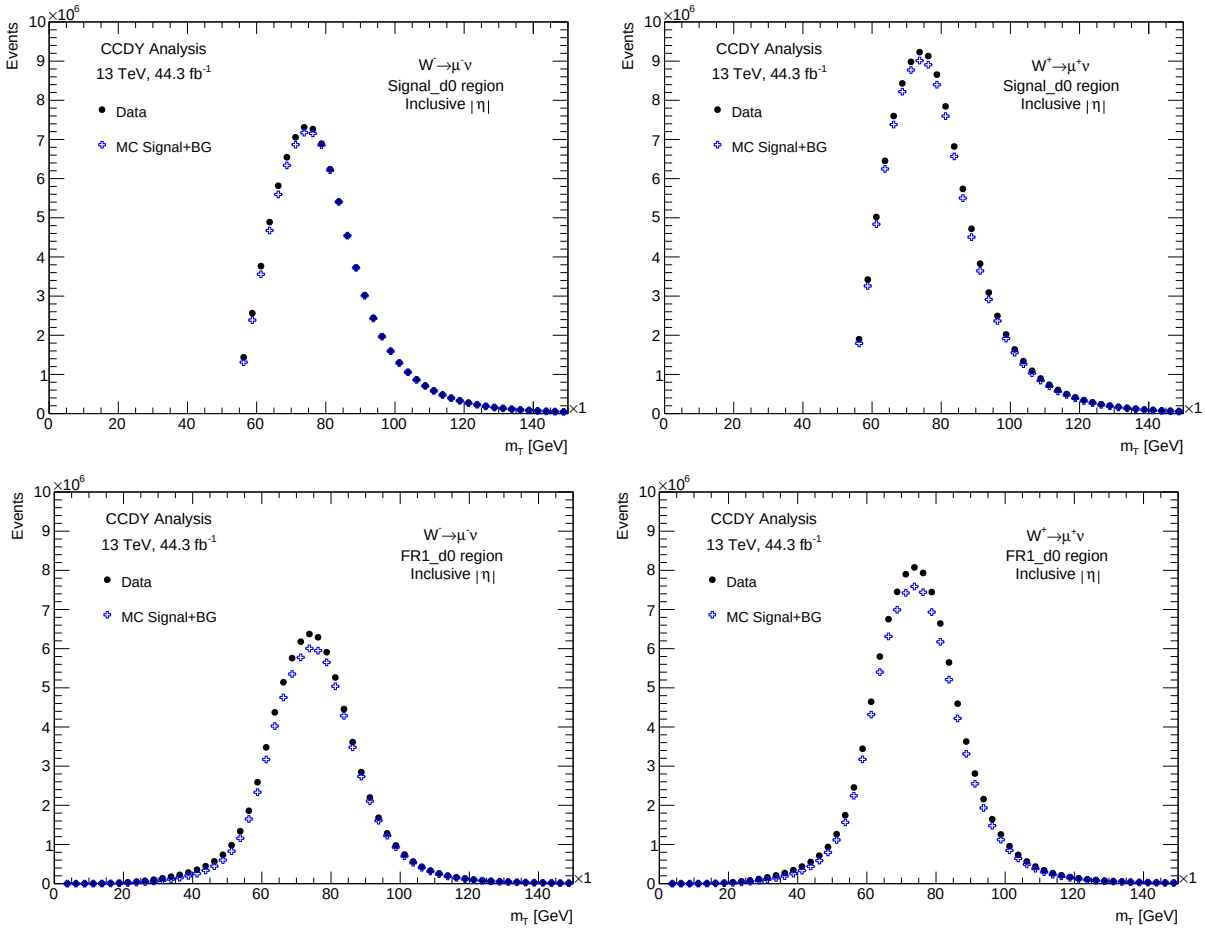

Figure 8.5: Multijet normalisation plots. Transverse mass distributions in a region where the full W boson selection is applied considering the d_0 significance applied (top) and dropping the missing energy and transverse mass cuts (bottom) for both data and MC. *Left-hand* plots are for the negative channel and *right-hand* plots are for the positive channel.

found for every muon pseudorapidity bin, the results of this are found in the Appendix A.

8.4 Multijet results

Computed yields of the multijet determination for every muon pseudorapidity bin utilising Equation (8.2) are presented in Table 8.2 and Table 8.3. In these tables, the T value found in the first column is the average value of the T calculation with Equation (8.1) using the transverse mass and transverse missing energy distributions. For reference, the data and Monte Carlo simulation number of events are also included in the tables through the third and fourth columns. The amount of multijet events in each $|\eta^{\mu}|$ bin, calculated with equation Equation (8.2), is presented in the fifth column. The last column in the tables contains a

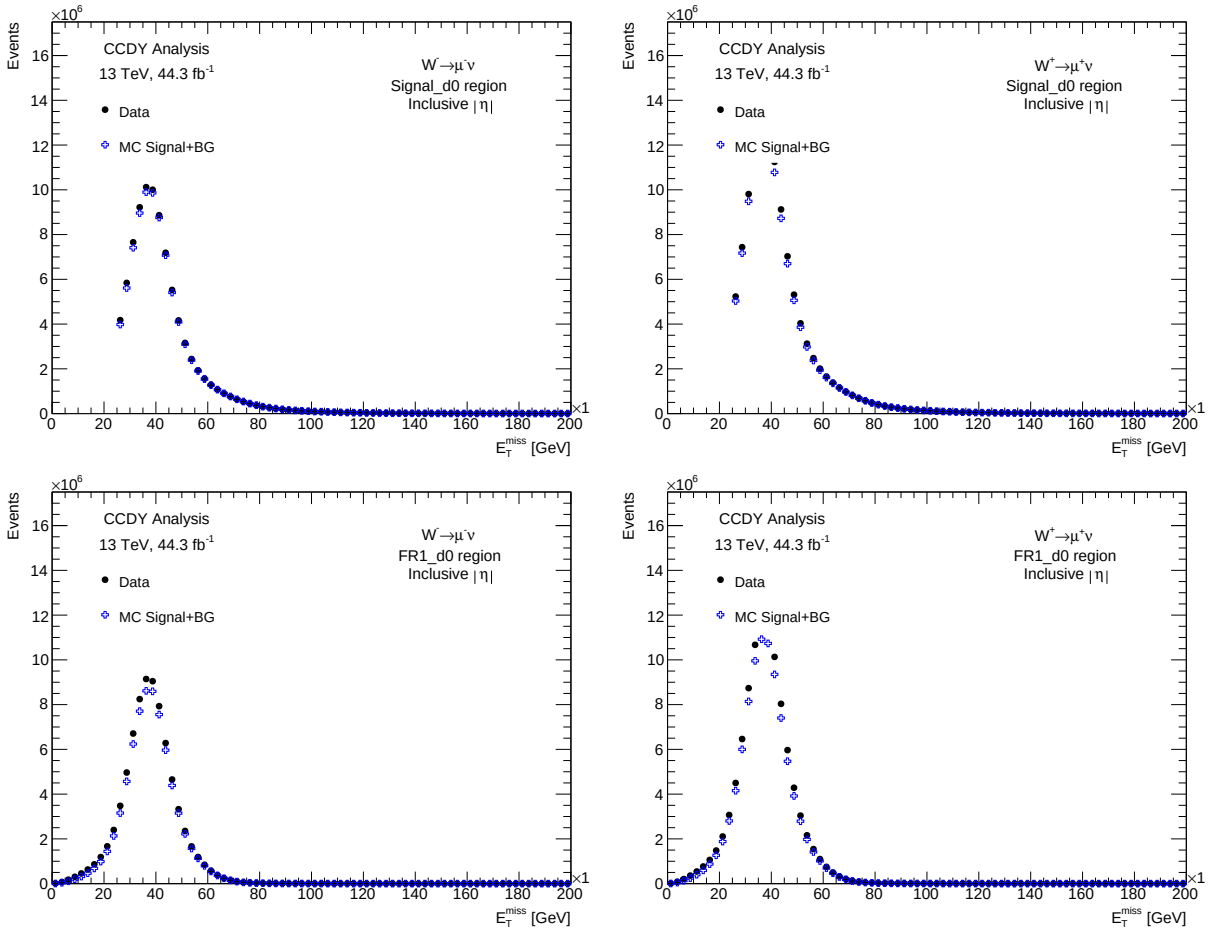

Figure 8.6: Multijet normalisation plots. Transverse missing energy distributions in a region where the full W boson selection is applied and the d_0 significance applied (top) and dropping the missing energy and transverse mass cuts (bottom) for both data and MC. *Left-hand* plots are for the negative channel and *right-hand* plots are for the positive channel.

percentage comparison ($N_{Multijet}/N_{Data}$) of the number of multijet events against the number of data events, these values exhibit the impact that the multijet background has on the total number of recorded events; it is found that the multijet contribution is close to 1% in both inclusively and in $|\eta^{\mu}|$ bins. Despite the fact that the amount of 2017 data is large, the highest $|\eta^{\mu}|$, in the multijet enriched phase space, suffers from poor statistics; in this case the multijet methodology described in this chapter fails, in which case and given that the multijet contribution in these bins is very small, the multijet background contribution is set to be zero, see Figure 8.2; furthermore, a conservative uncertainty of 200% is assigned to these low statistics muon pseudorapidity bins.

Table 8.4 gives the comparison between the positive and negative charged Drell-Yan multijet events, defined by $\Delta_{Multijet} = (N_{Multijet}(W^+) - N_{Multijet}(W^-))/N_{Multijet}(W^+)$.

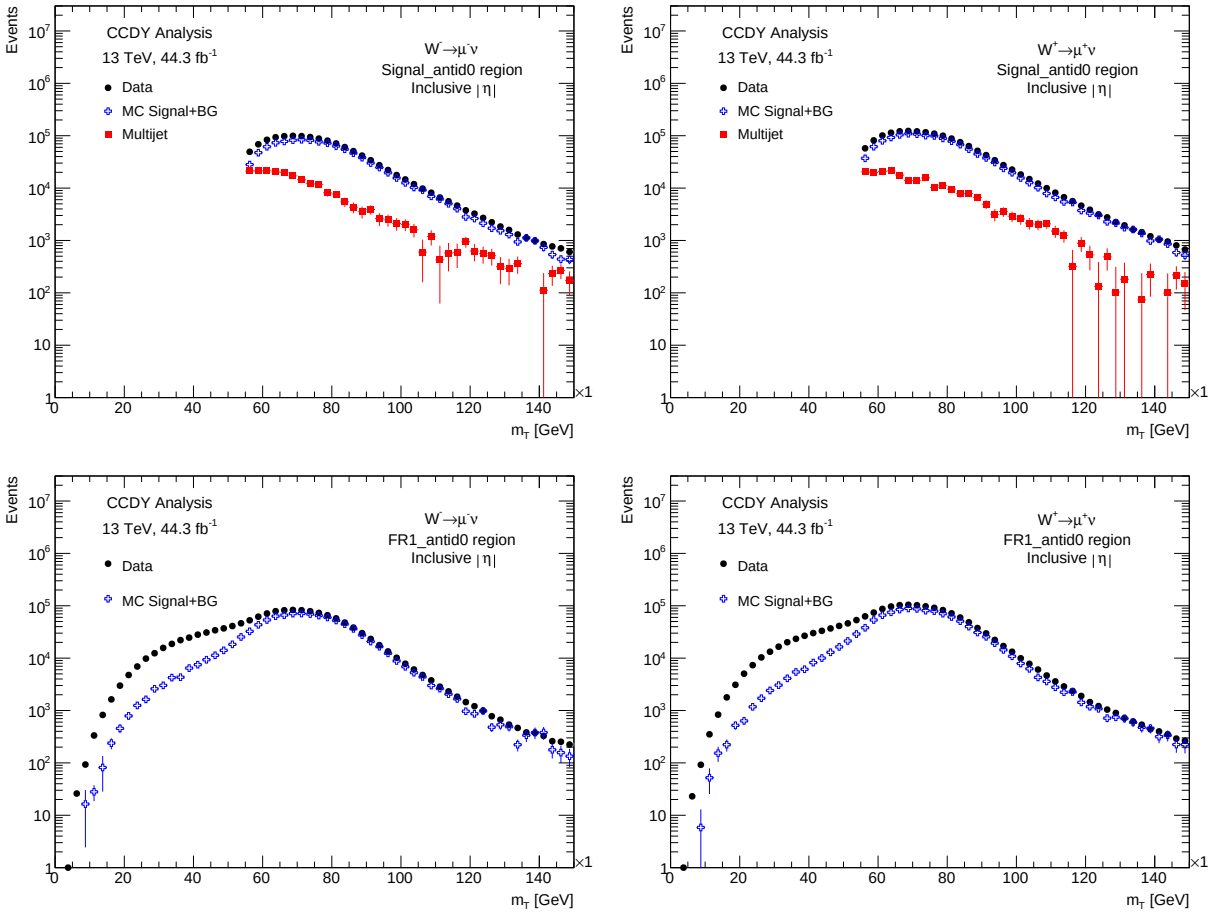

Figure 8.7: Multijet normalisation plots. Transverse mass distributions; top plots correspond to the region where the full W boson selection is applied considering the d_0 significance inverted, bottom plots correspond to the fit region and the d_0 significance inverted for both data and MC. *Left-hand* plots are for the negative channel and *right-hand* plots are for the positive channel.

Analysing the latter definition in the values from Table 8.4, a positive value indicates that the number of events in the $W^+ \to \mu^+\nu$ channel is larger and a negative value indicates that the number of events in the $W^- \to \mu^-\nu$ channel is larger. $\Delta_{Multijet}$ is given in percentage. A comparison with the previous result of the charge asymmetry measurement was done, and it is concluded that the results of this thesis are consistent with them [65].

In Chapter 10 the control distributions, including the multijet background are presented, it is found that prediction is describing good the data.

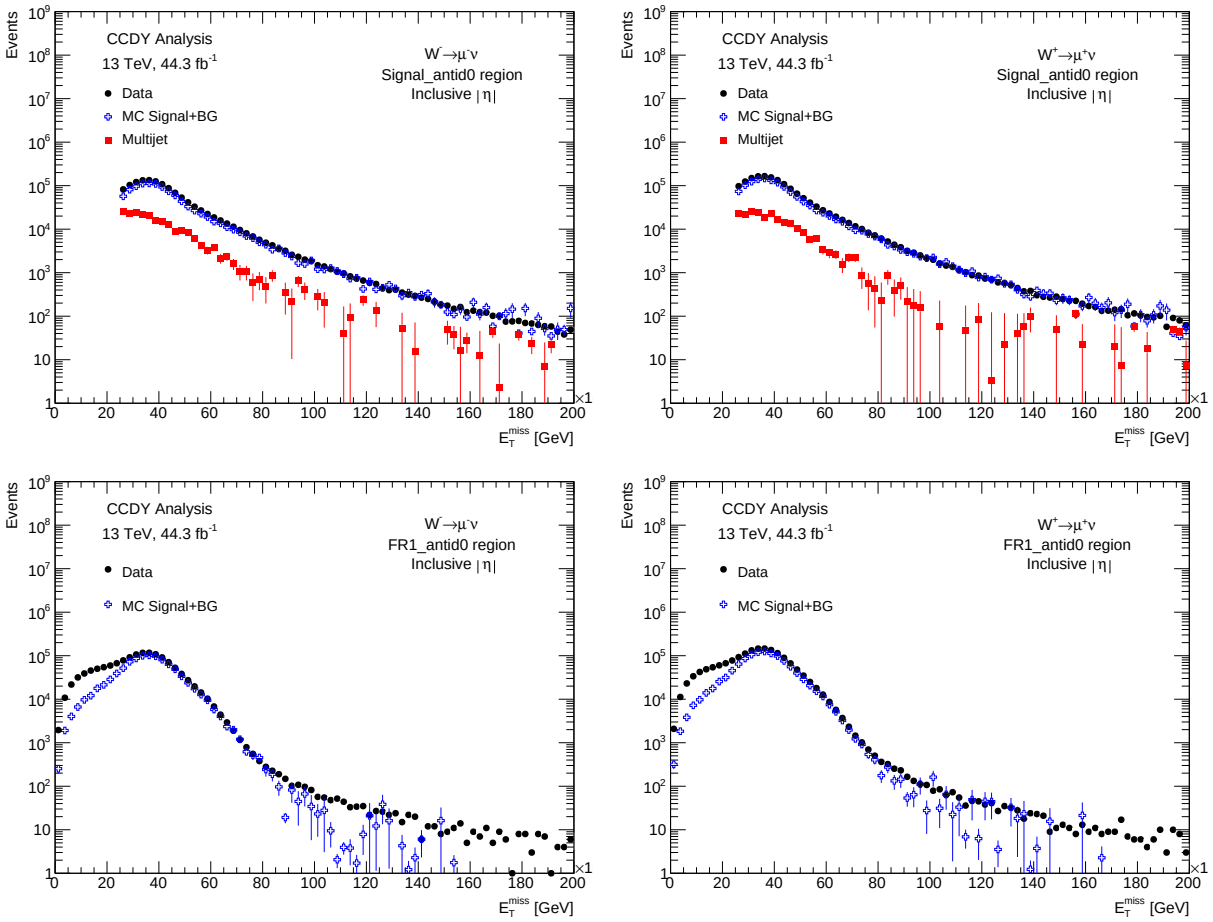

Figure 8.8: Multijet normalisation plots. Transverse missing energy distributions; top plots correspond to the region where the full W boson selection is applied and the d_0 significance inverted, bottom plots correspond to the fit region considering the d_0 significance inverted for both data and MC. *Left-hand* plots are for the negative channel and *right-hand* plots are for the positive channel.

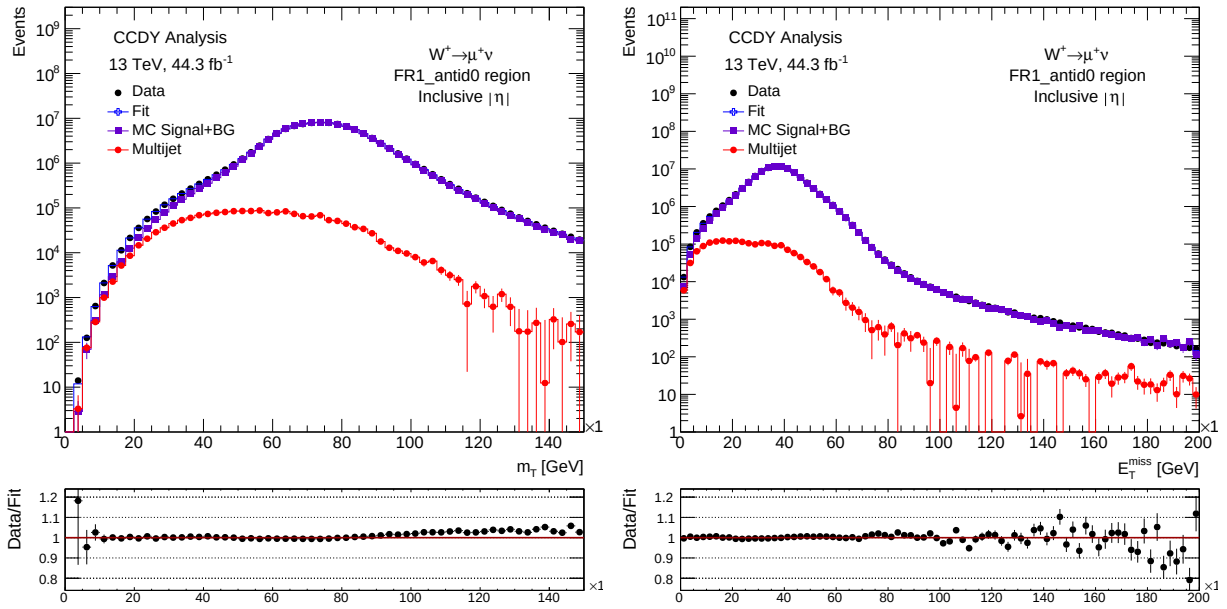

Figure 8.9: Multijet normalisation plots. Transverse mass (left) and missing energy (right) distributions; these plots show the result of the fit and compares the result with data; moreover, the multijet and the simulation backgrounds are displayed.

Eta bin	T	N_{Data}	N_{MC}	$N_{Multijet}$	$N_{Multijet}/N_{Data}$
Inclusive $\lvert\eta^{\mu}\rvert$	4.17	$9.02 \cdot 10^7$	$8.50 \cdot 10^7$	891 460	0.99
$0.0 \leq \lvert\eta^{\mu}\rvert < 0.21$	3.96	$5.86 \cdot 10^6$	$5.40 \cdot 10^6$	80 975.90	1.38
$0.21 \leq \lvert\eta^{\mu}\rvert < 0.42$	3.80	$7.54 \cdot 10^6$	$7.12 \cdot 10^6$	98 846.80	1.31
$0.42 \leq \lvert\eta^{\mu}\rvert < 0.63$	3.94	$8.19 \cdot 10^6$	$7.61 \cdot 10^6$	97 836.20	1.19
$0.63 \leq \lvert\eta^{\mu}\rvert < 0.84$	3.39	$6.43 \cdot 10^6$	$6.17 \cdot 10^6$	76 976.30	1.20
$0.84 \leq \lvert\eta^{\mu}\rvert < 1.05$	3.69	$6.61 \cdot 10^6$	$6.12 \cdot 10^6$	89 701.20	1.36
$1.05 \leq \lvert\eta^{\mu}\rvert < 1.37$	4.09	$1.37 \cdot 10^7$	$1.28 \cdot 10^7$	174 308	1.28
$1.37 \leq \lvert\eta^{\mu}\rvert < 1.52$	4.43	$6.43 \cdot 10^6$	$6.07 \cdot 10^6$	73 039.60	1.14
$1.52 \leq \lvert\eta^{\mu}\rvert < 1.74$	4.68	$9.15 \cdot 10^6$	$8.75 \cdot 10^6$	93 213.60	1.02
$1.74 \leq \lvert\eta^{\mu}\rvert < 1.95$	4.25	$8.90 \cdot 10^6$	$8.41 \cdot 10^6$	44 129.50	0.50
$1.95 \leq \lvert\eta^{\mu}\rvert < 2.18$	4.39	$9.09 \cdot 10^6$	$8.61 \cdot 10^6$	21 398.10	0.24
$2.18 \leq \lvert\eta^{\mu}\rvert < 2.40$	3.87	$8.31 \cdot 10^6$	$7.93 \cdot 10^6$	5282.25	0.06

Table 8.2: This table displays the results of the multijet calculation in each muon pseudorapidity bin for the $W^- \to \mu^- \nu$ selection. The first column indicates the muon pseudorapidity bin. The second column contains the T values corresponding to the multijet normalisation. The third, fourth, and fifth columns are the number of events found in each bin for data, Monte Carlo simulation, and multijet respectively. The last column is the multijet fraction of events w.r.t. the data number of events, given in percentage.

Eta bin	T	N_{Data}	N_{MC}	$N_{Multijet}$	$N_{Multijet}/N_{Data}$
Inclusive $\|\eta^{\mu}\|$	3.34	$1.15 \cdot 10^8$	$1.07 \cdot 10^8$	764 085	0.66
$0.0 \leq \|\eta^{\mu}\| < 0.21$	3.57	$6.74 \cdot 10^6$	$6.14 \cdot 10^6$	72 598	1.08
$0.21 \leq \|\eta^{\mu}\| < 0.42$	3.50	$8.74 \cdot 10^6$	$8.16 \cdot 10^6$	79 301.50	0.91
$0.42 \leq \|\eta^{\mu}\| < 0.63$	3.32	$9.64 \cdot 10^6$	$8.78 \cdot 10^6$	94 136.60	0.98
$0.63 \leq \|\eta^{\mu}\| < 0.84$	3.18	$7.61 \cdot 10^6$	$7.20 \cdot 10^6$	71 470.80	0.94
$0.84 \leq \|\eta^{\mu}\| < 1.05$	3.21	$7.99 \cdot 10^6$	$7.25 \cdot 10^6$	86 829.40	1.09
$1.05 \leq \|\eta^{\mu}\| < 1.37$	3.16	$1.70 \cdot 10^7$	$1.57 \cdot 10^7$	159 952	0.94
$1.37 \leq \|\eta^{\mu}\| < 1.52$	3.21	$8.30 \cdot 10^6$	$7.62 \cdot 10^6$	69 689.60	0.84
$1.52 \leq \|\eta^{\mu}\| < 1.74$	3.41	$1.22 \cdot 10^7$	$1.13 \cdot 10^7$	75 554.90	0.62
$1.74 \leq \|\eta^{\mu}\| < 1.95$	3.25	$1.21 \cdot 10^7$	$1.12 \cdot 10^7$	42 761.20	0.35
$1.95 \leq \|\eta^{\mu}\| < 2.18$	3.27	$1.27 \cdot 10^7$	$1.19 \cdot 10^7$	3819.34	0.03
$2.18 \leq \|\eta^{\mu}\| < 2.40$	3.54	$1.20 \cdot 10^7$	$1.14 \cdot 10^7$	0	0

Table 8.3: This table displays the results of the multijet calculation in each muon pseudorapidity bin for the $W^+ \to \mu^+\nu$ selection. The first column indicates the muon pseudorapidity bin. The second column contains the T values corresponding to the multijet normalisation. The third, fourth, and fifth columns are the number of events found in each bin for data, Monte Carlo simulation, and multijet respectively. The last column is the multijet fraction of events w.r.t. the data number of events, given in percentage.

Eta bin	$N_{Multijet}(W^-)$	$N_{Multijet}(W^+)$	$\Delta_{Multijet}$
Inclusive $\|\eta^{\mu}\|$	891 460	764 085	+14.29
$0.0 \leq \|\eta^{\mu}\| < 0.21$	80 975.90	72 598	+10.35
$0.21 \leq \|\eta^{\mu}\| < 0.42$	98 846.80	79 301.50	+19.77
$0.42 \leq \|\eta^{\mu}\| < 0.63$	97 836.20	94 136.60	+3.78
$0.63 \leq \|\eta^{\mu}\| < 0.84$	76 976.30	71 470.80	+7.15
$0.84 \leq \|\eta^{\mu}\| < 1.05$	89 701.20	86 829.40	+3.20
$1.05 \leq \|\eta^{\mu}\| < 1.37$	174 308	159 952	+8.24
$1.37 \leq \|\eta^{\mu}\| < 1.52$	73 039.60	69 689.60	+4.59
$1.52 \leq \|\eta^{\mu}\| < 1.74$	93 213.60	75 554.90	+18.94
$1.74 \leq \|\eta^{\mu}\| < 1.95$	44 129.50	42 761.20	+3.10
$1.95 \leq \|\eta^{\mu}\| < 2.18$	21 398.10	3819.34	+82.15
$2.18 \leq \|\eta^{\mu}\| < 2.40$	5282.25	0	+100

Table 8.4: This table compares the yields, in both positive and negative W boson selection channels, coming from the multijet calculation. The first column indicates the muon pseudorapidity bin; the second and third columns correspond to the multijet events coming from the $W^- \to \mu^-\nu$ and $W^- \to \mu^-\nu$ selections, respectively; the fourth column is the percentage difference between the positive channel w.r.t. the negative channel multijet events, defined as $\Delta_{Multijet} = (N_{Multijet}(W^+) - N_{Multijet}(W^-))/N_{Multijet}(W^+)$.

Chapter 9

Systematic uncertainties

Precision measurements heavily rely on how the uncertainties affect the final results, therefore it is vital to understand and study each source of uncertainty and how it propagates through the analysis. This chapter summarises the source of both experimental and theoretical uncertainties.

9.1 Systematic uncertainty definition

The uncertainties affect the cross section and asymmetry results through the shape of the distributions and the normalisation itself. This analysis considers *up* and *down* variations with respect to the *nominal* event yields, which correspond to shift these yields up and down by one standard deviation for a given uncertainty. Various expressions are used in different cases:

- To obtain the uncertainty of a single bin,

$$\delta^i = \frac{N^i_{nom} - N^i_{sys}}{N^i_{nom}} \tag{9.1}$$

  is used, where δ^i is the uncertainty in the ith bin, N^i_{nom} is the number of entries in the ith bin when there is no systematic variation applied (nominal) and N^i_{sys} is the number of entries in the bin i when a systematic variation is applied. δ^i helps to study the effect of each individual systematic bin-by-bin on the cross section and charge asymmetry; a positive sign is designated to the up variations and a negative sign to the down variations.

- A similar quantity to Equation (9.1) is the total contribution of each systematic,

$$\delta = \frac{N_{nom} - N_{sys}}{N_{nom}}. \tag{9.2}$$

- For every bin, the total uncertainty when the full set of uncertainties is taken into account, reads as,

$$\delta^{i,total} = \sqrt{\frac{(N^i_{nom} - N^i_{sys_1})^2}{(N^2_{nom})^2} + ... + \frac{(N^i_{nom} - N_{sys_n})^2}{N^2_{nom}}}. \tag{9.3}$$

- The total uncertainty, considering all the bins and uncertainties, is computed with

$$\delta^{total} = \sqrt{\frac{(N_{nom} - N_{sys_1})^2}{N^2_{nom}} + ... + \frac{(N_{nom} - N_{sys_n})^2}{N^2_{nom}}}, \tag{9.4}$$

  where δ^{total} is the total uncertainty, N_{nom} is the total number of events, and N_{sys} is the total number of events when a given systematic variation has been applied; the sum runs over all the systematics considered. δ^{total} is used for the total cross section and charge asymmetry.

The number of charged current Drell-Yan events, after passing the selection criteria, depends on each of these cuts. For example the kinematic cuts, *e.g.* p^{μ}_T, η^{μ}, E^{miss}_T, represent a source of uncertainty on the number of events, since the experimental determination of their values is affected by a number of systematic uncertainties. This is because, when considering fixed cuts, the fluctuation of the kinematic variables values could change the final number of events when applying a specific selection criterion. Counting the number of events is a linear function, therefore the error propagation could be expressed as in Equations 9.3 and 9.4 for the case when it is assumed that uncertainties of every kinematic variable are uncorrelated and independent of each other. This approximation yields a vanishingly small covariance between variables, hence the correlation between the different errors is small.

The above mentioned approximation is reasonable in light of the independent approaches used when determining the different kinematic variables and muon identification; for example, it is expected that the muon transverse momentum should be independent from the event missing energy calculation. A more detailed treatment needs to be considered to address the correlation between the transverse mass (Equation (7.3)) and the missing energy and the muon kinematics, as the transverse mass is a function of these. Nevertheless, the approach used in this thesis is *conservative* since taking into account the correlations would

reduce the total errors.

In the next sections, a simple definition, for display reasons, is used to express the systematic variations in such a way that the values are *symmetric*[1] with respect to the up and down variations:

$$\delta^{sim} = \frac{|\delta^{up}| + |\delta^{down}|}{2}, \tag{9.5}$$

a positive and negative signs are assigned to the symmetrised down and up variations, respectively, and thus only up variations are shown in the following plots.

Moreover, the systematics are displayed in the control distributions found in Chapter 10, to reflect the impact that the variation of the physics objects has, when a systematic uncertainty is evaluated on the number of expected signal and background events.

9.2 Experimental uncertainties

The experimental uncertainties originate due to the fact that it is not possible to have a perfect modelling of the ATLAS detector and the corrections to mitigate the latter, implicate statistical and systematic uncertainties. It is important to note that the values of the systematic variations were calculated utilising the binning defined in Equation (11.3), the cross section and charge asymmetry final binning. This section covers a brief description of the relevant uncertainties for the charged Drell-Yan measurement.

9.2.1 Muon efficiency scale factors

The muon efficiency scale factor systematic variations are displayed in Figure 9.1. An uncertainty coming from the muon identification is considered; additionally, selection efficiency variations from the isolation, trigger and TTVA selection criteria are studied. The present uncertainties are provided by the MCP group; nevertheless, the author of this document extracted the uncertainties appropriated for the charged Drell-Yan selection criteria. A summary of the source of these uncertainties is presented in the following.

[1] This definition is used to evaluate qualitatively the effect of the each systematic and to ease their visualisation in Figures 9.1,9.2,9.3,9.4; nevertheless the results presented in Table 9.6 are *asymmetric* where the up and down values are not averaged.

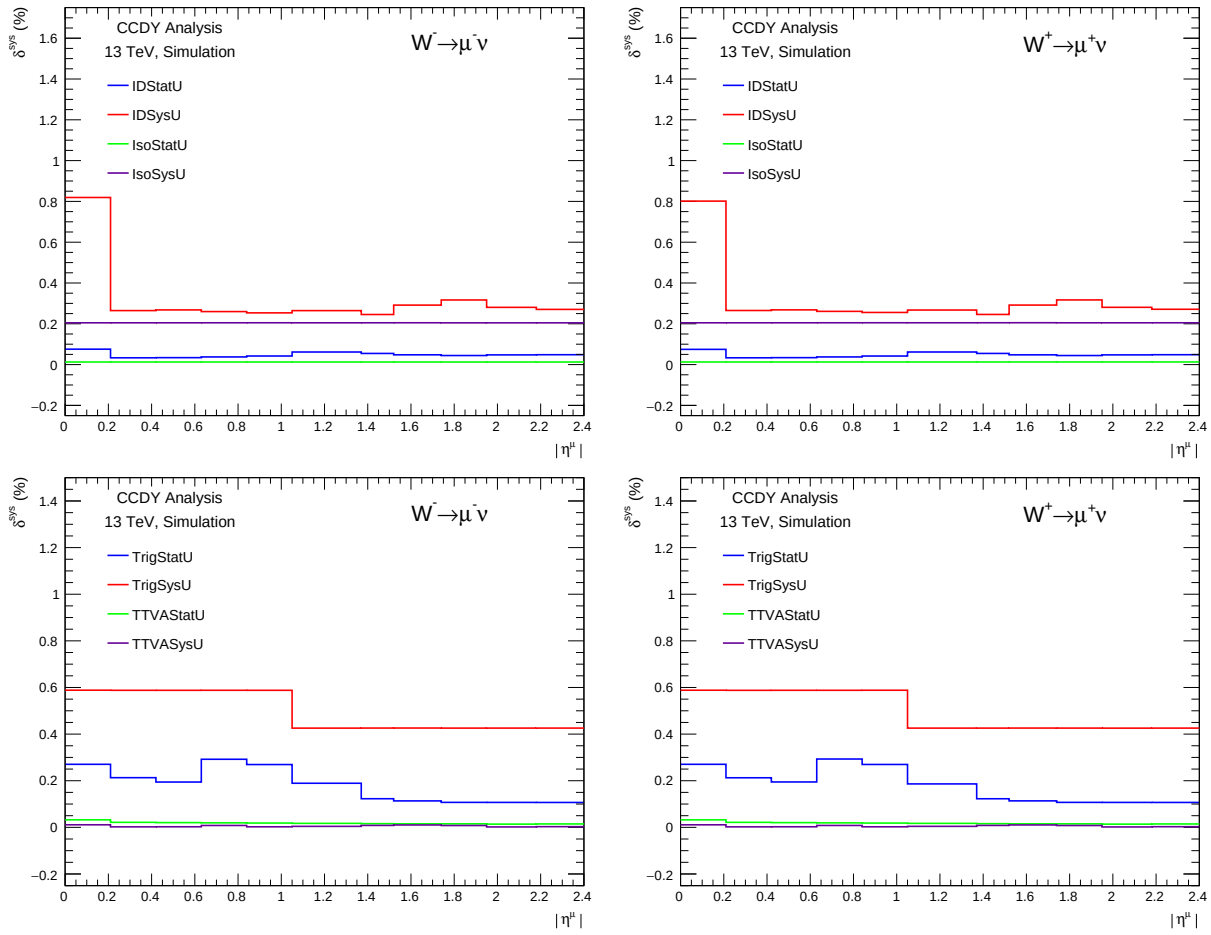

Figure 9.1: These plots show the individual contributions of the systematic variations to the number of events, expressed in Equations (9.1) and (9.5), given differentially in $|\eta^{\mu}|$ bins. *Top plots* display the effect of the event by event muon isolation and identification efficiency scale factor variations. *Bottom plots* display the effect of the event by event muon trigger and TTVA selection efficiency scale factor variations. The plots on the left correspond to the W^- selection whereas the plots on the right correspond to the W^+ selection. All the values are presented in percentage.

Muon identification scale factor uncertainties

- Given that the $Z \to \mu\mu$ and $J/\Psi \to \mu\mu$ data and simulated samples used to calculate the identification scale factors are finite, there is a statistical uncertainty associated with them.
- An uncertainty in the background subtraction is assessed.
- In the tag and probe method, a definite cone size is used; a variation arising from this choice is obtained varying the cone by ± 50 %.

- Reconstruction level tag and probe method was used. A comparison with a truth level tag and probe baseline method was performed. The agreement is found to be better than 0.1%.
- For muons of $p_T > 200$ GeV, a simulated 2-3% uncertainty is added to account for an upper limit on the identification efficiency scale factor variation for large muon momenta extracted from simulation.

Muon isolation scale factor uncertainties

- The statistical contribution to the systematics is considered.
- The backgrounds are varied within their uncertainties.
- Another source of systematic is obtained by changing the selection criteria in the tag and probe method.
- An uncertainty appears due to the fact that the η dependence of the isolation scale factors has been neglected.

Muon trigger scale factor uncertainties

- The statistical contribution to the systematics is considered.
- The systematics coming from the background are calculated by changing the nominal tag and probe selections.
- Systematic uncertainties related with the event topology and the p_T dependence are included.

Muon TTVA scale factor uncertainties

- The statistical contribution to the systematics is considered.
- The backgrounds are varied within their uncertainties and changing the selections of the tag and probe method.

The total uncertainty is the sum in quadrature of the individual contributions in every scale factor. For the isolation scale factor, the low p_T region it is found to be at permile level whilst at high p_T is at percentage level.

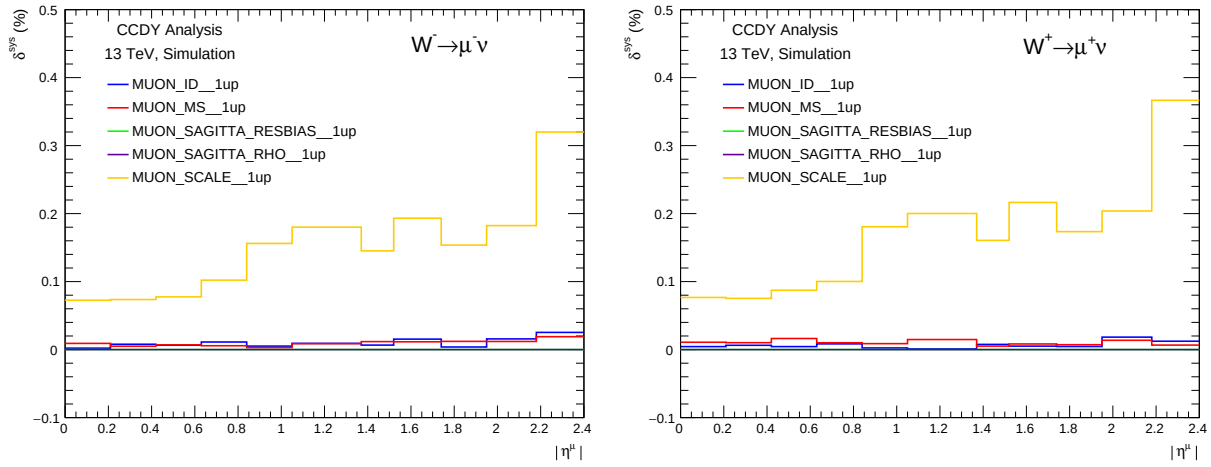

Figure 9.2: These plots show the individual contributions of the systematic variations to the number of events, expressed in Equations (9.1) and (9.5), given differentially in $|\eta^{\mu}|$ bins. Here it is displayed the effect of the muon scale and resolution, and muon sagitta correction uncertainties. The plots on the left correspond to the W^- selection whereas the plots on the left correspond to the W^+ selection. All the values are presented in percentage.

From Figure 9.1 it is seen that the dependence on $|\eta^{\mu}|$ and the contributions of these uncertainties are small (below half percent); however, in the first $|\eta^{\mu}|$ bins, for the identification scale factor efficiency, a large uncertainty value is present, the reason is that in this area of the detector the muon identification is more difficult to perform, see Figure 6.3. A similar behaviour can be seen in both the negative and positive charged Drell-Yan selections.

9.2.2 Muon momentum scale and resolution

- The muon momentum calibration was done using data and MC samples of $Z \to \mu\mu$ and $J/\Psi \to \mu\mu$ decays. The corresponding statistical error is added to the systematics.
- A source of resolution correction uncertainty arises from the alignment of the MS chambers.
- The choice of an arbitrary invariant mass window uncertainty is calculated by varying this quantity by ± 5 GeV.
- Scale uncertainties come from the fact that non-linear effects may appear when fitting the ID correction separately in the $Z \to \mu\mu$ and $J/\Psi \to \mu\mu$ samples.

Figure 9.2 shows the systematic variations that correspond to the muon calibration. The muon scale uncertainty shows a sizeable $|\eta^{\mu}|$ dependence, this is due to the fact that

the calibrations are $|\eta^{\mu}|$ dependent, since the amount of detector material traversed by the particle is different in each $|\eta^{\mu}|$ bin. The latter indicates that the more material the muon traverses the more difficult and inaccurate is the associated scale correction. The contributions coming from the muon calibration to the total uncertainty are below to 1%. A similar behaviour is observed for both the negative and positive charged Drell-Yan selections.

9.2.3 Muon Sagitta

The muon sagitta correction uncertainties are small. The source of uncertainties for the resolution of the muon momentum and the determination of the correction itself, are calculated when comparing the magnitude of the corrections for the negative and positive channels at detector level. Figure 9.2 shows the systematic variations that correspond to the muon sagitta bias corrections. These uncertainties do not depend on $|\eta^{\mu}|$ and their values are extremely small, most bins are comparable in size with the muon momentum scale and resolution uncertainties. A similar behaviour is present for both the negative and positive charged Drell-Yan selections.

9.2.4 Pileup reweighting

The pileup reweighting implements an additional *data scale factor* to further improve the agreement between data and simulation of the pileup distributions (see Section 6.5), that corresponds to the numerical value of 1/1.03; this correction aims to include the mismodelling originated by inelastic activity and to match the number of primary vertices as a function of average number of pileup interactions. The data scale factor is varied up and down by one standard deviation; these variations are taken as the systematic uncertainty of the pileup reweighting.

Figure 9.3 shows the systematic variations that correspond to the pileup reweighting. The $|\eta^{\mu}|$ dependence of the pileup contribution to the uncertainty is negligible. The contribution of the pileup reweighting is around 0.5% in every $|\eta^{\mu}|$ bin. A similar behaviour is present for both the negative and positive charged Drell-Yan selections.

9.2.5 Missing energy

The missing energy vector is constituted by leptons, photons and jets, therefore the uncertainties coming from these objects are propagated to the missing energy vector calculation. Another contribution to the E_T^{miss} variation arises by the reconstruction of the soft term: the track soft term uncertainties are calculated by comparing the data and Monte Carlo

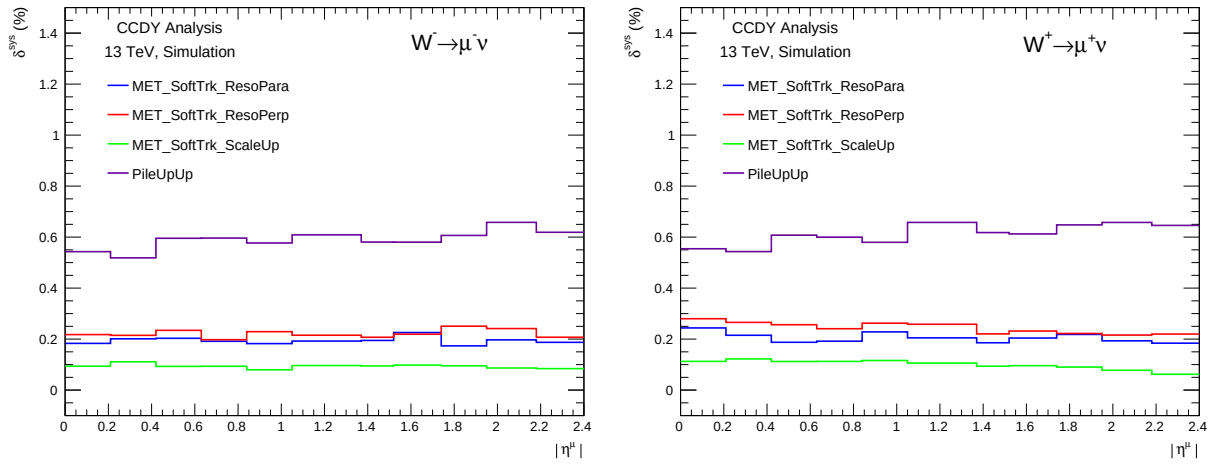

Figure 9.3: These plots show the individual contributions of the systematic variations to the number of events, expressed in Equations (9.1) and (9.5), given differentially in $|\eta^{\mu}|$ bins. The effect of the event by event pileup reweight variations is displayed. The plots on the left correspond to the W^- selection whereas the plots on the right correspond to the W^+ selection. All the values are presented in percentage. The labels contained in the legend of both plots use the conventional names given by the JetEtMiss group: "MET" stands for missing energy; "SofTrk" makes reference to the fact that E_T^{miss} is calculated with the TST methodology described in Section 6.4; "ResoPara" and "ResoPerp" refer to the resolution uncertainty on the parallel and perpendicular component, respectively.

simulation using the balance of the soft term and the hard objects. Additionally, the underlying event uncertainties are also included in the total missing energy uncertainty. Figure 9.3 show the missing energy uncertainties; the $|\eta^{\mu}|$ dependence is small, although not negligible being consistent with the uncertainties of the missing energy constituents; the value of these uncertainties is as large as 0.25%. A similar behaviour is observed for both the negative and positive charged Drell-Yan selections.

9.2.6 Jets

The first source of systematics that affects the jets is that coming from the scale and resolution of the objects (muons, electrons and photons) that conform the jet; furthermore, there is an uncertainty related with the efficiency of the JVT cut applied to select jets; there is an uncertainty originated by the statistical limitation of the data and MC samples used to perform the calibrations. The jet uncertainties account for assumptions made in the event topology, MC simulations and reconstruction algorithms; uncertainties from pileup are included to add the mismodelling of the number of primary vertices, number of interactions and residual p_T dependences. Monte Carlo corrections generated in η bins also contribute

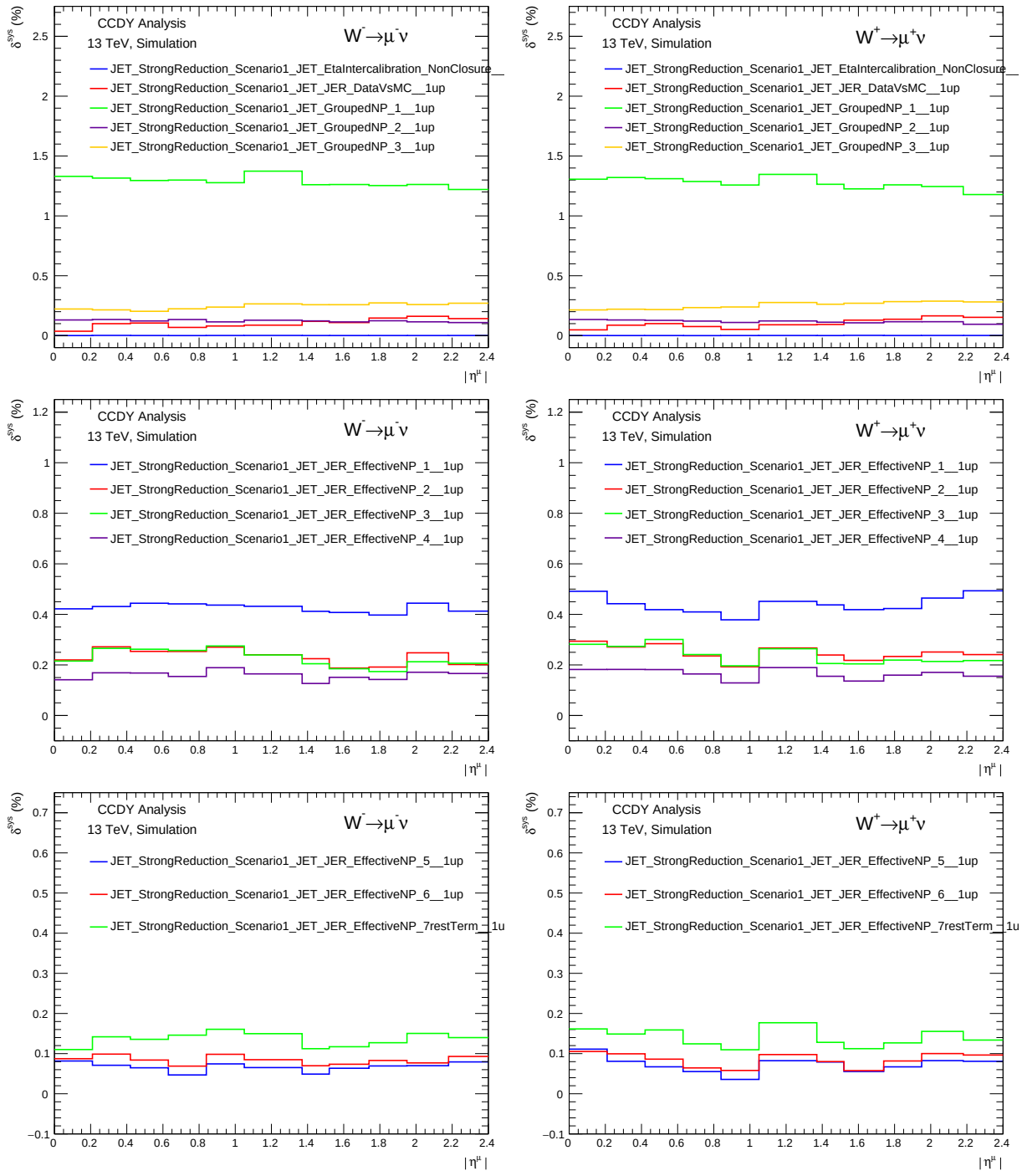

Figure 9.4: These plots show the individual contributions of the systematic variations to the number of events, expressed in Equations (9.1) and (9.5), given differentially in $|\eta^{\mu}|$ bins. The effect of jet uncertainties uncertainties is displayed. The plots on the left correspond to the W^- selection whereas the plots on the right correspond to the W^+ selection. All the values are presented in percentage.

Set name	Down	Up	Average	# of systematics
Strongly reduced scenario 1	0.0118012	0.0131250	0.0124631	4
Strongly reduced scenario 2	0.0116798	0.0119411	0.0118104	4
Strongly reduced scenario 3	0.0117200	0.0118869	0.0118035	4
Strongly reduced scenario 4	0.0116142	0.0124526	0.0120334	4
Category reduced	0.0116797	0.0119411	0.0118104	31
Globally reduced	0.0117200	0.0118869	0.0118035	23
All nuisance parameters	0.0116142	0.0124526	0.0120335	99

Table 9.1: Comparison of the jet systematics sets. This table displays the numerical values of the combined jet systematics effects on the selected number of events. The first column indicates the official set names. The second and third columns correspond to the values for up and down one sigma variation, respectively. The fourth column is the average of the up and down variations. The last column specifies the number of individual systematics contained in each set.

to the uncertainty. A high p_T jet uncertainty is derived from single-particle response and is applied to jets with $p_T > 2$ TeV. Additionally, uncertainties are considered to account for the difference in the jet response and composition of light-quark, b-quark, and gluon-initiated jets. In this analysis the flavour composition uncertainty is negligible.

The jet uncertainties are binned in jet η and p_T and are treated as fully correlated. The uncertainty value is a function of jet p_T, starting at 4.5% for low p_T, decreasing to 1% at 200 GeV (throughout this p_T region the uncertainties are statistically dominated) [66].

The number of jet uncertainties is large, making their processing computationally expensive. The ATLAS JetEtMiss group[2] recommends using sets of systematics that merge various individual systematics in order to reduce the computational resources needed for a given physics analysis; adopting a reduced set of systematics depends on each analysis, in some analyses is not appropriate to make such a choice and the full set must be incorporated. For the charged current Drell-Yan analysis, a reduced set was chosen following a study performed to compare different reduced sets and considering that a complete set of jet uncertainties is not necessary since the final state does not directly contain jets. Making use of Equation (9.4), the effect of each recommended set of jet systematics was calculated and the results of the latter, found in Table 9.1, express the sum in quadrature of the relative change of number of events when each individual variation is applied in comparison to the nominal case. The recommended sets are the strongly reduced scenarios referred to as 1,2,3 and 4, the category reduced, the globally reduced and all the systematic sources. Among these scenarios, it was decided to use the strongly reduced scenario 1 set as it is the one which

[2] https://twiki.cern.ch/twiki/bin/view/AtlasProtected/JetEtMiss

has the most conservative impact on the number of selected events. Table 9.6 shows a full list of the experimental systematics considered in this analysis (in which the jet systematics are included). The official names of the jet systematics are provided by the JetEtMiss group, the variations that each jet systematic takes care of are:

- JET_EtaIntercalibration_NonClosure. A jet correction is applied to take into account biases in the jet η reconstruction caused by the transition between different calorimeter environments and sudden changes in calorimeter granularity; the non-closure of the corrections is covered by this jet uncertainty.

- JET_JER_DataVsMC. The uncertainties coming from the use of different MC generators to study the agreement with data of the several kinematic jet variables.

- JET_GroupedNP_1,2,3. These uncertainties come from pileup, Z/γ+jet and multijet balance *in-situ* calibrations which account for assumptions made in the event topology, MC simulation, and sample statistics. Moreover, these uncertainties account electron, muon, and photon energy scales uncertainties. A combination of the nuisance parameters associated with these systematics is performed. The reduction is performed when components of the systematics are found to be the largest, these are kept and the remaining components are quadratically combined into a single nuisance parameter (NP). The losses on correlation across jet p_T and η are at percent level. The strongly reduced scenario 1 comprising four grouped NPs, considers a general representation with low, medium, and high p_T kinematic regimes [66].

- JET_JER_EffectiveNP_1,2,3,4,5,6,7. These uncertainties cover the same variations as the JET_GroupedNP_1,2,3 systematics; nevertheless, the manner in which the reduction of nuisance parameters is implemented is slightly different, considering an effective average of NPs.

Figure 9.4 shows the systematic variations that correspond to the jet objects. The $|\eta^{\mu}|$ dependence is small, nevertheless not negligible in accordance with the uncertainties of their constituents. The jet uncertainties are the largest of this analysis, the main component is the Scenario 1 JET_GroupedNP_1, being close to 1.5% in every muon pseudorapidity bin. A similar behaviour is noticed for both the negative and positive charged Drell-Yan selections.

9.2.7 Luminosity

The uncertainty in the 2017 integrated luminosity is 2.4%. It is derived following a methodology similar to that detailed in [67], and using the LUCID-2 detector for the baseline luminosity measurements [68], from calibration of the luminosity scale using x-y beam-separation

scans. The LUCID-2 detector consists of several Cherenkov detectors for luminosity measurements and monitoring, it uses thin quartz windows of photomultipliers as Cherenkov medium and employs radioactive sources deposited to these windows, arming the detector with the demanded stability; since more than one interaction take place when the bunches of particles cross each other at the LHC, the luminosity measurement translates into measure the average number of interactions; the LUCID-2 detectors surround the beam pipe on both sides of the interaction point [69].

9.3 Multijet estimation uncertainties

There are several sources of uncertainties that affect the calculated number of events coming from the multijet background. To handle the low statistics $|\eta^{\mu}|$ bins, a conservative uncertainty of 200% is assigned[3].

- Chapter 8 discusses the discriminant criteria between multijet background and signal processes; it was established the d_0 significance as this discriminant variable. To correctly select multijet events, it was necessary to reweight the MC simulation to improve the accuracy of the d_0 significance MC description seen in data; the reweighting itself is at some extent arbitrary, in the sense that the range of the fitting functions, and the value at which the weight starts to be a constant, are established under the assumption that in this fitting region the multijet effect is small; consequently, a systematic uncertainty is associated to the d_0 significance reweighting procedure, varying the Gaussian functions fitting ranges by $\pm 0.5\sigma$, furthermore, the value where the reweighting functions starts to be a constant is accommodated by the same length. Table 9.2 and Table 9.3 show the results of performing these variations; the last two columns display the up and down variations computed with Equation (9.2). The uncertainty in the inclusive pseudorapidity bin is around 30%, and differentially in each bin ranges between 12-50% in the high statistics bins. These values may appear large, nevertheless it is important to note that the effect on the final cross sections and charge asymmetry measurements is small, since the contribution of the multijet background in the signal region is close to 1%. A discussion of the propagation of the uncertainty is given in Chapter 11.

- The statistical uncertainty of the fraction fit calculation, is determined via a maximum

[3] Assigning a 200% uncertainty appears to be an overestimate; nevertheless, the pseudorapidity bins where this is assigned are almost free of multijet of background events, furthermore the percentage of total multijet events w.r.t. to data is below 1%; consequently, a large error in almost not multijet populated bins results in a small overall error in these bins.

Eta bin	$N^{nominal}_{Multijet}$	$N^{up}_{Multijet}$	$N^{down}_{Multijet}$	$\delta^{up}(\%)$	$\delta^{down}(\%)$
Inclusive $\lvert\eta^{\mu}\rvert$	891 460	629 628	$1.11 \cdot 10^6$	29.37	25.07
$0.0 \leq \lvert\eta^{\mu}\rvert < 0.21$	80 975.90	65 509.90	94 467.30	19.10	16.66
$0.21 \leq \lvert\eta^{\mu}\rvert < 0.42$	98 846.80	80 470.60	116 889	18.59	18.25
$0.42 \leq \lvert\eta^{\mu}\rvert < 0.63$	97 836.20	74 790	117 072	23.56	19.66
$0.63 \leq \lvert\eta^{\mu}\rvert < 0.84$	76 976.30	65 915	93 233.60	14.37	21.12
$0.84 \leq \lvert\eta^{\mu}\rvert < 1.05$	89 701.20	73 022.30	103 791	18.59	15.71
$1.05 \leq \lvert\eta^{\mu}\rvert < 1.37$	174 308	139 614	206 425	19.90	18.43
$1.37 \leq \lvert\eta^{\mu}\rvert < 1.52$	73 039.60	51 127.30	89 863.90	30.00	23.03
$1.52 \leq \lvert\eta^{\mu}\rvert < 1.74$	93 213.60	58 666.50	117 656	37.06	26.22
$1.74 \leq \lvert\eta^{\mu}\rvert < 1.95$	44 129.50	16 650.80	68 468	62.27	55.15
$1.95 \leq \lvert\eta^{\mu}\rvert < 2.18$	21 398.10	64 194.20	64 194.20	200	200
$2.18 \leq \lvert\eta^{\mu}\rvert < 2.40$	5282.25	15 846.70	15 846.70	200	200

Table 9.2: This table displays the systematics uncertainties arising from the d_0 significance weight variation by ± 0.5 standard deviation in the $W^- \to \mu^- \nu$ selection. The first column contains the muon pseudorapidity bins; the second column is the nominal number of multijet background events; the third and fourth columns are the up and down varied number of multijet events; the fifth and sixth columns show the up and down variation computed with Equation (9.1), in percentage.

likelihood fit, following the derivation presented in [70]. The statistical uncertainty on the determined multijet background fractions is found to be negligible. Note that this statistical uncertainty is independent of the estimated low statistic multijet background $|\eta^{\mu}|$ bins.

- Another source of uncertainty comes from the variation of the Monte Carlo cross sections used to build the pure multijet sample. The MC theoretical cross section uncertainty is close to 5%, accordingly these variations were applied to the simulation when calculating the multijet number of events. The results are found in tables Table 9.4 and Table 9.5. The last two right columns show the up and down variations computed with Equation (9.2). The uncertainty in the inclusive bin is close to 25% and for each pseudorapidity bin between 10-50%. The values propagated to the final measurements are small given that the multijet contribution to the final number of events is close to 1%. A discussion of the propagation of the uncertainty is given in Chapter 11.

Eta bin	$N^{nominal}_{Multijet}$	$N^{up}_{Multijet}$	$N^{down}_{Multijet}$	$\delta^{up}(\%)$	$\delta^{down}(\%)$
Inclusive $\lvert\eta^{\mu}\rvert$	764 085	634 365	$1.12 \cdot 10^6$	16.98	47.10
$0.0 \leq \lvert\eta^{\mu}\rvert < 0.21$	72 598	64 662.20	95 737.10	10.93	31.87
$0.21 \leq \lvert\eta^{\mu}\rvert < 0.42$	79 301.50	69 803.50	110 749	11.98	39.66
$0.42 \leq \lvert\eta^{\mu}\rvert < 0.63$	94 136.60	85 875.70	127 564	8.78	35.51
$0.63 \leq \lvert\eta^{\mu}\rvert < 0.84$	71 470.80	69 176.30	100 429	3.21	40.52
$0.84 \leq \lvert\eta^{\mu}\rvert < 1.05$	86 829.40	81 597.10	111 695	6.03	28.64
$1.05 \leq \lvert\eta^{\mu}\rvert < 1.37$	159 952	145 915	209 605	8.78	31.04
$1.37 \leq \lvert\eta^{\mu}\rvert < 1.52$	69 689.60	62 356.70	93 053.10	10.52	33.53
$1.52 \leq \lvert\eta^{\mu}\rvert < 1.74$	75 554.90	61 789.90	110 934	18.22	46.83
$1.74 \leq \lvert\eta^{\mu}\rvert < 1.95$	42 761.20	27 698	78 503.70	35.23	83.59
$1.95 \leq \lvert\eta^{\mu}\rvert < 2.18$	3819.34	11 458	11 458	200	200
$2.18 \leq \lvert\eta^{\mu}\rvert < 2.40$	0	0	0	200	200

Table 9.3: This table displays the systematics uncertainties arising from the d_0 significance weight variation by ± 0.5 standard deviation in the $W^+ \to \mu^+\nu$ selection. The first column contains the muon pseudorapidity bins; the second column is the nominal number of multijet background events; the third and fourth columns are the up and down varied number of multijet events; the fifth and sixth columns show the up and down variation computed with Equation (9.1), in percentage.

Eta bin	$N^{nominal}_{Multijet}$	$N^{up}_{Multijet}$	$N^{down}_{Multijet}$	$\delta^{up}(\%)$	$\delta^{down}(\%)$
Inclusive $\lvert\eta^{\mu}\rvert$	891 460	679 886	$1.15 \cdot 10^6$	23.73	28.63
$0.0 \leq \lvert\eta^{\mu}\rvert < 0.21$	80 975.90	67 195.70	98 141.90	17.02	21.20
$0.21 \leq \lvert\eta^{\mu}\rvert < 0.42$	98 846.80	84 486.40	123 047	14.53	24.48
$0.42 \leq \lvert\eta^{\mu}\rvert < 0.63$	97 836.20	77 838.30	122 659	20.44	25.37
$0.63 \leq \lvert\eta^{\mu}\rvert < 0.84$	76 976.30	74 207.40	97 629.80	3.60	26.83
$0.84 \leq \lvert\eta^{\mu}\rvert < 1.05$	89 701.20	75 952.60	106 227	15.33	18.42
$1.05 \leq \lvert\eta^{\mu}\rvert < 1.37$	174 308	146 119	214 363	16.17	22.98
$1.37 \leq \lvert\eta^{\mu}\rvert < 1.52$	73 039.60	54 942.70	85 853.10	24.78	17.54
$1.52 \leq \lvert\eta^{\mu}\rvert < 1.74$	93 213.60	63 829.30	106 286	31.52	14.02
$1.74 \leq \lvert\eta^{\mu}\rvert < 1.95$	44 129.50	23 693.40	65 072.70	46.31	47.46
$1.95 \leq \lvert\eta^{\mu}\rvert < 2.18$	21 398.10	64 194.20	64 194.20	200	200
$2.18 \leq \lvert\eta^{\mu}\rvert < 2.40$	5282.25	15 846.70	15 846.70	200	200

Table 9.4: This table displays the systematics uncertainties arising from the Monte Carlo cross section variation of $\pm 0.5\%$ in the $W^- \to \mu^-\nu$ selection. The first column contains the muon pseudorapidity bins; the second column is the nominal number of multijet background events; the third and fourth columns are the up and down varied number of multijet events; the fifth and sixth columns show the up and down variation computed with Equation (9.1), in percentage.

Eta bin	$N^{nominal}_{Multijet}$	$N^{up}_{Multijet}$	$N^{down}_{Multijet}$	$\delta^{up}(\%)$	$\delta^{down}(\%)$
Inclusive $\lvert\eta^{\mu}\rvert$	764 085	668 860	$1.10 \cdot 10^6$	12.46	44.16
$0.0 \leq \lvert\eta^{\mu}\rvert < 0.21$	72 598	66 730.20	94 342.30	8.08	29.95
$0.21 \leq \lvert\eta^{\mu}\rvert < 0.42$	79 301.50	72 090.90	109 039	9.09	37.50
$0.42 \leq \lvert\eta^{\mu}\rvert < 0.63$	94 136.60	88 129.10	125 711	6.38	33.54
$0.63 \leq \lvert\eta^{\mu}\rvert < 0.84$	71 470.80	69 401	101 590	2.90	42.14
$0.84 \leq \lvert\eta^{\mu}\rvert < 1.05$	86 829.40	82 605.20	110 436	4.86	27.19
$1.05 \leq \lvert\eta^{\mu}\rvert < 1.37$	159 952	152 160	206 392	4.87	29.03
$1.37 \leq \lvert\eta^{\mu}\rvert < 1.52$	69 689.60	63 726.30	90 049	8.56	29.21
$1.52 \leq \lvert\eta^{\mu}\rvert < 1.74$	75 554.90	66 428.10	105 857	12.08	40.11
$1.74 \leq \lvert\eta^{\mu}\rvert < 1.95$	42 761.20	33 305.60	73 737.30	22.11	72.44
$1.95 \leq \lvert\eta^{\mu}\rvert < 2.18$	3819.34	11 458	11 458	200	200
$2.18 \leq \lvert\eta^{\mu}\rvert < 2.40$	0	0	0	200	200

Table 9.5: This table displays the systematics uncertainties arising from the Monte Carlo cross section variation of $\pm 0.5\%$ in the $W^+ \to \mu^+\nu$ selection. The first column contains the muon pseudorapidity bins; the second column is the nominal number of multijet background events; the third and fourth columns are the up and down varied number of multijet events; the fifth and sixth columns show the up and down variation computed with Equation (9.1), in percentage.

9.4 Theory uncertainties

The theory uncertainties propagate to the measurements via the C_W factor examined in Chapter 11. The C_W is a ratio between two quantities that are affected by these variations; consequently, the effect of these uncertainties is mainly cancelled out and their effect is expected to be very small ($< 0.1\%$). The theory uncertainties enter via the k_{Factor} weight stated in Equation (5.1), the nominal NNLO correction is computed with the CT14 NNLO [10] PDF set, and the variation of the C_W is dictated by the variation of the k_{Factor}. For the control plots in Chapter 10 and the cross section and muon charge asymmetry measurements results presented in Chapter 11, the theory uncertainties are neglected. Appendix B presents the first steps to calculate the theory uncertainties.

9.5 Summary

In order to quantify the contribution of each systematic considered in this analysis, it is fruitful to examine their value inclusively with the use of Equation (9.2) (similar tables for every muon pseudorapidity bin are found in Appendix C). A list of the considered uncertainties is highlighted in Table 9.6 for the experimental uncertainties; this table presents the

value for the up and down variations in the positive and negative $W \to \mu\nu$ selections; it is important to add that the displayed values *do not* use the symmetric definition contained in Equation (9.5).

The experimental uncertainties provide the largest values coming from jet systematics variations, ranging from 0.1-1.4%; the second largest uncertainty values are from the missing energy and pileup ranging from 0.1-0.6%; likewise, the muon momentum scale and resolution uncertainties are close to 0.2%; next, the variations from scale factor efficiency corrections are in the range of 0.01-0.3%; the smallest uncertainties come from the ID and MS and are close to 0.01%; the sagitta bias correction uncertainties are negligible.

Systematic	$W^+(up)$	$W^+(down)$	$W^-(up)$	$W^-(down)$
MUON_ID	0.002	0.005	0.002	0.008
MUON_MS	0.003	0.013	0.005	0.012
MUON_SAGITTA_RESBIAS	0	0	0	0
MUON_SAGITTA_RHO	0	0	0	0
MUON_SCALE	0.178	0.173	0.155	0.150
MET_SoftTrk_ResoPara	0.204	0.204	0.194	0.194
MET_SoftTrk_ResoPerp	0.242	0.242	0.222	0.222
MET_SoftTrk_Scale	0.100	0.097	0.097	0.090
PileUp	0.648	0.590	0.623	0.563
IDStat	0.048	0.048	0.048	0.048
IDSys	0.306	0.306	0.309	0.309
IsoStat	0.013	0.013	0.013	0.013
IsoSys	0.205	0.205	0.205	0.205
TrigStat	0.168	0.172	0.173	0.177
TrigSys	0.482	0.487	0.487	0.492
TTVAStat	0.018	0.018	0.018	0.018
TTVASys	0.005	0.005	0.005	0.005
JET_EtaIntercalibration_NonClosure	0.001	0.000	0.001	0.000
JET_JER_DataVsMC	0.107	0.107	0.106	0.106
JET_GroupedNP_1	1.320	1.229	1.342	1.241
JET_GroupedNP_2	0.116	0.118	0.127	0.120
JET_GroupedNP_3	0.264	0.252	0.249	0.242
JET_JER_EffectiveNP_1	0.440	0.440	0.426	0.426
JET_JER_EffectiveNP_2	0.248	0.248	0.233	0.233
JET_JER_EffectiveNP_3	0.238	0.238	0.228	0.228
JET_JER_EffectiveNP_4	0.165	0.165	0.159	0.159
JET_JER_EffectiveNP_5	0.073	0.073	0.067	0.067
JET_JER_EffectiveNP_6	0.085	0.085	0.084	0.084
JET_JER_EffectiveNP_7restTerm	0.142	0.142	0.137	0.137
Monte Carlo statistics	0.184	0.184	0.198	0.198

Table 9.6: This table contains the contribution of each individual uncertainty in the inclusive muon pseudorapidity bin, following the definition given in Equation (9.2). The first column indicates the name of the systematic; the second and third columns, corresponding to the $W^+ \to \mu^+\nu$, are the up and down variation respectively; the fourth and fifth columns, corresponding to the $W^- \to \mu^-\nu$, are the up and down variation respectively. In this table the symmetric uncertainty definition is not considered. All the values are presented in percentage.

Chapter 10

Control distributions and cutflows

The behaviour of the kinematic distributions seen by the ATLAS detector is one of the corner stones of the present analysis; namely, the agreement of the number of events in a binned distribution, between the data collected by ATLAS and the cross sections predictions of the different processes, convoluted with detector response, is of particular importance. Furthermore, the impact that every selection criterion has on the number of events is of interest, these effects are summarised in what is called *cutflow tables*. This chapter contains key kinematic distributions and cutflows tables that help to compare the data with the prediction, throwing light on the validity of the W boson selection criteria and the cross section and charge asymmetry measurements.

10.1 Control distributions

The control distributions shown in Figures 10.1-10.8 display the events that fulfil the selection requirements explained in Chapter 7. The uncertainty bands in each plot include the systematic uncertainties discussed in Chapter 9 calculated with Equation (9.3), the uncertainties coming from the multijet calculation summarised in Chapter 8, and the statistical uncertainties. Furthermore, the Monte Carlo predictions are weighted using the product of the weights presented in Section 6.1.2, displayed in Figures 6.4,6.5,6.7,7.2,7.3,7.4 which are defined in Equation (6.9), Equation (5.1). The Monte Carlo simulations included in these plots are normalised according to the pp cross section, and a scale is applied to match the luminosity in data; moreover, the pileup reweighting is accounted in order to guarantee that the predicted cross section is unchanged by the pileup weight; this factor is referred to as luminosity scale,

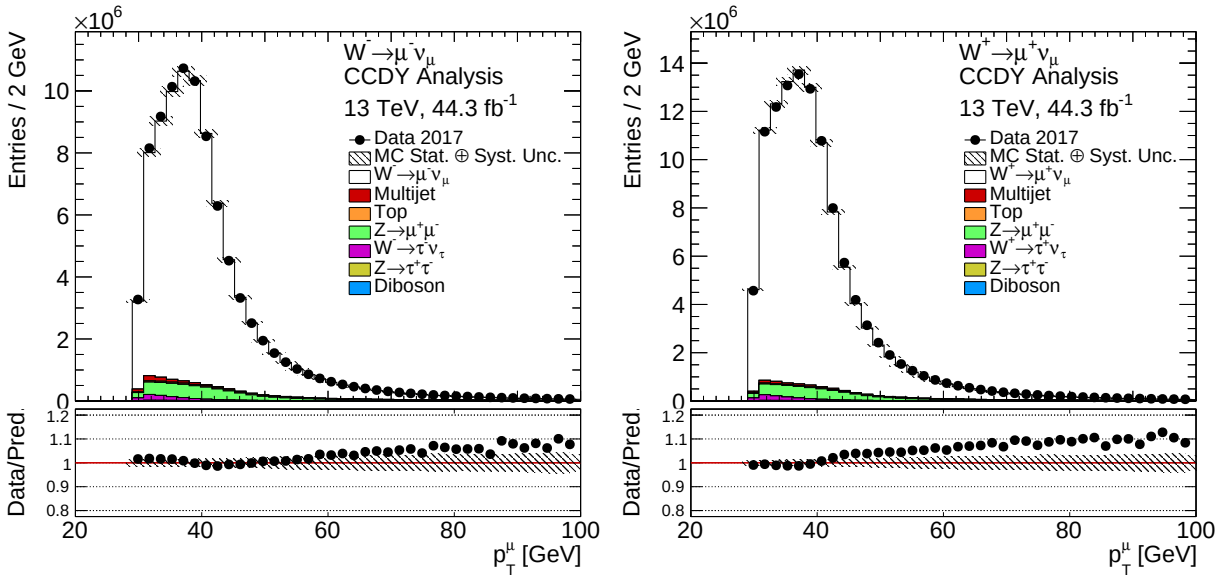

Figure 10.1: Muon transverse momentum control distributions. For $W^- \to \mu^-\nu$ events (left-hand plots) and for $W^+ \to \mu^+\nu$ (right-hand plots). Data are shown with black points and the background contributions with solid lines. Systematic experimental uncertainties are combined with MC statistics in the shaded band, and statistical uncertainties are shown on the data points. Luminosity uncertainties are not included.

$$\mathcal{L}_{scale} = \frac{\mathcal{L}_{data} \cdot \sigma_{MC}}{\sum_{i,allevents} w_i p_i}, \tag{10.1}$$

where $\mathcal{L}_{data}$ is the data integrated luminosity, σ_{MC} is the MC process cross section, w_i is the Monte Carlo generator weight and p_i is the pileup weight. Each MC sample is multiplied by Equation (10.1). The relevant kinematic variables considered in this document are:

- Muon transverse momentum, p_T^μ. The charged current Drell-Yan selection depends heavily on the cut performed on the p_T^μ, therefore it is essential to study the differential p_T^μ distribution; Figure 10.1 shows this distribution, at low transverse momentum values (30-50 GeV) the contribution of the background is the highest. The distribution is peaked at 40 GeV given the final state muons exhibit a transverse momentum nearly equal to the half of the W boson mass. The data and prediction agreement, displayed on the lower panel of Figure 10.1, is at percent level in the high statistics region; however, at higher p_T^μ values the difference between data and prediction becomes substantial ($\approx 20\%$) due to the known mismodelling of the W boson transverse momentum spectrum; this feature has been observed in previous analysis [64, 71].

- Muon pseudorapidity, η^μ. The geometrical distribution of the final state muons is

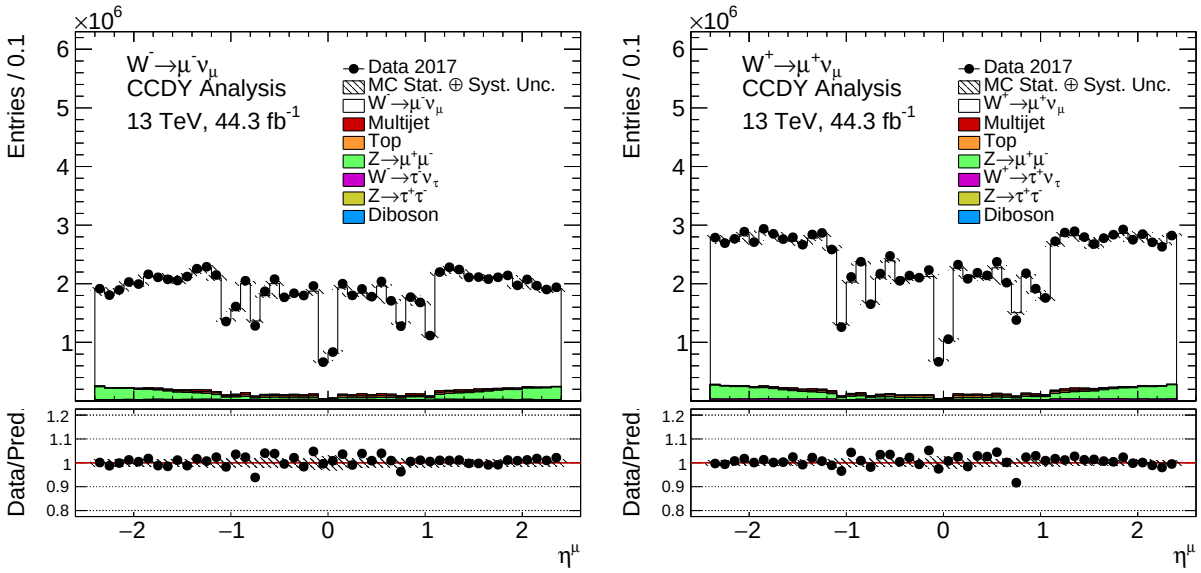

Figure 10.2: Muon pseudorapidity control distributions. For $W^- \to \mu^-\nu$ events (left-hand plots) and for $W^+ \to \mu^+\nu$ (right-hand plots). Data are shown with black points and the background contributions with solid lines. Systematic experimental uncertainties are combined with MC statistics in the shaded band, and statistical uncertainties are shown on the data points. Luminosity uncertainties are not included.

checked with the muon pseudorapidity; the distributions displayed in Figures 10.2 and 10.3 are flat as expected in signal and backgrounds[1], considering that this angular variable, defined in Equation (3.3), should not manifest any preferred value since the ATLAS detector is built to detect muons equally well in the region $|\eta^\mu| < 2.4$. The data and prediction agreement, displayed on the lower panels of Figures 10.2 and 10.3, is at percent level in all pseudorapidity bins. For this thesis, the η^μ is of special relevance due to the cross section and charge asymmetry measurements are performed in η^μ bins; the difference between Figures 10.2 and 10.3 is the binning, the latter corresponding to the binning used to perform this thesis' measurements.

- Muon azimuthal angle, ϕ^μ. A flat distribution of the muon azimuthal angle is expected since the muons, originated from charged current Drell-Yan and background events, do not have a definite preference on a ϕ^μ value; furthermore, the cylindrical geometry of the ATLAS detector allows to reconstruct objects equally well for the full azimuthal angle. Figure 10.4 shows these features and the data and prediction agreement, displayed on the lower panel, is at percent level in all ϕ^μ bins.

[1]The contribution from $Z \to \mu\mu$ background events is slightly larger in the high $|\eta^\mu|$, since for this process is more difficult two relate two muons in this region.

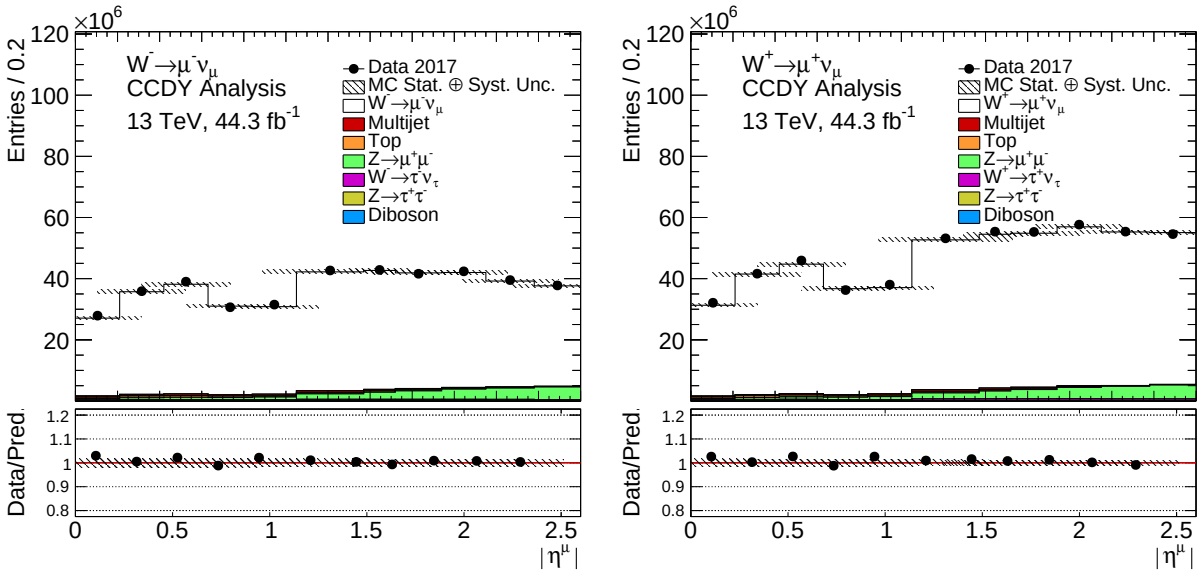

Figure 10.3: Muon pseudorapidity control distributions. For $W^- \to \mu^-\nu$ events (left-hand plots) and for $W^+ \to \mu^+\nu$ (right-hand plots). Data are shown with black points and the background contributions with solid lines. Systematic experimental uncertainties are combined with MC statistics in the shaded band, and statistical uncertainties are shown on the data points. Luminosity uncertainties are not included.

- Event missing energy, E_T^{miss}. The event missing energy defined in Equations (6.5)-(6.8) is used to select $W \to \mu\nu$ events inasmuch as it acts as an approximate of the neutrino transverse momentum; for these events, the neutrino and muon kinematics are roughly balanced, thus the E_T^{miss} distribution is likewise peaked at 40 GeV. The background events contribute the most in the low E_T^{miss} region. These features are presented in Figure 10.5 along with the data and prediction agreement, displayed on the lower panel, showing a percent level of agreement in the high statistics region; at higher E_T^{miss} values the difference between data and prediction becomes substantial ($\approx 10\%$).

- Missing azimuthal angle, $\phi^{E_T^{miss}}$. A flat distribution of the muon azimuthal angle is expected since the neutrinos (approximately missing energy), originated from charged current Drell-Yan and background events, do not have a definite preference on a $\phi^{E_T^{miss}}$ value; furthermore, the cylindrical geometry of the ATLAS detector allows to reconstruct objects equally well for the full azimuthal angle. Figure 10.6 shows these features and the data and prediction agreement, displayed on the lower panel, is at percent level in all $\phi^{E_T^{miss}}$ bins.

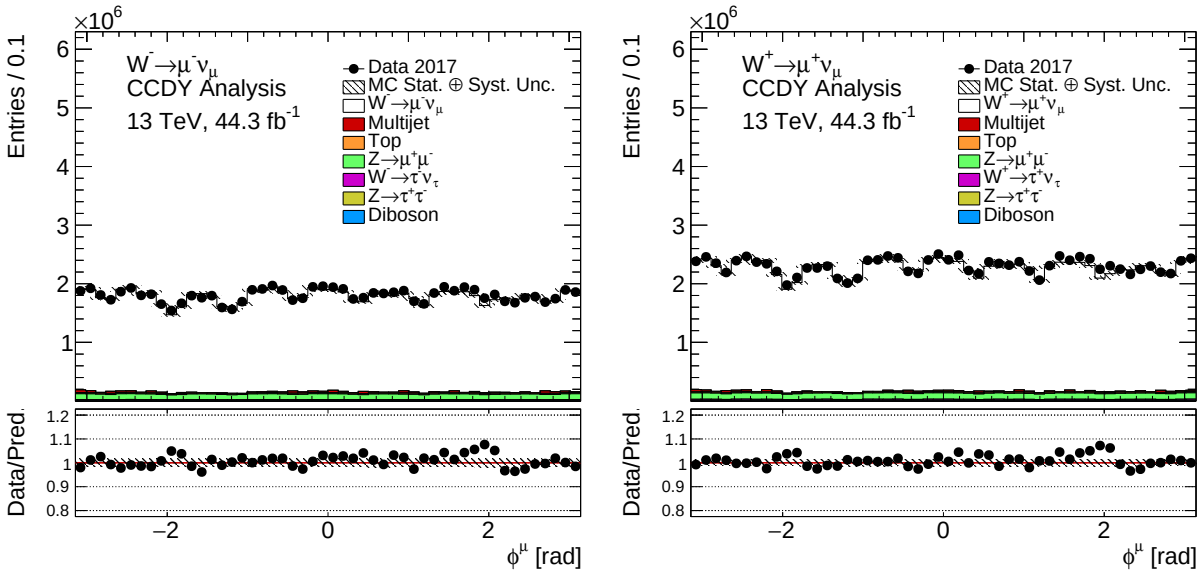

Figure 10.4: Muon azimuthal angle control distributions. For $W^- \to \mu^-\nu$ events (left-hand plots) and for $W^+ \to \mu^+\nu$ (right-hand plots). Data are shown with black points and the background contributions with solid lines. Systematic experimental uncertainties are combined with MC statistics in the shaded band, and statistical uncertainties are shown on the data points. Luminosity uncertainties are not included.

- Difference of azimuthal angle between the muon and the event missing energy, $\Delta\phi$. This distribution is an useful check to validate the $W \to \mu\nu$ selection criteria because the muon and the neutrino are expected to be produced mainly back-to-back, *i.e.* the azimuthal angle separation between them is close to π. In Figure 10.7 it is seen that the major part of the events agree with this expectation, including the events from the electroweak backgrounds; conversely, a muon and neutrino coming from multijet background processes, exhibit small azimuthal angle separation. The data and prediction agreement, displayed on the lower panel of Figure 10.7, is at percent level in the high statistics region, $\Delta\phi \approx \pi$; however, at smaller $\Delta\phi$ values the difference between data and prediction becomes substantial ($\approx 10\%$).

- Event transverse mass, m_T. The cut performed on the event transverse mass variable is used to select charged current Drell-Yan events; moreover, m_T serves as a discriminant between multijet background events and signal events. In Equation (7.3) the transverse mass dependency on p_T^μ, E_T^{miss} and $\Delta\phi$ is stated, therefore it is necessary that the behaviour of these distributions is consistent with m_T. Figure 10.8 displays the m_T distribution, it is peaked at $m_T \approx m_W$ since m_T is related to the W boson mass; most of the backgrounds events are found in the low m_T region, which probes consistency

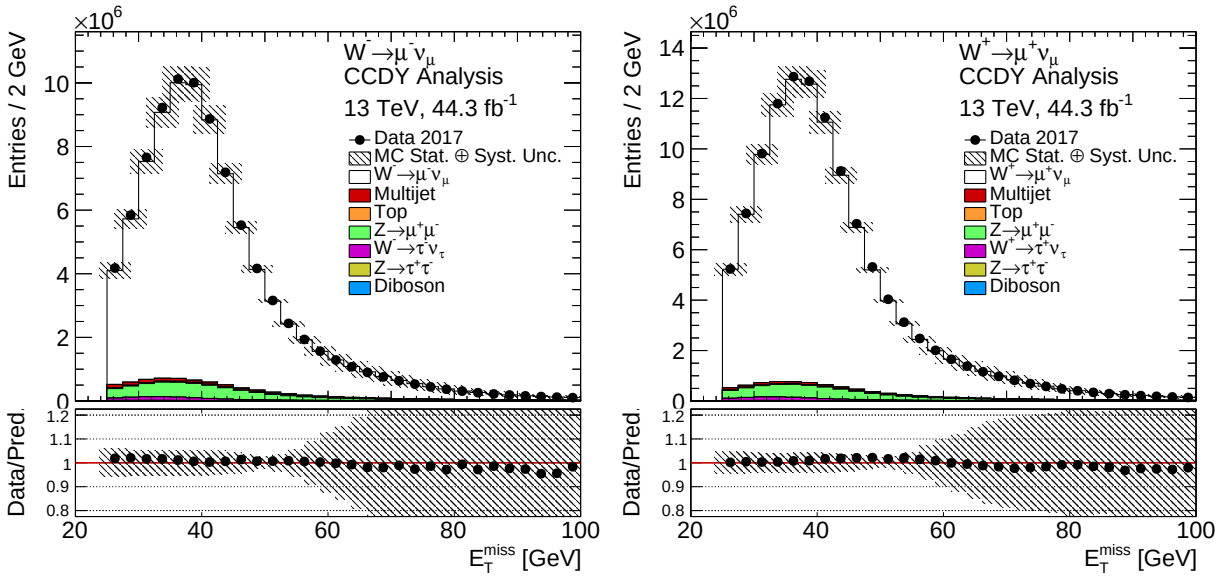

Figure 10.5: Missing transverse energy control distributions. For $W^- \to \mu^-\nu$ events (left-hand plots) and for $W^+ \to \mu^+\nu$ (right-hand plots). Data are shown with black points and the background contributions with solid lines. Systematic experimental uncertainties are combined with MC statistics in the shaded band, and statistical uncertainties are shown on the data points. Luminosity uncertainties are not included.

with the p_T^μ and E_T^{miss} distributions. The data and prediction agreement, displayed on the lower panel of Figure 10.8, is at percent level in the high statistics region; at smaller m_T values the difference between data and prediction becomes larger ($\approx 10\%$).

10.2 Cutflows

This section contains the *cutflow* tables. The cutflow tables show the effect on the number of events that each selection cut has. The cutflows were done for the data, signal MC and background MC; moreover, the relative efficiencies are included for each selection cut. Finally, in the last row the total efficiency is displayed, which is the ratio between the initial number of events over the final number of events after all the selection criteria were applied. All the numbers shown for the Monte Carlo simulations are multiplied by the luminosity and skimming normalisations.

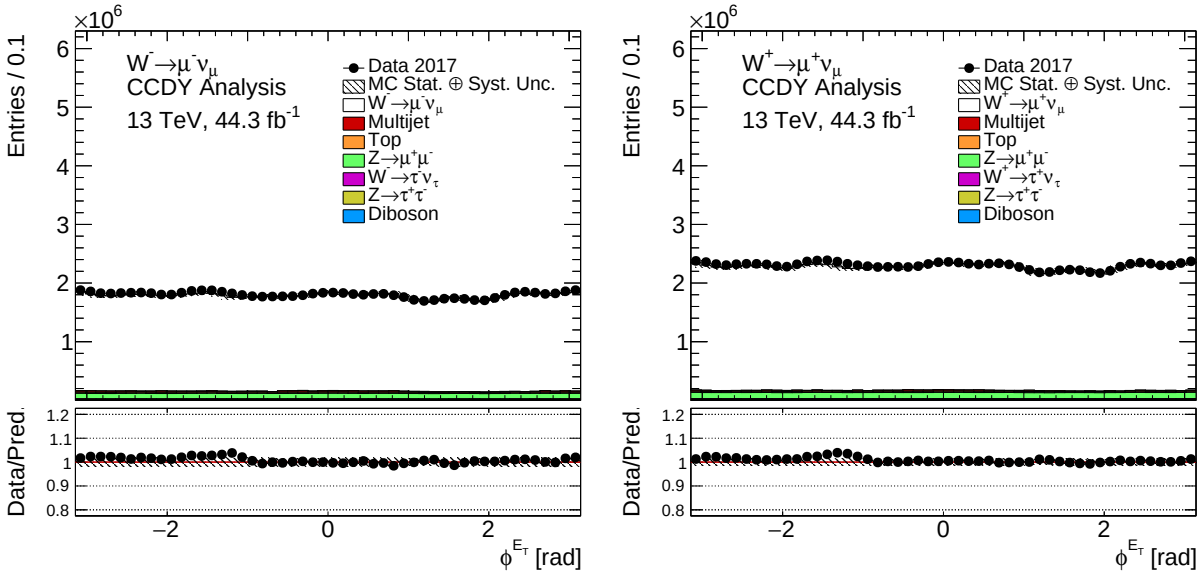

Figure 10.6: Missing energy azimuthal angle control distributions. For $W^- \to \mu^-\nu$ events (left-hand plots) and for $W^+ \to \mu^+\nu$ (right-hand plots). Data are shown with black points and the background contributions with solid lines. Systematic experimental uncertainties are combined with MC statistics in the shaded band, and statistical uncertainties are shown on the data points. Luminosity uncertainties are not included.

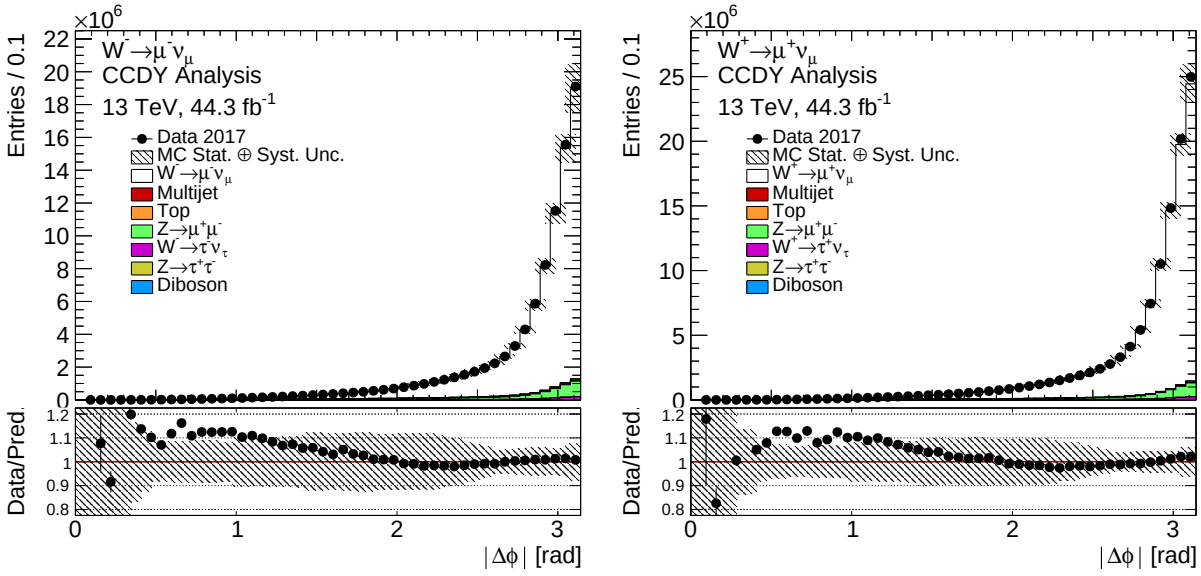

Figure 10.7: Muon and missing energy difference in azimuthal angle control distributions. For $W^- \to \mu^-\nu$ events (left-hand plots) and for $W^+ \to \mu^+\nu$ (right-hand plots). Data are shown with black points and the background contributions with solid lines. Systematic experimental uncertainties are combined with MC statistics in the shaded band, and statistical uncertainties are shown on the data points. Luminosity uncertainties are not included.

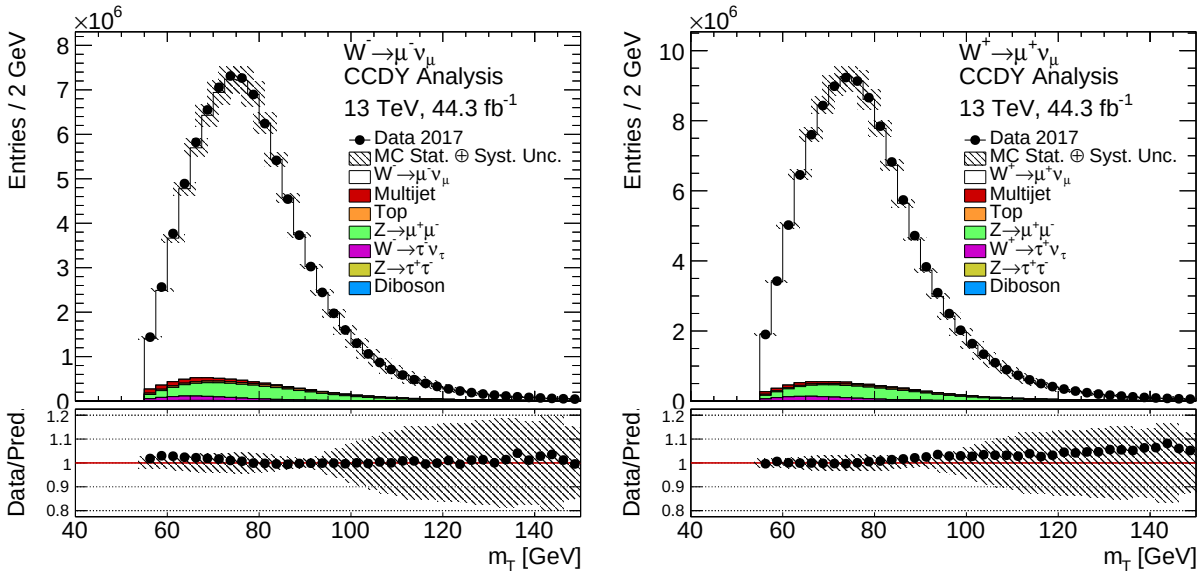

Figure 10.8: Transverse mass control distributions. For $W^- \to \mu^-\nu$ events (left-hand plots) and for $W^+ \to \mu^+\nu$ (right-hand plots). Data are shown with black points and the background contributions with solid lines. Systematic experimental uncertainties are combined with MC statistics in the shaded band, and statistical uncertainties are shown on the data points. Luminosity uncertainties are not included.

	Data	$W^- \to \mu\nu$	$W^- \to \tau\nu$	$Z \to \mu\mu$	$Z \to \tau\tau$	Top	Diboson
Initial	$1.743 \cdot 10^9$ (NA)	$3.646 \cdot 10^8$ (NA)	$2.816 \cdot 10^7$ (NA)	$8.510 \cdot 10^7$ (NA)	$1.235 \cdot 10^7$ (NA)	$1.481 \cdot 10^7$ (NA)	$2.129 \cdot 10^6$ (NA)
GRL	$1.687 \cdot 10^9$ (96.77%)	$3.646 \cdot 10^8$ (100%)	$2.816 \cdot 10^7$ (100%)	$8.510 \cdot 10^7$ (100%)	$1.235 \cdot 10^7$ (100%)	$1.481 \cdot 10^7$ (100%)	$2.129 \cdot 10^6$ (100%)
Good Calo	$1.686 \cdot 10^9$ (99.96%)	$3.646 \cdot 10^8$ (100%)	$2.816 \cdot 10^7$ (100%)	$8.510 \cdot 10^7$ (100%)	$1.235 \cdot 10^7$ (100%)	$1.481 \cdot 10^7$ (100%)	$2.129 \cdot 10^6$ (100%)
PriVtx	$1.686 \cdot 10^9$ (100%)	$3.646 \cdot 10^8$ (100%)	$2.816 \cdot 10^7$ (100%)	$8.510 \cdot 10^7$ (100%)	$1.235 \cdot 10^7$ (100%)	$1.481 \cdot 10^7$ (100%)	$2.129 \cdot 10^6$ (100%)
Trigger	$5.445 \cdot 10^8$ (32.3%)	$1.309 \cdot 10^8$ (35.91%)	$4.171 \cdot 10^6$ (14.81%)	$4.995 \cdot 10^7$ (58.7%)	$2.092 \cdot 10^6$ (16.94%)	$4.964 \cdot 10^6$ (33.52%)	$7.451 \cdot 10^5$ (35.01%)
At least one $p_T^\mu > 30$ GeV	$2.905 \cdot 10^8$ (53.35%)	$9.972 \cdot 10^7$ (76.17%)	$1.786 \cdot 10^6$ (42.82%)	$4.281 \cdot 10^7$ (85.7%)	$9.491 \cdot 10^5$ (45.36%)	$3.931 \cdot 10^6$ (79.19%)	$6.112 \cdot 10^5$ (82.03%)
Trigger match	$2.897 \cdot 10^8$ (99.72%)	$9.972 \cdot 10^7$ (100%)	$1.786 \cdot 10^6$ (100%)	$4.227 \cdot 10^7$ (98.74%)	$9.475 \cdot 10^5$ (99.83%)	$3.916 \cdot 10^6$ (99.62%)	$6.092 \cdot 10^5$ (99.67%)
JetCleaning: Loose Bad	$2.897 \cdot 10^8$ (99.99%)	$9.972 \cdot 10^7$ (100%)	$1.786 \cdot 10^6$ (100%)	$4.227 \cdot 10^7$ (99.99%)	$9.472 \cdot 10^5$ (99.97%)	$3.916 \cdot 10^6$ (99.99%)	$6.091 \cdot 10^5$ (99.99%)
Only one muon	$2.687 \cdot 10^8$ (92.77%)	$9.972 \cdot 10^7$ (100%)	$1.786 \cdot 10^6$ (100%)	$2.146 \cdot 10^7$ (50.77%)	$9.398 \cdot 10^5$ (99.22%)	$3.765 \cdot 10^6$ (96.14%)	$5.550 \cdot 10^5$ (91.11%)
No $e^+(e^-)p_T > 20$ GeV	$2.684 \cdot 10^8$ (99.88%)	$9.972 \cdot 10^7$ (100%)	$1.786 \cdot 10^6$ (99.99%)	$2.145 \cdot 10^7$ (99.97%)	$9.134 \cdot 10^5$ (97.19%)	$3.481 \cdot 10^6$ (92.46%)	$5.213 \cdot 10^5$ (93.93%)
$E_T^{miss} > 25$ GeV	$2.201 \cdot 10^8$ (82.02%)	$8.667 \cdot 10^7$ (86.92%)	$1.320 \cdot 10^6$ (73.92%)	$1.162 \cdot 10^7$ (54.16%)	$4.439 \cdot 10^5$ (48.6%)	$3.048 \cdot 10^6$ (87.57%)	$4.159 \cdot 10^5$ (79.79%)
$m_T > 55$ GeV	$2.057 \cdot 10^8$ (93.45%)	$8.348 \cdot 10^7$ (96.32%)	$1.003 \cdot 10^6$ (75.97%)	$1.027 \cdot 10^7$ (88.4%)	$2.334 \cdot 10^5$ (52.58%)	$2.136 \cdot 10^6$ (70.08%)	$3.367 \cdot 10^5$ (80.94%)
Lepton Veto	$2.053 \cdot 10^8$ (99.8%)	$8.297 \cdot 10^7$ (99.4%)	$9.810 \cdot 10^5$ (97.84%)	$9.704 \cdot 10^6$ (94.49%)	$2.228 \cdot 10^5$ (95.46%)	$2.122 \cdot 10^6$ (99.32%)	$3.328 \cdot 10^5$ (98.87%)
Charge Selection	$9.020 \cdot 10^7$ (43.94%)	$8.297 \cdot 10^7$ (100%)	$9.809 \cdot 10^5$ (99.99%)	$4.647 \cdot 10^6$ (47.89%)	$1.099 \cdot 10^5$ (49.32%)	$1.056 \cdot 10^6$ (49.79%)	$1.639 \cdot 10^5$ (49.25%)
$\lvert\eta\rvert^\mu < 2.4$	$9.020 \cdot 10^7$ (100%)	$8.297 \cdot 10^7$ (100%)	$9.809 \cdot 10^5$ (100%)	$4.647 \cdot 10^6$ (100%)	$1.099 \cdot 10^5$ (100%)	$1.056 \cdot 10^6$ (100%)	$1.639 \cdot 10^5$ (100%)
$p_T^\mu > 30$ GeV	$9.014 \cdot 10^7$ (99.94%)	$8.294 \cdot 10^7$ (99.97%)	$9.782 \cdot 10^5$ (99.73%)	$4.645 \cdot 10^6$ (99.97%)	$1.095 \cdot 10^5$ (99.67%)	$1.056 \cdot 10^6$ (99.96%)	$1.639 \cdot 10^5$ (99.96%)
Cumulative Efficiency	5.2%	23%	3.5%	5.5%	0.89%	7.1%	7.7%
ProcessMC/TotalMC	NA	92.27%	1.088%	5.168%	0.1218%	1.175%	0.1823%
Data/ProcessMC	NA	92.01%	1.085%	5.154%	0.1215%	1.172%	0.1818%
Data/TotalMC	100.3%						

Table 10.1: Cutflow table for W^- selection. This table displays the effect that an individual selection has on the number of events. First column contains the name of the selection cuts. The following columns contain the cutflow for each individual sample, *i.e.*, the number of events after each cut; in every entry, inside the parenthesis, the relative efficiency in percentage is found, which is defined as the number of events after the current cut divided by the number of events after the previous cut. The final four rows are as follows: *Cumulative efficiency* row displays the number of events after all the cuts have been applied divided by the number of events before any cut, in percentage; *ProcessMC/TotalMC* row displays the percentage of the number of events that each Monte Carlo sample contributes to the total sum of the Monte Carlo samples after all the selection cuts have been applied; *ProcessMC/Data* row displays the number of events ratio in percentage of each Monte Carlo sample between the full data sample, after all the selection cuts have been applied; *Data/TotalMC* row is the number of events ratio in percentage of the total sum of the Monte Carlo samples to data, after all the selection cuts have been applied. The Monte Carlo samples are normalised to data luminosity and contain the pileup and generator weights.

	Data	$W^+ \to \mu\nu$	$W^+ \to \tau\nu$	$Z \to \mu\mu$	$Z \to \tau\tau$	Top	Diboson
Initial	$1.743 \cdot 10^9$ (NA)	$4.976 \cdot 10^8$ (NA)	$3.708 \cdot 10^7$ (NA)	$8.506 \cdot 10^7$ (NA)	$1.234 \cdot 10^7$ (NA)	$1.481 \cdot 10^7$ (NA)	$2.127 \cdot 10^6$ (NA)
GRL	$1.687 \cdot 10^9$ (96.77%)	$4.976 \cdot 10^8$ (100%)	$3.708 \cdot 10^7$ (100%)	$8.506 \cdot 10^7$ (100%)	$1.234 \cdot 10^7$ (100%)	$1.481 \cdot 10^7$ (100%)	$2.127 \cdot 10^6$ (100%)
Good Calo	$1.686 \cdot 10^9$ (99.96%)	$4.976 \cdot 10^8$ (100%)	$3.708 \cdot 10^7$ (100%)	$8.506 \cdot 10^7$ (100%)	$1.234 \cdot 10^7$ (100%)	$1.481 \cdot 10^7$ (100%)	$2.127 \cdot 10^6$ (100%)
PriVtx	$1.686 \cdot 10^9$ (100%)	$4.976 \cdot 10^8$ (100%)	$3.708 \cdot 10^7$ (100%)	$8.506 \cdot 10^7$ (100%)	$1.234 \cdot 10^7$ (100%)	$1.481 \cdot 10^7$ (100%)	$2.127 \cdot 10^6$ (100%)
Trigger	$5.445 \cdot 10^8$ (32.3%)	$1.746 \cdot 10^8$ (35.1%)	$5.155 \cdot 10^6$ (13.9%)	$4.993 \cdot 10^7$ (58.7%)	$2.091 \cdot 10^6$ (16.94%)	$4.965 \cdot 10^6$ (33.52%)	$7.444 \cdot 10^5$ (35%)
At least one $p_T^\mu > 30$ GeV	$2.905 \cdot 10^8$ (53.35%)	$1.278 \cdot 10^8$ (73.17%)	$2.146 \cdot 10^6$ (41.62%)	$4.279 \cdot 10^7$ (85.7%)	$9.483 \cdot 10^5$ (45.36%)	$3.932 \cdot 10^6$ (79.19%)	$6.106 \cdot 10^5$ (82.03%)
Trigger match	$2.897 \cdot 10^8$ (99.72%)	$1.278 \cdot 10^8$ (100%)	$2.146 \cdot 10^6$ (100%)	$4.225 \cdot 10^7$ (98.74%)	$9.467 \cdot 10^5$ (99.83%)	$3.917 \cdot 10^6$ (99.62%)	$6.086 \cdot 10^5$ (99.67%)
JetCleaning: Loose Bad	$2.897 \cdot 10^8$ (99.99%)	$1.278 \cdot 10^8$ (100%)	$2.145 \cdot 10^6$ (100%)	$4.225 \cdot 10^7$ (99.99%)	$9.464 \cdot 10^5$ (99.97%)	$3.916 \cdot 10^6$ (99.99%)	$6.085 \cdot 10^5$ (99.99%)
Only one muon	$2.687 \cdot 10^8$ (92.77%)	$1.278 \cdot 10^8$ (100%)	$2.145 \cdot 10^6$ (100%)	$2.145 \cdot 10^7$ (50.77%)	$9.391 \cdot 10^5$ (99.22%)	$3.765 \cdot 10^6$ (96.14%)	$5.544 \cdot 10^5$ (91.1%)
No $e^+(e^-)p_T > 20$ GeV	$2.684 \cdot 10^8$ (99.88%)	$1.278 \cdot 10^8$ (100%)	$2.145 \cdot 10^6$ (99.99%)	$2.144 \cdot 10^7$ (99.97%)	$9.126 \cdot 10^5$ (97.19%)	$3.481 \cdot 10^6$ (92.45%)	$5.207 \cdot 10^5$ (93.92%)
$E_T^{miss} > 25$ GeV	$2.201 \cdot 10^8$ (82.02%)	$1.112 \cdot 10^8$ (87.06%)	$1.607 \cdot 10^6$ (74.9%)	$1.161 \cdot 10^7$ (54.15%)	$4.435 \cdot 10^5$ (48.6%)	$3.049 \cdot 10^6$ (87.57%)	$4.154 \cdot 10^5$ (79.79%)
$m_T > 55$ GeV	$2.057 \cdot 10^8$ (93.45%)	$1.068 \cdot 10^8$ (96.04%)	$1.239 \cdot 10^6$ (77.11%)	$1.027 \cdot 10^7$ (88.4%)	$2.332 \cdot 10^5$ (52.58%)	$2.136 \cdot 10^6$ (70.07%)	$3.363 \cdot 10^5$ (80.94%)
Lepton Veto	$2.053 \cdot 10^8$ (99.8%)	$1.060 \cdot 10^8$ (99.22%)	$1.206 \cdot 10^6$ (97.32%)	$9.699 \cdot 10^6$ (94.49%)	$2.226 \cdot 10^5$ (95.46%)	$2.122 \cdot 10^6$ (99.32%)	$3.324 \cdot 10^5$ (98.86%)
Charge Selection	$1.151 \cdot 10^8$ (56.06%)	$1.060 \cdot 10^8$ (100%)	$1.206 \cdot 10^6$ (99.98%)	$5.054 \cdot 10^6$ (52.11%)	$1.128 \cdot 10^5$ (50.68%)	$1.065 \cdot 10^6$ (50.2%)	$1.719 \cdot 10^5$ (51.72%)
$\lvert\eta\rvert^\mu < 2.4$	$1.151 \cdot 10^8$ (100%)	$1.060 \cdot 10^8$ (100%)	$1.206 \cdot 10^6$ (100%)	$5.054 \cdot 10^6$ (100%)	$1.128 \cdot 10^5$ (100%)	$1.065 \cdot 10^6$ (100%)	$1.719 \cdot 10^5$ (100%)
$p_T^\mu > 30$ GeV	$1.150 \cdot 10^8$ (99.95%)	$1.060 \cdot 10^8$ (99.97%)	$1.203 \cdot 10^6$ (99.79%)	$5.053 \cdot 10^6$ (99.97%)	$1.126 \cdot 10^5$ (99.77%)	$1.065 \cdot 10^6$ (99.97%)	$1.719 \cdot 10^5$ (99.97%)
Cumulative Efficiency	6.6%	21%	3.2%	5.9%	0.91%	7.2%	8.1%
ProcessMC/TotalMC	NA	93.3%	1.059%	4.449%	0.09911%	0.9375%	0.1513%
Data/ProcessMC	NA	92.12%	1.046%	4.393%	0.09786%	0.9257%	0.1494%
Data/TotalMC	101.3%						

Table 10.2: Cutflow table for W^+ selection. This table displays the effect that an individual selection has on the number of events. First column contains the name of the selection cuts. The following columns contain the cutflow for each individual sample, *i.e.*, the number of events after each cut; in every entry, inside the parenthesis, the relative efficiency in percentage is found, which is defined as the number of events after the current cut divided by the number of events after the previous cut. The final four rows are as follows: *Cumulative efficiency* row displays the number of events after all the cuts have been applied divided by the number of events before any cut, in percentage; *ProcessMC/TotalMC* row displays the percentage of the number of events that each Monte Carlo sample contributes to the total sum of the Monte Carlo samples after all the selection cuts have been applied; *ProcessMC/Data* row displays the number of events ratio in percentage of each Monte Carlo sample between the full data sample, after all the selection cuts have been applied; *Data/TotalMC* row is the number of events ratio in percentage of the total sum of the Monte Carlo samples to data, after all the selection cuts have been applied. The Monte Carlo samples are normalised to data luminosity and contain the pileup and generator weights.

Chapter 11

Results

This chapter presents the differential cross sections and the muon charge asymmetry measurements. First, a general measurement strategy is discussed. Then, the choice of the *fiducial phase space* with which the data will be unfolded and defines the final measured cross sections is discussed.

11.1 Cross section strategy

The basic expression to determine W boson production cross sections, σ_W, from recorded events in a detector is given in the following equation,

$$\sigma_W = \frac{N - B}{C_W \cdot \mathcal{L}}, \tag{11.1}$$

where N and B are the number of data recorded and background estimated events respectively, after applying the charged current Drell-Yan selection, C_W is the unfolding correction factor defined in Equation (11.6), and $\mathcal{L}$ is the data integrated luminosity.

To measure the muon charge asymmetry, As_μ,

$$As_\mu = \frac{\sigma_{W^+} - \sigma_{W^-}}{\sigma_{W^+} + \sigma_{W^-}}, \tag{11.2}$$

is employed; where σ_{W^+} is the cross section for the $W^+ \to \mu^+\nu$ production, and σ_{W^-} is the cross section for the $W^- \to \mu^-\nu$ production calculated with Equation (11.1).

11.1.1 Binning in η

The cross section for the charged current Drell-Yan process and the muon charge asymmetry are measured differentially in absolute muon η bins. The binning is selected by taking into account several aspects:

- The limited statistics. Despite the fact that a copious amount of data was collected in 2017, the estimation of multijet background requires well populated bins.
- The same bin edges were used for the 7 and 8 TeV measurements. It was found useful to be able to directly compare and in the future combine this measurement results with those results.
- The physics sensitivity. The binning has to consider interesting physics that can be potentially extracted with the measurement.
- The effect of having different binning, w.r.t. the one set in Equation (11.3), on the cross sections and charge asymmetry depends on whether the bins are wider or narrower; the former would enhance the purity and the stability (defined in Equations (11.7) and (11.8)), nevertheless the sensitivity to interesting physics effects could be dimmed; the later would have the opposite effect. For the present case and near future it was decided to keep the binning established below.

The binning edges are:

$$|\eta^{\mu}| = [0.0, 0.21, 0.42, 0.63, 0.84, 1.05, 1.37, 1.52, 1.74, 1.95, 2.18, 2.4]. \tag{11.3}$$

This binning corresponds to eleven bins. Figure 11.1 shows the η distributions at truth Born level; only truth weights, that do not consider for detector effects, are applied.

The absolute muon pseudorapidity differential versions of Equation (11.1) and Equation (11.2) read as,

$$\frac{d\sigma_W}{d|\eta^{\mu}|} = \frac{N - B}{C_W \cdot \mathcal{L} \cdot \Delta|\eta^{\mu}|}, \tag{11.4}$$

where $\Delta|\eta^{\mu}|$ is the size of each $|\eta^{\mu}|$ bin, and

$$\frac{dAs_{\mu}}{d|\eta^{\mu}|} = \frac{d\sigma_{W^+}/d|\eta^{\mu}| - d\sigma_{W^-}/d|\eta^{\mu}|}{d\sigma_{W^+}/d|\eta^{\mu}| + d\sigma_{W^-}/d|\eta^{\mu}|}. \tag{11.5}$$

11.1.2 Fiducial phase space

This section contains a summary of the phase space chosen to perform the measurements. To be able to perform cross sections and charge asymmetry measurements and compare the

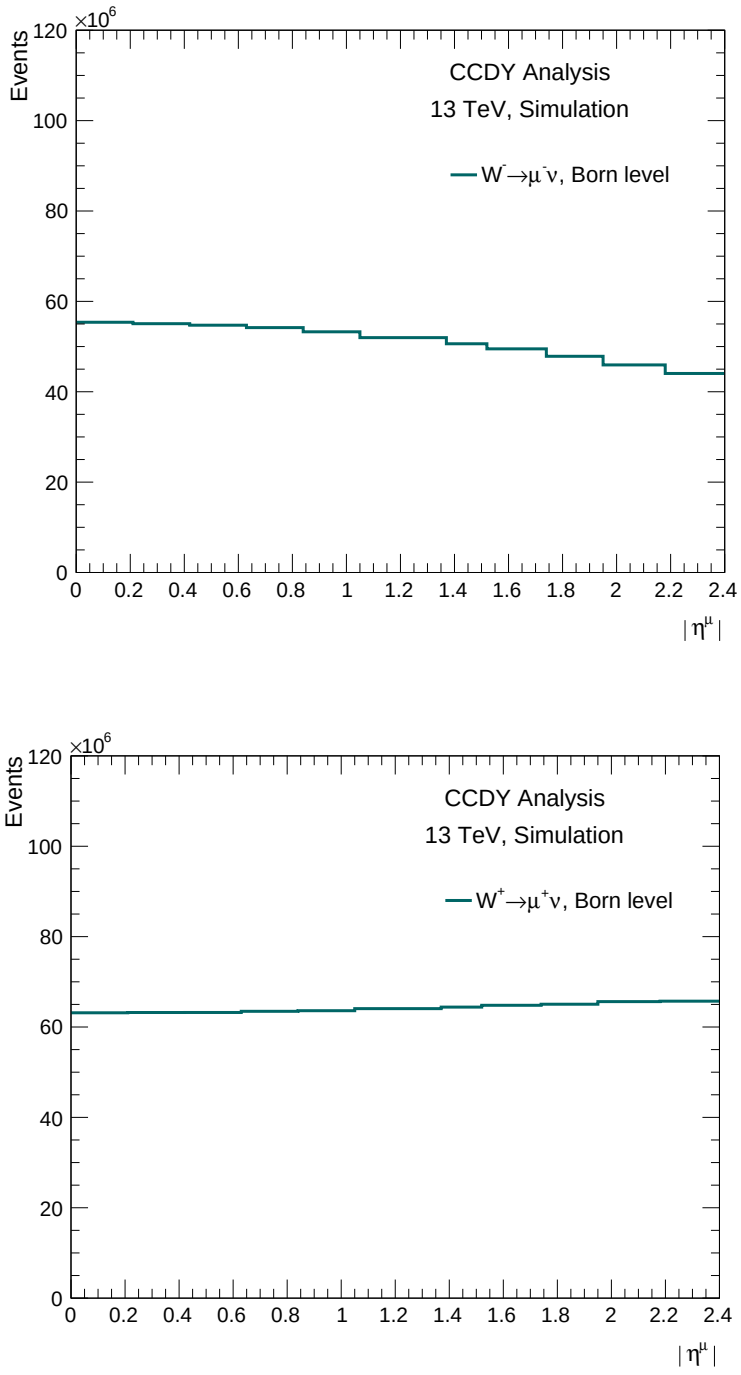

Figure 11.1: Truth level muon η distributions. In this set of plots the binning and the phase space selection were applied. The top plot corresponds to the $W^- \to \mu^-\nu$ and the bottom plots shows the $W^+ \to \mu^+\nu$ channel. The distributions only include the pileup, generator, luminosity weights.

results with theory calculations, it is important to carefully designate a phase space with the target of minimising the systematic uncertainties coming from theory. It is convenient to define the kinematic phase space close to the experimental acceptance to comply with the ID and MS capabilities to minimise model-dependent corrections. Additionally, given the triggers selected for the $W \to \mu\nu$ signature, a muon transverse momentum is chosen above the lowest p_T threshold trigger; likewise, the E_T^{miss} is expected to roughly balance the muon transverse momentum, hence a cut on E_T^{miss} is considered as well. Finally, the transverse mass of the event is selected to be consistent with all the above mentioned cuts and the W boson signature. A *fiducial volume* is therefore constructed with the variables η^μ, p_T^μ, E_T^{miss} and m_T:

- A muon acceptance of $|\eta^\mu| < 2.4$.
- A muon transverse momentum threshold of $p_T^\mu > 30$ GeV.
- The magnitude of the missing energy vector cut of $E_T^{miss} > 25$ GeV[1].
- A transverse mass cut of $m_T > 55$ GeV.

The fiducial volume boundaries are performed on the so-called *truth level* Monte Carlo. The truth level simulation refers to the event simulation without any detector constraints. There are several truth level lepton definitions, depending on how the photons radiated by the final state leptons are handled [72]:

- Born truth level. This level takes into account the lepton before photon emissions (FSR).
- Bare truth level. This level considers the lepton after it has radiated photons.
- Dressed truth level. This level is an intermediate case between the Born and bare level, *i.e.*, after the photons have been radiated, the photons within a $\Delta R < 0.1$ cone are summed to the lepton four-momentum.

This thesis analysis only considers Born truth level leptons, since Born leptons are fully comparable particle-level objects and their measurements can be directly combined with other experiments or in this case be able to potentially combine the muon and electron channels. Furthermore the comparison with theory is more direct.

The use of dressed leptons is the most appropriate approach when the topology of the final state of a measurement is complex, *e.g.* when the final state includes jets that could

[1]The asymmetric $p_T - E_T^{miss}$ selection was suggested by the theorists, see Appendix A.

contain photons. The CCDY final state is simple containing only leptons. Nevertheless, the majority of the final state radiation photons are collinear to the charged leptons, the difference between observables calculated with dressed leptons is as small as $\lesssim 0.1\%$.

It is of utmost interest to perform a measurement which does not depend on the technicalities of the Monte Carlo generator that is used. The bare leptons suffer from being dependent on the details of the implementation of the QED, consequently combination with other experiments become difficult. The advantage of the bare truth level is that the unfolded results are not affected by QED radiation modelling and are closer to the raw experimental recorded data.

It is straightforward to change to a different definition if needed.

Figure 11.2 depicts a comparison among the three different truth levels, the boson kinematics were constructed using the muon and neutrino[2] four momenta. Accompanying the construction of the W boson kinematics with the use of leptons, the direct boson kinematics at Born level is shown in the plots and it is used to check and compare the different truth levels. The lower panel in the plots presents the ratio of the direct boson kinematics over the lepton-constructed boson kinematics; there is a perfect agreement between the direct boson kinematics and the lepton-constructed boson kinematics at Born level; the dressed and bare levels show discrepancies with respect to the Born level, specially at low invariant mass, this effect is expected since photons in this regime take a larger fraction of the parent's lepton energy to be emitted. It is essential to perform this class of checks at truth level in order to confirm that the determination of the fiducial volume is correct.

11.2 Unfolding factor, C_W

The correction factor, found in the denominator of Equation (11.1) and Equation (11.4), is used to account for detector responses, it is called the correction *unfolding factor*, C_W, more precisely,

$$C_W = \frac{N^{reco}}{N^{truth}}, \tag{11.6}$$

where N^{reco} is the number of simulated events that satisfy the charged current Drell-Yan selection criteria listed in Section 7.1.11, these events and their kinematic properties are convoluted with the ATLAS detector simulation; N^{truth} is the number of simulated events that satisfy the fiducial phase space described in Section 11.1.2 and are generated in absence of the ATLAS detector. The C_W factor is a quantity computed exclusively from signal

[2]At truth level the neutrino kinematics are fully available, as opposed to the reconstruction level.

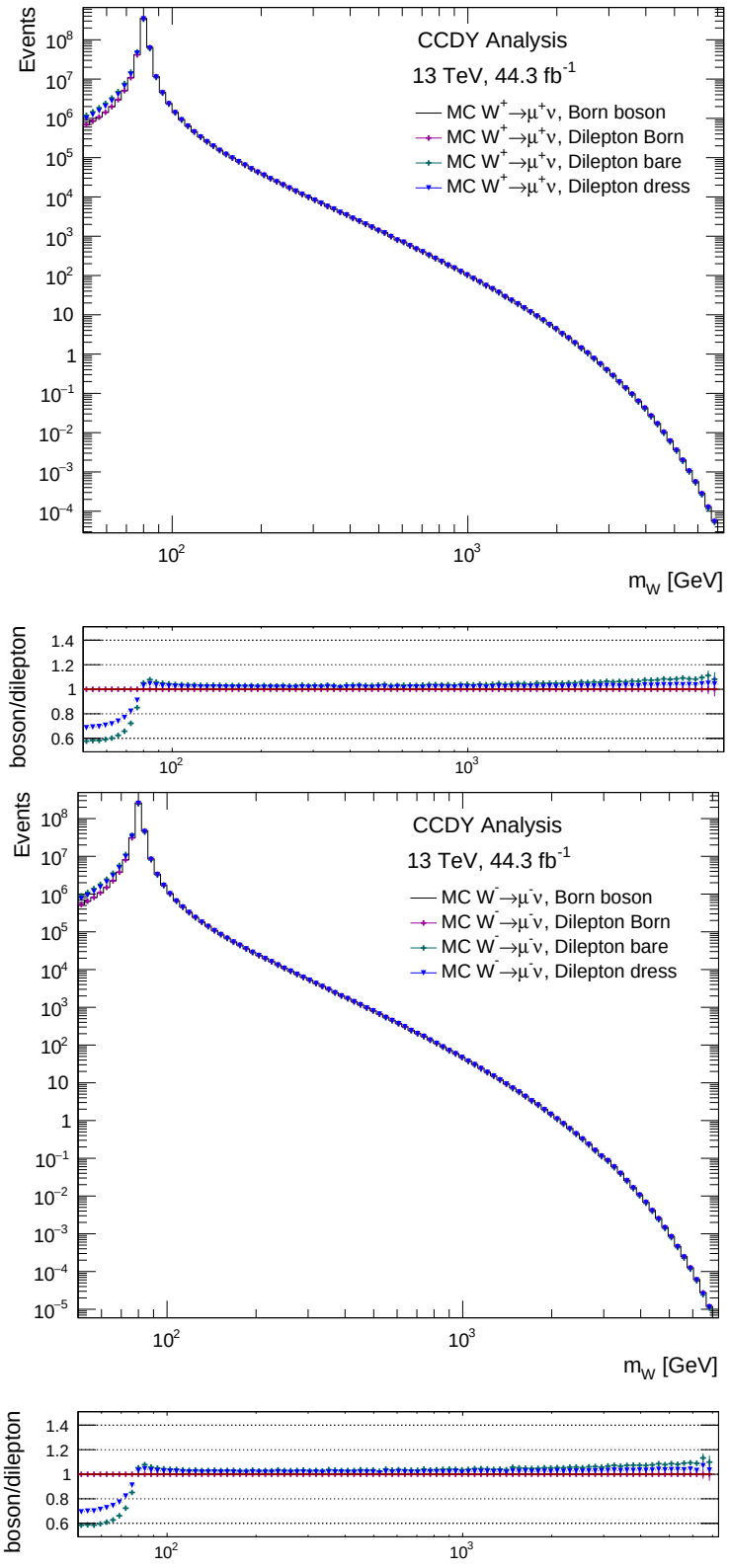

Figure 11.2: Comparison between the different truth level definitions. $W^+ \to \mu^\mu\nu$ (top) and $W^- \to \mu^-\nu$ (bottom) corresponding to the W boson invariant mass distributions.

simulation.

In general, the correcting procedure for detector effects, in the final count of signal data events, is referred to as unfolding; *bin-by-bin unfolding* in $|\eta^{\mu}|$ bins, was performed in this analysis, which means that an unfolding factor is computed for every bin of Equation (11.3), these values are utilised to compute the differential cross section and asymmetry measurements with Equation (11.4) and Equation (11.5).

The bin-by-bin unfolding is simple and powerful; nevertheless, its applicability is limited by the so-called *bin migration*, which is characterised with the fraction of events that are reconstructed and generated in the same bin. Therefore, it is indispensable to assure that the bin migration is low, *i.e.* when the unfolding factor is close to unity. Related quantities are used along with the C_W factor to validate the bin-by-bin unfolding procedure, namely, the *purity, P,* and the *stability, S* defined in Equation (11.7) and Equation (11.8) respectively. The purity serves to establish the amount of reconstructed events that were originally generated in a given bin,

$$P = \frac{N_{stay}^{truth}}{N_{tot}^{reco}}, \tag{11.7}$$

where N_{stay}^{truth} is the number of events generated at truth level in a given bin and that are reconstructed in the same bin and N_{tot}^{reco} is the total number of reconstructed events in a given bin. The stability expresses how many events abandon the bin were they generated,

$$S = \frac{N_{stay}^{truth}}{N_{tot}^{truth}}, \tag{11.8}$$

where N_{stay}^{truth} is the number of events generated at truth level in a given bin and that are reconstructed in the same bin and N_{tot}^{reco} is the total number of truth events in a given bin.

The purity plots found in Figure 11.3 include the reconstruction weights treated in Chapter 6, the events in the numerator of Equation (11.7) are required to pass the fiducial phase space and the reconstruction $W \to \mu\nu$ cuts; the events in the denominator are required to pass the reconstruction cuts solely. In Figure 11.3 it is appreciated that the purity is close to 90% in all the $|\eta^{\mu}|$ bins for the negative and positive channel. This check provides confidence for the unfolding bin-by-bin methodology considering that bias are expected to appear when the purity is typically below 60-70% [65].

The stability plots found in Figure 11.5 include the truth level weights, *i.e.* the pileup weight, the MC generator weight, and the luminosity normalisation. The events in the numerator of Equation (11.8) are required to pass the fiducial phase space and the reconstruction $W \to \mu\nu$ cuts; the events in the denominator are required to pass the fiducial phase space cuts solely. In Figure 11.5 it is appreciated that the stability is close or above 50% in

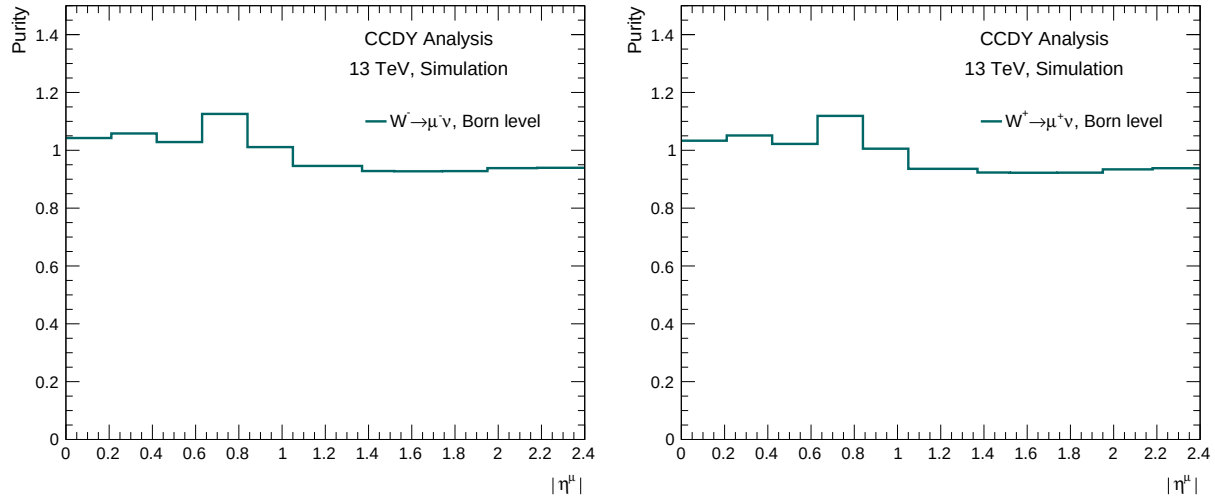

Figure 11.3: Displayed are the purities calculated with Equation (11.8) for $W^- \to \mu^-\nu$ (left) and $W^+ \to \mu^+\nu$ (right) for charged current Drell-Yan events in every $|\eta^\mu|$ bin. Reconstruction weights are taken into account.

all the $|\eta^\mu|$ bins for the negative and positive channel.

11.3 Uncertainty propagation

The uncertainties are propagated to the final results through the unfolding factor defined in Chapter 11 and the number of background events B in Equation (11.1). Considering uncorrelated errors it is found,

$$(\delta\sigma)^2 = \sigma^2 \left(\frac{\delta C_W}{C_W}\right)^2 + \left(\frac{\delta B}{C_W \cdot \mathcal{L}}\right)^2, \tag{11.9}$$

where $\delta\sigma$, δC_W and δB are the uncertainties associated to the cross section, the unfolding factor and the background events, respectively. Several remarks on the individual uncertainties components are:

- Examining the definition of the unfolding factor in terms of the N^{reco} and N^{truth}, it is found that $\delta C_W/C_W$ is equivalent to the values already computed in Section 9.2.
- The uncertainties in the number of background of events, include the uncertainties already discussed for signal Monte Carlo plus the uncertainties arising from the multijet background, see Section 9.3. The contribution of these uncertainties enter via the

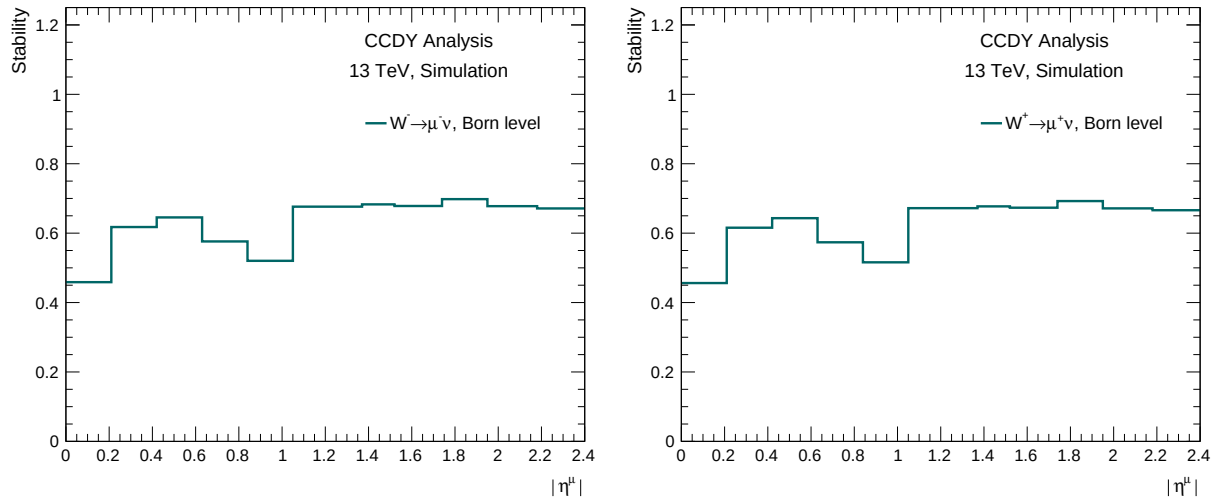

Figure 11.4: Displayed are the stabilities calculated with Equation (11.7) for $W^- \to \mu^-\nu$ (left) and $W^+ \to \mu^+\nu$ (right) for charged current Drell-Yan events in every $|\eta^\mu|$ bin. Truth level weights are taken into account.

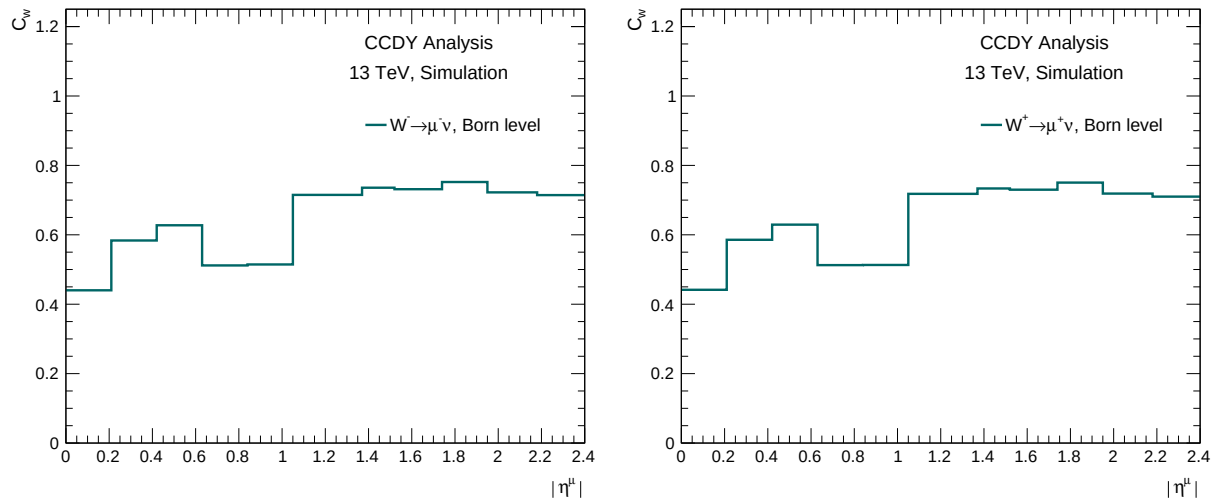

Figure 11.5: Displayed are the C_W calculated with Equation (11.6) for $W^- \to \mu^-\nu$ (left) and $W^+ \to \mu^+\nu$ (right) for charged current Drell-Yan events in every $|\eta^\mu|$ bin. Truth level and reconstruction weights are properly taken into account.

second factor on the right side of Equation (11.9) and it is found to be vanishingly small.

- The MC statistical component of the C_W factor uncertainty requires special care. The reason is the intrinsic dependence[3] between N^{reco} and N^{truth}, consequently, to be able to apply the standard error propagation methodology it is necessary to rewrite these quantities in terms of independent variables, namely [73],

$$C_W = \frac{N^{reco}_{stay} + N^{reco}_{come}}{N^{truth}_{stay} + N^{truth}_{leave}}, \tag{11.10}$$

where N^{reco}_{stay} is the sum of weights reconstructed and generated in the same bin, N^{reco}_{come} is the sum of weights reconstructed in a bin and generated outside the bin, N^{truth}_{stay} is sum of truth weights equivalent to N^{reco}_{stay} (without considering detector corrections), and N^{truth}_{leave} is the sum of truth weights that are generated in a bin but reconstructed outside that bin. Note that $N^{reco} \equiv N^{reco}_{tot} = N^{reco}_{stay} + N^{reco}_{come}$ and $N^{truth} \equiv N^{truth}_{tot} = N^{truth}_{stay} + N^{truth}_{leave}$. Therefore, the error propagation can be applied to Equation (11.10) and the C_W statistical uncertainty is written as,

$$(\delta^{new}_{stat})^2 = \frac{(N^{truth}_{tot} - N^{rec}_{tot})^2}{(N^{truth}_{tot})^4}(\delta N_{stay})^2 + \frac{1}{(N^{truth}_{tot})^2}(\delta N^{rec}_{come})^2 + \frac{(N^{rec}_{tot})^2}{(N^{truth}_{tot})^4}(\delta N^{gen}_{leave})^2 \tag{11.11}$$

where δN^{reco}_{stay}, δN^{truth}_{stay}, δN^{reco}_{come}, δN^{truth}_{leave} are the statistical errors, following a Poisson distribution ($\delta^{stat} = \sqrt{N}$), corresponding to N^{reco}_{stay}, N^{truth}_{stay}, N^{reco}_{come}, N^{truth}_{leave}, respectively. Equation (11.11) assumed $N^{truth}_{stay} \approx N^{reco}_{stay}$, which holds for high scale factor efficiencies. Tables 11.2 and 11.1 display the all the quantities needed to use Equation (11.11); in these tables the difference between the calculation between the statistical uncertainties assuming that the N^{reco} and N^{truth} are independent and the statistical uncertainties utilising Equation (11.11) is found, the former shows an underestimation of these uncertainties of about 50%. The corrected statistical uncertainties are named as δ^{new}_{stat} and their contribution is below 0.1%.

- The uncertainty of the muon charge asymmetry of Equations (11.2) and (11.5) is calculated assuming uncorrelated errors, employing

$$\delta As_{\mu} = \frac{2}{(\sigma_{W^-} + \sigma_{W^+})^2} \cdot [\sigma^2_{W^-}\delta^2_{\sigma_{W^+}} + \sigma^2_{W^+}\delta^2_{\sigma_{W^-}}]^{1/2}, \tag{11.12}$$

[3] N^{reco} and N^{truth} are not independent since the number of reconstructed events in a given bin is a fraction of the number of generated events in that bin.

where $\sigma_{W^{-,+}}$ are the cross sections defined in Equations (11.1) and (11.4), $\delta\sigma_{W^{-,+}}$ are the sum in quadrature of the uncertainties previously considered. The values of the charge asymmetry uncertainties are summarised in Section 11.5.

- The data statistical uncertainty is computed in analogy with Equation (11.9) and included in the measurements of Sections 11.5 and 11.4.

Eta bin	N_{tot}^{reco}	N_{stay}^{reco}	N_{come}^{reco}	N_{tot}^{truth}	N_{stay}^{truth}	N_{leave}^{truth}	C_W	$\delta_{stat}(\%)$	$\delta_{stat}^{new}(\%)$
Inclusive $\|\eta^\mu\|$	$7.821 \cdot 10^7$	$6.928 \cdot 10^7$	$8.935 \cdot 10^6$	$1.227 \cdot 10^8$	$7.677 \cdot 10^7$	$4.590 \cdot 10^7$	0.638	0.369	0.198
$0.0 \leq \|\eta^\mu\| < 0.21$	$5.118 \cdot 10^6$	$4.548 \cdot 10^6$	570 353	$1.163 \cdot 10^7$	$5.335 \cdot 10^6$	$6.294 \cdot 10^6$	0.440	0.081	0.057
$0.21 \leq \|\eta^\mu\| < 0.42$	$6.749 \cdot 10^6$	$5.983 \cdot 10^6$	765 967	$1.156 \cdot 10^7$	$7.141 \cdot 10^6$	$4.422 \cdot 10^6$	0.584	0.098	0.058
$0.42 \leq \|\eta^\mu\| < 0.63$	$7.211 \cdot 10^6$	$6.397 \cdot 10^6$	814 075	$1.149 \cdot 10^7$	$7.417 \cdot 10^6$	$4.076 \cdot 10^6$	0.627	0.104	0.057
$0.63 \leq \|\eta^\mu\| < 0.84$	$5.824 \cdot 10^6$	$5.156 \cdot 10^6$	668 184	$1.138 \cdot 10^7$	$6.557 \cdot 10^6$	$4.824 \cdot 10^6$	0.512	0.089	0.058
$0.84 \leq \|\eta^\mu\| < 1.05$	$5.756 \cdot 10^6$	$5.106 \cdot 10^6$	649 616	$1.119 \cdot 10^7$	$5.819 \cdot 10^6$	$5.366 \cdot 10^6$	0.515	0.092	0.059
$1.05 \leq \|\eta^\mu\| < 1.37$	$1.189 \cdot 10^7$	$1.055 \cdot 10^7$	$1.341 \cdot 10^6$	$1.663 \cdot 10^7$	$1.125 \cdot 10^7$	$5.384 \cdot 10^6$	0.715	0.097	0.048
$1.37 \leq \|\eta^\mu\| < 1.52$	$5.586 \cdot 10^6$	$4.927 \cdot 10^6$	658 871	$7.593 \cdot 10^6$	$5.185 \cdot 10^6$	$2.407 \cdot 10^6$	0.736	0.147	0.072
$1.52 \leq \|\eta^\mu\| < 1.74$	$7.964 \cdot 10^6$	$7.036 \cdot 10^6$	927 405	$1.089 \cdot 10^7$	$7.385 \cdot 10^6$	$3.503 \cdot 10^6$	0.731	0.122	0.060
$1.74 \leq \|\eta^\mu\| < 1.95$	$7.557 \cdot 10^6$	$6.683 \cdot 10^6$	874 652	$1.005 \cdot 10^7$	$7.013 \cdot 10^6$	$3.035 \cdot 10^6$	0.752	0.129	0.062
$1.95 \leq \|\eta^\mu\| < 2.18$	$7.632 \cdot 10^6$	$6.756 \cdot 10^6$	875 789	$1.057 \cdot 10^7$	$7.161 \cdot 10^6$	$3.405 \cdot 10^6$	0.722	0.122	0.060
$2.18 \leq \|\eta^\mu\| < 2.40$	$6.923 \cdot 10^6$	$6.133 \cdot 10^6$	789 467	$9.690 \cdot 10^6$	$6.504 \cdot 10^6$	$3.186 \cdot 10^6$	0.714	0.126	0.063

Table 11.1: This table shows the elements needed to calculate the MC statistical uncertainty defined in Equation (11.11) for the $W^- \to \mu^- \nu$ selection. The first column is the muon pseudorapidity bins; the second, third and fourth column are the total, stay and total reconstructed number of events, respectively; the fifth, sixth and seven are total, stay and leave truth number of events, respectively; the seventh column is the unfolding correction factor; the eighth colum is the statistical uncertainty calculated for considering the reconstruction and truth total number of events independent; finally, the right last column is the correctly calculated statistical uncertainties, in percentage.

Eta bin	N_{tot}^{reco}	N_{stay}^{reco}	N_{come}^{reco}	N_{tot}^{truth}	N_{stay}^{truth}	N_{leave}^{truth}	C_W	$\delta_{stat}(\%)$	$\delta_{stat}^{new}(\%)$
Inclusive $\|\eta^\mu\|$	$9.925 \cdot 10^7$	$8.724 \cdot 10^7$	$1.201 \cdot 10^7$	$1.541 \cdot 10^8$	$9.644 \cdot 10^7$	$5.769 \cdot 10^7$	0.644	0.337	0.184
$0.0 \leq \|\eta^\mu\| < 0.21$	$5.855 \cdot 10^6$	$5.154 \cdot 10^6$	700 763	$1.326 \cdot 10^7$	$6.049 \cdot 10^6$	$7.211 \cdot 10^6$	0.442	0.078	0.056
$0.21 \leq \|\eta^\mu\| < 0.42$	$7.774 \cdot 10^6$	$6.832 \cdot 10^6$	941 930	$1.327 \cdot 10^7$	$8.172 \cdot 10^6$	$5.102 \cdot 10^6$	0.586	0.095	0.056
$0.42 \leq \|\eta^\mu\| < 0.63$	$8.354 \cdot 10^6$	$7.348 \cdot 10^6$	$1.006 \cdot 10^6$	$1.328 \cdot 10^7$	$8.538 \cdot 10^6$	$4.737 \cdot 10^6$	0.629	0.100	0.056
$0.63 \leq \|\eta^\mu\| < 0.84$	$6.833 \cdot 10^6$	$5.995 \cdot 10^6$	838 276	$1.333 \cdot 10^7$	$7.646 \cdot 10^6$	$5.683 \cdot 10^6$	0.513	0.085	0.056
$0.84 \leq \|\eta^\mu\| < 1.05$	$6.854 \cdot 10^6$	$6.031 \cdot 10^6$	822 814	$1.336 \cdot 10^7$	$6.892 \cdot 10^6$	$6.466 \cdot 10^6$	0.513	0.087	0.056
$1.05 \leq \|\eta^\mu\| < 1.37$	$1.472 \cdot 10^7$	$1.294 \cdot 10^7$	$1.783 \cdot 10^6$	$2.050 \cdot 10^7$	$1.378 \cdot 10^7$	$6.724 \cdot 10^6$	0.718	0.091	0.045
$1.37 \leq \|\eta^\mu\| < 1.52$	$7.086 \cdot 10^6$	$6.203 \cdot 10^6$	883 472	$9.661 \cdot 10^6$	$6.542 \cdot 10^6$	$3.119 \cdot 10^6$	0.734	0.134	0.066
$1.52 \leq \|\eta^\mu\| < 1.74$	$1.041 \cdot 10^7$	$9.124 \cdot 10^6$	$1.284 \cdot 10^6$	$1.426 \cdot 10^7$	$9.600 \cdot 10^6$	$4.658 \cdot 10^6$	0.730	0.110	0.055
$1.74 \leq \|\eta^\mu\| < 1.95$	$1.025 \cdot 10^7$	$8.994 \cdot 10^6$	$1.257 \cdot 10^6$	$1.366 \cdot 10^7$	$9.458 \cdot 10^6$	$4.201 \cdot 10^6$	0.750	0.114	0.055
$1.95 \leq \|\eta^\mu\| < 2.18$	$1.085 \cdot 10^7$	$9.545 \cdot 10^6$	$1.304 \cdot 10^6$	$1.509 \cdot 10^7$	$1.013 \cdot 10^7$	$4.960 \cdot 10^6$	0.719	0.105	0.053
$2.18 \leq \|\eta^\mu\| < 2.40$	$1.027 \cdot 10^7$	$9.076 \cdot 10^6$	$1.189 \cdot 10^6$	$1.446 \cdot 10^7$	$9.630 \cdot 10^6$	$4.828 \cdot 10^6$	0.710	0.106	0.054

Table 11.2: This table shows the elements needed to calculate the MC statistical uncertainty defined in Equation (11.11) for the $W^+ \to \mu^+\nu$ selection. The first column is the muon pseudorapidity bins; the second, third and fourth column are the total, stay and total reconstructed number of events, respectively; the fifth, sixth and seven are total, stay and leave truth number of events, respectively; the seventh column is the unfolding correction factor; the eighth colum is the statistical uncertainty calculated for considering the reconstruction and truth total number of events independent; finally, the right last column is the correctly calculated statistical uncertainties, in percentage.

11.4 Cross sections

This section presents the cross section measurements inclusively and differentially in $|\eta^{\mu}|$ bins for both the positive and negative charged current Drell-Yan processes.

Table 11.3 summarises the inclusive results for both the cross section and muon charge asymmetry measurements; in this table the inclusive unfolding factors, used to compute the results, are displayed; furthermore, the different contributions of the uncertainties are shown and are constituted by the sum in quadrature of their corresponding components; finally, the number of events for data, MC simulation (reconstruction and truth) and the background number of events is presented; the numbers within the tables provide all the needed quantities to utilise Equations (11.1) and (11.2).

The $|\eta^{\mu}|$ binned results are presented in Tables 11.4 and 11.5; these tables show the equivalent numbers of Table 11.3. Figure 11.6 exhibits graphically the cross section measurements; the results found in these plots are computed using Equation (11.4). The ratio plots in the lower panels are a comparison between the results obtained using background subtracted data events against results using only signal MC. It is seen that the agreement between data and prediction is good, being the worst case only few percent difference at low muon pseudorapidity bins, for both the negative and positive charged current Drell-Yan selections.

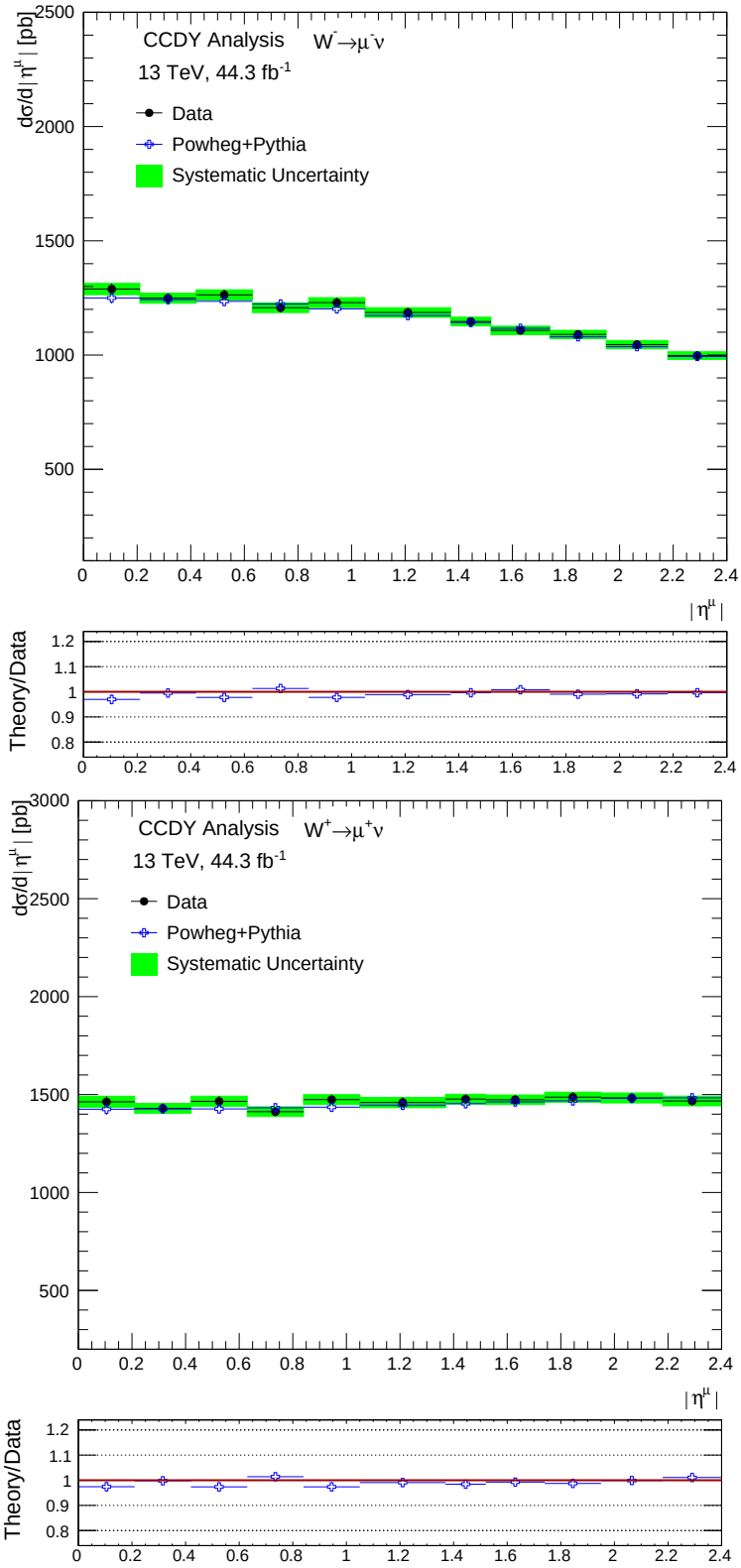

Figure 11.6: Displayed are the differential cross sections calculated with Equation (11.4) for $W^- \to \mu^-\nu$ (top) and $W^+ \to \mu^+\nu$ (bottom) for charged current Drell-Yan events in $|\eta^\mu|$ bins. The green error band corresponds to the systematic uncertainties added in quadrature with the MC statistical uncertainty. The bottom plot is the ratio between data and simulation.

	$Data$	MC	C_W	$\delta_{sys}^{up}(\%)$	$\delta_{sys}^{down}(\%)$	$\delta_{stat}(\%)$	N^{Data}	N^{reco}	N^{truth}	N^{BG}
σ_{W^+}[nb]	3.508	3.479	0.686	1.789	1.702	0.010	$1.151 \cdot 10^8$	$1.057 \cdot 10^8$	$1.541 \cdot 10^8$	$8.003 \cdot 10^6$
σ_{W^-}[nb]	2.792	2.769	0.666	1.785	1.690	0.009	$9.020 \cdot 10^7$	$8.169 \cdot 10^7$	$1.227 \cdot 10^8$	$7.468 \cdot 10^6$
As_μ	0.114	0.114	NA	1.248	1.184	0.008	NA	NA	NA	NA

Table 11.3: This table contains the inclusive cross section and muon charge asymmetry results. The first column displays the measured quantity; the second and third columns are the data and predicted cross sections and charge asymmetry computed with Equations (11.1) and (11.2), respectively; the fourth column contains the unfolding factor; the fifth, sixth and seventh columns show the up, down and data statistical uncertainties in percentage, respectively; last right four columns contain the data, reconstructed, truth and background number of events in that order.

	σ_{Data} [nb]	σ_{MC} [nb]	C_W	$\delta_{sys}^{up}(\%)$	$\delta_{sys}^{down}(\%)$	$\delta_{stat}(\%)$	N^{Data}	N^{reco}	N^{truth}	N^{BG}
$0.0 \leq \lvert\eta^\mu\rvert < 0.21$	1.289	1.250	0.460	2.016	1.911	0.036	$5.860 \cdot 10^6$	$5.346 \cdot 10^6$	$1.163 \cdot 10^7$	347 298
$0.21 \leq \lvert\eta^\mu\rvert < 0.42$	1.249	1.243	0.610	1.826	1.749	0.028	$7.540 \cdot 10^6$	$7.049 \cdot 10^6$	$1.156 \cdot 10^7$	457 219
$0.42 \leq \lvert\eta^\mu\rvert < 0.63$	1.264	1.235	0.655	1.836	1.753	0.026	$8.193 \cdot 10^6$	$7.532 \cdot 10^6$	$1.149 \cdot 10^7$	487 690
$0.63 \leq \lvert\eta^\mu\rvert < 0.84$	1.207	1.223	0.535	1.801	1.726	0.033	$6.437 \cdot 10^6$	$6.084 \cdot 10^6$	$1.138 \cdot 10^7$	432 278
$0.84 \leq \lvert\eta^\mu\rvert < 1.05$	1.230	1.202	0.537	1.744	1.702	0.032	$6.618 \cdot 10^6$	$6.012 \cdot 10^6$	$1.119 \cdot 10^7$	468 737
$1.05 \leq \lvert\eta^\mu\rvert < 1.37$	1.186	1.173	0.747	1.863	1.768	0.024	$1.366 \cdot 10^7$	$1.242 \cdot 10^7$	$1.663 \cdot 10^7$	$1.095 \cdot 10^6$
$1.37 \leq \lvert\eta^\mu\rvert < 1.52$	1.147	1.142	0.768	1.723	1.655	0.024	$6.428 \cdot 10^6$	$5.835 \cdot 10^6$	$7.593 \cdot 10^6$	571 407
$1.52 \leq \lvert\eta^\mu\rvert < 1.74$	1.108	1.117	0.764	1.707	1.625	0.025	$9.153 \cdot 10^6$	$8.318 \cdot 10^6$	$1.089 \cdot 10^7$	902 006
$1.74 \leq \lvert\eta^\mu\rvert < 1.95$	1.090	1.080	0.786	1.767	1.666	0.025	$8.903 \cdot 10^6$	$7.894 \cdot 10^6$	$1.005 \cdot 10^7$	933 130
$1.95 \leq \lvert\eta^\mu\rvert < 2.18$	1.046	1.037	0.754	1.778	1.673	0.027	$9.093 \cdot 10^6$	$7.971 \cdot 10^6$	$1.057 \cdot 10^7$	$1.054 \cdot 10^6$
$2.18 \leq \lvert\eta^\mu\rvert < 2.40$	0.998	0.994	0.746	1.742	1.653	0.029	$8.313 \cdot 10^6$	$7.231 \cdot 10^6$	$9.690 \cdot 10^6$	$1.056 \cdot 10^6$

Table 11.4: This table contains the cross section values for $W^- \to \mu^- \nu$. The first column displays the muon pseudorapidity bins; the second and third columns are the data measured and predicted cross sections computed with Equation (11.4); the fourth column contains the unfolding factor; the fifth, sixth and seventh columns show the up, down and data statistical uncertainties in percentage, respectively; last right four columns contain the data, reconstructed, truth and background number of events in that order.

	σ_{Data} [nb]	σ_{MC} [nb]	C_W	$\delta_{sys}^{up}(\%)$	$\delta_{sys}^{down}(\%)$	$\delta_{stat}(\%)$	N^{Data}	N^{reco}	N^{truth}	N^{BG}
$0.0 \leq \lvert\eta^{\mu}\rvert < 0.21$	1.463	1.425	0.470	2.013	1.908	0.035	$6.745 \cdot 10^6$	$6.233 \cdot 10^6$	$1.326 \cdot 10^7$	347 391
$0.21 \leq \lvert\eta^{\mu}\rvert < 0.42$	1.429	1.427	0.623	1.820	1.743	0.027	$8.742 \cdot 10^6$	$8.275 \cdot 10^6$	$1.327 \cdot 10^7$	450 252
$0.42 \leq \lvert\eta^{\mu}\rvert < 0.63$	1.465	1.427	0.670	1.831	1.748	0.025	$9.647 \cdot 10^6$	$8.893 \cdot 10^6$	$1.328 \cdot 10^7$	512 965
$0.63 \leq \lvert\eta^{\mu}\rvert < 0.84$	1.413	1.433	0.546	1.795	1.720	0.031	$7.618 \cdot 10^6$	$7.275 \cdot 10^6$	$1.333 \cdot 10^7$	443 889
$0.84 \leq \lvert\eta^{\mu}\rvert < 1.05$	1.474	1.436	0.546	1.736	1.695	0.030	$7.989 \cdot 10^6$	$7.296 \cdot 10^6$	$1.336 \cdot 10^7$	496 326
$1.05 \leq \lvert\eta^{\mu}\rvert < 1.37$	1.459	1.446	0.764	1.857	1.761	0.022	$1.702 \cdot 10^7$	$1.567 \cdot 10^7$	$2.050 \cdot 10^7$	$1.204 \cdot 10^6$
$1.37 \leq \lvert\eta^{\mu}\rvert < 1.52$	1.477	1.454	0.781	1.719	1.651	0.021	$8.306 \cdot 10^6$	$7.545 \cdot 10^6$	$9.661 \cdot 10^6$	641 021
$1.52 \leq \lvert\eta^{\mu}\rvert < 1.74$	1.473	1.463	0.777	1.703	1.621	0.021	$1.216 \cdot 10^7$	$1.108 \cdot 10^7$	$1.426 \cdot 10^7$	998 879
$1.74 \leq \lvert\eta^{\mu}\rvert < 1.95$	1.487	1.468	0.799	1.763	1.661	0.020	$1.211 \cdot 10^7$	$1.091 \cdot 10^7$	$1.366 \cdot 10^7$	$1.058 \cdot 10^6$
$1.95 \leq \lvert\eta^{\mu}\rvert < 2.18$	1.483	1.481	0.765	1.772	1.666	0.021	$1.274 \cdot 10^7$	$1.155 \cdot 10^7$	$1.509 \cdot 10^7$	$1.175 \cdot 10^6$
$2.18 \leq \lvert\eta^{\mu}\rvert < 2.40$	1.467	1.483	0.756	1.736	1.647	0.022	$1.201 \cdot 10^7$	$1.093 \cdot 10^7$	$1.446 \cdot 10^7$	$1.196 \cdot 10^6$

Table 11.5: This table contains the cross section values for $W^+ \to \mu^+\nu$. The first column displays the muon pseudorapidity bins; the second and third columns are the data measured and predicted cross sections computed with Equation (11.4); the fourth column contains the unfolding factor; the fifth, sixth and seventh columns show the up, down and data statistical uncertainties in percentage, respectively; last right four columns contain the data, reconstructed, truth and background number of events in that order.

	$As_{\mu,Data}$	$As_{\mu,MC}$	$\delta^{up}_{sys}(\%)$	$\delta^{down}_{sys}(\%)$	$\delta_{stat}(\%)$
$0.0 \leq \lvert\eta^{\mu}\rvert < 0.21$	0.063	0.066	1.418	1.345	0.026
$0.21 \leq \lvert\eta^{\mu}\rvert < 0.42$	0.067	0.069	1.283	1.229	0.020
$0.42 \leq \lvert\eta^{\mu}\rvert < 0.63$	0.074	0.072	1.290	1.231	0.018
$0.63 \leq \lvert\eta^{\mu}\rvert < 0.84$	0.078	0.079	1.263	1.211	0.022
$0.84 \leq \lvert\eta^{\mu}\rvert < 1.05$	0.091	0.088	1.221	1.192	0.022
$1.05 \leq \lvert\eta^{\mu}\rvert < 1.37$	0.103	0.104	1.301	1.234	0.016
$1.37 \leq \lvert\eta^{\mu}\rvert < 1.52$	0.126	0.120	1.199	1.152	0.016
$1.52 \leq \lvert\eta^{\mu}\rvert < 1.74$	0.142	0.134	1.184	1.127	0.016
$1.74 \leq \lvert\eta^{\mu}\rvert < 1.95$	0.154	0.152	1.219	1.149	0.016
$1.95 \leq \lvert\eta^{\mu}\rvert < 2.18$	0.173	0.176	1.216	1.144	0.017
$2.18 \leq \lvert\eta^{\mu}\rvert < 2.40$	0.190	0.197	1.182	1.122	0.017

Table 11.6: This table contains muon charge asymmetry values. The first column displays the muon pseudorapidity bins; the second and third columns are the data measured and predicted asymmetry values computed with Equation (11.5); the fourth, fifth and sixth columns show the up, down and data statistical uncertainties in percentage, respectively.

11.5 Muon charge asymmetry

This section presents the muon charge asymmetry measurement results. The inclusive result is found in Table 11.3 along with the cross sections. The last row of this table corresponds to the muon charge asymmetry measured inclusively with Equation (11.2); the latter uses the cross sections and unfolding factors also found in Table 11.3. The muon charge asymmetry uncertainties derive from the uncertainties of the cross sections, and are calculated with Equation (11.12); the rest of the columns are empty as these numbers are already taken into account within the quantities above mentioned. Table 11.6 contains the differential results for the charge muon asymmetry measurements; the results are calculated with Equation (11.5); a comparison between the asymmetry determination using only MC signal and data subtracted events, can be found; moreover, the systematic up and down, and data statistical uncertainties are shown. Graphically, these results are established in Figure 11.7, in the upper panel plot it is seen the asymmetry measured and compared with the simulation, the errors correspond to the sum in quadrature of all the error sources treated in this analysis; the lower panel shows a more explicit comparison between data subtracted events and MC predictions, a good agreement is observed in most of the muon pseudorapidity bins, the largest discrepancy ($\sim 5\%$) is in few bins that cover [0.21,0.42] and [1.37,1.74] ranges.

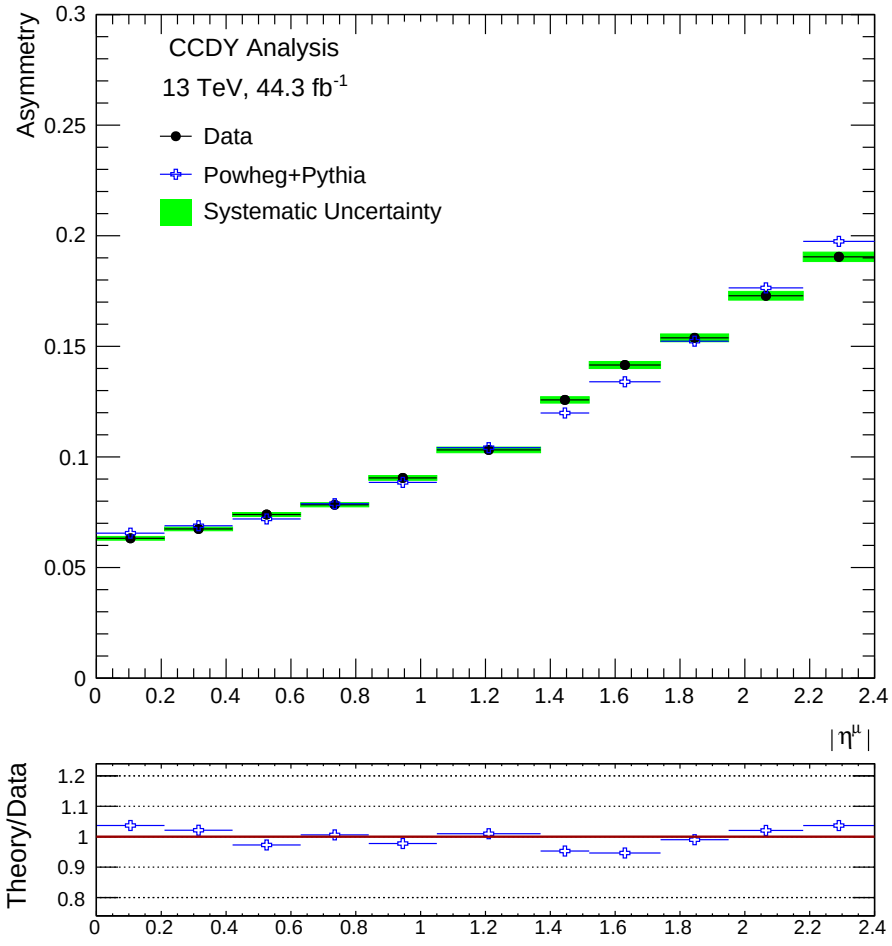

Figure 11.7: Displayed are the differential muon charge asymmetry calculated with Equation (11.5) for charged current Drell-Yan events in $|\eta^{\mu}|$ bins. The green error band corresponds to the systematic uncertainties added in quadrature with the MC statistical uncertainty. The bottom plot is the ratio between data and simulation.

	σ_{W^-}[pb]	σ_{W^+}[pb]	As_μ
$0.0 \leq \lvert\eta^\mu\rvert < 0.21$	$1288.9 \pm 0.5^{+26.0}_{-24.6} \pm 30.9$	$1462.8 \pm 0.5^{+29.4}_{-27.9} \pm 35.1$	$0.063 \pm 0.001^{+0.001}_{-0.001} \pm 0.002$
$0.21 \leq \lvert\eta^\mu\rvert < 0.42$	$1248.8 \pm 0.4^{+22.8}_{-21.8} \pm 30.0$	$1429.5 \pm 0.4^{+26.0}_{-24.9} \pm 34.3$	$0.067 \pm 0.001^{+0.001}_{-0.001} \pm 0.002$
$0.42 \leq \lvert\eta^\mu\rvert < 0.63$	$1263.5 \pm 0.3^{+23.2}_{-22.2} \pm 30.3$	$1465.4 \pm 0.4^{+26.8}_{-25.6} \pm 35.2$	$0.074 \pm 0.001^{+0.001}_{-0.001} \pm 0.002$
$0.63 \leq \lvert\eta^\mu\rvert < 0.84$	$1207.3 \pm 0.4^{+21.7}_{-20.8} \pm 29.0$	$1412.7 \pm 0.4^{+25.4}_{-24.3} \pm 33.9$	$0.078 \pm 0.002^{+0.001}_{-0.001} \pm 0.002$
$0.84 \leq \lvert\eta^\mu\rvert < 1.05$	$1229.6 \pm 0.4^{+21.4}_{-20.9} \pm 29.5$	$1474.3 \pm 0.4^{+25.6}_{-25.0} \pm 35.4$	$0.091 \pm 0.002^{+0.001}_{-0.001} \pm 0.002$
$1.05 \leq \lvert\eta^\mu\rvert < 1.37$	$1186.4 \pm 0.3^{+22.1}_{-21.0} \pm 28.5$	$1459.3 \pm 0.3^{+27.1}_{-25.7} \pm 35.0$	$0.103 \pm 0.002^{+0.001}_{-0.001} \pm 0.002$
$1.37 \leq \lvert\eta^\mu\rvert < 1.52$	$1146.8 \pm 0.3^{+19.8}_{-19.0} \pm 27.5$	$1476.8 \pm 0.3^{+25.4}_{-24.4} \pm 35.4$	$0.126 \pm 0.003^{+0.002}_{-0.001} \pm 0.003$
$1.52 \leq \lvert\eta^\mu\rvert < 1.74$	$1108.0 \pm 0.3^{+18.9}_{-18.0} \pm 26.6$	$1473.5 \pm 0.3^{+25.1}_{-23.9} \pm 35.4$	$0.142 \pm 0.003^{+0.002}_{-0.002} \pm 0.003$
$1.74 \leq \lvert\eta^\mu\rvert < 1.95$	$1090.3 \pm 0.3^{+19.3}_{-18.2} \pm 26.2$	$1486.7 \pm 0.3^{+26.2}_{-24.7} \pm 35.7$	$0.154 \pm 0.003^{+0.002}_{-0.002} \pm 0.004$
$1.95 \leq \lvert\eta^\mu\rvert < 2.18$	$1045.6 \pm 0.3^{+18.6}_{-17.5} \pm 25.1$	$1482.6 \pm 0.3^{+26.3}_{-24.7} \pm 35.6$	$0.173 \pm 0.003^{+0.002}_{-0.002} \pm 0.004$
$2.18 \leq \lvert\eta^\mu\rvert < 2.40$	$997.7 \pm 0.3^{+17.4}_{-16.5} \pm 23.9$	$1467.2 \pm 0.3^{+25.5}_{-24.2} \pm 35.2$	$0.190 \pm 0.004^{+0.002}_{-0.002} \pm 0.005$

Table 11.7: This table displays a summary of the charged current Drell-Yan cross sections and the muon charge asymmetry measurements. The first column is the muon pseudorapidity binning; the second and the third columns are the $W^- \to \mu^-\nu$ and $W^+ \to \mu^+\nu$ cross sections, respectively, calculated utilising Equation (11.4); the fourth column is the muon charge asymmetry computed with Equation (11.5). The numbers are presented in the following order: the value of the process, the data statistical uncertainty, the systematic uncertainties up and down, and the luminosity uncertainty.

11.6 Summary

This section condenses the above results in Table 11.7. This table presents the cross section and charge asymmetry measurements differentially, along with the corresponding contribution of the uncertainties to the measured value. In this table, the results are presented in such a manner that the measured value is followed by the statistical uncertainty, the systematic up and down uncertainties and finally the systematic coming from the luminosity measurements. This thesis results are consistent with previous results of 7 TeV and 8 TeV muon charge asymmetry [74][65] and inclusive W cross section measurements at 13 TeV [75].

11.7 Measurement conclusions

The precision achieved with the cross section and muon charge asymmetry measurements in this thesis is high, with an uncertainty as low as 2%; moreover, the agreement between data and simulation is good. Given that the measurements were performed differentially in muon

pseudorapidity, which is related with the momentum fraction that a particle carries inside the proton, these results provide the capability to further constrain the parton distribution functions corresponding to the up and down quarks and antiquarks, which are responsible of producing positive and negative muons via the charged Drell-Yan process.

Chapter 12

Conclusions

The sophistication of modern accelerators and detectors has achieved an outstanding development, allowing physicists to prove robust quantum field theories and find guidance to construct new ones. Particularly, the successful operation of the Large Hadron Collider and the ATLAS detector has played a major role to obtain the results presented in this thesis. The results presented aimed to obtain a precision measurement of the charged current Drell-Yan production cross section and muon charge asymmetry, inclusively and differentially in muon pseudorapidity bins.

The measurements performed in this analysis have displayed a competitive precision of 2%, the reason of this are several: The calibration of the physics objects, calculated by the ATLAS performance groups, in particular the muons seen by the detector, has an unprecedented precision for the run2 analyses. Theory predictions made for the proton-proton collision cross sections have been in constant improvement tracing the path to find interesting physics that could be found in precision analyses. The results presented in this thesis exhibit a good agreement (the worst case is 5% discrepancy in few bins) of the unfolded data compared to the prediction. Consequently, the results of this thesis can be used to constrain the proton's quark parton distribution functions corresponding to the charged current Drell-Yan production.

The measurements mentioned in Section 2.5 use quite similar phase spaces to the one presented in this thesis. The studies performed here aim to improve the precision of the charge asymmetry determination; in the case of the CMS result, the statistical uncertainty is not negligible; furthermore, it is expected that the systematic uncertainties will be reduced for the run2 analyses. The precision achieved in this thesis is comparable to the CMS and ATLAS previous results, nevertheless the centre of mass energy permits the study of the

PDFs in a higher x range. The results communicated in this document could be improved by adding the full run2 data, controlling the uncertainty result of multiple proton-proton interactions, and refining the computation of the missing energy and the multijet background.

It is worth to mention that these measurements have never been reported before in literature using 13 TeV data, therefore the results presented here are the first muon charge asymmetry measurements using recent ATLAS 13 TeV proton-proton collision data. The author of the thesis carried out the full analysis, therefore numerous checks and studies were performed to evaluate the consistency of the results presented in Chapter 11; namely, the event weights and normalisation were carefully addressed, the detector efficiencies were also cautiously studied along with their uncertainties. Monte Carlo simulation of signal and background events were compared against data in several kinematic variables to ensure that the event selection criteria efficiently discriminates background from $W \to \mu\nu$ events, good agreement was found in every kinematic distribution. One of the most challenging parts of the analysis was the multijet background estimation that proved to be difficult, and special care had to be taken to address the use of different lepton triggers; the multijet was studied in detail along with its systematics and found to be small for the charged current Drell-Yan selection established. The systematic uncertainties were also addressed with care and presented in Appendix C for every muon pseudorapidity bin, this provides confidence in the procedures to study the uncertainties. Truth level studies were fundamental to guarantee the validity of the bin-by-bin unfolding technique chosen to compute the cross section and muon charge asymmetry. Finally, the results obtained were carefully checked and analysed, these yield satisfactory results.

The prospects of the analysis presented here to be published in a peer reviewed journal, are to work further on improving the systematic uncertainties to obtain a world leading result. The work will be continued by the author and a younger PhD student. Also different unfolding techniques and the use of different Monte Carlo simulations need to be addressed as consistency checks to make the analysis more robust and reliable. Fitting the data results to constrain the PDFs could be performed afterwards and be included in the same paper or in a second one.

The charged current Drell-Yan production is a very interesting physics process. The results of this thesis have shown to be precise enough to extract detailed information of the proton structure. There is still an enormous amount of interesting physics that could be extracted with this kind of measurements; for example, in recent years people have turned

their attention to look for new physics using precision measurements. Hence, precision measurements, in particular Drell-Yan measurements, are still young (physicists have learned and tested the Standard Model to the highest accuracy) and have many exciting results awaiting to be discovered.

Appendices

Appendix A

Multijet background estimation consistency checks

This appendix contains additional information regarding the multijet estimation. Namely, it contains in more detail how the normalisation of the multijet was determined, a breakdown of the steps is discussed. In addition, the analogue of Figures 8.5-8.9 for one muon pseudorapidity bin are presented.

A.1 Multijet background normalisation

Chapter 8 establishes the procedure to extract the contribution of the multijet and electroweak backgrounds in a multijet enriched phase space. This section provides with supplementary checks that help to ensure that the procedure was performed consistently.

The results of the TFraction function are in terms of normalised distributions, *i.e.* the input distributions are first normalised to unit area, and then the determination of the fractions is carried out; therefore, it is necessary to correctly normalise the fractions using,

$$T = T' \times MJ_{norm},$$

$$\alpha = \alpha' \times MC_{norm}, \tag{A.1}$$

where (T,α) and (T',α') are the final and unit area normalised fractions, respectively; MJ_{norm} and MC_{norm} are data normalised number of events for the multijet and Monte Carlo backgrounds, respectively, in the corresponding phase space. The top plots of Figure A.1 show the unit area normalised components of the fit, where the MC and multijet components are not scaled by T' and α', moreover the normalised data distribution is displayed along with

the normalised fit result; it is seen that the sum of the component samples do not describe the data. The bottom plots of Figure A.1 make a comparison between the scaled sum of MC and multijet backgrounds, these distributions were scaled with α' and T' respectively; the lower panel of the plot shows the ratio of data with this sum; a good agreement is found in the high statistics bins. The last step is equivalent to consider Equation (8.1) and making the changes $T \to T'$ and $\alpha \to \alpha'$. In Figure A.1 only the $W^- \to \mu^-\nu$ channel is shown, notwithstanding, the same holds for the $W^+ \to \mu^+\nu$ channel.

Figure A.2 shows the fraction fit methodology component distributions without the unit area normalisation. The top plots enclose a comparison of the data with the MC and the multijet background without applying the T and α scaling; the bottom plots display the scaled sum of MC and multijet background. The lower panels in each plot are correlated with the ratio of data against the sum of the MC and multijet in both the top and bottom plots, a significant improvement it is seen when the scaling is applied.

Figures A.1 and A.2 help to validate the use of the T fraction to normalise the multijet background in the signal region.

A.2 Multijet background estimation in a given $|\eta^\mu|$

The plots presented in Chapter 8 correspond to the calculation of the multijet background performed in the inclusive $|\eta^\mu|$ bin. Nevertheless this was done for each bin of Equation (11.3), as an example, this section contains the plots for the bin $0.00 \leq |\eta^\mu| \leq 0.21$ (Figures A.3-A.7) which are the analogue to 8.5-8.9; the multijet fraction T results shown in Tables 8.2 and 8.3 where computed in every bin, therefore similar plots are available for every bin not shown here. The vertical axes in the plots were intentionally set with the same range as in the inclusive case, in order to appreciate the difference in statistics when considering only one muon pseudorapidity bin.

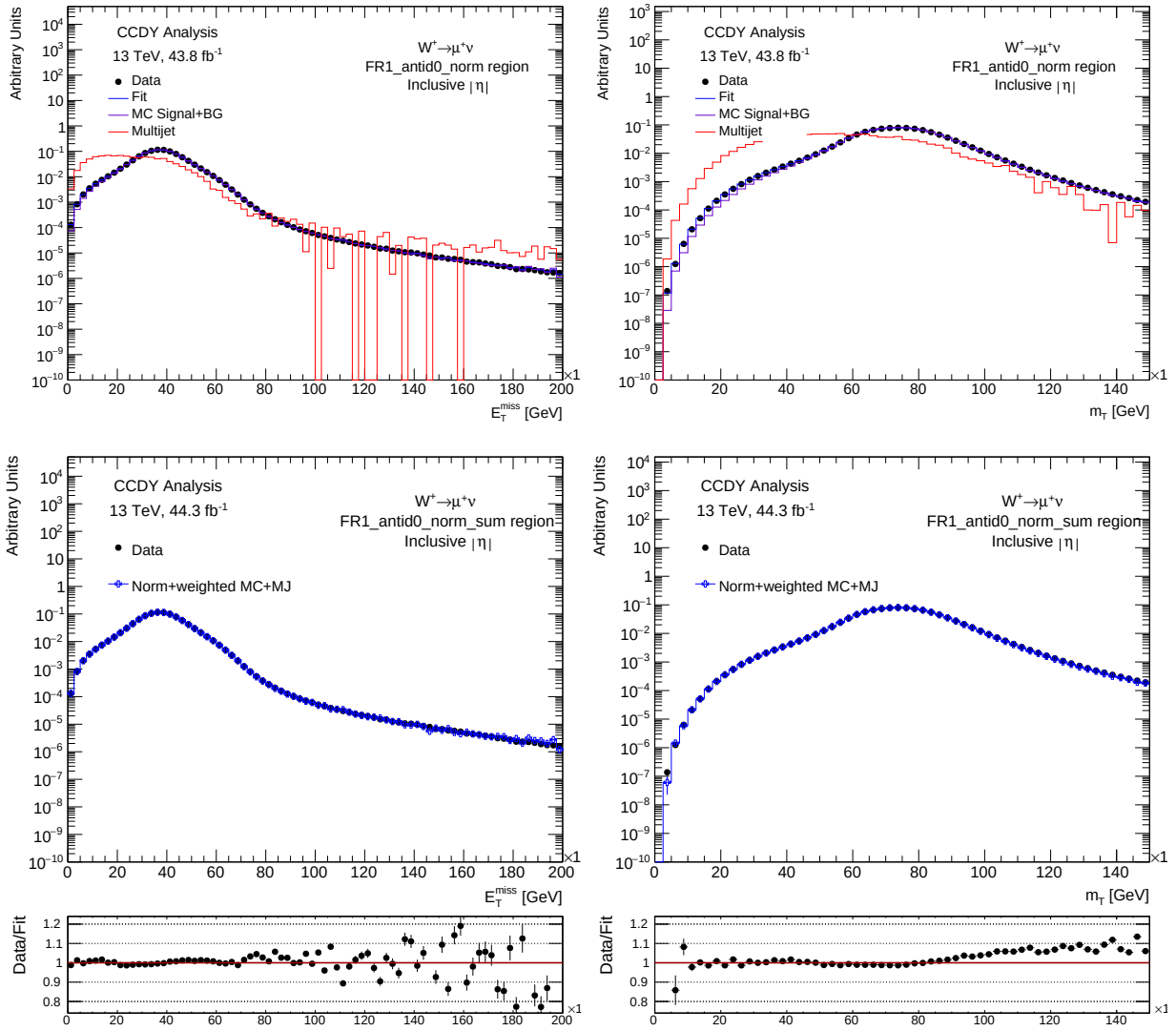

Figure A.1: Multijet normalisation plots. Top plots display the unit area normalised distributions in the fit region, considering an inverted muon d_0 significance cut; the background distributions are not scaled by the fractions. Bottom plots display the unit area normalised distributions in the fit region, considering an inverted muon d_0 significance cut; the backgrounds are scaled by the corresponding fractions; the lower panels show the ratio between data and the sum of backgrounds. Left plots display the missing transverse energy distributions, whilst the right plots display the transverse mass distributions.

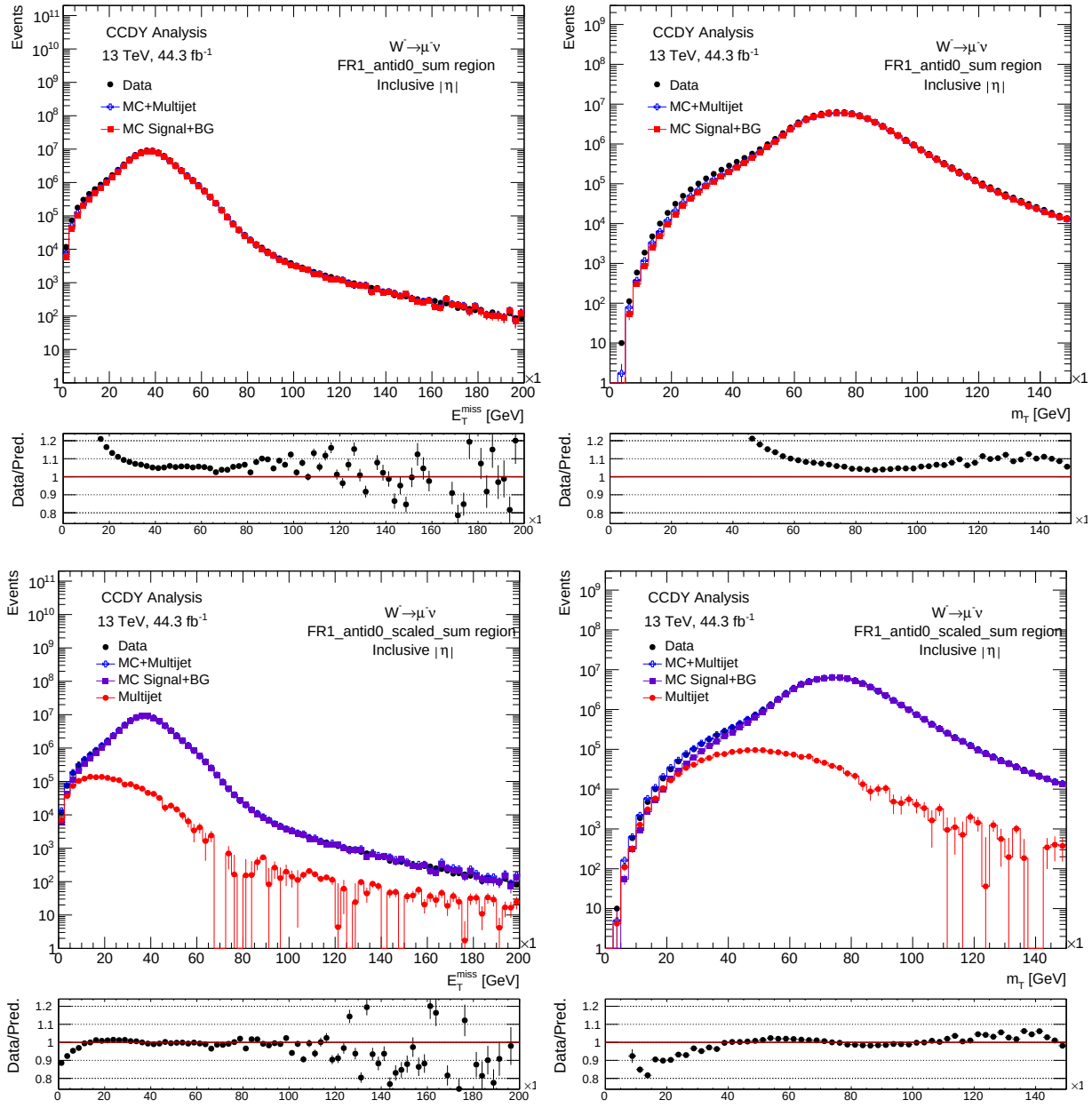

Figure A.2: Multijet normalisation plots. Top plots display the distributions in the fit region, considering an inverted muon d_0 significance cut; the background distributions are not scaled by the fractions. Bottom plots display the distributions in the fit region, considering an inverted muon d_0 significance cut; the backgrounds are scaled by the corresponding fractions. Left plots display the missing transverse energy distributions, whilst the right plots display the transverse mass distributions.

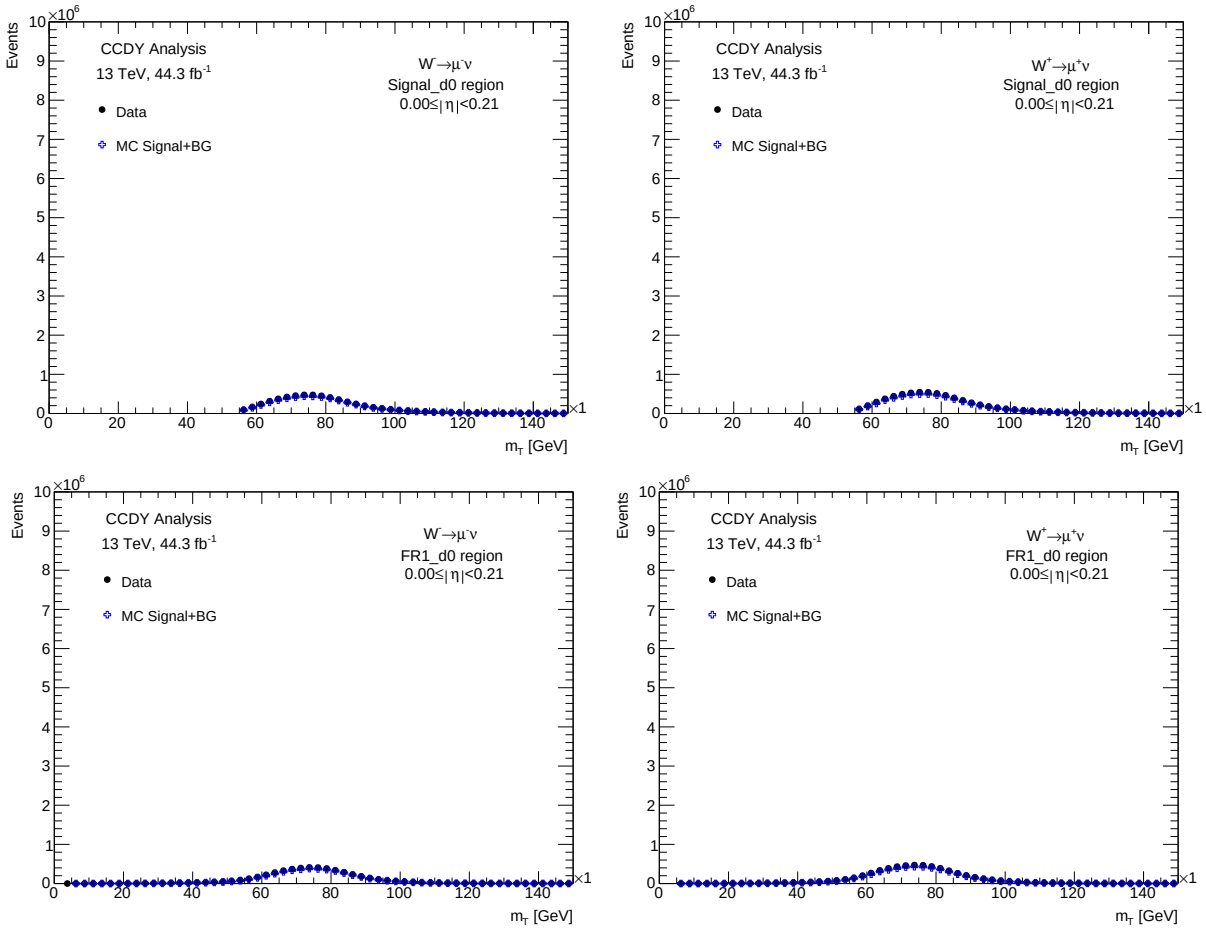

Figure A.3: Multijet normalisation plots. Transverse mass distributions in a region where the full W boson selection is applied considering the d_0 significance applied (top) and dropping the missing energy and transverse mass cuts (bottom) for both data and MC. *Left-hand* plots are for the negative channel and *right-hand* plots are for the positive channel.

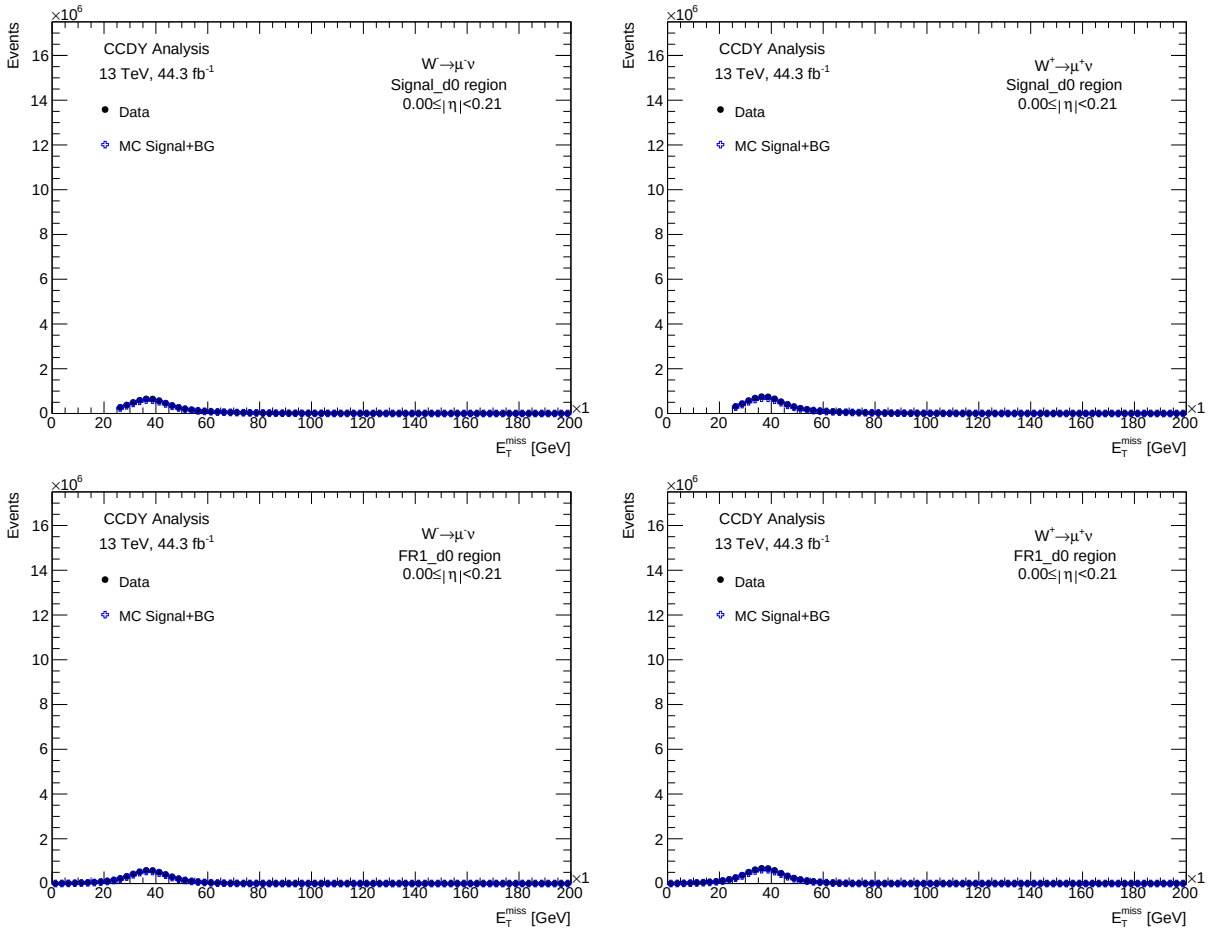

Figure A.4: Multijet normalisation plots. Transverse missing energy distributions in a region where the full W boson selection is applied and the d_0 significance applied (top) and dropping the missing energy and transverse mass cuts (bottom) for both data and MC. *Left-hand* plots are for the negative channel and *right-hand* plots are for the positive channel.

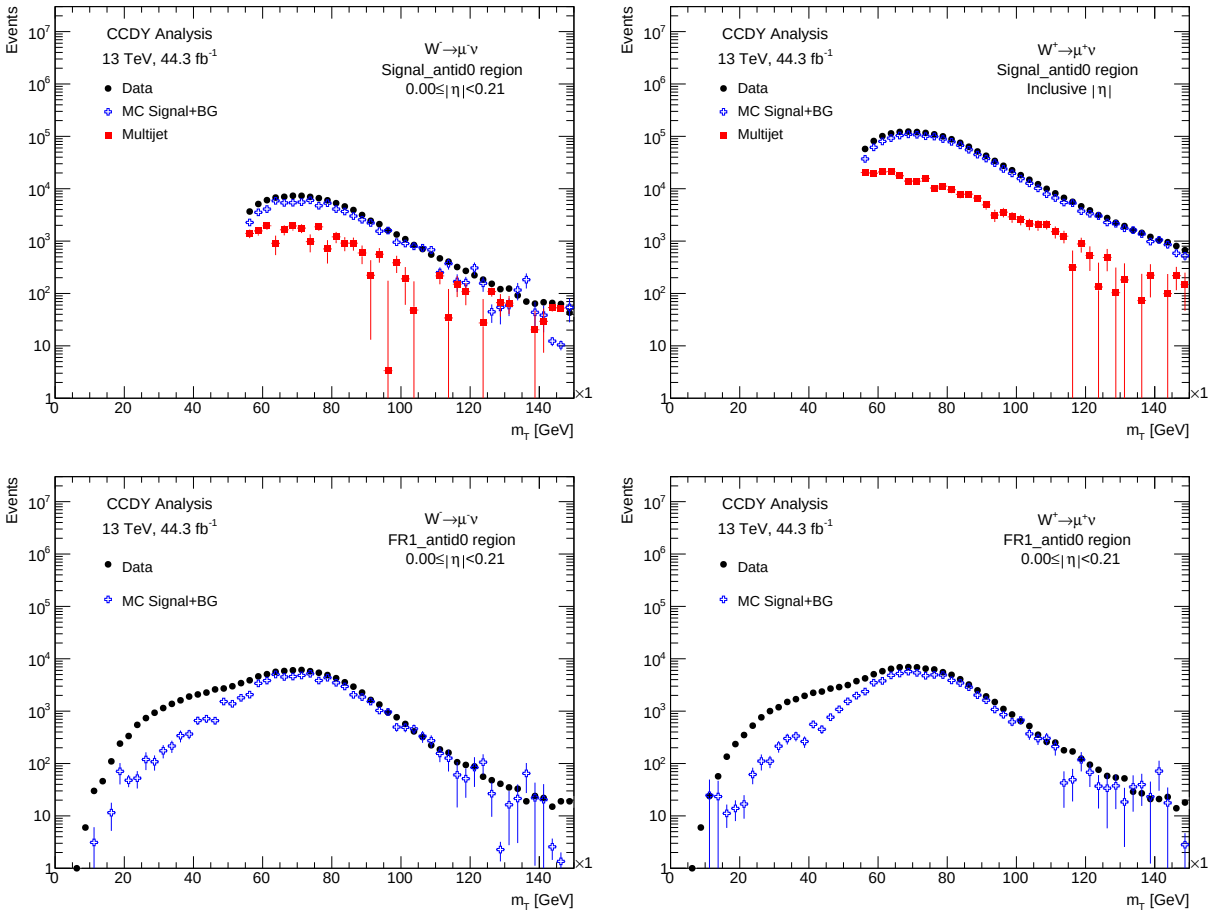

Figure A.5: Multijet normalisation plots. Transverse mass distributions; top plots correspond to the region where the full W boson selection is applied considering the d_0 significance inverted, bottom plots correspond to the fit region and the d_0 significance inverted for both data and MC. *Left-hand* plots are for the negative channel and *right-hand* plots are for the positive channel.

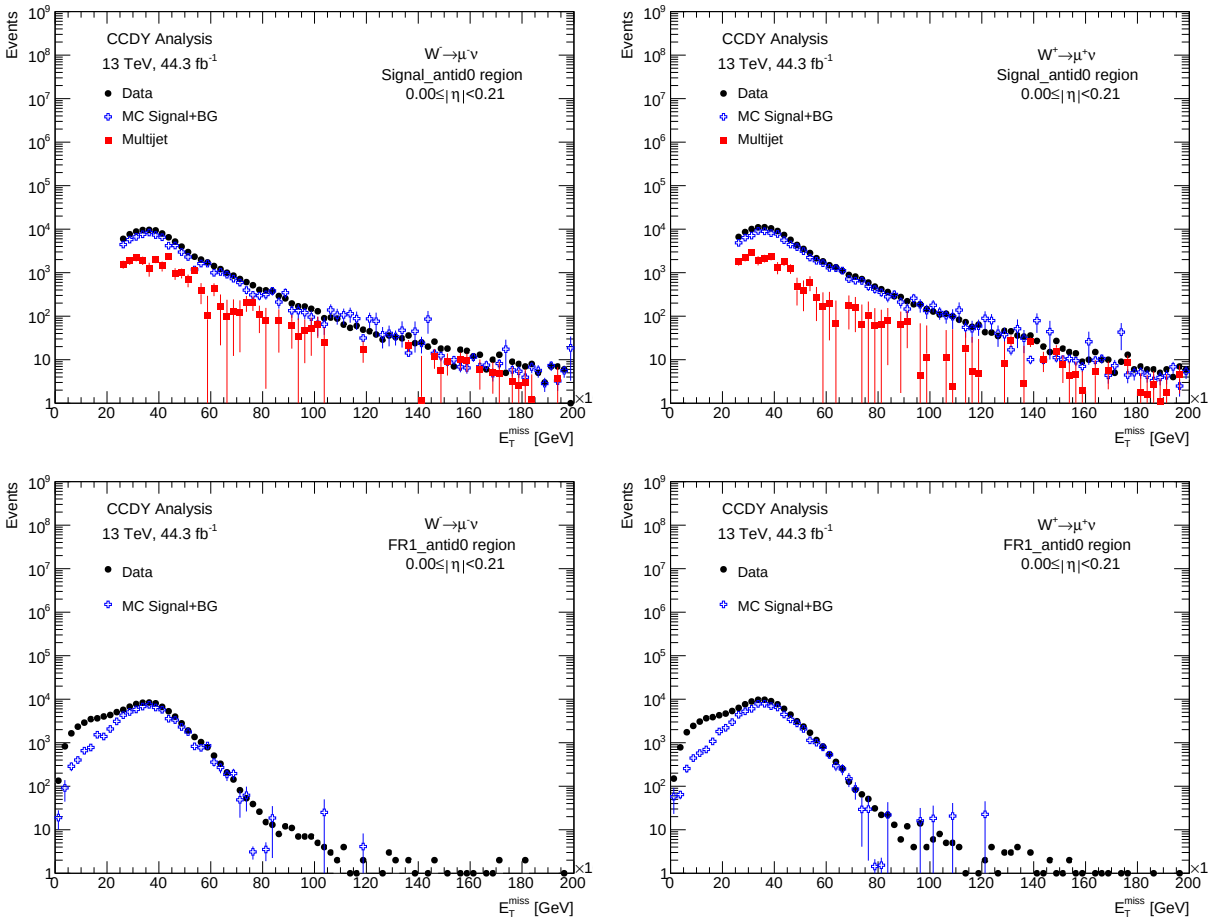

Figure A.6: Multijet normalisation plots. Transverse missing energy distributions; top plots correspond to the region where the full W boson selection is applied and the d_0 significance inverted, bottom plots correspond to the fit region considering the d_0 significance inverted for both data and MC. *Left-hand* plots are for the negative channel and *right-hand* plots are for the positive channel.

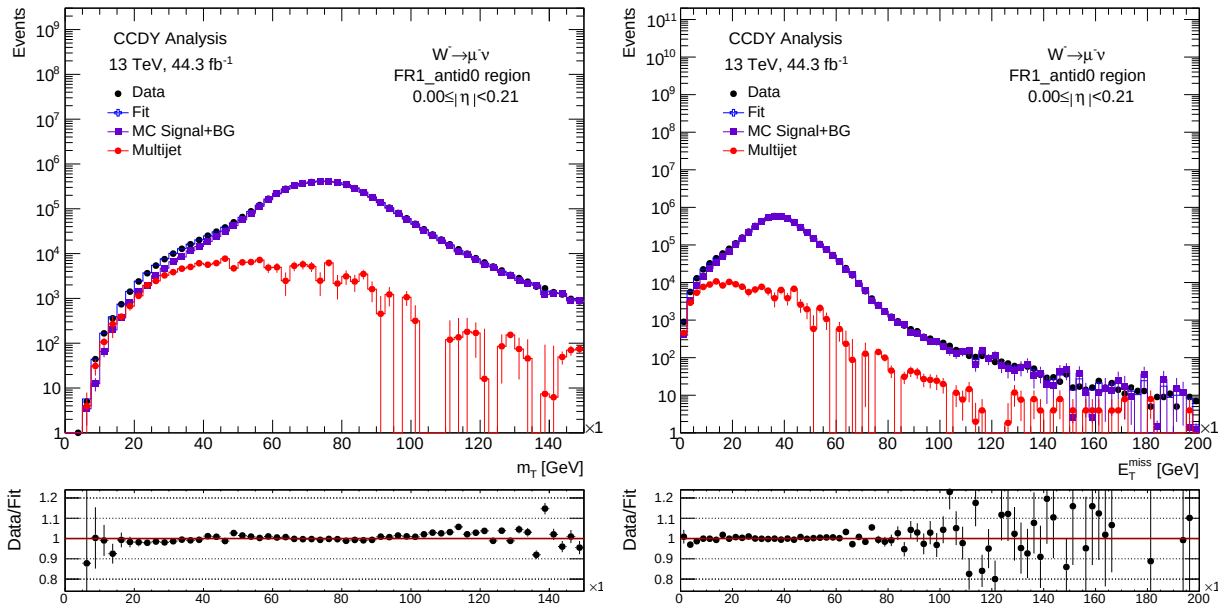

Figure A.7: Multijet normalisation plots. Transverse mass (left) and missing energy (right) distributions; these plots show the result of the fit and compares the result with data; moreover, the multijet and the simulation backgrounds are displayed.

Appendix B

First steps to calculate the theory uncertainties

As briefly discussed in Section 9.4, the theory uncertainties are very small; nevertheless, these uncertainties are not zero and their calculation requires extra steps with respect to the experimental uncertainties since they affect both the reconstruction and truth levels. This appendix presents the source of the theory uncertainties and the first steps to calculate their propagation, through the C_W unfolding factor, to the cross section and muon charge asymmetry measurements.

B.1 Theory uncertainties contributions

The theory uncertainties enter via the k_{Factor} correction defined in Equation (5.1), this definition assumes that the high order corrections to the cross section are factorised into QCD and electroweak contributions. Therefore, the uncertainties that appear in the k_{Factor} corrections are also factorised to cover the QCD and electroweak contributions.

The theory uncertainties from the QCD correction are summarised as follows:

- The variation of α_s[1] by ± 0.0003. This uncertainty is named as ALPHAS.
- The renormalisation μ_R and factorisation μ_F scales are simultaneously varied up and down by a factor of two at each invariant mass point. This uncertainty is called SCALE_W.
- An uncertainty arising from the beam energy plugged in the calculation of the cross section is considered and referred to as BEAM_ENERGY.

[1]The running QCD coupling α_s is identified with g_s established in Equation (2.19).

- The nominal PDF set uncertainties are evaluated using the standard prescription for Hessian PDF sets using a 90% confidence level eigenvector fluctuation; this uncertainty is referred to as PDF.
- A PDF choice uncertainty associated to the HERAPDF2.0 and NNPDF3.0 PDF sets is considered. These are named as CHOICE_HERAPDF2.0 and CHOICE_NNPDF3.0.
- The CT14 PDF eigenvectors are bundled into seven bundles with similar mass dependency; this helps preventing an overconstrain in the high mass PDF uncertainty, the bundles are named as PDF_V1,2,3,4,5,6,7.

The theory uncertainties from the electroweak corrections are applied in an additive way. The systematic uncertainty on these corrections is calculated by comparing the nominal k_{Factor} with corrections using a factorisation approach. These uncertainties cover higher effects in QED not considered by the MC generator, *i.e.* initial state radiation, interference among initial and final state radiation, and Sudakov logarithm single-loop corrections.

B.2 Theory uncertainties: reconstruction level

The theory variations at reconstructed level are calculated with Equation (9.1). The uncertainties in each pseudorapidity bin, displayed in Figure B.1, adopt the symmetric definition of Equation (9.5).

B.3 Theory uncertainties: next steps

To complete the calculation of the theory uncertainties is necessary to obtain their effect at truth level; furthermore, including the theory uncertainties to the measurements, a propagation of error is needed. The methodology to carry out this, should be closely related to the propagation of experimental uncertainties described in Section 11.3, nevertheless special care needs to be taken to cope with the dependence in both the numerator and denominator of the unfolding factor: it is expected that the theoretical uncertainties are largely cancelled trough this ratio, therefore a correlation study needs to be performed to complement the propagation. The total uncertainty should be the sum in quadrature of the experimental and theoretical uncertainties. These steps are not covered in this thesis and were left for continuing work.

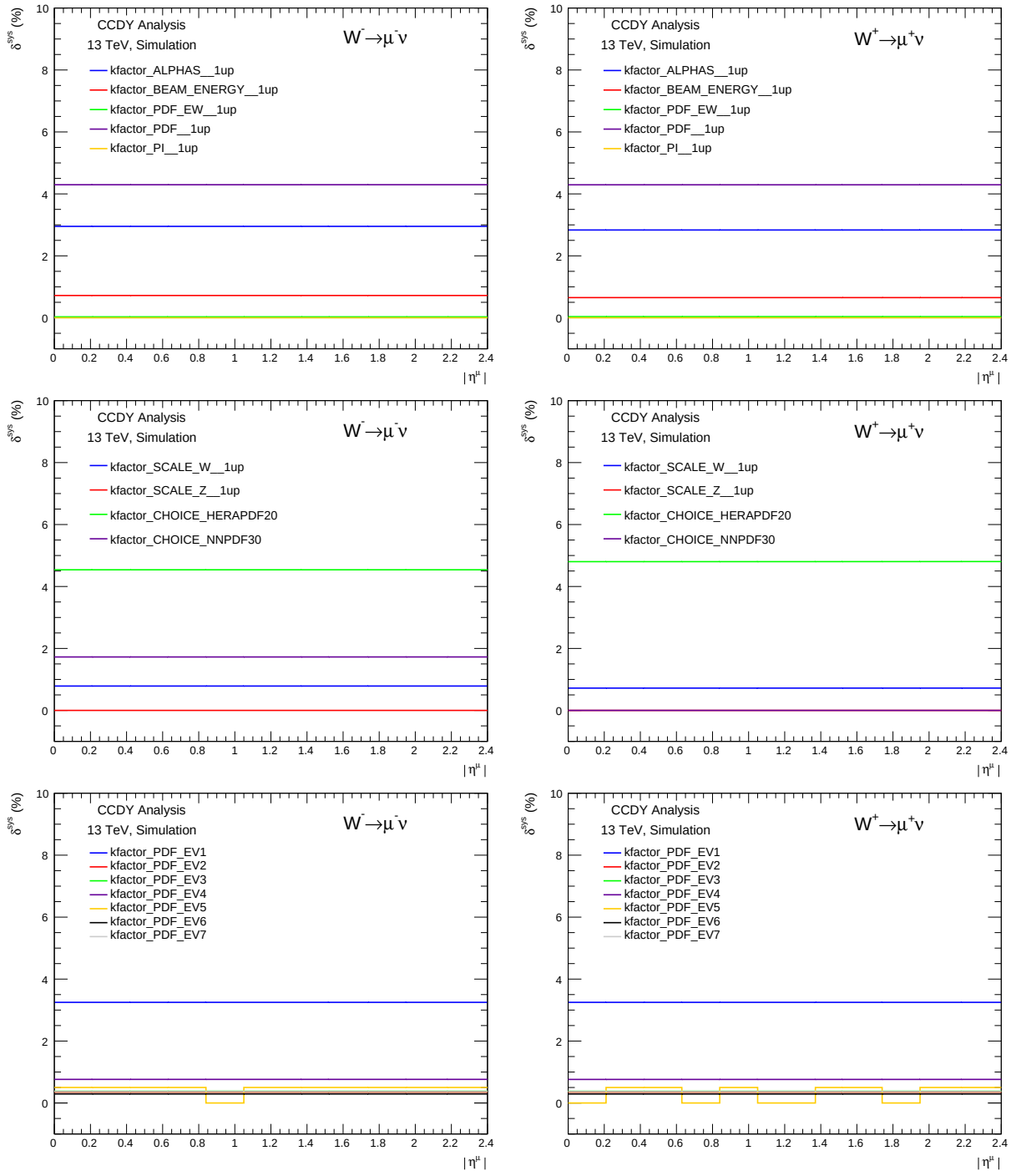

Figure B.1: These plots show the individual contributions of the systematic variations to the number of events, expressed in Equations (9.1) and (9.5), given differentially in $|\eta^{\mu}|$ bins. Here it is displayed the effect of jet uncertainties uncertainties. The plots on the left correspond to the W^{-} selection whereas the plots on the left correspond to the W^{+} selection. All the values are presented in percentage.

Appendix C

Systematic uncertainties in muon pseudorapidity bins

This appendix contains a detailed breakdown of the systematic uncertainties for every $|\eta^{\mu}|$ bin. The tables contained are the analogue of the inclusive Table 9.6. In the following a table corresponds to the muon pseudorapidity bins defined in Equation (11.3).

Systematic	$W^+(up)$	$W^+(down)$	$W^-(up)$	$W^-(down)$
MUON_ID	0.003	0.006	0.003	0.001
MUON_MS	0.010	0.012	0.010	0.008
MUON_SAGITTA_RESBIAS	0	0	0	0
MUON_SAGITTA_RHO	0	0	0	0
MUON_SCALE	0.078	0.075	0.074	0.071
MET_SoftTrk_ResoPara	0.244	0.244	0.183	0.183
MET_SoftTrk_ResoPerp	0.280	0.280	0.218	0.218
MET_SoftTrk_Scale	0.103	0.122	0.084	0.104
PileUp	0.528	0.581	0.518	0.568
IDStat	0.075	0.075	0.076	0.076
IDSys	0.801	0.801	0.819	0.819
IsoStat	0.013	0.013	0.013	0.013
IsoSys	0.205	0.205	0.205	0.205
TrigStat	0.272	0.269	0.272	0.269
TrigSys	0.592	0.585	0.592	0.585
TTVAStat	0.032	0.032	0.032	0.032
TTVASys	0.011	0.011	0.011	0.011
JET_EtaIntercalibration_NonClosure	0.001	0.001	0.001	0.000
JET_JER_DataVsMC	0.048	0.048	0.037	0.037
JET_GroupedNP_1	1.238	1.375	1.273	1.387
JET_GroupedNP_2	0.138	0.131	0.136	0.126
JET_GroupedNP_3	0.211	0.218	0.222	0.222
JET_JER_EffectiveNP_1	0.491	0.491	0.422	0.422
JET_JER_EffectiveNP_2	0.294	0.294	0.220	0.220
JET_JER_EffectiveNP_3	0.282	0.282	0.215	0.215
JET_JER_EffectiveNP_4	0.182	0.182	0.141	0.141
JET_JER_EffectiveNP_5	0.111	0.111	0.082	0.082
JET_JER_EffectiveNP_6	0.105	0.105	0.087	0.087
JET_JER_EffectiveNP_7restTerm	0.161	0.161	0.110	0.110

Table C.1: This table contains the contribution of each individual uncertainty in the $0.00 \leq |\eta^{\mu}| < 0.21$ bin, following the definition given in Equation (9.2). The first column indicates the name of the systematic; the second and third columns, corresponding to the $W^+ \to \mu^+\nu$, are the up and down variation respectively; the fourth and fifth columns, corresponding to the $W^- \to \mu^-\nu$, are the up and down variation respectively. In this table the symmetric uncertainty definition is not considered. All the values are presented in percentage.

Systematic	$W^+(up)$	$W^+(down)$	$W^-(up)$	$W^-(down)$
MUON_ID	0.007	0.005	0.006	0.009
MUON_MS	0.011	0.009	0.009	0.001
MUON_SAGITTA_RESBIAS	0	0	0	0
MUON_SAGITTA_RHO	0	0	0	0
MUON_SCALE	0.080	0.071	0.078	0.069
MET_SoftTrk_ResoPara	0.215	0.215	0.201	0.201
MET_SoftTrk_ResoPerp	0.266	0.266	0.215	0.215
MET_SoftTrk_Scale	0.118	0.126	0.118	0.104
PileUp	0.521	0.566	0.495	0.542
IDStat	0.033	0.033	0.033	0.033
IDSys	0.265	0.265	0.265	0.265
IsoStat	0.013	0.013	0.013	0.013
IsoSys	0.205	0.205	0.205	0.205
TrigStat	0.214	0.211	0.214	0.212
TrigSys	0.591	0.584	0.591	0.584
TTVAStat	0.021	0.021	0.022	0.022
TTVASys	0.002	0.002	0.002	0.002
JET_EtaIntercalibration_NonClosure	$8.041 \cdot 10^{-5}$	0.001	0.000	0.003
JET_JER_DataVsMC	0.087	0.087	0.100	0.100
JET_GroupedNP_1	1.278	1.364	1.280	1.351
JET_GroupedNP_2	0.135	0.126	0.134	0.136
JET_GroupedNP_3	0.211	0.230	0.211	0.219
JET_JER_EffectiveNP_1	0.442	0.442	0.431	0.431
JET_JER_EffectiveNP_2	0.271	0.271	0.272	0.272
JET_JER_EffectiveNP_3	0.273	0.273	0.265	0.265
JET_JER_EffectiveNP_4	0.182	0.182	0.169	0.169
JET_JER_EffectiveNP_5	0.081	0.081	0.071	0.071
JET_JER_EffectiveNP_6	0.100	0.100	0.099	0.099
JET_JER_EffectiveNP_7restTerm	0.149	0.149	0.142	0.142

Table C.2: This table contains the contribution of each individual uncertainty in the $0.21 \leq |\eta^{\mu}| < 0.42$ bin, following the definition given in Equation (9.2). The first column indicates the name of the systematic; the second and third columns, corresponding to the $W^+ \to \mu^+\nu$, are the up and down variation respectively; the fourth and fifth columns, corresponding to the $W^- \to \mu^-\nu$, are the up and down variation respectively. In this table the symmetric uncertainty definition is not considered. All the values are presented in percentage.

Systematic	$W^+(up)$	$W^+(down)$	$W^-(up)$	$W^-(down)$
MUON_ID	0.007	0.002	0.003	0.010
MUON_MS	0.031	0.002	0.006	0.007
MUON_SAGITTA_RESBIAS	0	0	0	0
MUON_SAGITTA_RHO	0	0	0	0
MUON_SCALE	0.082	0.093	0.070	0.085
MET_SoftTrk_ResoPara	0.187	0.187	0.203	0.203
MET_SoftTrk_ResoPerp	0.256	0.256	0.234	0.234
MET_SoftTrk_Scale	0.121	0.103	0.085	0.101
PileUp	0.582	0.633	0.561	0.630
IDStat	0.034	0.034	0.034	0.034
IDSys	0.268	0.268	0.268	0.268
IsoStat	0.013	0.013	0.013	0.013
IsoSys	0.205	0.205	0.205	0.205
TrigStat	0.196	0.193	0.196	0.193
TrigSys	0.591	0.584	0.591	0.584
TTVAStat	0.020	0.020	0.020	0.020
TTVASys	0.002	0.002	0.002	0.002
ALPHAS	0	0	0	0
JET_EtaIntercalibration_NonClosure	0.000	0.001	0.001	0.000
JET_JER_DataVsMC	0.100	0.100	0.105	0.105
JET_GroupedNP_1	1.264	1.357	1.240	1.351
JET_GroupedNP_2	0.131	0.124	0.119	0.127
JET_GroupedNP_3	0.209	0.226	0.197	0.209
JET_JER_EffectiveNP_1	0.419	0.419	0.444	0.444
JET_JER_EffectiveNP_2	0.284	0.284	0.254	0.254
JET_JER_EffectiveNP_3	0.301	0.301	0.262	0.262
JET_JER_EffectiveNP_4	0.182	0.182	0.168	0.168
JET_JER_EffectiveNP_5	0.067	0.067	0.065	0.065
JET_JER_EffectiveNP_6	0.086	0.086	0.084	0.084
JET_JER_EffectiveNP_7restTerm	0.159	0.159	0.136	0.136

Table C.3: This table contains the contribution of each individual uncertainty in the $0.42 \leq |\eta^{\mu}| < 0.63$ bin, following the definition given in Equation (9.2). The first column indicates the name of the systematic; the second and third columns, corresponding to the $W^+ \to \mu^+\nu$, are the up and down variation respectively; the fourth and fifth columns, corresponding to the $W^- \to \mu^-\nu$, are the up and down variation respectively. In this table the symmetric uncertainty definition is not considered. All the values are presented in percentage.

Systematic	$W^+(up)$	$W^+(down)$	$W^-(up)$	$W^-(down)$
MUON_ID	0.002	0.015	0.008	0.014
MUON_MS	0.009	0.011	0.007	0.004
MUON_SAGITTA_RESBIAS	0	0	0	0
MUON_SAGITTA_RHO	0	0	0	0
MUON_SCALE	0.094	0.106	0.091	0.114
MET_SoftTrk_ResoPara	0.192	0.192	0.191	0.191
MET_SoftTrk_ResoPerp	0.241	0.241	0.198	0.198
MET_SoftTrk_Scale	0.118	0.107	0.088	0.099
PileUp	0.566	0.634	0.577	0.615
IDStat	0.038	0.038	0.038	0.038
IDSys	0.261	0.261	0.260	0.260
IsoStat	0.013	0.013	0.013	0.013
IsoSys	0.205	0.205	0.205	0.205
TrigStat	0.295	0.292	0.294	0.290
TrigSys	0.591	0.584	0.592	0.584
TTVAStat	0.019	0.019	0.019	0.019
TTVASys	0.008	0.008	0.008	0.008
JET_EtaIntercalibration_NonClosure	$4.905 \cdot 10^{-5}$	0.000	0.000	0.000
JET_JER_DataVsMC	0.076	0.076	0.069	0.069
JET_GroupedNP_1	1.250	1.324	1.251	1.347
JET_GroupedNP_2	0.122	0.121	0.130	0.139
JET_GroupedNP_3	0.233	0.235	0.224	0.224
JET_JER_EffectiveNP_1	0.410	0.410	0.441	0.441
JET_JER_EffectiveNP_2	0.236	0.236	0.253	0.253
JET_JER_EffectiveNP_3	0.241	0.241	0.257	0.257
JET_JER_EffectiveNP_4	0.164	0.164	0.154	0.154
JET_JER_EffectiveNP_5	0.055	0.055	0.047	0.047
JET_JER_EffectiveNP_6	0.064	0.064	0.069	0.069
JET_JER_EffectiveNP_7restTerm	0.124	0.124	0.146	0.146

Table C.4: This table contains the contribution of each individual uncertainty in the $0.63 \leq |\eta^{\mu}| < 0.84$ bin, following the definition given in Equation (9.2). The first column indicates the name of the systematic; the second and third columns, corresponding to the $W^+ \to \mu^+\nu$, are the up and down variation respectively; the fourth and fifth columns, corresponding to the $W^- \to \mu^-\nu$, are the up and down variation respectively. In this table the symmetric uncertainty definition is not considered. All the values are presented in percentage.

Systematic	$W^+(up)$	$W^+(down)$	$W^-(up)$	$W^-(down)$
MUON_ID	0.003	0.002	0.006	0.005
MUON_MS	0.012	0.006	0.001	0.004
MUON_SAGITTA_RESBIAS	0	0	0	0
MUON_SAGITTA_RHO	0	0	0	0
MUON_SCALE	0.158	0.203	0.136	0.176
MET_SoftTrk_ResoPara	0.228	0.228	0.182	0.182
MET_SoftTrk_ResoPerp	0.262	0.262	0.229	0.229
MET_SoftTrk_Scale	0.122	0.110	0.073	0.087
PileUp	0.551	0.608	0.555	0.599
IDStat	0.042	0.042	0.042	0.042
IDSys	0.256	0.256	0.254	0.254
IsoStat	0.013	0.013	0.013	0.013
IsoSys	0.205	0.205	0.205	0.205
TrigStat	0.271	0.268	0.271	0.268
TrigSys	0.592	0.585	0.591	0.584
TTVAStat	0.018	0.018	0.018	0.018
TTVASys	0.002	0.002	0.002	0.002
JET_EtaIntercalibration_NonClosure	0.001	0.001	0.001	0.001
JET_JER_DataVsMC	0.052	0.052	0.080	0.080
JET_GroupedNP_1	1.241	1.275	1.219	1.335
JET_GroupedNP_2	0.116	0.104	0.098	0.131
JET_GroupedNP_3	0.249	0.230	0.231	0.245
JET_JER_EffectiveNP_1	0.379	0.379	0.437	0.437
JET_JER_EffectiveNP_2	0.193	0.193	0.270	0.270
JET_JER_EffectiveNP_3	0.197	0.197	0.275	0.275
JET_JER_EffectiveNP_4	0.129	0.129	0.189	0.189
JET_JER_EffectiveNP_5	0.036	0.036	0.074	0.074
JET_JER_EffectiveNP_6	0.058	0.058	0.098	0.098
JET_JER_EffectiveNP_7restTerm	0.110	0.110	0.161	0.161

Table C.5: This table contains the contribution of each individual uncertainty in the $0.84 \leq |\eta^{\mu}| < 1.05$ bin, following the definition given in Equation (9.2). The first column indicates the name of the systematic; the second and third columns, corresponding to the $W^+ \to \mu^+\nu$, are the up and down variation respectively; the fourth and fifth columns, corresponding to the $W^- \to \mu^-\nu$, are the up and down variation respectively. In this table the symmetric uncertainty definition is not considered. All the values are presented in percentage.

Systematic	$W^+(up)$	$W^+(down)$	$W^-(up)$	$W^-(down)$
MUON_ID	0.002	0.000	0.010	0.008
MUON_MS	0.022	0.008	0.014	0.004
MUON_SAGITTA_RESBIAS	0	0	0	0
MUON_SAGITTA_RHO	0	0	0	0
MUON_SCALE	0.155	0.245	0.141	0.219
MET_SoftTrk_ResoPara	0.205	0.205	0.192	0.192
MET_SoftTrk_ResoPerp	0.258	0.258	0.215	0.215
MET_SoftTrk_Scale	0.099	0.113	0.097	0.096
PileUp	0.628	0.687	0.577	0.641
IDStat	0.062	0.062	0.062	0.062
IDSys	0.267	0.267	0.265	0.265
IsoStat	0.013	0.013	0.013	0.013
IsoSys	0.205	0.205	0.205	0.205
TrigStat	0.191	0.182	0.194	0.184
TrigSys	0.428	0.424	0.428	0.424
TTVAStat	0.017	0.017	0.017	0.017
TTVASys	0.004	0.004	0.004	0.004
JET_EtaIntercalibration_NonClosure	0.001	0.001	0.001	0.002
JET_JER_DataVsMC	0.091	0.091	0.087	0.087
JET_GroupedNP_1	1.305	1.388	1.331	1.416
JET_GroupedNP_2	0.116	0.129	0.127	0.130
JET_GroupedNP_3	0.267	0.287	0.266	0.264
JET_JER_EffectiveNP_1	0.452	0.452	0.432	0.432
JET_JER_EffectiveNP_2	0.267	0.267	0.240	0.240
JET_JER_EffectiveNP_3	0.264	0.264	0.239	0.239
JET_JER_EffectiveNP_4	0.189	0.189	0.165	0.165
JET_JER_EffectiveNP_5	0.082	0.082	0.065	0.065
JET_JER_EffectiveNP_6	0.098	0.098	0.085	0.085
JET_JER_EffectiveNP_7restTerm	0.177	0.177	0.150	0.150

Table C.6: This table contains the contribution of each individual uncertainty in the $1.05 \leq |\eta^{\mu}| < 1.37$ bin, following the definition given in Equation (9.2). The first column indicates the name of the systematic; the second and third columns, corresponding to the $W^+ \to \mu^+\nu$, are the up and down variation respectively; the fourth and fifth columns, corresponding to the $W^- \to \mu^-\nu$, are the up and down variation respectively. In this table the symmetric uncertainty definition is not considered. All the values are presented in percentage.

Systematic	$W^+(up)$	$W^+(down)$	$W^-(up)$	$W^-(down)$
MUON_ID	0.006	0.009	0.006	0.007
MUON_MS	0.008	0.002	0.013	0.011
MUON_SAGITTA_RESBIAS	0	0	0	0
MUON_SAGITTA_RHO	0	0	0	0
MUON_SCALE	0.134	0.188	0.125	0.165
MET_SoftTrk_ResoPara	0.186	0.186	0.195	0.195
MET_SoftTrk_ResoPerp	0.220	0.220	0.207	0.207
MET_SoftTrk_Scale	0.096	0.091	0.088	0.101
PileUp	0.595	0.640	0.541	0.620
IDStat	0.055	0.055	0.055	0.055
IDSys	0.246	0.246	0.245	0.245
IsoStat	0.013	0.013	0.013	0.013
IsoSys	0.205	0.205	0.205	0.205
TrigStat	0.125	0.121	0.125	0.121
TrigSys	0.428	0.424	0.428	0.424
TTVAStat	0.016	0.016	0.016	0.016
TTVASys	0.008	0.008	0.008	0.008
JET_EtaIntercalibration_NonClosure	0.001	0.000	0.001	0.001
JET_JER_DataVsMC	0.093	0.093	0.119	0.119
JET_GroupedNP_1	1.234	1.294	1.214	1.307
JET_GroupedNP_2	0.113	0.111	0.119	0.127
JET_GroupedNP_3	0.252	0.272	0.265	0.251
JET_JER_EffectiveNP_1	0.437	0.437	0.412	0.412
JET_JER_EffectiveNP_2	0.239	0.239	0.225	0.225
JET_JER_EffectiveNP_3	0.206	0.206	0.205	0.205
JET_JER_EffectiveNP_4	0.155	0.155	0.127	0.127
JET_JER_EffectiveNP_5	0.079	0.079	0.049	0.049
JET_JER_EffectiveNP_6	0.080	0.080	0.070	0.070
JET_JER_EffectiveNP_7restTerm	0.128	0.128	0.112	0.112

Table C.7: This table contains the contribution of each individual uncertainty in the $1.37 \leq |\eta^{\mu}| < 1.52$ bin, following the definition given in Equation (9.2). The first column indicates the name of the systematic; the second and third columns, corresponding to the $W^+ \to \mu^+\nu$, are the up and down variation respectively; the fourth and fifth columns, corresponding to the $W^- \to \mu^-\nu$, are the up and down variation respectively. In this table the symmetric uncertainty definition is not considered. All the values are presented in percentage.

Systematic	$W^+(up)$	$W^+(down)$	$W^-(up)$	$W^-(down)$
MUON_ID	0.006	0.004	0.012	0.019
MUON_MS	0.009	0.007	0.022	0.001
MUON_SAGITTA_RESBIAS	0	0	0	0
MUON_SAGITTA_RHO	0	0	0	0
MUON_SCALE	0.234	0.198	0.208	0.179
MET_SoftTrk_ResoPara	0.204	0.204	0.226	0.226
MET_SoftTrk_ResoPerp	0.232	0.232	0.219	0.219
MET_SoftTrk_Scale	0.102	0.090	0.091	0.105
PileUp	0.582	0.644	0.549	0.611
IDStat	0.048	0.048	0.048	0.048
IDSys	0.292	0.292	0.292	0.292
IsoStat	0.013	0.013	0.013	0.013
IsoSys	0.205	0.205	0.205	0.205
TrigStat	0.116	0.112	0.115	0.111
TrigSys	0.428	0.424	0.428	0.424
TTVAStat	0.015	0.015	0.015	0.015
TTVASys	0.010	0.010	0.010	0.010
JET_EtaIntercalibration_NonClosure	0.001	0.003	0.001	0.000
JET_JER_DataVsMC	0.129	0.129	0.109	0.109
JET_GroupedNP_1	1.181	1.271	1.204	1.320
JET_GroupedNP_2	0.114	0.100	0.116	0.113
JET_GroupedNP_3	0.268	0.273	0.256	0.260
JET_JER_EffectiveNP_1	0.419	0.419	0.408	0.408
JET_JER_EffectiveNP_2	0.218	0.218	0.188	0.188
JET_JER_EffectiveNP_3	0.204	0.204	0.185	0.185
JET_JER_EffectiveNP_4	0.136	0.136	0.151	0.151
JET_JER_EffectiveNP_5	0.055	0.055	0.064	0.064
JET_JER_EffectiveNP_6	0.058	0.058	0.074	0.074
JET_JER_EffectiveNP_7restTerm	0.112	0.112	0.117	0.117

Table C.8: This table contains the contribution of each individual uncertainty in the $1.52 \leq |\eta^{\mu}| < 1.74$ bin, following the definition given in Equation (9.2). The first column indicates the name of the systematic; the second and third columns, corresponding to the $W^+ \to \mu^+\nu$, are the up and down variation respectively; the fourth and fifth columns, corresponding to the $W^- \to \mu^-\nu$, are the up and down variation respectively. In this table the symmetric uncertainty definition is not considered. All the values are presented in percentage.

Systematic	$W^+(up)$	$W^+(down)$	$W^-(up)$	$W^-(down)$
MUON_ID	0.005	0.004	0.007	0.000
MUON_MS	0.000	0.014	0.016	0.009
MUON_SAGITTA_RESBIAS	0	0	0	0
MUON_SAGITTA_RHO	0	0	0	0
MUON_SCALE	0.176	0.171	0.159	0.148
MET_SoftTrk_ResoPara	0.218	0.218	0.173	0.173
MET_SoftTrk_ResoPerp	0.222	0.222	0.251	0.251
MET_SoftTrk_Scale	0.085	0.096	0.096	0.095
PileUp	0.621	0.675	0.572	0.641
IDStat	0.044	0.044	0.044	0.044
IDSys	0.317	0.317	0.317	0.317
IsoStat	0.013	0.013	0.013	0.013
IsoSys	0.205	0.205	0.205	0.205
TrigStat	0.109	0.105	0.109	0.105
TrigSys	0.428	0.424	0.428	0.424
TTVAStat	0.015	0.015	0.015	0.015
TTVASys	0.008	0.008	0.008	0.008
JET_EtaIntercalibration_NonClosure	0.002	0.001	0.001	0.001
JET_JER_DataVsMC	0.137	0.137	0.147	0.147
JET_GroupedNP_1	1.205	1.314	1.236	1.271
JET_GroupedNP_2	0.116	0.116	0.125	0.124
JET_GroupedNP_3	0.275	0.293	0.270	0.276
JET_JER_EffectiveNP_1	0.423	0.423	0.397	0.397
JET_JER_EffectiveNP_2	0.233	0.233	0.192	0.192
JET_JER_EffectiveNP_3	0.219	0.219	0.174	0.174
JET_JER_EffectiveNP_4	0.160	0.160	0.142	0.142
JET_JER_EffectiveNP_5	0.067	0.067	0.069	0.069
JET_JER_EffectiveNP_6	0.082	0.082	0.083	0.083
JET_JER_EffectiveNP_7restTerm	0.127	0.127	0.127	0.127

Table C.9: This table contains the contribution of each individual uncertainty in the $1.74 \leq |\eta^{\mu}| < 1.95$ bin, following the definition given in Equation (9.2). The first column indicates the name of the systematic; the second and third columns, corresponding to the $W^+ \to \mu^+\nu$, are the up and down variation respectively; the fourth and fifth columns, corresponding to the $W^- \to \mu^-\nu$, are the up and down variation respectively. In this table the symmetric uncertainty definition is not considered. All the values are presented in percentage.

Systematic	$W^+(up)$	$W^+(down)$	$W^-(up)$	$W^-(down)$
MUON_ID	0.015	0.021	0.010	0.021
MUON_MS	0.017	0.010	0.018	0.006
MUON_SAGITTA_RESBIAS	0	0	0	0
MUON_SAGITTA_RHO	0	0	0	0
MUON_SCALE	0.229	0.179	0.207	0.158
MET_SoftTrk_ResoPara	0.193	0.193	0.197	0.197
MET_SoftTrk_ResoPerp	0.216	0.216	0.241	0.241
MET_SoftTrk_Scale	0.073	0.082	0.079	0.094
PileUp	0.622	0.693	0.625	0.691
IDStat	0.048	0.048	0.048	0.048
IDSys	0.281	0.281	0.281	0.281
IsoStat	0.013	0.013	0.013	0.013
IsoSys	0.205	0.205	0.205	0.205
TrigStat	0.108	0.105	0.109	0.105
TrigSys	0.427	0.424	0.428	0.424
TTVAStat	0.014	0.014	0.014	0.014
TTVASys	0.002	0.002	0.002	0.002
JET_EtaIntercalibration_NonClosure	0.002	0.001	0.001	0.001
JET_JER_DataVsMC	0.165	0.165	0.161	0.161
JET_GroupedNP_1	1.189	1.302	1.180	1.345
JET_GroupedNP_2	0.114	0.118	0.106	0.124
JET_GroupedNP_3	0.278	0.298	0.247	0.272
JET_JER_EffectiveNP_1	0.464	0.464	0.444	0.444
JET_JER_EffectiveNP_2	0.251	0.251	0.248	0.248
JET_JER_EffectiveNP_3	0.214	0.214	0.213	0.213
JET_JER_EffectiveNP_4	0.171	0.171	0.171	0.171
JET_JER_EffectiveNP_5	0.083	0.083	0.070	0.070
JET_JER_EffectiveNP_6	0.100	0.100	0.077	0.077
JET_JER_EffectiveNP_7restTerm	0.155	0.155	0.150	0.150

Table C.10: This table contains the contribution of each individual uncertainty in the $1.95 \leq |\eta^{\mu}| < 2.18$ bin, following the definition given in Equation (9.2). The first column indicates the name of the systematic; the second and third columns, corresponding to the $W^+ \to \mu^+\nu$, are the up and down variation respectively; the fourth and fifth columns, corresponding to the $W^- \to \mu^-\nu$, are the up and down variation respectively. In this table the symmetric uncertainty definition is not considered. All the values are presented in percentage.

Systematic	$W^+(up)$	$W^+(down)$	$W^-(up)$	$W^-(down)$
MUON_ID	0.017	0.008	0.018	0.033
MUON_MS	0.008	0.005	0.028	0.010
MUON_SAGITTA_RESBIAS	0	0	0	0
MUON_SAGITTA_RHO	0	0	0	0
MUON_SCALE	0.400	0.333	0.357	0.283
MET_SoftTrk_ResoPara	0.184	0.184	0.187	0.187
MET_SoftTrk_ResoPerp	0.220	0.220	0.207	0.207
MET_SoftTrk_Scale	0.054	0.070	0.087	0.081
PileUp	0.615	0.677	0.586	0.652
IDStat	0.048	0.048	0.048	0.048
IDSys	0.271	0.271	0.271	0.271
IsoStat	0.013	0.013	0.013	0.013
IsoSys	0.205	0.205	0.205	0.205
TrigStat	0.108	0.105	0.108	0.105
TrigSys	0.428	0.424	0.428	0.424
TTVAStat	0.015	0.015	0.015	0.015
TTVASys	0.003	0.003	0.003	0.003
JET_EtaIntercalibration_NonClosure	0.001	0.002	0.001	0.001
JET_JER_DataVsMC	0.153	0.153	0.142	0.142
JET_GroupedNP_1	1.122	1.235	1.163	1.278
JET_GroupedNP_2	0.093	0.097	0.102	0.116
JET_GroupedNP_3	0.276	0.287	0.260	0.281
JET_JER_EffectiveNP_1	0.493	0.493	0.413	0.413
JET_JER_EffectiveNP_2	0.241	0.241	0.202	0.202
JET_JER_EffectiveNP_3	0.217	0.217	0.207	0.207
JET_JER_EffectiveNP_4	0.155	0.155	0.166	0.166
JET_JER_EffectiveNP_5	0.081	0.081	0.079	0.079
JET_JER_EffectiveNP_6	0.097	0.097	0.093	0.093
JET_JER_EffectiveNP_7restTerm	0.134	0.134	0.140	0.140

Table C.11: This table contains the contribution of each individual uncertainty in the $2.18 \leq |\eta^{\mu}| < 2.40$ bin, following the definition given in Equation (9.2). The first column indicates the name of the systematic; the second and third columns, corresponding to the $W^+ \to \mu^+\nu$, are the up and down variation respectively; the fourth and fifth columns, corresponding to the $W^- \to \mu^-\nu$, are the up and down variation respectively. In this table the symmetric uncertainty definition is not considered. All the values are presented in percentage.

Bibliography

[1] "CERN website LHC, description." https://home.cern. Accessed: 2018-04-12. 14

[2] A. Salam, "Renormalizability of gauge theories," *Phys. Rev.*, vol. 127, pp. 331–334, Jul 1962. 17, 18

[3] G. S. Guralnik, C. R. Hagen, and T. W. B. Kibble, "Global conservation laws and massless particles," *Phys. Rev. Lett.*, vol. 13, pp. 585–587, Nov 1964. 18

[4] Tanabashi et.al., "Review of particle physics," *Phys. Rev. D*, vol. 98, p. 030001, Aug 2018. 18, 19, 84, 217

[5] Bagnaia, P. and M. Banner and Hansen and Jorn Dines and Hansen and John Renner and Hansen and Peter Henrik and Nilsson and Bjorn Stefan, "Evidence for $Z \to e^+e^-$ at the CERN collider," *Physics Letters B: Particle Physics, Nuclear Physics and Cosmology*, vol. 129, pp. 130–140, 9 1983. 23

[6] G. Arnison and et. al, "Experimental observation of isolated large transverse energy electrons with associated missing energy at $\sqrt{s}$ =540 GeV," *Physics Letters B*, vol. 122, no. 1, pp. 103 – 116, 1983. 23

[7] E. Perez and E. Rizvi, "The quark and gluon structure of the proton," *Reports on Progress in Physics*, vol. 76, no. 4, p. 046201, 2013. 24, 29

[8] F. Close, "The quark parton model," *Reports on Progress in Physics*, vol. 42, no. 8, p. 1285, 1979. 24

[9] A. Buckley, J. Ferrando, S. Lloyd, K. Nordström, B. Page, M. Rüfenacht, M. Schönherr, and G. Watt, "LHAPDF6: parton density access in the LHC precision era," *The European Physical Journal C*, vol. 75, p. 132, Mar 2015. 25

[10] S. Dulat, T.-J. Hou, J. Gao, M. Guzzi, J. Huston, P. Nadolsky, J. Pumplin, C. Schmidt, D. Stump, and C.-P. Yuan, "New parton distribution functions from a global analysis of quantum chromodynamics," *Phys. Rev. D*, vol. 93, p. 033006, Feb 2016. 136

[11] L. A. Harland-Lang, A. D. Martin, P. Motylinski, and R. S. Thorne, "Parton distributions in the LHC era: MMHT 2014 PDFs," *The European Physical Journal C*, vol. 75, p. 204, May 2015.

[12] The NNPDF collaboration, R. D. Ball, V. Bertone, S. Carrazza, C. S. Deans, L. Del Debbio, S. Forte, A. Guffanti, N. P. Hartland, J. I. Latorre, J. Rojo, and M. Ubiali, "Parton distributions for the LHC run II," *Journal of High Energy Physics*, vol. 2015, p. 40, Apr 2015. 25, 28, 29, 205

[13] R. Hickling, *Measuring the Drell-Yan Cross Section at High Mass in the Dimuon Channel*. PhD thesis, Queen Mary University of London, 2015. PhD. thesis. 27, 205

[14] S. D. Drell and T.-M. Yan, "Massive lepton-pair production in hadron-hadron collisions at high energies," *Phys. Rev. Lett.*, vol. 25, pp. 316–320, Aug 1970. 25

[15] J. M. Campbell, J. W. Huston, and W. J. Stirling, "Hard interactions of quarks and gluons: a primer for LHC physics," *Reports on Progress in Physics*, vol. 70, no. 1, p. 89, 2007. 25

[16] M. Klein and R. Yoshida, "Collider physics at HERA," *Progress in Particle and Nuclear Physics*, vol. 61, no. 2, pp. 343 – 393, 2008. 29

[17] I. A. et.al., "Measurement of the proton structure function $F_2(x, Q^2)$ in the low-x region at HERA," *Nuclear Physics B*, vol. 407, no. 3, pp. 515 – 535, 1993. 29

[18] ZEUS collaboration, "Measurement of high-Q^2 charged current deep inelastic scattering cross sections with a longitudinally polarised positron beam at HERA," *The European Physical Journal C*, vol. 70, pp. 945–963, Dec 2010. 29

[19] G. Moreno, C. N. Brown, W. E. Cooper, D. Finley, Y. B. Hsiung, A. M. Jonckheere, H. Jostlein, D. M. Kaplan, L. M. Lederman, Y. Hemmi, K. Imai, K. Miyake, T. Nakamura, N. Sasao, N. Tamura, T. Yoshida, A. Maki, Y. Sakai, R. Gray, K. B. Luk, J. P. Rutherfoord, P. B. Straub, R. W. Williams, K. K. Young, M. R. Adams, H. Glass, D. Jaffe, R. L. McCarthy, J. A. Crittenden, and S. R. Smith, "Dimuon production in proton-copper collisions at $\sqrt{s} = 38.8$ GeV," *Phys. Rev. D*, vol. 43, pp. 2815–2835, May 1991. 29

[20] P. L. McGaughey, J. M. Moss, D. M. Alde, H. W. Baer, T. A. Carey, G. T. Garvey, A. Klein, C. Lee, M. J. Leitch, J. Lillberg, C. S. Mishra, C. N. Brown, W. E. Cooper, Y. B. Hsiung, M. R. Adams, R. Guo, D. M. Kaplan, R. L. McCarthy, G. Danner,

M. Wang, M. Barlett, and G. Hoffmann, "Erratum: Cross sections for the production of high-mass muon pairs from 800 GeV proton bombardment of ^{2}H [Phys. Rev. D 50, 3038 (1994)]," *Phys. Rev. D*, vol. 60, p. 119903, Oct 1999. 29

[21] C. Collaboration, "Measurement of the lepton charge asymmetry in W-boson decays produced in $p\overline{p}$ collisions," *Phys. Rev. Lett.*, vol. 81, pp. 5754–5759, Dec 1998. 29, 30

[22] D0 Collaboration, "Measurement of the muon charge asymmetry from W boson decays," *Phys. Rev. D*, vol. 77, p. 011106, Jan 2008. 29, 30

[23] D0 Collaboration, "Measurement of the shape of the boson rapidity distribution for $p\overline{p} \to Z/\gamma^* \to e^+e^- + X$ events produced at $\sqrt{s}$ of 1.96 TeV," *Phys. Rev. D*, vol. 76, p. 012003, Jul 2007. 29

[24] T. Aaltonen, *et.al.*, "Measurement of $d\sigma/dy$ of Drell-Yan e^+e^- pairs in the Z mass region from $p\overline{p}$ collisions at $\sqrt{s} = 1.96$ TeV," *Physics Letters B*, vol. 692, no. 4, pp. 232–239, 2010. 29

[25] CDF Collaboration, "Charge Asymmetry in W-Boson Decays Produced in $p\overline{p}$ Collisions at $\sqrt{s} = 1.8$ TeV," *Phys. Rev. Lett.*, vol. 74, pp. 850–854, Feb 1995. 30

[26] D0 Collaboration, "Measurement of the Electron Charge Asymmetry in $p\overline{p} \to W + X \to e\nu + X$ Events at $\sqrt{s} = 1.96$ TeV," *Phys. Rev. Lett.*, vol. 101, p. 211801, Nov 2008. 30

[27] CDF Collaboration, "Direct Measurement of the W Production Charge Asymmetry in $p\overline{p}$ Collisions at $\sqrt{s} = 1.96$ TeV," *Phys. Rev. Lett.*, vol. 102, p. 181801, May 2009. 30

[28] ATLAS Collaboration, "Measurement of the W charge asymmetry in the $W \to \mu\nu$ decay mode in pp collisions at $\sqrt{s} = 7$ TeV with the ATLAS detector," *Physics Letters B*, vol. 701, no. 1, pp. 31 – 49, 2011. 30

[29] CMS Collaboration, "Measurement of the lepton charge asymmetry in inclusive W production in pp collisions at $\sqrt{s} =$ TeV," *Journal of High Energy Physics*, vol. 2011, p. 50, Apr 2011. 30

[30] CMS Collaboration, "Measurement of the Electron Charge Asymmetry in Inclusive W Production in pp Collisions at $\sqrt{s} = 7$ TeV," *Phys. Rev. Lett.*, vol. 109, p. 111806, Sep 2012. 30

[31] CMS collaboration, "Measurement of the muon charge asymmetry in inclusive $pp \to W + X$ production at $\sqrt{s} = 7$ TeV and an improved determination of light parton distribution functions," *Phys. Rev. D*, vol. 90, p. 032004, Aug 2014. 30

[32] "CERN accelerator webpage, https://home.cern/science/accelerators." 32, 33, 205

[33] V. Khoze, A. Martin, R. Orava, and M. Ryskin, "Luminosity measuring processes at the LHC," *The European Physical Journal C - Particles and Fields*, vol. 19, pp. 313–322, Feb 2001. 32

[34] L. Evans and P. Bryant, "LHC Machine," *Journal of Instrumentation*, vol. 3, no. 08, p. S08001, 2008. 33, 34

[35] G. Soyez, *Pileup mitigation at the LHC, A theorist's view*. PhD thesis, Institut de Physique Theorique, CEA Saclay, 2018. PhD. thesis. 33

[36] "http://twiki.cern.ch/twiki/bin/view/AtlasPublic/LuminosityPublicResultsRun2." 34, 205

[37] L. Armitage, *Measurement of the Drell-Yan triple-differential cross-section in pp collisions at $\sqrt{s}$ = 8 TeV with the ATLAS detector*. PhD thesis, Queen Mary University of London, 2016. PhD. thesis. 35

[38] ATLAS Collaboration, "The ATLAS Experiment at the CERN Large Hadron Collider," *Journal of Instrumentation*, vol. 3, no. 08, p. S08003, 2008. 36, 37, 38, 39, 42, 43, 46, 205

[39] ATLAS Collaboration, "Measurement of the top quark pair production cross-section with atlas in the single lepton channel," *Physics Letters B*, vol. 711, no. 3, pp. 244 – 263, 2012. 70

[40] "https://atlas-tagservices.cern.ch/tagservices/RunBrowser/index.html." 71, 218

[41] "Athena framework webpage, https://atlassoftwaredocs.web.cern.ch/athena/." 70, 71

[42] "Physics Modelling Group (PMG) twiki page, https://twiki.cern.ch/twiki/bin/view/AtlasProtected/PhysicsModellingGroup." 71

[43] P. Nason, "A new method for combining NLO QCD with shower Monte Carlo algorithms," *Journal of High Energy Physics*, vol. 2004, no. 11, p. 040, 2004. 73

[44] S. Alioli, P. Nason, C. Oleari, and E. Re, "NLO vector-boson production matched with shower in POWHEG," *Journal of High Energy Physics*, vol. 2008, no. 07, p. 060, 2008.

[45] C. Oleari, "The POWHEG BOX," *Nuclear Physics B - Proceedings Supplements*, vol. 205-206, pp. 36 – 41, 2010. Loops and Legs in Quantum Field Theory. 73

[46] T. Sjostrand, S. Mrenna, and P. Skands, "A brief introduction to PYTHIA 8.1," *Computer Physics Communications*, vol. 178, no. 11, pp. 852 – 867, 2008. 73

[47] P. Golonka and Z. Was, "PHOTOS Monte Carlo: a precision tool for QED corrections in Z and W decays," *The European Physical Journal C - Particles and Fields*, vol. 45, pp. 97–107, Jan 2006. 73, 74

[48] M. Guzzi, P. Nadolsky, E. Berger, H. L. Lai, F. Olness, and C. Yuan, "CT10 parton distributions and other developments in the global QCD analysis," 2006. 74

[49] ATLAS collaboration, "Measurement of the Z/γ* boson transverse momentum distribution in pp collisions at $\sqrt{s}$ =7 TeV with the ATLAS detector," *Journal of High Energy Physics*, vol. 2014, p. 145, Sep 2014. 74

[50] GEANT Collaboration, "Geant4-a simulation toolkit," *Nuclear Instruments and Methods in Physics Research Section A: Accelerators, Spectrometers, Detectors and Associated Equipment*, vol. 506, no. 3, pp. 250 – 303, 2003. 75

[51] "ATLAS Metadata Interface, `https://ami.in2p3.fr/`." 76

[52] J. R. Andersen *et al.*, "Les Houches 2013: Physics at TeV Colliders: Standard Model Working Group Report," vol. arXiv:1405.1067, 2014. 77

[53] ATLAS Collaboration, "Muon reconstruction performance of the ATLAS detector in proton-proton collision data at $\sqrt{s}$ =13 TeV," *The European Physical Journal C*, vol. 76, p. 292, May 2016. 84, 86, 88, 208

[54] ATLAS Collaboration, "Alignment of the ATLAS Inner Detector and its Performance in 2012." ATLAS-CONF-2014-047, 2014. 88

[55] ATLAS Collaboration, "Electron reconstruction and identification efficiency measurements with the ATLAS detector using the 2011 LHC proton–proton collision data," *The European Physical Journal C*, vol. 74, p. 2941, Jul 2014. 89

[56] Matteo Cacciari and Gavin P. Salam and Gregory Soyez, "The anti-k_T jet clustering algorithm," *Journal of High Energy Physics*, vol. 2008, no. 04, p. 063, 2008. 89

[57] ATLAS Collaboration, "Jet Calibration and Systematic Uncertainties for Jets Reconstructed in the ATLAS Detector at 13 TeV." ATL-PHYS-PUB-2015-015, 2015. 89

[58] ALEPH Collaboration, DELPHI Collaboration, L3 Collaboration, OPAL Collaboration, LEP Electroweak Working Group, "Electroweak measurements in electron-positron collisions at W-boson-pair energies at LEP," *Physics Reports*, vol. 532, no. 4, pp. 119 – 244, 2013. Electroweak Measurements in Electron-Positron Collisions at W-Boson-Pair Energies at LEP. 89

[59] ATLAS Collaboration, "Electron efficiency measurements with the ATLAS detector using 2012 LHC proton–proton collision data," *The European Physical Journal C*, vol. 77, p. 195, Mar 2017. 91

[60] W. Buttinger, "Using event weights to account for differences in instantaneous luminosity and trigger prescale in monte carlo and data," 2017. 92

[61] Olivier Simard and the ATLAS Liquid Argon Calorimeter Group, "The monitoring and data quality assessment of the ATLAS liquid argon calorimeter," *Journal of Physics: Conference Series*, vol. 587, no. 1, p. 012008, 2015. 97

[62] ATLAS Collaboration, "Reconstruction of primary vertices at the ATLAS experiment in Run 1 proton–proton collisions at the LHC," *The European Physical Journal C*, vol. 77, p. 332, May 2017. 97

[63] ATLAS Collaboration, "Selection of jets produced in 13 TeV proton-proton collisions with the ATLAS detector." ATLAS-CONF-2015-029, 2015. 97

[64] ATLAS Collaboration, "Measurement of the W-boson mass in pp collisions at $\sqrt{s}$ =7 TeV with the ATLAS detector," *The European Physical Journal C*, vol. 78, p. 110, Feb 2018. 107, 140

[65] ATLAS Collaboration, "Measurement of the muon charge asymmetry from W bosons produced in proton-proton collisions at 8 TeV with the ATLAS detector," 2015. 118, 155, 168

[66] ATLAS Collaboration, "Jet energy scale measurements and their systematic uncertainties in proton-proton collisions at $\sqrt{s} = 13$ TeV with the ATLAS detector," *Phys. Rev. D*, vol. 96, p. 072002, Oct 2017. 131, 132

[67] ATLAS Collaboration, "Luminosity determination in pp collisions at $\sqrt{s}$ =8 TeV using the ATLAS detector at the LHC," *The European Physical Journal C*, vol. 76, p. 653, Nov 2016. 132

[68] F. L. Manghi, "The LUCID detector ATLAS luminosity monitor and its electronic system," *Nuclear Instruments and Methods in Physics Research Section A: Accelerators, Spectrometers, Detectors and Associated Equipment*, vol. 824, pp. 311 – 312, 2016. Frontier Detectors for Frontier Physics: Proceedings of the 13th Pisa Meeting on Advanced Detectors. 132

[69] G. Avoni and M. Bruschi and G. Cabras and D. Caforio and N. Dehghanian and A. Floderus and B. Giacobbe and F. Giannuzzi and F. Giorgi and P. Grafstrom and V. Hedberg and F. Lasagni Manghi and S. Meneghini and J. Pinfold and E. Richards and C. Sbarra and N. Semprini Cesari and A. Sbrizzi and R. Soluk and G. Ucchielli and S. Valentinetti and O. Viazlo and M. Villa and C. Vittori and R. Vuillermet and A. Zoccoli, "The new LUCID-2 detector for luminosity measurement and monitoring in ATLAS," *Journal of Instrumentation*, vol. 13, pp. P07017–P07017, jul 2018. 133

[70] R. Barlow and C. Beeston, "Fitting using finite Monte Carlo samples," *Computer Physics Communications*, vol. 77, no. 2, pp. 219 – 228, 1993. 134

[71] ATLAS collaboration, "Measurement of the double-differential high-mass Drell-Yan cross section in pp collisions at $\sqrt{s}$ =8 TeV with the ATLAS detector," *Journal of High Energy Physics*, vol. 2016, p. 9, Aug 2016. 140

[72] ATLAS Collaboration, "Proposal for particle-level object and observable definitions for use in physics measurements at the LHC." ATL-PHYS-PUB-2015-013, 2015. 152

[73] B. Laforge and L. Schoeffel, "Elements of statistical methods in high-energy physics analyses," *Nuclear Instruments and Methods in Physics Research Section A: Accelerators, Spectrometers, Detectors and Associated Equipment*, vol. 394, no. 1, pp. 115 – 120, 1997. 158

[74] ATLAS Collaboration, "Measurement and QCD Analysis of Differential Inclusive W and Z Production and Leptonic Decay Cross Sections with 2011 ATLAS data," 2013. 168

[75] ATLAS Collaboration, "Measurement of W and Z-boson production cross sections in pp collisions at $\sqrt{s}$ =13 TeV with the ATLAS detector," *Physics Letters B*, vol. 759, pp. 601 – 621, 2016. 168

List of Figures

List of Tables